Grupo de Física de Coloides y Polímeros

Departamento de Física de la Materia Condensada

Facultad de Física

Tesis doctoral, 2012

Self-Assembly of Synthetic and Biological Polymeric Systems of Technological Interest

Josué Elías Juárez Onofre

Víctor Mosquera Tallón, Catedrático, y **Pablo Taboada Antelo**, Profesor Titular, ambos del Departamento de Física de la Materia Condensada de la Universidad de Santiago de Compostela,

INFORMAN:

Que el trabajo de investigación titulado "*Self-assembly of Synthetic and Biological Polymeric Systems of Technological Interest*", presentado por Josué Elías Juárez Onofre ha sido dirigido por ellos en el Grupo de Física de Coloides y Polímeros del Departamento de Física de la Materia Condensada de la Universidad de Santiago de Compostela, y reúne los requisitos de calidad y rigor científicos necesarios para optar al Grado de Doctor en Ciencia y Tecnología de Materiales.

Para que así conste a los efectos oportunos.

Santiago de Compostela, 6 de febrero de 2012

Fdo. Víctor Mosquera Tallón

Fdo. Pablo Taboada Antelo

Agradecimientos

A mi Familia

A mi Padre y Madre

Nuestra vida está dividida en diferentes períodos y en cada uno de ellos siempre se encuentran personas que influyen de forma esencial en su devenir, regalándonos su amistad y compartiendo gran parte de su tiempo y conocimiento.

Primero, y de la manera más atenta, agradezco a mis supervisores de este trabajo, Víctor Mosquera Tallón y Pablo Taboada Antelo, por el conocimiento y soporte científico que me han dado durante la etapa académica y dirigiendo esta tesis doctoral. También agradecerles el haber hecho lo "imposible" para que pudiera iniciar (ellos recordarán lo difícil y cómico de la situación) y desarrollar este Doctorado en Ciencia y Tecnología de Materiales en la Universidad de Santiago de Compostela.

También me gustaría agradecer al profesor Stephen Yeates por el apoyo científico y paciencia durante mi estancia en la Facultad de Química de la Universidad de Manchester. También quiero agradecer al profesor Miguel Valdéz de la Universidad de Sonora por su apoyo técnico y científico.

Por otra parte, también mi más sincero agradecimiento mis compañeros-amigos-colegas del Grupo de Física de Coloides y Polímeros: Emilio Castro, Sonia Goy, Silvia Barbosa, Adriana Cambón, Antonio Topete y Manuel Alatorre, por formar parte de este período, compartiendo su tiempo y conocimiento.

Me siento afortunado en tener a otros muchos compañeros-amigos-colegas y, por eso, aprovecho para agradecerles su amistad incondicional, y haciendo uso de la poca memoria que tengo trataré de citarlos en orden cronológico: Felipe Areais, Ceila Fong, Tareixa Regueira, Joel Pinto, Bea Ordoñez, "Mary Joe", "Mallegue", Agueda, "Cío", Hassan, Irais Batista y José Ríos, Alejandra Parra, Natalia Hassan (Wua yu Min), Elena Blanco, Paula y Miguel, Liliana, Fernando, "Toyis" y pido disculpas porque seguro olvidé a alguien. A mis amigos de la residencia Cadarso.

Quiero agradecer también al equipo de microscopía electrónica: Miro, Raquel y Merche, por el tiempo y paciencia que dedicaron en enseñarme a manejar los equipos de TEM, microscopía confocal y SEM.

A TODOS, MUCHAS GRACIAS!!!

List of papers

I. *Self-assembly process of different poly(oxystyrene)-poly(oxyethylene) block copolymers: spontaneous formation of vesicular structures and elongated micelles*. **Juárez, J.; Taboada, P.; Valdez, M. A.; Mosquera, V.** 2008, Langmuir, Vol. 24, pp. 7107-7116.

II. *Existence of different structural intermediates on the fibrillation pathway of human serum albumin.* **Juárez, J.; Taboada, P.; Mosquera, V.** 2009, Biophysical Journal, Vol. 96, pp. 2353-2370.

III. *Influence of electrostatic interactions on the fibrillation process of human serum albumin.* **Juárez, J.; Taboada, P.; Mosquera, V.** 2009, J. Phys. Chem. B, Vol. 113, pp. 10521-10529.

IV. *Additional supra-self-assembly of human serum albumin under amyloid-like-forming solution conditions.* **Juárez, J.; Taboada, P.; Goy-López, S.; Cambón, A.; Madec, M. B.; Yeates, S. G.; Mosquera, V.** 2009, J. Phys. Chem. B, Vol. 113, pp. 12391-12399.

V. *Surface properties of monolayers of amphiphilic poly(ethylene oxide)-poly(styrene oxide) block copolymers*. **Juárez, J.; Goy-López, S.; Cambón, A.; Valdez, M. A.; Taboada, P.; Mosquera, V.** 2010, J. Phys. Chem. Vol. 114, pp. 15703-15712.

VI. *Obtention of metallic nanowires by protein biotemplating and their catalytic application*. **Juárez, J.; Cambón, A.; Goy-López, S.; Topete, A.; Taboada, P.; Mosquera, V.** 2010, J. Phys. Chem. Lett. Vol. 1 pp. 2680-2687.

VII. *One-dimensional magnetic nanowires obtained by protein fibril biotemplating*. **Juárez, J.; Cambón, A.; Topete, A.; Taboada, P.; Mosquera, V.** 2011, Chem. Eur. J. Vol. 17 pp. 7366-7373.

VIII. *Hydration effects on the fibrillation process of a globular protein: The case of human serum albumin.* **Juárez, J.; Alatorre-Meda, M.; Cambón, A.; Topete, A.; Barbosa, S.; Taboada, P.; Mosquera, V.** 2012, Soft Matter. DOI:10.1039/C2SM06762E.

Índice general

Chapter 6

Papers on amyloid fibrils

Resumen

Desde tiempos ancestrales, las moléculas poliméricas, también conocidas como macromoléculas o moléculas gigantes, han representado un material útil para el desarrollo de la humanidad. Actualmente, es difícil imaginar el desarrollo de una sociedad organizada sin el uso de materiales poliméricos. Por ejemplo, desde hace algunas décadas hasta nuestros días, estos materiales poliméricos son utilizados para satisfacer diferentes necesidades de gran importancia como son la construcción de refugios, viviendas (casas, residencias, etc.) y vestimenta; dependiendo del uso que se requiera, se emplearán materiales poliméricos sintéticos (tales como el poliéster, polietileno, polipropileno, teflón, resinas, entre otros) y/o naturales, también conocidos como biopolímeros (madera, pieles, gomas y resinas naturales, algodón seda, lana). Por otra parte, diferentes macromoléculas desempeñan una función de gran importancia biológica. Biomacromoléculas como los ácidos ribonucleicos (ADN y ARN), proteínas y polisacáridos son de vital importancia en distintos procesos bioquímicos para el crecimiento y desarrollo de un organismo vivo; además, proteínas y polisacáridos son utilizados por los organismos vivos como soportes estructurales de células, tejidos y órganos.

El uso de los materiales poliméricos no sólo está limitado a los usos descritos anteriormente. Hoy en día una gran variedad de materiales poliméricos, tanto sintéticos como naturales, están siendo utilizados en diferentes áreas tecnológicas como la ciencia de materiales, medicina clínica o industria farmacéutica, entre otras. Además, los procesos de síntesis química, hacen posible diseñar una macromolécula con propiedades fisicoquímicas deseadas. Con este fin, diversos grupos de investigación han sintetizado diferentes tipos de copolímeros con carácter anfifílico. El diseño de la arquitectura molecular del copolímero puede ser tan sencillo como un polímero lineal, o tan complejo como un copolímero de injerto o tipo estrella; la arquitectura molecular puede controlarse por medio de procedimientos de síntesis química.

Nuestro trabajo de investigación se divide en dos etapas: la primera parte se enfocó a la caracterización estructural y de las propiedades físico-químicas de tres copolímeros de bloque con potencial interés para ser empleados como sistemas de liberación farmacológica; mientras que en la segunda parte se ha realizado un estudio del proceso de autoensamblaje en la forma de fibras

amiloides de la proteína albúmina de suero humano (HSA), su caracterización estructural y de sus propiedades físico-químicas, y su uso potencial como biomateriales.

Debido a que parte de este trabajo consiste en la caracterización de tres copolímeros de bloque, describiremos brevemente este tipo de macromoléculas. Para un copolímero, el "esqueleto" de la cadena macromolecular está constituido por más de un monómero o unidad de repetición. Por lo tanto, la estructura molecular de un copolímero de bloque consiste en la unión química de dos o más macromoléculas de homopolímeros diferentes. De acuerdo al número de bloques (unidades homopoliméricas) estos polímeros se denominan copolímeros dibloque, tribloque o multibloque. Generalmente, estos homopolímeros son de diferente naturaleza (hidrófilo o hidrófobo) proporcionando a la macromolécula un carácter anfifílico.

Bajo ciertas condiciones, los copolímeros pueden adoptar una configuración tipo gusano o espagueti, mientras que para otras, el polímero puede auto-asociarse hasta formar nanoestructuras regulares. Por ejemplo, si un copolímero de bloque se encuentra en disolución acuosa, en donde el agua es un solvente selectivo para uno de los bloques, los segmentos hidrófobos de las macromoléculas tienden a auto-asociarse, formando estructuras específicas, evitando el contacto con las moléculas del disolvente. La auto-asociación origina un amplio rango de comportamientos de fases, en los que se incluye la formación de micelas, nanovarillas, vesículas o grandes agregados. Estas estructuras poliméricas presentan, en particular, un especial interés en el área biomédica. Así, las estructuras micelares y vesiculares pueden ser utilizados como sistemas de liberación de fármacos y proteínas, así como en el desarrollo de nanoreactores y de biosensores.

Los copolímeros de bloque de oxialquilenos están constituidos, generalmente, por el bloque hidrófilo polióxido de etileno (OCH_2CH_2 es la unidad de óxido de etileno, EO) y por un segundo bloque hidrófobo que puede ser: un bloque de polióxido de propileno (PO), un bloque de polióxido de estireno (SO) u otro tipo de bloque hidrófobo. En medio acuoso, la estructura de los agregados que forman estos copolímeros de bloque está gobernada por el balance de las fuerzas de interacción entre los bloques moleculares que constituyen el esqueleto del copolímero con las moléculas de agua, y por las interacciones intermoleculares entre las cadenas del copolímero (ya

que las cadenas hidrófilas se expanden evitando las interacciones entre segmentos que no sean favorables, mientras que las hidrófobas se contraen para minimizar el contacto con las moléculas del disolvente). Este tipo de interacciones pueden modificarse por medio de factores físicos y, de esta manera, se puede controlar la arquitectura de los agregados. Los factores físicos que se varían con más frecuencia son: el peso molecular, la longitud relativa de los bloques, la estructura de los bloques hidrófobos, las propiedades en disolución, etc. De esta forma, se ha observado que en disoluciones acuosas diluidas estos copolímeros de bloque anfifílicos se asocian para formar micelas esféricas. Al aumentar la concentración del copolímero se obtienen mesofases liotrópicas cristalinas (geles), en donde las micelas se encuentran altamente empaquetadas en una estructura cúbica centrada en las caras (fcc) o centrada en el cuerpo (bcc).

En el presente trabajo, se estudió el proceso de micelización, gelificación y la estructura de los agregados de tres copolímeros de poli(óxido de etileno)-poli(óxido de estireno): $EO_{12}SO_{10}$, $EO_{10}SO_{10}EO_{10}$, y $EO_{137}SO_{18}EO_{137}$, donde los subíndices indican la longitud de cada bloque. De estos polímeros, dos tienen la misma longitud del bloque de poli(óxido de estireno) ($EO_{12}SO_{10}$ y $EO_{10}SO_{10}EO_{10}$,), mientras que la longitud del bloque EO para el tercer copolímero es mucho más largo ($EO_{137}SO_{18}EO_{137}$). Es importante mencionar que estos copolímeros de bloque fueron sintetizados en colaboración con los Profs. David Attwood y Colin Booth de la en la School of Pharmacy and Pharmaceutical Sciences y en la School of Chemistry of the University of Manchester, respectivamente. La caracterización de estos copolímeros de bloque se realizó en dos fases: La primera parte consistió en el análisis de las propiedades estructurales y físico-químicas de los copolímeros en el seno de disoluciones acuosas, mediante diversas técnicas experimentales tales como: medidas de tensión superficial, medidas de dispersión de luz láser (DLS y SLS), microscopía óptica de luz polarizada (POM), microscopía de transmisión electrónica (TEM) y microscopía electrónica de barrido (SEM). Por medio de las medidas experimentales para los copolímeros $EO_{12}SO_{10}$, $EO_{10}SO_{10}EO_{10}$, y $EO_{137}SO_{18}EO_{137}$, combinado con modelos teóricos (según los datos experimentales obtenidos) ya publicados, se determinaron la concentración micelar crítica, así como propiedades micelares (tamaño de las micelas y número de agregación) y vesiculares (para el caso del copolímero $EO_{12}SO_{10}$); imágenes de los agregados estructurados y el comportamiento reológico. En este trabajo, en particular se observó por primera vez la posibilidad de que los copolímeros de poli(óxido de etileno)-poli(óxido de estireno) pueden formar estructuras vesiculares, sin necesidad de aportes externos de energía. Estas estructuras

vesiculares son el resultado de la auto-asociación del copolímero $EO_{12}SO_{10}$ en disolución acuosa, y se encuentran en coexistencia con estructuras micelares esféricas. Este resultado se confirmó por dispersión de luz láser, TEM y cryo- SEM. El tamaño de las vesículas varía entre 60 y 500 nm. Para los copolímeros $EO_{10}SO_{10}EO_{10}$ y $EO_{137}SO_{18}EO_{137}$ se observaron estructuras en la forma de micelas alargadas y esféricas, respectivamente. Comparando el alto número de agregación obtenido para las micelas del copolímero $EO_{10}SO_{10}EO_{10}$ por dispersión de luz láser con el número máximo de agregación teórico que correspondería a una micela esférica, se puede concluir que la geometría micelar no se corresponde con una geometría esférica, pero sí con una geometría más alargada. Este resultado es confirmado por medio de imágenes obtenidas por TEM. La prueba de inversión de tubo se utilizó para definir las fronteras que dividen la fase de un gel blando con la fase de un gel duro de las disoluciones del copolímero $EO_{137}SO_{18}EO_{137}$. De acuerdo con los resultados obtenidos por reología, los copolímeros $EO_{12}SO_{10}$ y $EO_{10}SO_{10}EO_{10}$ no forman geles en el rango de concentraciones estudiados en este trabajo.

Por otra parte, la capacidad de adsorción y de auto-organización molecular en una interface de un copolímero de bloque para formar nanoestructuras bien definidas en dos dimensiones permiten que estos materiales poliméricos puedan utilizarse como estabilizantes coloidales, o como agentes recubridores y estabilizantes de espumas y emulsiones.

Así, un amplio rango de estudios han analizado el comportamiento interfacial de copolímeros de poli(óxido de etileno)-poli(óxido de propileno)-poli(óxido de etileno) (EO-PO-EO) ó “Pluronics”, copolímeros de estrella de EO-PO-EO, también conocidos como “Tetronics” y de los copolímeros poli(óxido de butileno)-poli(óxido de etileno) (BO-EO). Sin embargo, pocos estudios existen sobre la caracterización en la interfase de los copolímeros de poli(óxido de etileno)-poli(óxido de estireno). El análisis de sus propiedades de adsorción es interesante ya que puede proporcionar importante información sobre su estabilidad intefacial y posterior agregación. Así, en el presente trabajo, se estudiaron las propiedades de adsorción en la interface aire-agua y en la interface cloroformo-agua de los copolímeros $EO_{12}SO_{10}$, $EO_{10}SO_{10}EO_{10}$ y $EO_{137}SO_{18}EO_{137}$. El trabajo de investigación se desarrolló mediante las técnicas experimentales: tensiómetro de gota , monocapas o películas de Langmuir-Blodgett y microscopía de fuerza atómica (AFM). Las cinéticas de adsorción de las disoluciones copoliméricas, en ambas interfaces, se determinaron por la técnica de gota suspendida. Los resultados de tensión superficial muestran que la adsorción en la

interface aire-agua de los copolímeros estudiados disminuye conforme se incrementa la hidrofobicidad del copolímero. Los datos obtenidos mediante reología interfacial de la película copolimérica adsorbida en la interface aire-agua muestran que la capa adsorbida en la interface se comporta como un sólido en todo el rango de frecuencias analizadas, mientras que la capa polimérica adsorbida en la interface cloroformo-agua se comporta como un fluido viscoso para el mismo rango de frecuencias. Las isotermas de compresión, presión superficial vs área (Π vs A), y las monocapas de Langmuir-Blodgett se obtuvieron con una balanza de Langmuir-Blodgett. Las diferencias en las isotermas de Langmuir obtenidas para los tres copolímeros de bloque tienen su origen en la diferente relación entre los bloques hidrófobo/hidrófilo. Bajo esta consideración, el copolímero $EO_{137}SO_{18}EO_{137}$ muestra una isoterma de adsorción con cuatro estados característicos, mientras que en las isotermas de adsorción de los otros dos copolímeros ($EO_{12}SO_{10}$ y $EO_{10}SO_{10}EO_{10}$), sólo se observan dos regiones. Las monocapas de Langmuir-Blodgett se obtuvieron a dos diferentes valores de presión superfcial (5 y 11 mN/m), y sus imágenes topográficas fueron analizadas por AFM. Para ambas presiones, las imágenes topográficas revelan la existencia de micelas circulares en la superficie de la película. Sin embargo, el tamaño de las micelas disminuye con el aumento de la presión interfacial y, a su vez se observa un incremento del espesor de la monocapa.

En la segunda etapa de nuestro trabajo, se estudiaron los procesos de ensamblaje molecular en la forma de fibras en disolución acuosa de la proteína seroalbúmina humana (HSA, sus siglas en inglés), bajo diferentes condiciones de temperatura, pH y fuerza iónica; y la posible aplicación de estas nanoestructuras en diversas aplicaciones como catalizadores o elementos de contraste de imagen.

In vivo, la agregación incontrolada de ciertas proteínas está relacionada directamente con diferentes dolencias que afectan la salud humana. Uno de los productos de mayor interés originados por la inadecuada agregación proteica son las fibras amiloides. Estas estructuras fibrilares se han detectado en con más de 20 enfermedades (neurodegenerativas o no) tales como el Alzheimer, Huntington, el mal de Parkinson, o la diabetes tipo II, entre otras. La capacidad de fibrilación es independiente de la estructura nativa de la proteína, no obstante, la estructura proteica primaria aparece como un factor importante en las primeras fases del proceso de formación de las fibras amiloides, en su cinética de formación y en su estabilidad. La fibrilación se

origina debido a condiciones ambientales en las que se promueve la desnaturalización parcial o completa de la estructura nativa de la proteína, por lo que para una proteína o cadena polipeptídica, la formación de la fibra amiloide representa una estructura estable alternativa a la estructura nativa.

Las fibras tipo amiloide presentan características termodinámicas y estructurales bien definidas Estas fibras se caracterizan, en general, por ser lineales, rígidas y sin ramificaciones, con una anchura que varía entre los 5-12 nm, tal como se ha observado por microscopía de transmisión electrónica; además, tienen la propiedad de enlazarse a marcadores orgánicos específicos, como Congo Red y Tioflavina T. Muestran también un patrón común de difracción de rayos-X característico para una estructura β-cruzada. Como se mencionó anteriormente, las fibras de amiloide son responsables de distintas enfermedades como el mal de Parkinson, deficiencia de α_1-tripsina, Alzheimer y encefalopatías espongiformes. El origen de estas enfermedades está asociado a la conversión de proteínas monoméricas a agregados proteicos insolubles, los cuales se depositan en los tejidos/órganos del cuerpo.

La proteína plasmática más abundante del sistema circulatorio es la albúmina (representa aproximadamente del 52 al 60 % de las proteínas plasmáticas), cuyas funciones son la regulación de la presión osmótica sanguínea y en el transporte y almacenamiento de moléculas endógenas y exógenas (hormonas, iones, ácidos grasos, drogas). A nivel industrial, la albúmina tiene un rol importante en la tecnología médica, de alimentos, fármacos y en el desarrollo de biosensores debido a sus fuertes propiedades de adsorción. La HSA es una proteína globular formada por una sola cadena polipeptídica. La estructura de esta proteína está constituida por 585 residuos de aminoácidos, con un peso molecular de aproximadamente 66,500 g/mol. La estructura secundaria de la HSA consta principalmente de hélices α (60 %); además presenta 17 puentes disulfuro, los que le confiere una gran estabilidad estructural. La estructura globular de la HSA está compuesta por tres dominios principales y seis subdominios unidos por puentes disulfuro. Debido a su importancia fisiológica como proteína de transporte y reguladora de la presión osmótica, y a su facilidad de agregación *in vitro*, la HSA se puede considerar como un modelo adecuado para realizar estudios sobre los mecanismos de agregación proteica, con el fin de obtener una aproximación y un mejor entendimiento de los mecanismos de agregación proteica asociada a la amiloidogénesis. Ya que la estructura nativa de la HSA carece de cualquier predisposición a formar

fibras amiloides, la agregación de la albúmina sérica se puede promover cambiando las condiciones de disolución (tales como de pH, altas temperaturas y por medio de agentes químicos desnaturalizantes), favoreciendo la desestabilización de la estructura nativa de la HSA.

Así, en este trabajo se analizó la predisposición a la fibrilación de la HSA bajo diferentes condiciones de disolución (pH, temperatura, fuerza iónica, composición del disolvente), así como las propiedades físicas y estructurales de las fibras amiloidales resultantes. Las cinéticas de agregación, los cambios conformacionales durante la auto-asociación de los monómeros de albúmina y las estructuras de las diferentes estructuras intermedias en la ruta de fibrilación se determinaron por fluorescencia de Tioflavina T (ThT) y absorbencia del Congo red; dicroísmo circular (CD); fluorescencia intrínseca de la HSA; espectroscopía de infra-rojo (FTIR); difracción de rayos-X; TEM; SEM y AFM. El proceso de la fibrilación de la HSA se prolonga durante varios días de incubación, y se lleva a cabo sin la presencia de una fase de demora; excepto cuando las disoluciones de albúmina se incubaron a pH ácido, temperatura ambiente y en ausencia de electrólito. La ausencia de la fase de demora se debe al hecho de que la agregación inicial está dirigida por el mecanismo denominado “cuesta abajo”, que no requiere de una alta organización estructural ni de la formación de núcleos proteicos inestables. El proceso de fibrilación de la HSA está acompañada por un incremento progresivo de la estructura secundaria hoja-β y estructuras ordenadas al azar; esta transición se lleva a cabo a expensas de la estructura α-hélice, como se observó mediante espectroscopía de fluorescencia de ThT, de CD y de FTIR. De acuerdo a las distintas condiciones de incubación, la estructura nativa de la proteína se altera de distinta manera/grado, implicando una variación en el contenido de las diferentes estructuras secundarias; estas variaciones implican la aparición de diversos agregados estructurales que se forman en el proceso de agregación fibrilar. Estos agregados pueden tomar la forma de: clústeres oligoméricos globulares, estructuras rígidas esféricas y agregados en forma de anillos. La formación fibrilar puede tener lugar a través de la asociación de los intermedios oligoméricos mencionados, conduciendo a la formación de protofibras y, posteriormente, fibras. Estas fibras resultantes son alargadas, con ondulaciones. La longitud de las fibras obtenidas depende de las condiciones de incubación. Probablemente las hebras-β que componen la estructura de hoja-β en las fibras de HSA se encuentran en un arreglo antiparalelo. La aparición de fibras amiloides maduras con estructuras morfológicas más complejas tiene lugar a largos periodos de incubación (fibras largas y rígidas, estructuras planas y alargadas, etc.). La tendencia de los oligómeros proteicos a alinearse

con las fibras vecinas más cercanas puede resultar en el crecimiento y maduración de las fibras rígidas. Además, estas fibras pueden asociarse en otras estructuras supramoleculares tales como esferulitas e incluso geles fibrilares. La presencia de esferulitas de fibras amiloides se confirmó por POM, microscopía confocal y TEM. La HSA tiene la capacidad de formar geles fibrilares entrecruzados, los cuales se forman por medio de interacciones intermoleculares no específicas a valores de pH que se encuentran lejos del punto isoeléctrico de la HSA, cuando se sobrepasa un umbral de concentración de proteínas y/o de fuerza iónica (punto de gelificación), tal como se observó por reología. Por otra parte, cuando la HSA se encuentra cerca de su punto isoeléctrico, el proceso de agregación proteica es tan rápido, que no permite una organización estructural substancial para permitir la formación de estructuras ordenadas, formando así un gel de tipo particulado.

A pesar de la importancia de las fibras amiloides en el área clínica, actualmente existen otras áreas científicas que prestan especial interés en el estudio de las propiedades estructurales y de agregación fibrilar, en la búsqueda de nuevos materiales y posibles aplicaciones en campos de ingeniería y nanotecnología. El desarrollo de estructuras a escala mesoscópica es de gran importancia en el desarrollo de dispositivos opto-electrónicos, como biosensores, materiales biocompatibles, etc. Usualmente, los materiales nanoestructurados se obtienen a través de dos estrategias: La primera, llamada “top-down”, consiste en la reducción de tamaño de un material más grande; sin embargo, mediante esta estrategia se obtienen materiales en escala micrométrica debido a que la reducción del tamaño sólo se puede realizar hasta donde las propiedades del tamaño del material lo permita. En la segunda estrategia, “bottom-up”, se utilizan moléculas pequeñas, como las proteínas, péptidos, fosfolípidos y ácidos nucleicos (ADN y RNA) como elementos constituyentes, que bajo condiciones controladas, permiten obtener estructuras bien ordenadas gracias a las propiedades de auto-ensamblaje que poseen este tipo de biomoléculas.

Las propiedades de auto-asociación y ensamblaje que tienen estos biomateriales permiten, bajo condiciones controladas, obtener complejos nanoestructurados definidos. Las proteínas son una alternativa muy atractiva para la construcción de estas nanoestructuras, ya que además de tener un tamaño físico adecuado una gran estabilidad (comparado con los estructutras basadasen ácidos nucleicos y fosfolípidos), y unas excelentes propiedades de adsorción a sustratos como vidrio, óxido de silicio, u oro; por otra parte las proteínas presentan una serie de funciones que pueden

ser acopladas, por ejemplo, a circuitos electrónicos durante la construcción de nanodispositivos gracias a su alta flexibilidad, aún cuando estos materiales son no conductores, pueden recubrirse con metales conductores.

En la parte final de nuestro trabajo hemos analizado el potencial de las fibras amiloides como nuevos nanomateriales con potenciales aplicaciones en distintos campos como la catálisis o la biomedicina Bajo este contexto, en perime lugar se obtuvieron nanocables de oro por medio de un proceso de crecimiento de "semillas" de oro utilizando fibras de la proteína lisozima como bioplantillas. Se decidió emplear lisozima pues sus fiobras han sido muy estudiadas y7 presnetan una geomtería recta sin ramificaciones, muy adecuada para el objetivo de la construcción de un nanocable metálico. El grado de metalización de la fibra se controló por la adicción secuencial de sal de oro hasta alcanzar un recubrimiento completo de la fibra. Los híbridos orgánico-metálicos obtenidos se utilizaron como catalizadores en la reducción del *p*-nitrofenol a *p*-aminofenol.

Por otra parte, se obtuvieron nanocables magnéticos utilizando como bioplantillas las fibras de lisozima y de HSA. La obtención de estos materiales híbridos se realizó por medio de una reacción de precipitación *in situ* de la mezcla de sales de hierro Fe^{+2}:Fe^{+3} en una relación 1:2, en presencia de NH_4OH, siendo el producto de esta reacción nanopartículas de magnetita. Las propiedades magnéticas de los híbridos se determinaron mediante SQUID (por sus siglas en inglés: superconducting quantum interference device), y se compararon con las propiedades magnéticas de nanopartículas libres de magnetita, observándose una mejora sustancial en sus propiedades magnéticas. Finalmente, la posible utilidad de estos materiales biohíbridos como agentes de contraste se corroboró mediante imágenes de resonancia magnética nuclear a diferentes proporciones de dopado de la fibra proteica.

Abstract

In the present work, we investigated the micellization, gelation and the structure of aggregates of three poly(ethylene oxide)-poly(styrene oxide)-poly(ethylene oxide) block copolymers ($EO_{12}SO_{10}$, $EO_{10}SO_{10}E_{10}$ and $EO_{137}SO_{18}EO_{137}$, where E represents the oxyethylene unit, S the oxystyrene unit, and the subscripts correspond to the number of monomeric unit constituting the polymeric chain) in solution. We also investigated the adsorption process and the surface properties of these block copolymers at the air-water (a/w) and chloroform-water (c/w) interfaces. Since these copolymers possess a more hydrophobic middle block –the styrene oxide unit, they should gives rise to more efficient drug delivery systems, in which geometry might play a key role for drug solubilisation and cell uptake. For these reasons, a detailed characterization of the physicochemical properties of these copolymers is required.

In this work, the spontaneous formation of vesicles by the block copolymer $EO_{12}SO_{10}$ without the need of external energy input has been observed In aqueous bulk solution. This is the first time that vesicle formation for styrene oxide based-block copolymers is reported. These vesicular structures are in coexistence with spherical micelles, as confirmed by dynamic light scattering (DLS), polarized optical microscopy and transmission and cryo-scanning electron microscopies. Meanwhile, for block copolymers $EO_{10}SO_{10}E_{10}$ and $EO_{137}SO_{18}EO_{137}$ only one species is found in solution, assigned to elongated and spherical micelles, respectively. The adsorption kinetics of these block copolymers at both (a/w) and (c/w) interfaces were determined by the pendant drop method. Measurements of their interfacial rheological behaviour showed that the adsorption layer at the (a/w) interface manifests solid-like properties in the whole accessible frequency range, whereas a viscous fluid-like behaviour is displayed at the (c/w) interface. The adsorption isotherm for the block copolymer $EO_{137}SO_{18}EO_{137}$ displays the four classical regions (pancake, mushroom, brush, and condensed states), whereas for $EO_{12}SO_{10}$ and $EO_{10}SO_{10}E_{10}$ copolymers only two regions were observed. Probably, these observed differences in the monolayer isotherms arose from their different hydrophobic/hydrophilic block ratios and block lengths.

On the other hand, the fibrillation propensity of the protein human serum albumin (HSA) was analysed under different solution conditions (varying pH, temperature, ionic strength and solvent

composition). Fibrillation is an important self-assembly mechanism of proteins which allows them to achieve an energy state even lower than their own native state. Also, the presence of protein fibrils has been related to the appearance and development of more than 20 neurodegenerative and non-neurodegenerative diseases, known as amyloid diseases. Hence, a profound knowledge about the fibrillation mechanisms and the structure of the resulting protein assemblies is required to develop new therapeutical strategies, but also to exploit the special structural properties of such protein aggregates in new technological fields.

In this way, the kinetics of HSA fibril formation under different solution conditions and the structures of resulting fibrillar aggregates were determined. It was observed that fibril formation is largely affected by electrostatic shielding: At physiological pH, fibrillation is more efficient and faster in the presence of up 50 mM NaCl. In contrast, under acidic conditions a continuous progressive enhancement of HSA fibrillation is observed as the electrolyte concentration in solution increases. The fibrillation process is accompanied by a progressive increase in β-sheet and unordered conformations at the expense of α-helix one as revealed by CD, FT-IR and tryptophan fluorescence spectra. The presence of structural intermediates in the aggregation pathway, such as oligomeric clusters (globules), bead-like structures, and ring-shaped aggregates suggest that fibril formation takes place by the competent-association of these aggregates. The resultant fibrils are elongated but curly, and differ in length depending on solution conditions. In addition, very long incubation times lead to a complex morphological variability of amyloid fibrils, such as long straight fibrils or flat-ribbon structures, amongst other. In addition, the formations of ordered aggregates of amyloid fibrils, such as spherulites, which possess a radial arrangement of the fibrils around a disorganized protein core, or fibrillar gels were also observed. All these observations lead to the conclusion that HSA can be used as a suitable model to study protein fibrillogenesis.

On the other hand, the utility of the obtained HSA fibrils as building blocks to construct new and useful nanomaterials as tested. We reported a method to obtain metallic Au nanowires by using lysozyme protein fibrils as bioscaffolds to generate a complete gold coating layer on the biotemplate surface by the attachment of gold seeds and subsequent overgrowth of the coating layer by sequential addition of gold salt growth solution (seeded-mediated mechanism). We decided to use lysozyme fibrils since these display a straight and uniform core, which is more suitable for the generation of nanowires. To obtain full coverage of the protein fibril, suitable

[Au]/[protein] molar ratio and number of sequential additions of Au ions must be chosen. The hybrid metallic fibrils have been proved to be useful as catalytic substrates, provided their great catalytically activity when incorporated in the reduction reaction of *p*-nitrophenol to *p*-aminophenol by $NaBH_4$. On the other hand, we also reported a method to obtain magnetic Fe_3O_4 nanowires by using HSA and lysozyme protein fibrils as bioscaffolds to generate a magnetic Fe_3O_4 coating layer on the biotemplate surface by the *in situ* controlled Fe nanoprecipitation method. The magnetic properties of the magnetic nanowires have been tested by using a superconducting quantum interference device (SQUID), and their potential applicability as MRI contrast agents was analysed by means of magnetic resonance imaging at different Fe doping concentration in phantoms.

CHAPTER 1

SYNTHETIC AND NATURAL POLYMERS

Contents

1.1.- Introduction

Since many years ago, polymeric molecules have progressively gained a key role in human´s life and activity. Many examples about the use of polymers can be easily found in our daily activity in different fields such as clothing, health care, packing or waste water treatments; from the early times, humans have taken advantage of polymeric materials in the form of wood, leather, natural gums and resins, cotton fibres, wool and silk (1).

Polymeric molecules found in Nature also possess very important biological functions as in the case of nucleic acids, proteins or carbohydrates. These biomacromolecules take part in different biochemical processes and are necessary in anabolic and catabolic processes; furthermore, they fulfill an essential structural role during the development and growth of living organisms as evidenced, for example, in plants, which are mainly built from cellulose fibres, or animals, composed of linear protein materials such collagen in skin, sinew and bone, myosin in muscles, and keratin in nails and hair. Polymers are giant molecules built up by repetitive covalent unions of small chemical units known as monomers. Polymers usually have high molecular weights and, for this reason, are also called “macromolecules”. They can be classified in two main groups regarding their origin: synthetic and biological ones. In general,

synthetic polymers are obtained from processes developed in laboratories while biological polymers (biopolymers) are found in nature, but many of them can be also synthetically synthesized (1)-(3).

From a historical perspective, first attempts to obtain lab-synthesized polymers dated from 1868 with the synthesis of cellulose nitrate by the chemical modification of natural polymers (pyroxin made from cotton and nitric acid with camphor). However, in 1909, Leo Hendrick Baekeland synthesized a plastic material, the bakelite, which can be considered as the true first synthetic polymer. From 1920s, different polymers of commercial importance were synthesised; however, the main interest was focused on controlling their chemical composition along the synthetic process, and no cautions about a suitable control of the final molecular structure were considered since the synthesis of macromolecules was an empirical work. In the middle of 20^{th} century, chemists and physicists provided new methods to establish the structural description of polymeric molecules. In this regard, Herman Staudinger´s, a German chemist who introduced the concept of macromolecule, and W. T. Carother´s, an American chemist who classified the polymers according to their preparation method (i.e., addition and condensation polymers), works deserve special attention.

From a general point of view, polymer molecules show considerable flexibility due to rotation around molecular bonds. In solution, the shape of these macromolecules alters continuously due to thermal energy so they can be treated as random coils, even when the rotation around molecular bonds does allow complete flexibility, while steric and excluded volume effects oppose the formation of this kind of configuration. For these reasons, dissolved linear polymer molecules will tend to be more extended than random coils. In addition, polymer-polymer and polymer-solvent interactions exert an important effect in polymer chain configurations and must be taken into account. If segments of the polymer chains stick together, then a tighter configuration than random coil will result, enabling aggregate formation or precipitation (3).

1.2.- Classification of polymers.

Polymers can be classified in many different ways. The most obvious classification is based on the origin of the polymer; i.e., natural polymers (biological macromolecules) such as proteins, celluloses or natural gums, and synthetic polymers (non biological polymers). Overall, non-biological polymers are formed by flexible chains with a relatively “low” number of monomers

in contrast to biological polymers, which consist of a larger number of monomers and with stiffer chains.

1.2.1.- Synthetic polymers.

Synthetic polymers can be classified taking into account their physical and chemical characteristics, molecular structure, polymerisation mechanisms, chemical composition, building blocks or thermal behaviour. Among all of them, synthetic polymers have been classified into two classes according to their preparation method: i.e., condensation and addition polymers. For condensation polymers, the reaction occurs between two polyfunctional molecules by eliminating a small molecule, for example, water. In contrast, addition polymers are formed in a chain reaction of monomers which have double bonds in their molecular structure.

According to polymer structure, it is possible to divide synthetic polymers into three wide categories: linear, branched (non-linear) and cross-linked polymers. When the structural units are repeated in only one dimension, linear polymers are obtained. Their molecular structure is shown in Figure 1.1a. On the other hand, when the monomeric units are repeated in two or three dimensions through covalent bonds, branched, cross-linked or network polymers are obtained. In the case of branched polymers (also known as graft copolymers), single side-branched chains are connected to polymer backbones during the synthesis, and which remain singly dispersed (see Figure 1b). For cross-linked polymers, adjacent linear chains are chemically or physically connected to two or more polymer backbones serving as “bridges” to reticulate the polymeric system (see Figure 1.1c).

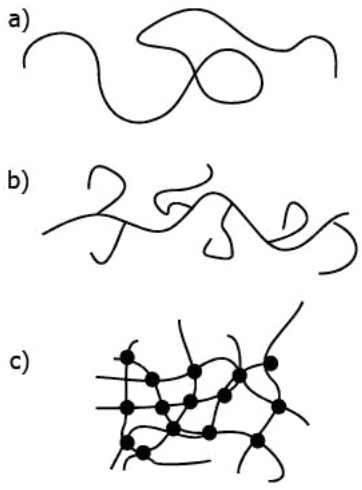

Figure 1.1. a) Linear, b) branched, and c) cross-linked polymers.

On the other hand, in terms of chemical composition, polymers can be classified as homopolymers and copolymers. Homopolymers are those polymers composed of only one type of structural unit, whereas copolymers posses two or more different monomers. Copolymers can be additionally classified considering the sequential and structural order of their constituent building blocks (see Figure 1.2):

- Random copolymer: the building segments in the backbone follow a random sequence.
- Alternate copolymer: the segments that configure the copolymer show a specific alternating sequence.
- Block copolymer: the polymer backbone is formed by the covalent bonding of large sequences of different homopolymers (each one forming a monomer).
- Graft copolymers: the copolymer molecule posses several segments grafted along the polymeric backbone.

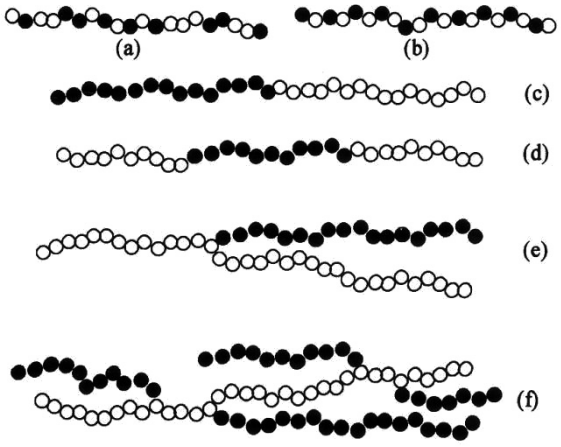

Figure 1.2. Schematic representation of different copolymers: (a) Random copolymer (b) alternating copolymer, (c) and (d) block copolymer, (e) and (f) graft copolymer.

1.2.2.- Biopolymers.

Natural polymers are vital for the development, growth and perpetuation of any living organism. Under this consideration, the most important ones are nucleic acids, proteins and polysaccharides. The building units of these biological polymers are nucleotides, amino acids, and carbohydrates, respectively. Among all these types, the present work is focused on the study of proteins since they are an essential constituent of all organisms and virtually participate in every process within cells.

1.2.3.- Proteins.

The most versatile macromolecules in living organisms are proteins. These play an important and crucial function in almost all biological processes, and are formed by the linkage of repetitive structural units, called amino acids, through peptides bonds (4). These are covalent chemical bonds formed between two amino acids, in which the carboxyl group of one molecule reacts with the amino group of the other, as shown in Figure 1.3. Thus, polypeptide chains have two different terminal groups: on one side, the polypeptide chain posses an amino group with positive polarity and, on the other, a carboxylic group with negative polarity. By convention, the amino group has been considered the beginning of the polypeptide chain.

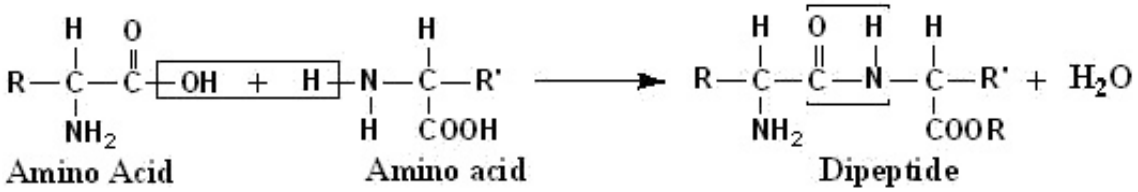

Figure 1.3. Peptide bond formation between the amino group of one amino acid and the carboxyl group of the other.

1.3.- (Bio)polymer structure.

It is known from elemental organic chemistry that the physical state of a homologous series of any type of chemical compound changes as their molecular size increases. From the low to the high molecular weight end of the molecular spectrum, the members of a series change progressively from the gaseous state, passing through liquids of increasing viscosity (decreasing volatility) to low melting solids and, ultimately, terminate in high-strength solids. Polymers belong to the high molecular weight end of the molecular spectrum, which provides them very interesting and useful properties such as unusual crystallinity, a wide range of thermal and mechanical behavior, and high resistance to chemical degradation. All these properties are related to the chemical and structural aspects of polymers, which can be divided into three different levels:

1. The monomer chemical structure (primary structure)
2. The single polymer chain (secondary level)
3. Aggregation of polymer chains (tertiary structure)

Additionally, to obtain a better knowledge about the macromolecular structure, it is necessary to study the molecular forces existing between polymer chains, such as ionic and covalent bonds, dipole-dipole interactions, hydrogen bonding, induction forces or van der Waals interactions, amongst others (5).

1.3.1.- Primary Structure.

The primary structure refers to the atomic composition and chemical structure of the monomers, which compose the polymeric chains. The electrical and chemical properties of polymeric chains are much related to the nature and chemistry of the constituent monomers and the kind of bonds established between them. Also, the macromolecular size of the polymer is responsible of their physical and mechanical properties.

1.3.2.- Secondary Structure.

To understand the properties of polymers, it is necessary to develop a physical picture of what these long molecules are really like. The secondary structure is a real physical description of the polymer, and describes the size and shape of a single individual macromolecule. The polymer molecular architecture can be influenced by both the nature of monomers and how they are bonded each other. In order to have a suitable description about the molecular architecture of a polymer, it is necessary to define two important terms: configuration and conformation.

Configuration refers to the relative position of the atoms in a polymeric chain, which is determined by the chemical bonds. The mechanical and thermal properties of polymers are a function of chain configuration; thus, the configuration of a polymer cannot be altered unless these bonds are broken. The different possible configurations of polymers which have the same stoichiometric molecular formula but different structural formulation are called isomers.

There are two main geometrical configurations of polymers: *cis* and *trans*. These structures cannot be changed by physical means (e.g. rotation). The *cis* configuration originates when substituent groups are located at the same side of a carbon-carbon double bond. *Trans* configuration refers to the case when the chemical substituents are on opposite sides of the double bond (see Figure 1.4a,b). On the other hand, taking into account the position of the atoms in a polymer chain three main configurations are observed: atactic polymers, in which the substituent groups have a random orientation (below and/or above) along the polymeric backbone; isotactic polymers, where the substituent groups are in the same plane along the

main polymeric chain; and sindiotactic polymers, in which the substituent groups are in an alternating opposite orientation along the polymer backbone (see Figure 1.4c-e).

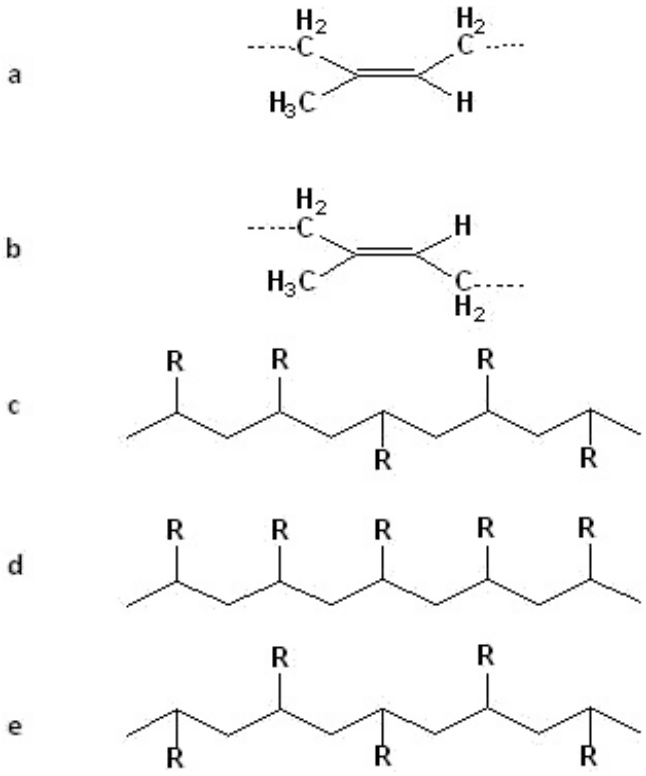

Figure 1.4. Schematic representation of the polymers configuration a) *cis*, b) *trans*, c) polymer atactic, d) isotactic polymer, and e) sindiotactic polymer.

Molecular conformation refers to the special spatial orientation of a macromolecule. To modify the macromolecular conformation it is not necessary to break out covalent bonds, but it is only necessary to rotate the atoms around single bonds in the polymer backbone. Therefore, the conformation of a polymeric molecule can be changed, for example, by application of thermal energy or by interactions between the macromolecules and the solvent molecules. The great number of possible conformations of macromolecules depends on different factors such as polymer crystallinity, steric effects or their physical state (i.e., if the polymer is in solution or in its molten or solid state), with the constraint that macromolecules tend to adopt a minimum energy conformations state. Typical macromolecular conformations, as random coil, fully extended chain, folded chain or helix are depicted in Figure 1.5. The random coil is an asymmetric conformation characterized by a random orientation of macromolecular segments. It is typical of polymers in solution, of molten polymers and solid amorphous polymers. All other conformations reported in Figure 1.5 are symmetric and,

therefore, characteristic of solid crystalline polymers. Hence, when the concept of macromolecular conformation is limited to a single macromolecule, it defines the polymer`s secondary structure.

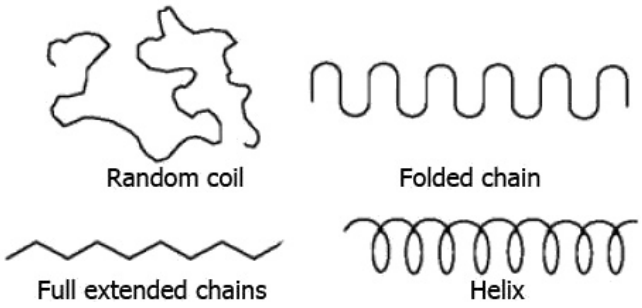

Figure 1.5. Secondary structure of polymers.

1.3.3.- Tertiary Structure.

Macromolecular conformation related to several macromolecules arranged together in any liquid or solid phase defines the polymer´s tertiary structure. Usual tertiary structures are depicted in Figure 1.6. These can be represented either by a tight arrangement of random coil chains (spaghetti-like structure) as in molten or amorphous solid polymer; by a fringed-micelle structure as observed in semi-crystalline solid polymers; or in regularly folded chains or super-helix tertiary structures as in the case of highly crystalline solid polymers.

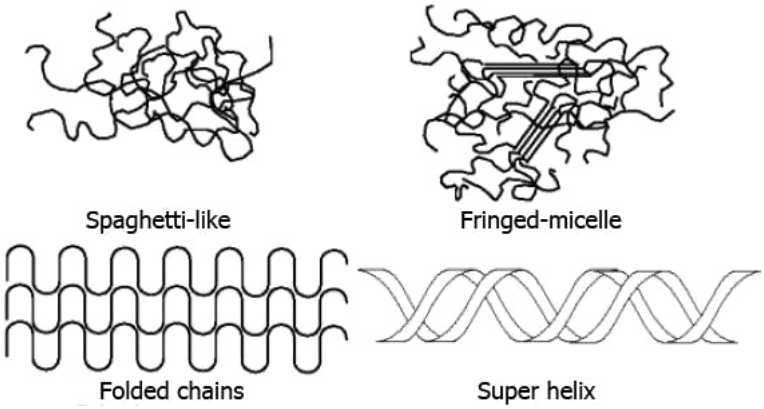

Figure 1.6. Tertiary structure of polymer.

Any polymeric material in the solid state posses great amounts of polymeric molecules in the form of aggregates. The process of molecular aggregation can lead to the formation of either crystalline or amorphous materials, which depend on both the polymer molecular structure

and the available configurations of the polymeric backbone´s building blocks. The ability of polymer chains to establish a sufficient high number of dipole-dipole interactions, hydrogen bonding, or van der Waals interactions, amongst others, is also a key factor in promoting and controlling the molecular aggregation process in spite of the energy involved in this kind of intermolecular forces is very weak (0.5-10 kcal/mol) if compared with covalent bonds (50-100 kcal/mol)

1.4.- Molecular self-assembly.

Molecular self-assembly is a spontaneous process by which molecules interact with each other to form well-ordered supramolecular structures. The self-association between molecular building blocks is mediated through non-covalent association of molecules (molecular recognition processes). In this way, extraordinarily complex assemblies are formed in various natural systems, and synthetic preformed molecular building blocks are assembled together by keeping a delicate balance between non-covalent repulsive and attractive interaction by using forces such as van der Waals and ionic interactions, metal coordination, H-bonding, π-π interactions or hydrophobic forces. This process has motivated many different studies in the fields of nanotechnology and materials science based on the design of new functional nanostructures (6)(7). The only requirement for self-assembly is that the building block should contain moieties able to establish non-covalent interactions in specific environments (6)(7). Thus, advanced self-assembled nanomaterials have already been prepared from many different types of molecules such as lipids, synthetic peptides, nucleic acids, low molecular weight surfactants, dendrons, transition metals, inorganic nanoparticles or polymers (8)(9). The latter have recently received great attention due to their increasingly scientific importance and vast utility in a wide range of technological applications by their ability to spontaneously self-organize into well-ordered aggregates, either in the solid state or in semidilute and dilute solutions (9)(10).

Nowadays, the self-organization of molecular building blocks is probably one of the most prominent topics of modern sciences. Indeed, supramolecular self-assembly is the key strategy of Nature for fabricating multifunctional structures such as enzymes, ribosomes, membranes channel or transport proteins from rather simple molecules such peptides, sugars and lipids. For instance, Nature produces complex intermolecular structures with biomolecules, through the control of biomolecular primary, secondary, tertiary and quaternary structure. The

presence of electrostatic charge in biomolecular primary structure provides natural systems with a molecular-level tool to control intramolecular conformation (secondary and tertiary structure) and intermolecular aggregation (quaternary structure), such as the association of lipids to form cellular membranes, the protein folding mechanisms to construct functional peptides and proteins, or the supramolecular organization of relevant biological entities such as enzymes, ribosomes or transport channels.

In order to mimic the self-assembly processes observed in Nature (10)(11), block copolymers have become of great scientific importance because of their unique and associative properties as a consequence of their molecular structure. In particular, synthetic block copolymers can self-organize spontaneously into unprecedented morphologies (which are related to their segmental incompatibility), either in solid state or in semidilute or dilute solutions. For instance, in bulk block copolymers made of thermodynamically incompatible segments phase-separate into organized discrete nanophases, which can be exploited in many applications ranging from impact-resistant materials to nanolithography and nanoelectronics. Similarly, in dilute solutions block copolymers lead to the formation of colloidal aggregates such as polymeric micelles or polymer vesicles, which have an enormous potential for applications in cosmetic, the food industry, medicine and biotechnology.

In solution, the main attraction forces leading to block copolymer self-assembly are: hydrophobic and electrostatic interactions, and hydrogen bonding. In this context, these macromolecules can be considered as building blocks. In a selective solvent, blocks that can be solubilized in this solvent tend to get in contact with the main phase, whereas blocks that are insoluble in the solvent tend to be hidden from the main phase, leading to the formation of organizated aggregates such spherical micelles, cylindrical micelles or vesicles (12). However, amphiphilicity is not the only driving force that can be exploited for creating aggregates in solution. The pairing of complementary charges in the polymer backbone is also a vector for self-organization. Hydrogen bonding interactions are also important for the development of self-assembling supramolecular aggregates, in which monomeric units are reversibly bound via weak non-covalent interactions to form well-ordered structures.

For example, due to the great current interest in the development and improvement of nano-devices, many of these synthetic block copolymers are being used in nanopatterning using the top-down and bottom-up fabrication methods (Figure 1.7). The top-up strategy uses physical engineering tools for carving of materials with a considerable macro-size to obtain a small

nanodevice. During the process, the lateral dimension of the material is reduced until having a nanostructured material as occurred, for example, in the case of silicon integrated circuits fabricated by selective layer deposition. In contrast, the bottom-up strategy takes advantage of the self-association properties of molecular blocks, which possess nanometric size. The living cell is a complex construction given by the Nature, and it is the best example for the bottom-up strategy (8)(13)(14).

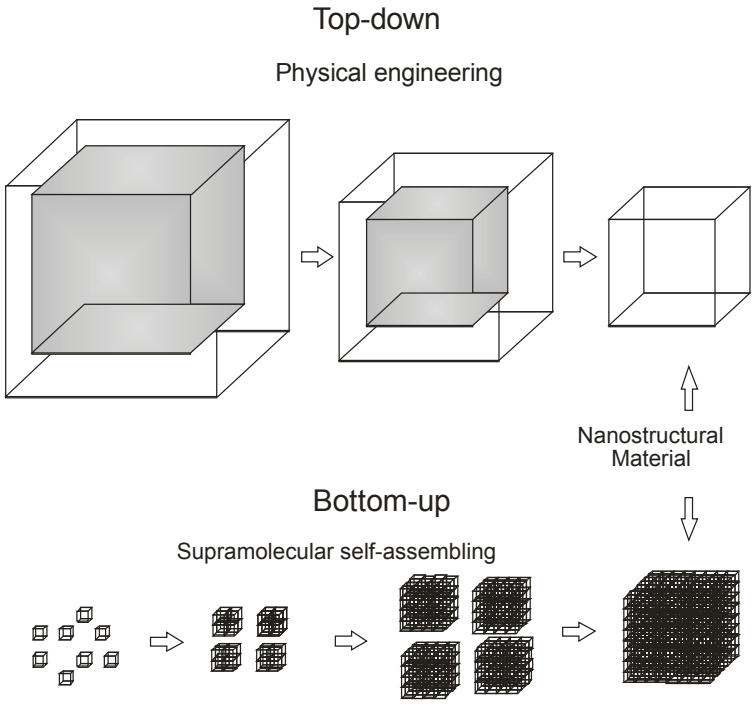

Figure 1.7. Schematic representation of two both strategies used to get nanostructured materials: a) Top-down and b) Bottom-up.

On the other hand, peptides and proteins show also amphipathic properties. The intramolecular fold of these macromolecules allows to show specific faces or display specific regions toward the bulk solvent phase; in this way, it is logical to assume that these regions have hydrophilic or hydrophobic nature. For instance, the cylindrical structure of the α-helix contain a sequence of hydrophobic amino acids which are positioned on one side of the cylindrical face, and another sequence of hydrophobic amino acids on the opposite face of the cylindrical structure. For β-sheet structure, hydrophobic and hydrophilic amino acids of a polypeptide chain can be ordered in an alternating way. In this manner, the side lateral chains of the amino acids are on opposite faces into the β-sheet structure (8).

CHAPTER 2
Methods

Contents

2.1.- Introduction

There are many analytical techniques suitable for the characterization of synthetic and biological macromolecules. This chapter is a brief summary of the basic theoretical background and experimental setups used to perform the different experiments discussed in this Thesis.

In aqueous solutions of amphiphilic self-assembled systems, the aggregation process mostly depends on concentration or/and temperature. The most usual experimental tools to follow their self-assembly process into structural aggregates (micelles, vesicles...) are surface tension, fluorescence spectroscopy, light scattering or nuclear magnetic resonance, amongst others. On the other hand, the structural characteristics of the resulting self-assembled nanostructures can be determined by techniques such as X-ray diffraction, light scattering or electron and atomic microscopies.

2.2.- Surface tension

The critical micelle concentration (cmc) of amphiphilic systems and, in particular, in block copolymer solutions can be determined by measuring their surface tension (γ) as a function of concentration. Surface tension depends on polymer concentration below its cmc and, therefore, such behavior is denoted by a fairly sharp decrease in a γ *vs.* log (c) plot. There are several methods for determining the surface tension of amphiphilic polymer solutions such as the Du Noüy ring, the Wilhelmy plate, the pendant drop, the bubble pressure or the sessile drop methods. The most common ones are the Du Noüy ring and Wilhelmy plate techniques (15).

2.2.1.- Wilhelmy plate method

The Whilhelmy plate method measures the force (F) with which a platinum plate of known perimeter ($L = l + d$) is pulled downward by an interface, in our particular case the air/water and air/chloroform interfaces. The surface tension force, $L\gamma cos\theta$, is equal to the weight of the liquid meniscus adsorbed onto the plate and detected by a balance (16), which can be expressed through the following equation:

$$w = 2(l + d)\gamma cos\theta \qquad 2.01$$

where w is the meniscus' weight detected by the balance, θ is the contact angle defined by the meniscus shape on the wet platinum surface plate, and l is the width and d the plate thickness, respectively (Figure 2.1). Considering θ very small and the plate thickness negligible compared with its width, the former expression is simplified to:

$$w = 2\gamma l \qquad 2.02$$

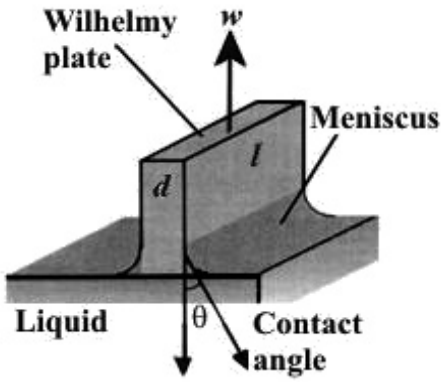

Figure 2.1. Illustration of a fully wet Wilhelmy plate in contact with an aqueous solution.

2.2.2.- Monolayers and Langmuir-Blodgett films

Many insoluble substances such as long chain fatty acids, alcohols, surfactants and polymers can be spread from a solvent onto water to form a one-molecule thick film, called monolayer. Molecules in a monolayer can be arranged in different ways, especially when they are closely packed, depending on the lateral forces between them (17). The obtention of surface pressure-area isotherms is one of the main methods used to study monolayer formation. Surface pressure, Π, is the reduction of the surface tension due to the presence of the monolayer: $\Pi = \gamma_0 - \gamma$, where γ_0 is the surface tension of the solvent (usually water), and γ the surface tension of the system. Surface pressure-area isotherms are often measured for films/monolayers compressed using a Langmuir trough (Figure 2.2).

In general, an insoluble substance is spread from a volatile solvent to ensure the formation of a uniform monolayer, and its area is controlled through a moveable barrier. The horizontal force necessary to maintain the float at a fixed position is measured using a torsion balance, which provides the surface tension values. Since only micrograms of materials are present in

monolayers, it is necessary to ensure that the water is as pure as possible (17). On the other hand, it is also possible to deposit the monolayer film onto a solid substrate, or build up a multilayer by successive depositions of monolayer films. In this case, this technique is called Langmuir-Blodgett and the films are named Langmuir-Blodgett (or LB) films. A monolayer is adsorbed homogeneously with each immersion or emersion step, thus films with very accurate thickness can be formed. This thickness is accurate because the thickness of each monolayer is known and can therefore be added to find the total thickness of a Langmuir-Blodgett film. These LB films are of great interest since they enable the construction of functional multilayer stacks which can be used in molecular electronic devices, such as gas sensors, diodes or in semiconductor devices as insulators in transistors.

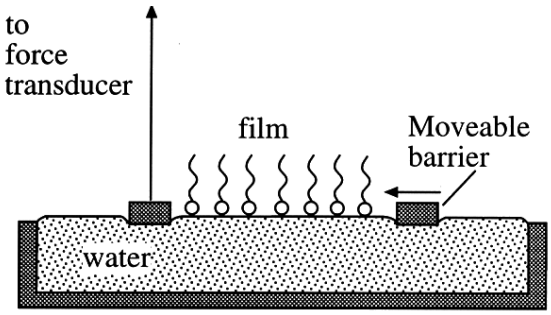

Figure 2.2. Scheme of a Langmuir trough.

When a monolayer is compressed on the water surface, several phase transformations can be observed. These changes are almost analogous to those present in bulk phase matter, where the most common states are gas, liquid and solid. The phase changes may be readily identified by monitoring the surface pressure Π as a function of the area occupied by the film (surface pressure-area isotherm) (18). This is the two dimensional equivalent of the pressure-volume isotherm for bulk materials (gas/liquid/solid). Figure 2.3 shows the surface pressure-area isotherm plot of a hypothetical long chain organic monolayer material (e.g., a long-chain fatty acid). This diagram displays most of the characteristic features observed for long chain compounds (18). The shape of the surface pressure-area isotherm depends on the lateral interactions between molecules. These, in turn, depends on the molecular packing, which is influenced by factors such as the size of the hydrophilic group, the presence of polar groups, the length and number of hydrocarbon chains, and their conformation.

Briefly, in the gaseous state (G) the molecules are far enough apart on the water surface so

that they exert little force one on another. As the surface area of the monolayer is reduced, the hydrophobic chains of the molecules will begin to interact. The liquid state formed is generally called the expanded monolayer phase (E). At this stage, molecules at the water surface are in a random rather than in a regular orientation, with their polar groups in contact with the subphase. As the molecular area is progressively reduced, a condensed (C) phase may appear. In the condensed monolayer state the molecules are closely packed and are oriented with the hydrophobic groups pointing away from the water surface.

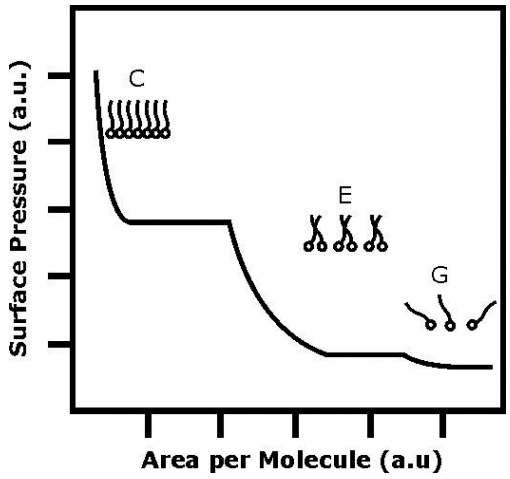

Figure 2.3. Surface pressure-area isotherm for a chain organic monolayer.

2.2.3.- Axisymetric drop shape analysis (ADSA)

Axisymetric drop shape analysis (ADSA) is a drop shape technique for measuring the interfacial surface tension, γ. This method can be performed on the measured profiles of captive bubbles, sessile drops, pendant drops or bubbles. The principle of the technique is based on the determination of the drop shape by the balance between: i) the force of gravity which deforms the drop and ii) the surface tension which resists the deformation by minimizing the drop surface area (17). The relationship between these two forces is described by the Laplace equation (19):

$$\gamma\left(\frac{1}{R_1}+\frac{1}{R_2}\right)=\Delta P \qquad 2.03$$

The Laplace equation is written in terms of the surface tension, γ, the principal radii of the drop, $R_1$and R_2, and the pressure difference across the curved interface, ΔP. The pressure drop has two contributions, $\Delta P=\Delta P_0-\rho g z$, where ΔP_0 is the pressure difference at a

reference plane, and the term ρgz is an additional pressure which arises from the gravitational component at any point on the surface. This is given by the surface density difference, ρ, between the bubble and the continuous phase, and its vertical distance z from the reference plane (17).

ADSA technique allows to determine both the surface area, A, as well as the surface tension, γ. Additionally, both quantities enable the derivation of important surface rheological properties, such the elasticity or the surface dilatational modulus, E, of a film, defined as $E = -A(d\gamma/dA)$. This can also be defined as a complex function written as $E(\omega) = E'(\omega) + iE''(\omega)$, where E' and E'' correspond to the storage and loss moduli, respectively, by analogy with 3D rheology. Assuming the mechanical properties of the adsorbed layer follow Maxwell's behavior, the storage and loss moduli can be written as (20)-(22)

$$E'(\omega) = \sum_i E_{0i} \frac{\left(\omega/\omega_{0i}\right)^2}{1+\left(\omega/\omega_{0i}\right)^2} \qquad 2.04a$$

$$E''(\omega) = \sum_i E_{0i} \frac{\left(\omega/\omega_{0i}\right)}{1+\left(\omega/\omega_{0i}\right)^2} \qquad 2.04b$$

where E_{0i} and ω_{0i} ($\omega_{0i} = 2\pi/\tau_{0i}$) are the corresponding weights of the *i-th* relaxation element to the total elasticity modulus, E_0, and the characteristic relaxation frequency, respectively, and τ_{0i} is the characteristic relaxation time of the Maxwell model.

2.3.- Light scattering

Scattering is a general physical process in which a form of radiation, such as, sound or a moving particle, are forced to deviate from its straight trajectory by one or more localized non-uniformities in the medium through it propagates. In the case of light, it is fairly simple to understand the origin of its scattering considering it as an electromagnetic wave. Light will interact with the charges inside a given molecule remodelling their spatial charge distribution. The quantification of this effect is reported by a certain physical quantity, the polarizability (α). The charge distribution follows the time-modulation of the electric wave vector of the incident light beam and, therefore, the molecule constitutes an oscillating dipole or electric oscillator.

This oscillating dipole acts as an emitter of an electromagnetic wave with the same wavelength as the incident one (the scattering process is elastic), which is emitted isotropically in all perpendicular directions to the oscillator, as illustrated in Figure 2.4. The angle of observation with respect to the direction of the incident light beam is called the scattering angle, and it provides a measure of the accessible length scales by a light scattering experiment (23).

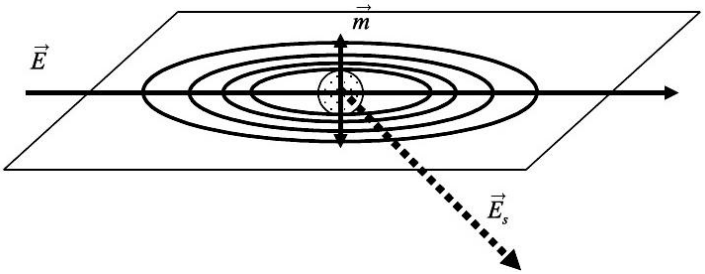

Figure 2.4. Oscillating dipole induced by an incident light wave, and emitting light (23).

For molecules or particles equal or larger than $\lambda/20$, being λ the wavelength of the incident radiation, several of these oscillating dipoles are created simultaneously within one given particle. As a consequence, some of the emitted light waves possess a significant phase difference. Accordingly, interference of the scattered light emitted from such individual particles leads to a non-isotropic angular dependence of the scattered light intensity. The interference pattern of intra-particular scattered light, also called the particle form factor, is characteristic of the geometry of the scattering particle. Hence, this provides a quantitative means for the structural characterization of particles in very dilute solutions by light scattering. On the other hand, for particles smaller than $\lambda/20$, only a negligible phase difference exists between light emitted from various scattering centers within a given particle; in this case, the detected scattered intensity will be independent of the scattering angle, and it only will depend on the particle mass, which is proportional to the total number of scattering centers one particle contains. The difference in the interference pattern of light scattered by small and large particles, is illustrated in Figure 2.5 (23).

So far, we have considered light scattering as a purely elastic process where the emitted light has exactly the same wavelength as the incident light. Particles in solution, however, usually show a random motion (Brownian motion) caused by thermal density fluctuations of the solvent. As a consequence of temporal changes in inter-particle positions and the corresponding temporal concentration fluctuations, both the interference pattern and the resulting scattered intensity detected at a given scattering angle also change with time,

reflecting the Brownian motion of the scattering particles (23). This phenomenon provides the basis of dynamic light scattering, an experimental procedure which yields a quantitative measure for the mobility of scattering particles in solution, characterized by their self-diffusion coefficients. Most modern particle size analyzers used to determine the size of particles in solution are based on this principle, further commented in detail below (23)-(25).

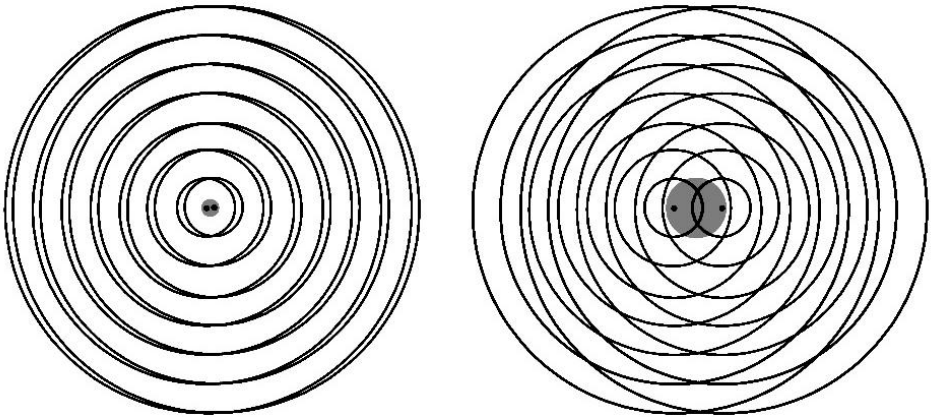

Figure 2.5. Interference pattern of light scattered from small particles (*left*) and large particles (*right*). For simplification, only two scattering centers are shown (23).

General standard light scattering setups consist of the following components (Figure 2.6) (23)-(26):

1. The incident light source, typically a laser source. This provides coherent and monochromatic light with an intensity between some few milliwatts (mW) and several watts (W). In practice, the light intensity needed for a successful scattering experiment depends on the sensitivity of the optical detector and on the scattering power of the sample itself, as determined by its size, concentration, and refractive index increment. As shown in Figure 2.6, typically, the primary laser beam is guided and focused onto the sample by optical mirrors and lenses. The laser beam diameter within the sample is well below 1 mm, which defines the scattering volume.
2. The light scattering cell, in most cases a cylindrical quartz glass cuvette of outer diameter between 10 and 30 mm, embedded within an index matching and thermostating bath. Using an index matching bath around the cylindrical light scattering cuvette is important to suppress unwanted diffraction effects of the incident and the scattered light at the sample-air interfaces.
3. The detector, either a photo-multiplier tube or a very sensitive avalanche photo diode

(APD) and its associated optics (pinhole or optical fiber) mounted on the arm of a goniometer. The detector optics determines the horizontal and vertical dimensions of the scattering volume, whereas its depth is defined by the incident laser beam width. Band pass filters with high transmission at the incident laser light wavelength are often used in front of the detector to suppress undesired contributions of stray light or fluorescence from the sample.

4. The electronic hardware components associated with the detector used for signal processing. The scattered intensity I (q,t), which is monitored by the optical detector, is typically digitalized and stored in a computer. These raw data have to be further processed: in the case of static light scattering, particle form factor models can be used to fit the experimental data; in a dynamic light scattering experiment, the raw data have to be converted into the time intensity correlation function g_2 (q, τ). This is done during the measurement using a very fast hardware correlator as, for example, the ALV 5000 from ALV, Langen, Germany.

5. In a typical light scattering experiment, light from a laser source passes through a polarizer, which defines the polarization of the incident beam and, then, enters the scattering medium. The scattered light, then, passes through an analyser, which selects a given polarization and finally enters a detector. The position of the detector defines the scattering angle, θ. In addition, the intersection of the incident beam and the beam intercepted by the detector defines a scattering region of volume V. In modern light scattering experiments the scattered light spectral distribution is measured by a photomultiplier, which is the main detector (24).

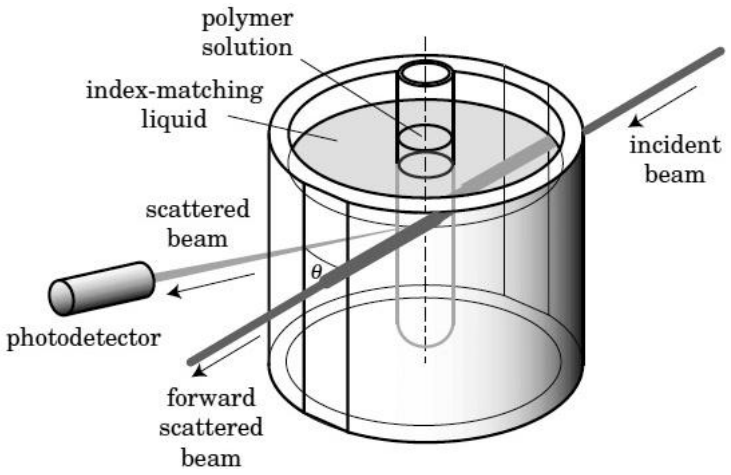

Figure 2.6. Schematic representation of an usual light scattering experiment (26).

2.3.1.- Static light scattering (SLS)

As mentioned above, matter scatters electromagnetic waves due to the induction of an oscillating electromagnetic dipole which serves as a source for the scattered light wave. In this way, Rayleigh scattering is described in terms of three factors: the incident light, the particle (i.e. a macromolecule), which serves as an oscillating dipole, and the scattered light. The schematic model is shown in Figure 2.7. The equation for the electric field of incident polarized light beam at x position and at time, t, may be expressed by the following well-known equation (27)-(32):

$$E = E_0 cos2\pi\left(\nu t - \frac{x}{\lambda}\right) \qquad 2.05$$

where E is the electric field or electric intensity, E_0 is the amplitude of the incident electrical wave, ν is the light frequency in solution, and t is the propagation time.

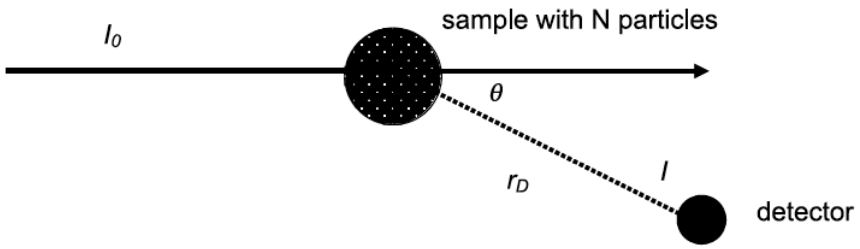

Figure 2.7. Sketch of a light scattering process (23).

If an incident light reach a particle (i.e. macromolecule), whose size is smaller than the wavelength λ, d<<λ/20, the electron distribution around the particle is distorted, resulting in particle's polarization and, hence, creating a new oscillating dipole, p (the own particle). Then, the generated dipolar moment is related to the electric field by:

$$p = \alpha E = \alpha E_0 cos2\pi\left(\nu t - \frac{x}{\lambda}\right) \qquad 2.06$$

where α is the polarizability of the particle. If the incident light is plane polarized, the scattered light can then expressed:

$$E_S = \frac{(d^2p/dt^2)(\sin\theta/r)}{c^2} \quad 2.07$$

where r is the distance of the dipole from the observer (from the scattered light sample to the detector) and θ is the angle between the dipole axis and the line r. The division by the square of the light velocity, c^2, is a dimensional correction. Substituting d^2p/dt^2 in the above equation:

$$E = \frac{4\pi^2\nu^2\alpha E_0 \sin\theta}{r\lambda^2}\cos 2\pi\left(\nu t - \frac{x}{\lambda}\right) \quad 2.08$$

Comparing the intensity I of the scattered radiation to the intensity I_0 of the incident radiation, which is proportional to the square of *its* amplitude E_0:

$$\frac{I}{I_0} = \frac{16\pi^4\alpha^2 \sin^2\theta}{r^2\lambda^4} \quad 2.09$$

This equation is called the Rayleigth equation for plane polarized light. The scattering intensity increases rapidly as the light wavelength decreases. The intensity also depends on the angle θ: there is no radiation along the direction (θ=0) in which the dipole vibrates.

Let us consider a system of volume V containing N independent identical scattering particles. Then, the total intensity I of scattered light is:

$$\frac{I_\theta}{I_0} = \frac{N}{V}\frac{16\pi^4\alpha^2(1-\cos^2\theta)}{\lambda^4 r^2} \quad 2.10$$

Generally, the Rayleight scattering equation is directly applicable to gases, where molecules move randonly. In liquids, there exists fluctuations in particle concentration inside a volume element, which results in fluctuations of the polarizability α. Therefore, to apply the Rayleigh scattering equation to the liquid state, it is necessary to account for these fluctuations by using α. In this way, since the polarizability α depens on the dielectric permitittivity ε, and correspondingly on the index of refraction n, then:

$$4\pi\frac{N}{V}\alpha = \varepsilon - 1 = n^2 - 1 \quad 2.11$$

For a dilute solution, polarizability α may be written as:

$$\alpha = \frac{V}{2\pi N}\left(\frac{dn}{dc}\right)c \qquad 2.12$$

where *dn/dc* is the differential refractive index and is an experimentally measurable quantity. Substitution of the equation 2.12 into equation 2.10, and considering that N/V can be expressed as $N/V = cN_A/M$, where M is the molecular weight and N_A is the Avogadro's number:

$$\frac{I_\theta}{I_0} = \frac{4\pi^2\left(\frac{dn}{dc}\right)^2 Mc(1-\cos^2\theta)}{\lambda^4 r^2 N_A} \qquad 2.13$$

Defining the Rayleigh ratio and is often designed as R:

$$R = \left(\frac{I_\theta r^2}{I_0(1+\cos^2\theta)}\right) \qquad 2.14$$

which is independents of *r* and θ. Simplifying:

$$R = \frac{4\pi^2\left(\frac{dn}{dc}\right)^2 Mc}{\lambda^4 N_A} \qquad 2.15$$

Then the light scattering becomes:

$$R = KcM \qquad 2.16$$

where $K = 4\pi^2(dn/dc)^2/\lambda^4 N_A$.

As mentioned above, for very dilute solution of small particles (for example, nanoparticles or polymer chains of size smaller than λ/20) the scattering intensity is independent of the scattering angle, and the density fluctuation from the surrounding solvent can be substracted by considering the excess Rayleigh ratio, ΔR ($\Delta R = R_{solution} - R_{solvent}$); then, the scattering intensity only depends on the scattering power of the dissolved particles (i.e., from their molecular mass) and the osmotic pressure. For non ideal solutions, and after several theoretical considerations (3), the scattering equation can be rewritten:

$$\frac{Kc}{\Delta R} = \frac{1}{M} + 2A_2c + 3A_3c^2 \qquad 2.17$$

When $c \to 0$, the former equation can be simplified to the so-called Rayleigh-Gans-Debye relation:

$$\Delta R = KcM_w \qquad 2.18$$

Actually, ΔR cannot be experimentally measured since I_0 and r are unknown during the experiment. However, in a routine experiment ΔR is determined from the experimentally measured scattered intensities of the solution, $I_{solution}$, and a reference substance, I_{ref} (usually benzene or toluene) (23) which enables the derivation of their respective Rayleigh ratios. Hence, the following equation can be derived providing a relation between the molecular weight, Mw, of the particle considered and the second virial coefficient, A_2 (29)-(30):

$$K^*c/(S_{90} - S_{90}^S) = 1/M_w + 2A_2c + \cdots \qquad 2.19$$

where $K^* = 4\pi^2/\lambda^4 N_A (dn/dc)^2\, n_{ref}^2/R_{ref}$, $S_{90} = {}^{I}/_{I_{ref}}$ and $S_{90}^S = {}^{I_S}\!/_{I_{ref}}$. I, I_s and I_{ref}, are

the experimentally measured scattered intensities of the solution, solvent, and reference, respectively. For small particles at dilute concentrations equation 2.19 can be reduced to:

$$K^*c/(S_{90} - S_{90}^S) = 1/M_w \qquad 2.20$$

On the other hand, for large scattering particles the scattered intensity is no longer independent of the scattering angle. The scattering vector q, which is experimentally determined by the scattering angle θ and the laser light wavelength, λ, provides a quantitative measure of the length scale of the static light scattering experiment, given by:

$$q = \frac{4\pi\, n \sin(\theta/2)}{\lambda} \qquad 2.21$$

For very dilute solutions, interference between different scattering particles, the so-called

structure factor, can be neglected. In this case, the angular dependence of the measured scattered intensity $I(q)$ is only caused by intraparticle interference. For dilute and semidilute solutions, to take into account the effects of particle concentration and solute-solvent interactions on the measured scattering intensity, the Zimm equation can be used:

$$Kc/R(\theta, c) = (1/M_w)\left(1 + q^2 R_g/3\right) + 2A_2 c \qquad 2.22$$

In order to determine M_w, R_g, and A_2 it is necessary to prepare several dilute solutions of different concentration and measuring the scattering intensities data at various scattering angles (27)(28).

2.3.2.- Dynamic light scattering (DLS)

Light scattered by a set of mesoscopic particles produces a random interference pattern on a screen. This pattern, generally possess the form of irregularly spaced and sized bright spots called speckles. The scattered light intensity pattern remains unchanged as long as the particles do not change their position. Particle motion naturally leads to a temporal evolution of the scattered speckle field since one interference pattern is continuously replaced by another. In a single speckle spot, this evolution is observed as strong temporal intensity fluctuations, with a certain well-defined temporal correlation. The intensity fluctuations are inherently related to the scatterers' dynamics and, therefore, the temporal correlation function depends on the particles shift. Thus, the measurable correlation properties of light can be linked to the dynamical properties of particles which, in turn, can provide information about their flow velocity and direction, particle size, density of moving scatterers...

In dynamic light scattering, also known as photon correlation spectroscopy (PCS) or quasi-elastic light scattering (QELS), the diffusive motions of particles in solution gives rise to fluctuations in the scattered light intensity on the microsecond timescale. This technique is one of the most popular methods used to determine the particles size by measuring the temporal fluctuations of the scattered light intensity. Roughly, this is made by focusing a monochromatic light beam, such a laser, on a solution with particles in Brownian motion; this causes a Doppler shift when the light "hits" the moving particle, changing the light wavelength. This change is related to the size particle (27)(32).

In the scope of DLS, temporal fluctuations are usually analyzed by means of the intensity

autocorrelation function (ACF). In the time domain, the correlation function usually decays with time (Figure 2.8), and faster dynamics leads to faster decorrelation of the scattered intensity trace. It can be shown that for a random process the intensity ACF is the Fourier transform of the power spectrum and, therefore, DLS measurements can be equally well-performed in the spectral domain. In fact, DLS experiments were initially discussed in terms of the broadening of the spectrum peak of monochromatic light due to Doppler shifts experienced by propagating light waves scattered by moving particles (31).

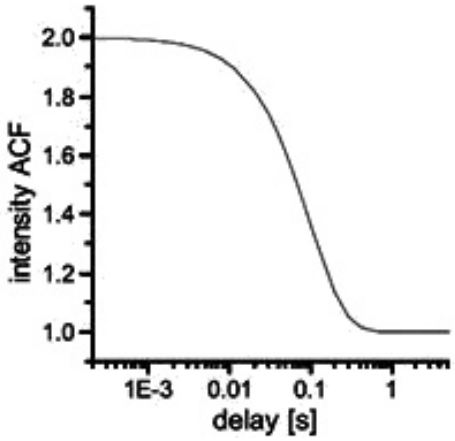

Figure 2.8. Illustration of autocorrelation function (31).

To detect the intensity fluctuation with time, a DLS system requires an autocorrelator on top of a regular SLS system, as shown in Figure 2.9.

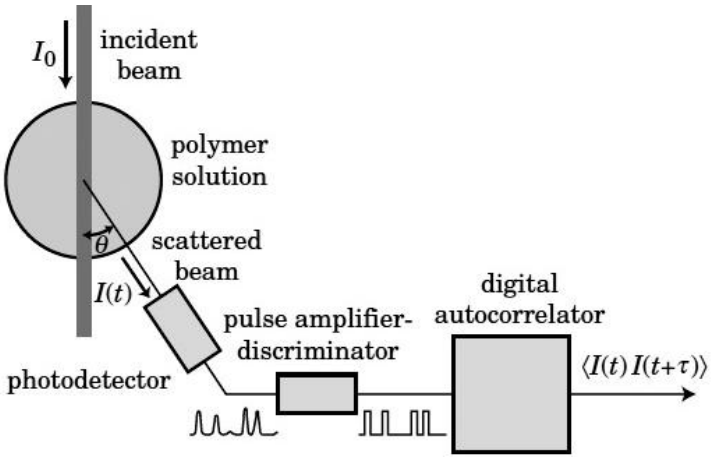

Figure 2.9. Sketch of a dynamic light scattering system. The pulse amplifier discriminator converts the analogic signal of the photodetector, $I(t)$, in a digitalized signal, which is further processed by the autocorrelator into the autocorrelation function.

As commented above, Figure 2.10a illustrates how the intensity (I) varies with time (t). $I(t)$ fluctuates around its mean value, $<I>$. It may appear completely random and, therefore, meaningless, but it is not. Motions of particles (i.e. polymer molecules) and solvent molecules contribute to the change of $I(t)$ with time. This apparently noisy signal carries the information about particles motions.

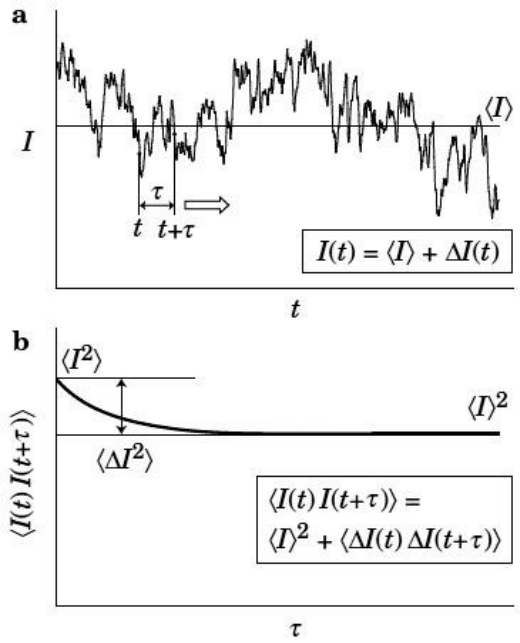

Figure 2.10. a) Light scattering intensity $I(t)$ fluctuates around its mean value $\langle I\rangle$. b) Autocorrelation function $\langle I(t)I(t+\tau)\rangle$ is obtained as the long-time average of $I(t)I(t+\tau)$ for various delay times τ. The aurocorrelation function decays from $\langle I^2\rangle$ to $\langle I\rangle^2$ over time. The amplitude of the decaying component is $\langle \Delta I^2\rangle$.

The autocorrelator calculates the product average of two scattering intensities $I(t)$ and $I(t+\tau)$ measured at two different times separated by τ, the delay time. The average product $\langle I(t)I(t+\tau)\rangle$ is a function of τ and is called the correlation function of $I(t)$, or the intensity-intensity correlation function. The correlator converts $I(t)$ into $\langle I(t)I(t+\tau)\rangle$. Hence, the intensity-intensity correlation function is the average of $I(t)I(t+\tau)$ over a long period T. Hence, assuming that the long time average is equal to the ensemble average, we can write:

$$\langle I(t)I(t+\tau)\rangle = \lim_{T\to\infty} \frac{1}{T}\int_0^T I(t)I(t+\tau)dt \qquad 2.23$$

Note that, if the system is at equilibrium, the ensemble average does not change with time

and, therefore, $\langle I(t)I(t+\tau)\rangle = \langle I(t0)I(\tau)\rangle$. The autocorrelation function of $I(t)$ (Figure 2.10a) is shown in Figure 2.10b. When τ = 0, $\langle I(t)I(t+\tau)\rangle = \langle I^2\rangle$. With increasing τ, $\langle I(t)I(t+\tau)\rangle$ decays to an asymptotic level (baseline), $\langle I\rangle^2$.

Because the scattering intensity $I(t)$ fluctuates around a mean value $\langle I\rangle$, it is convenient to separate its fluctuating component, $\Delta I(t)$, as $I(t) = \langle I\rangle + \Delta I(t)$. By definition, $\langle \Delta I(t)\rangle = 0$. Then, the correlation function can be rewritten as:

$$\langle I(t)I(t+\tau)\rangle = \langle I\rangle^2 + \langle \Delta I(t)\Delta I(t+\tau)\rangle \quad 2.24$$

The autocorrelation of $\Delta I(t)$is zero upon increases of τ. When $\tau \to \infty$, $\langle \Delta I(t)\Delta I(t+\tau)\rangle = \langle \Delta I(t)\rangle\langle \Delta I(t+\tau)\rangle = 0$. The decaying componet in $\langle I(t)I(t+\tau)\rangle$ is $\langle \Delta I(t)\Delta I(t+\tau)\rangle$. The initial height of the decaying component is $\Delta I^2 = \langle I^2\rangle - \langle I\rangle^2$. Division of $\langle I(t)I(t+\tau)\rangle$ by $\langle I\rangle^2$ leads to the intensity autocorrelation function as:

$$\langle I(t)I(t+\tau)\rangle/\langle I\rangle^2 = 1 + \langle \Delta I(t)\Delta I(t+\tau)\rangle/\langle I\rangle^2 = 1 + f_c g_2(\tau) \quad 2.25$$

where $f_c \equiv \langle \Delta I^2\rangle/\langle I\rangle^2$ (the coherent factor), and the second factor is the baseline-subtracted, normalized intensity autocorrelation function:

$$g_2(\tau) \equiv \langle \Delta I(t)\Delta I(t+\tau)\rangle/\langle \Delta I\rangle^2 \quad 2.26$$

The coherent factor depends on the coherence of the light reaching the photodetector. The measured intensity correlation function is related to the field correlation function by the Siegert relation:

$$g_1(\tau) = 1 + b|g_2(\tau)|^2 \quad 2.27$$

where $g_1(\tau)$ is:

$$g_1(\tau) = |E^*(t)E(t+\tau)|/\langle |E(t)|^2\rangle \quad 2.28$$

where $E^*(t)$ is the electric field conjugate function. For monodisperse spherical particles:

$$g_1(t) = exp(-\Gamma\tau) \quad 2.29$$

where Γ is the characteristic delay rate, which is related to the translational diffusion coefficient, *D*, of a solute by means of the expression:

$$\Gamma = q^2 D \quad 2.30$$

The diffusion coefficient is frequently used to determine the hydrodynamic radius, R_H, of the constituent particles by using the Stokes-Einstein equation:

$$D = {K_B T}/{6\pi\eta R_H} \quad 2.31$$

where K_B is the Boltzmann constant, T the absolute temperature and η the liquid viscosity. The hydrodynamic radius obtained by DLS represents an ideal hard sphere that diffuses with the same speed as the particle under examination. Actually, particles are solvated and the radius calculated from the particle diffusion corresponds to the size of the dynamic solvated particle.

2.4.- Electron microscopy

Microscopy is an important tool for the characterization of nanomaterials structure. For example, this set of imaging techniques may be used to examine the detailed shape, size and distribution of a wide range of nanoscopic objects. There are different available classes of microscopic techniques, such as the traditional optical microscopy, or more powerful ones such as scanning electron microscopy (SEM), transmission electron microscopy (TEM), and scanning probe microscopy (SPM), amongst others.

2.4.1.- Transmission electron microscopy (TEM)

Transmission electron microscopy (TEM) involves the transmission of an electron beam through a sample in a high-vacuum environment. The images and their associated contrasts arise from regional differences in electron densities in such sample. TEM has a resolution of ca. 1 to 100 nm and can provide very detailed structural information of polymeric materials. The TEM specimens need to be very thin in order to enable the transmission of electron beams through the sample.

A transmission electron microscope (Figure 2.11a) is constituted by an electron source (electron gun) which emits electrons travelling through the vacuum created into the microscope column. A condenser lens focus the electron beam on the sample, and several objective lenses are used to form the diffraction pattern at the back focal plane and the sample image at the image plane; there are also some intermediate lenses to magnify the image or the diffraction screen. To obtain an improved contrasted image, an objective diaphragm is inserted in the back focal plane to select the transmitted beam. At the bottom of the microscope, the non-scattered electrons reach a fluorescent screen, which provides a contrasted image of the specimen, with a darkness distribution corresponding to its different electron densities.

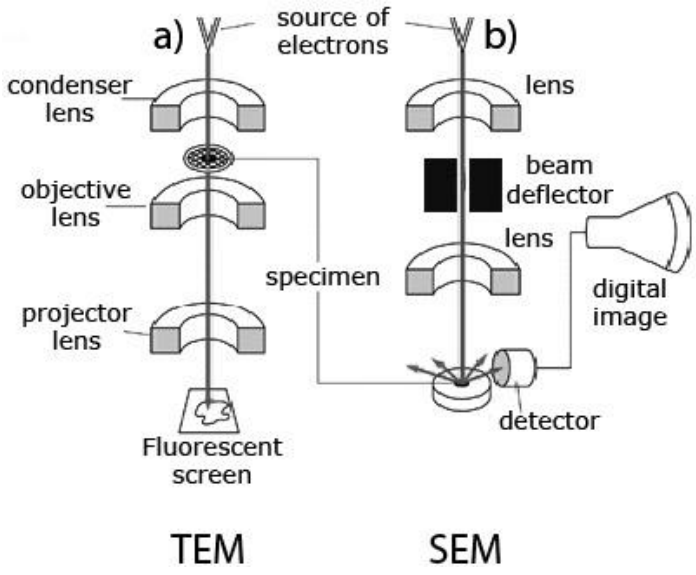

Figure 2.11. Schematic diagram of electron microscopes: a) TEM; b) SEM .

In order to solve the material´s structure on the mesoscopic scale at even high resolutions comparable to interatomic distances, high-resolution transmission electron microscopes (HRTEM) emerge as a powerful tool. HRTEM uses the transmitted and scattered electron beams directed to a sample to create a diffraction image, in contrast to conventional TEM that only uses the transmitted beams. The high resolution image recorded can be interpretable directly in terms of projections of individual atomic positions. In this way, defects and other inhomogeneities present in a material specimen can be accurately determined. A great advantage of the HRTEM microscope is the capability to observe both electron microscope images and diffraction patterns for determined selected area electron diffractions from a

sample (33)-(35). The selected area electron diffraction in an electron microscope is formed by setting an aperture in the imaging plane of the objective lens. Only rays passing through this aperture contribute to the diffraction pattern at the far field. For a perfect lens without aberrations, the diffracted rays come from an area that is defined by the back-projected image of the selected aperture. The aperture image is typically a factor of 20 times smaller because of the objective lens magnification. The smallest area that can be selected in SAED is limited by the objective aberration (36).

2.4.2.- Scanning electron microscopy (SEM)

Scanning electron microscopy (SEM) is another valuable electron microscopy technique for the examination and analysis of the microstructural characteristics of solid objects, with a resolution of ca. 5 nm. SEM can also be used to obtain compositional information of nanomaterials by coupling an electron diffraction X-ray scattering detector. SEM enables the observation of heterogeneous organic and inorganic materials on the mesoscopic scale (37). In a typical SEM experiment, an electron beam is focused to obtain a very fine spot size that is rastered over the surface, and an appropriate detector collects the electrons emitted from each point. In this way, an image having a great field depth and a remarkable three-dimensional appearance is built up line by line. The specimen is usually coated with a conducting film prior to examination to enhance electron conductivity and, thus, improving image contrast.

A scanning electron microscope (Figure 2.11b) consists of an electron gun at the top of the column, which creates a divergent electron beam. In the column, which is under vacuum, a series of magnetic apertures focuses the electron beam, and an electrostatic field drives the electrons through a small spot called crossover and accelerates them through the column until the sample chamber, where the electron beam interacts with the sample. The signals resulting from the beam-sample interaction are monitored. Finally, SEM constructs a virtual image from the signal emitted from the sample by scanning the electron beam line by line through a rectangular (raster) pattern on the sample surface. The scan pattern defines the area represented in the image. At any time, the beam illuminates only a single point in the pattern. As the beam moves, the signals it generates vary in strength, reflecting structural/morphological differences in the sample.

2.5.- Atomic force microscopy (AFM)

An atomic force microscope (AFM) is part of a large family of instruments termed as scanning probe microscopes (SPM). The common factor in all SPM techniques is the use of a very sharp tip probe, which is scanned across a surface of interest. The interactions between the probe and the surface are able to produce a high resolution image of the sample (potentially up to the sub-nanometre scale) depending on the technique and sharpness of the probe tip. For AFM, the probe usually interacts directly with the surface probing the repulsive and attractive forces which exist between the probe and the sample surface to produce a high resolution three-dimensional topographic image of the latter. The great versatility of AFM makes possible measurements in air or fluid environments rather than in high vacuum, which allows the imaging of polymeric and biological samples in their native states. In addition, it is highly adaptable, with tip probes being able to be chemically functionalised to allow quantitative measurement of interactions between many different types of materials (38).

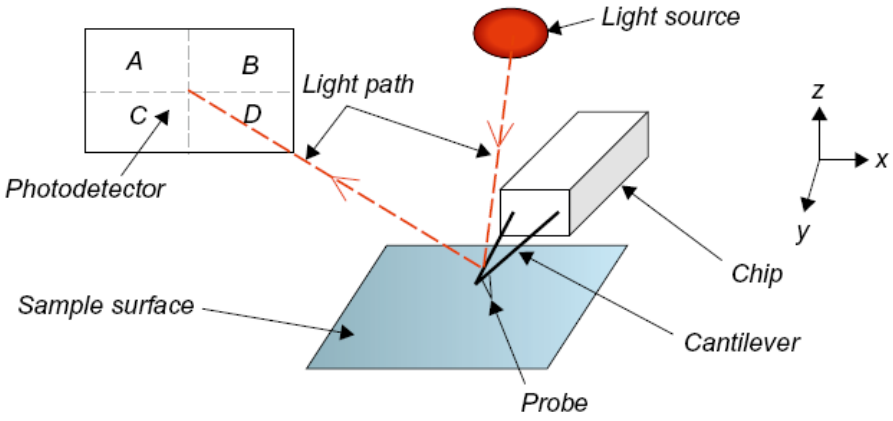

Figure 2.12. Typical AFM setup. A tip probe is mounted at the apex of a flexible cantilever, made of Si or Si_3N_4. The cantilever itself or the sample surface is mounted on a piezo-crystal, which allows the position of the probe to be shifted respect to the surface. The deflection of the cantilever is monitored by changes in the path of a laser light beam deflected from the upper side end of the cantilever recorded by a photodetector (38).

An AFM instrument consists of a sharp tip probe mounted near the end of a cantilever arm, which is able to make a full scanning across the entire sample surface. By means of monitoring the arm's deflection originated by the topographic features present on the sample surface, a three dimensional picture can be built up at high resolution. In Figure 2.12 the basic setup of a

typical AFM is shown. Cantilevers commonly are either V-shaped or a rectangular "diving board" shaped. The cantilever posses a sharp tip at its free end, which acts as the interaction probe. This probe has most commonly the form of a square-based pyramid or cylindrical cone. The probe is brought into and out of contact with the sample surface by the use of a piezo-crystal where the cantilever or the surface itself is mounted, depending on the particular equipment used. The movement in this direction is conventionally referred to as the Z-axis. A laser light beam is reflected from the reverse side of the cantilever onto a position-sensitive photodetector. The configuration of the photodetector consisted of a quadrant photodiode divide into four parts with a horizontal and vertical dividing line. If each section of the detector is labelled from A to D, as shown in Figure 2.12, then the deflection signal is calculated by the signal difference detected in each part of the detector (38).

2.6.- Fluorescence spectroscopy

Once a molecule is excited by the absorption of a photon, this can return its ground state through either fluorescence emission, internal energy conversion (i.e. direct return to the ground state without fluorescence emission for example, by heat radiation), intersystem crossing (possibly followed by phosphorescence emission), intramolecular charge transfer and/or conformational change. All these processes can be visualized in the Perrin-Jablonski diagram (Figure 2.13). The singlet electronic states are denoted as S_0 (fundamental electronic state), S_1, S_2, ... and the triplet states as, T_1, T_2, ..., with different vibrational levels associated with each electronic state. It is important to note that energy absorption is very fast ($\approx 10^{-15}$ s) with respect to all other processes (so that there is no concomitant displacement of the nuclei according to the Franck-Codon principle) (39)(40). The vertical arrows corresponding to the energy absorption process start from the 0 vibrational energy level, S_0, since most of molecules are in this state at room temperature. Absorption of a photon, hence, can bring a molecule to one of the vibrational levels of S_1, S_2, ...

Emission of photons accompanying the $S_1 \rightarrow S_0$ relaxation is called fluorescence. It should be emphasized that, apart from a few exception, fluorescence emission occurs from S_1 and, therefore, its characteristics (except polarization) do not depend on the excitation wavelength (of course only one species exists in the ground state). The transition between the ground state and the excited stated (0-transition) is usually the same for absorption and fluorescence. However, the fluorescence spectrum is located at higher wavelengths than the absorption one

because of the energy loss in the excited state due to vibrational relaxation (Figure 2.14). According to the Stokes rule the fluorescence emission wavelength should be always higher than that of absorption. However, in most cases the absorption spectrum partly overlaps the fluorescence spectrum, i.e. a fraction of light is emitted at shorter wavelengths than the absorbed light. Such an observation seems to be, at first, in contradiction with the energy conservation principle. However, such energy defect is compensated by the fact that a small fraction of molecules is in a higher vibrational level in the ground state as well as in the excited state at room temperature (39).

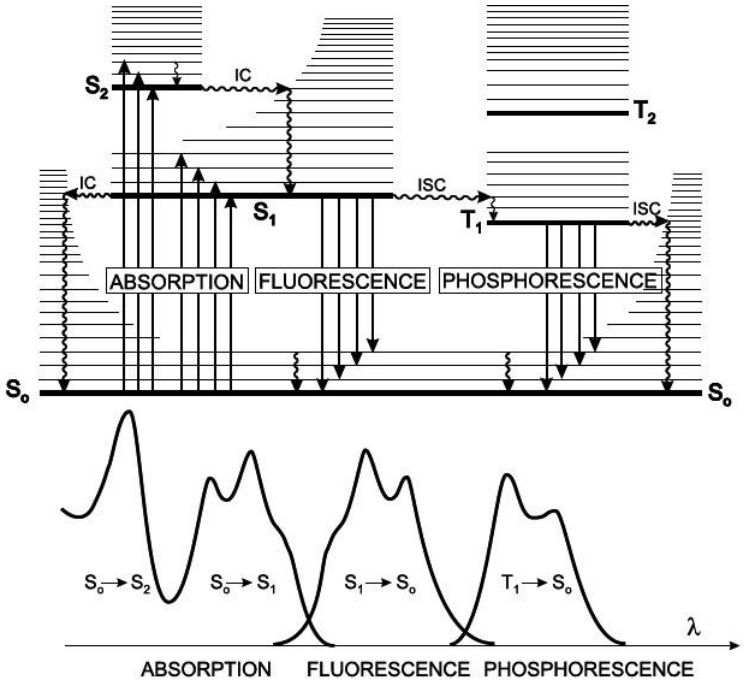

Figure 2.13. Perrin-Jablonski diagram and illustration of the relative positions of absorption, fluorescence and phosphorescence processes (39).

In general, differences between the vibrational levels are similar in the ground and excited states, so that the fluorescence spectrum often resembles the first absorption band. The gap, expressed in wavenumber, between the maximum of the first absorption band and the maximum of fluorescence is called the Stokes shift.

It should be noted that photon emission is as fast as photon absorption. However, excited molecules remain in the S_1 state for a certain time (a few tens of picoseconds to a few hundreds of nanoseconds, depending on the type of molecule and its surrounding medium) before emitting a photon or undergoing other relaxation processes. Thus, after excitation of a

population of molecules by a very short light pulse, the fluorescence intensity decreases exponentially with a characteristic time, reflecting the average lifetime of the molecules in the S_1 excited state.

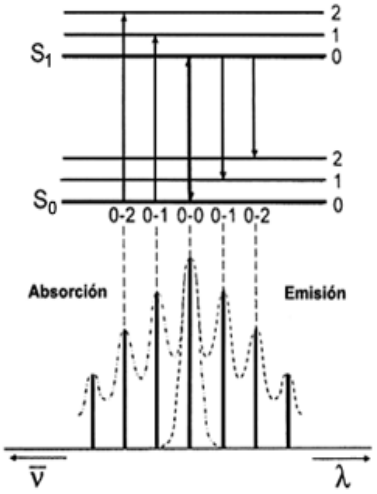

Figure 2.14. Illustration of the vibrational bands in the absorption and fluorescence spectra.

As a consequence of the strong influence of the local environment or surrounding medium on fluorescence emission, fluorescent molecules are currently used for physicochemical, biochemical and biological investigation. For example, fluorescence spectroscopy can be employed as a highly sensitive method for protein analysis. Intrinsic protein fluorescence deriving from the naturally fluorescent amino acid tryptophan (and to a lesser extent from tyrosine and phenylalanine) can provide information on the protein conformational structure and it changes. On the other hand, the use of extrinsic fluorescent dyes offer additional possibilities for protein characterization, i.e. to monitor their refolding and unfolding processes, to detect molten globule intermediates, or to characterize protein aggregation and fibrillation amongst others. For example, the dye 1-anilinonaphthalene-8-sulfonate (ANS) is hardly fluorescence in aqueous environments but become highly fluorescent in apolar-organic solvents or upon adsorption to solid phases. Other important dyes for protein characterization are, for example, Nile Red (used for monitoring protein conformational changes), 9-(dicyanovinyl)-julolidine (DCVJ, used to probe tubulin structure and the formation of hydrophobic microdomains along protein aggregation), or Congo Red and Thioflavin T (used to characterize the extent of β-sheet formation along protein fibrillation) (40)(41).

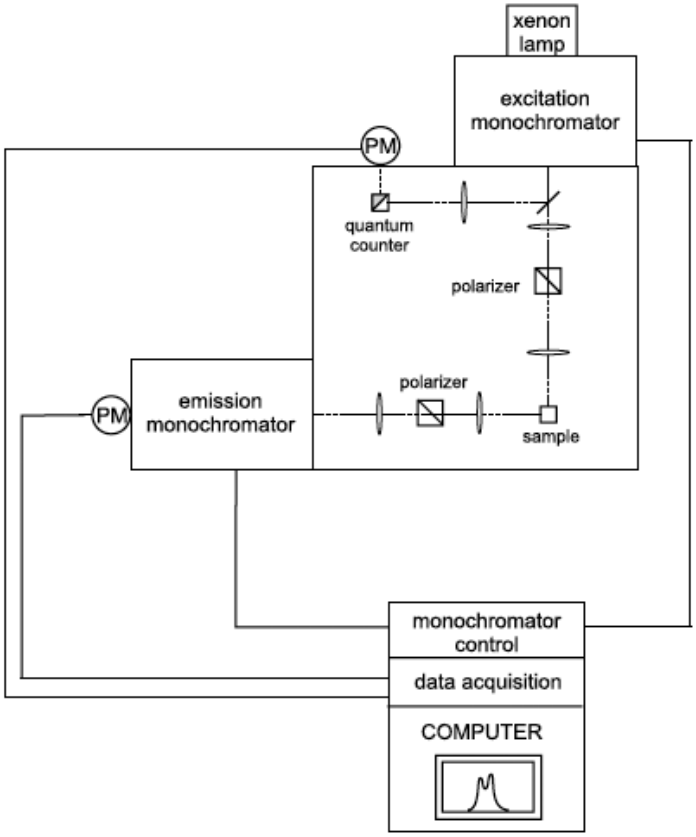

Figure 2.15. Schematic representation of a spectrofluorometer (40).

Figure 2.15 shows the components of a conventional spectrofluorometer. The light source is commonly a high-pressure xenon arc lamp, which offers the advantage of a continuous emission from 250 nm to the infrared. A monochromator is used to select the excitation wavelength. Fluorescence is collected at right angles with respect to the incident beam and detected through a monochromator by a photomultiplier. Automatic scanning of wavelengths is achieved by motorized monochromators, which are controlled by the electronic devices and the computer, in which the data are stored (39)(40). The optical module contains various parts: a sample holder, shutters, polarizers if necessary, and a beam splitter consisting of a quartz plate reflecting a few per cent of the exciting light towards a quantum counter or a photodiode. A quantum counter usually consists of a triangular cuvette, containing a concentrated solution of a dye whose fluorescence quantum yield is independent of the excitation wavelength.

2.7.- Circular dichroism (CD)

Circular dichroism (CD) spectroscopy is commonly used for the study of macromolecules (synthetic and natural). CD technique is based on the rotation and absorption of left and right circularly polarized light passing through a sample so < CD signal will be generated when the circularly polarized light pass through a chiral sample. In this regard, a plane-polarised light beam can be considered to consist of two equal and opposing left and right circularly polarized light beams. In Figure 2.16, the electric vector of these beams is viewed looking down the direction of the light source. When the magnitudes of these vectors are equal, their resultant will trace the linear path of the electric vector amplitude of a plane-polarised light beam. This means that the magnitudes of the vector will be no longer the same. This difference involves that the resultant vector will be that of an elliptically polarized light beam passing through the sample (40)(42):

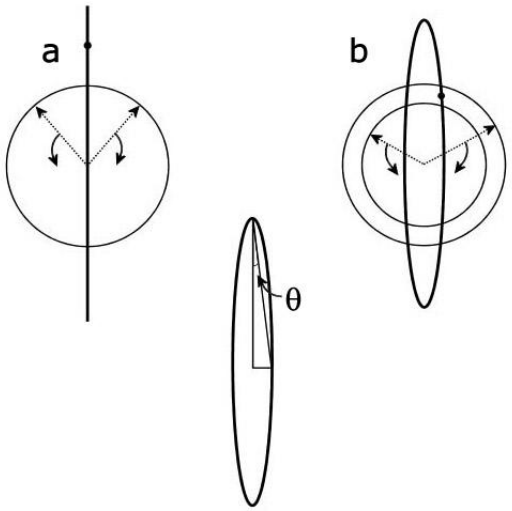

Figure 2.16. Illustration of how circularly polarized light interacts with achiral and chiral molecules. Plane polarized light can be considered as composed of the sum of two equal and opposing left and right circularly beams. These views represent the electric vector component of the beams looking down the direction of propagation of the light source. a) The resultant transmitted beam is still present when the plane polarized light pass through an achiral sample; b) circularly polarized light is present when it passes through a chiral sample; and c) pictorial representation defining ellipticity (42).

In many biological systems, the presence of different asymmetric chemical groups around a carbon atom originates chirality, as in the case of amino acids forming the polypeptide

backbone of proteins. Since proteins, then, are built by units that are chiral, they will interact with left and right circularly polarized light to different extents giving rise to circular dichroism (40)(42). Hence, circular dichroism can be defined as the difference between the absorption of left and right circularly polarized light by a chiral molecule:

$$\Delta A = A_L - A_R \qquad 2.32$$

where A_L and A_R are the absorption of the left and right circularly polarized light, respectively, by the chiral molecule. For achiral molecules $\Delta A = 0$, and no CD signal is present. For chiral molecules, $A_L \neq A_R$ at some wavelength, and the resulting ΔA will be non-zero; it can have either a positive or negative value depending on the relative intensities of the left and right-handed light absorbance. Usually, in the analysis of protein structures CD instruments scale the chirality as ellipticity, θ, expressed in millidegrees. Therefore, a CD signal can be viewed either as an absorption difference or as the produced ellipticity, although both are related each other. However, ellipticity is not a useful quantity to compare different samples as its magnitude differs depending on the amount of protein present in the sample. For CD spectral data, the most useful units are delta epsilon the molar circular dichroism, $\Delta\varepsilon$, and the mean residue ellipticity $[\theta]_{MRE}$ (MRE).

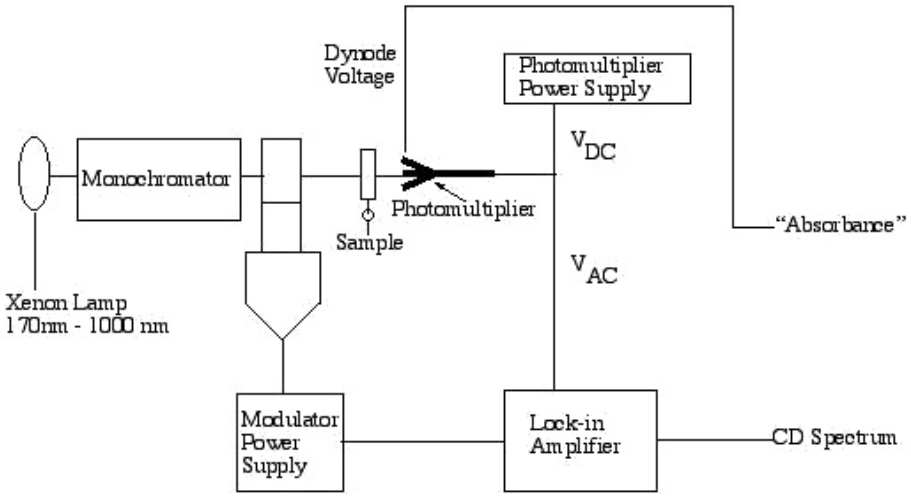

Figure 2.17. Schematic representation of a typical circular dichroism spectrometer.

To obtain a circular dichroism spectrum (Figure 2.17), a periodic variation in the polarization of the light beam is induced by the polarization modulator through all ellipticities. This polarized light passes through the sample to a photomultiplier detector. If the sample is not optically

active, the light beam does not vary through this cycle. With the introduction of an optically active sample, a preferential absorption is seen during one of the polarization periods, and the intensity of the transmitted light now varies during the modulation cycle. The variation is directly related to the circular dichroism of the sample at that specific wavelength. Successive detection is performed at various wavelengths leading to the generation of the full CD spectrum.

2.8.- Infrared spectroscopy

Molecules consist of atoms which have a certain mass and are connected by elastic bonds. As a result, they can perform periodic motions, i.e. they have vibrational degrees of freedom. All motions of the atoms in a molecule relative one each other are a superposition of the so-called normal frequencies. These are described by a normal coordinate. For polyatomic molecules, the number of characteristic frequencies is $3N-6$ for non-linear molecules and $3N-5$ for linear molecules, where N is the number of atoms in the molecule, which define their vibrational spectra. These spectra depend on atoms mass, their geometrical arrangement, and the strength of their chemical bonds. Molecular aggregates such as crystals or complexes behave like "super-molecules" in which the vibrations of the individual components are coupled. As a first approximation the normal vibrations are considered not coupled, i.e. they do not interact. However, the bonds elasticity does not strictly follow Hooke's law. Therefore, overtone and combinations of normal vibrations may appear (40)(43).

Infrared (and RAMAN) spectrometers are the most important tools for observing vibrational spectra. Depending on the nature of the vibration, which is determined by the symmetry of the molecule, vibration may be active or forbidden in the infrared (or RAMAN) spectrum.

From basic theory, it is easy to understand that a molecule can take up an amount of energy, $h\nu$, to reach a vibrationally excited state only when the frequency of the incident radiation on a molecule is the same as the vibrational frequency of the latter. This phenomenon involves either a change of the molecule's dipole moment or a change in its polarizability. If the former phenomenon takes place, we will observe an IR band; if the second one occurs, we will observe a RAMAN band. The absorption wavelength range of IR spectroscopy is from 2.5 to 1000 μm, which corresponds to the energy $h\nu = hc\tilde{\upsilon}$ with $\tilde{\upsilon}$ = 4000-10 cm^{-1}, with c the light velocity.

According to classical mechanics, the vibrating atoms groups in a molecule can be modelled as balls joined by springs (the molecular bonds). To take the simplest example, let us consider two balls joined by one spring representing a diatomic molecule. In this approximation, two atoms and the connecting bond are treated as a simple harmonic oscillator composed of 2 masses (atoms or balls). These two balls can vibrate with a characteristic frequency that depends on the mass of the balls and on the spring force (spring force can be approximated by Hooke's law). Matematically, the equation $\nu = (1/(2\pi))\sqrt{\kappa/\mu}$, describes the characteristic oscillation frequency ν and how it depends on mass μ and spring constant force κ. According to this equation, stiffer spring constant (stronger bonds) result in a higher frequency, whereas heavier atoms result in lower frequencies. This simple system possess only a single characteristic frequency. The balls can only vibrate with this characteristic frequency or an integer multiple of this frequency. A more complex molecule can still be modelled quite accuarately as balls of different massess joined by springs of different tensions (representing different atoms with different bonds). Figure 2.18 shows a diagram representing the vibration of a diatomic molecule or one vibrational degree of freedom of a polyatomic molecule, which is excited by a transition from energy level $\upsilon = 0$ to $\upsilon = 1$ (40)(43)-(45).

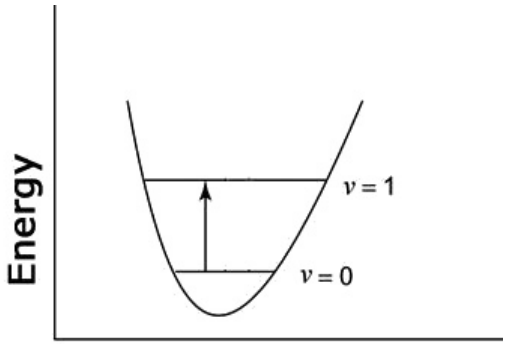

Figure 2.18. Observation of the excitation of a vibrational state in the electronic ground state by infrared absorption.

In the classical harmonic oscillator, $E = \frac{1}{2}\kappa x^2 = h\nu$, where x is the displacement of the spring. Thus, the energy or frequency is dependent on how far one stretches or compresses the spring. If this simple model were true, a molecule could absorb energy of any wavelength. However, vibrational motion is quantized and, therefore, the molecules can only exist in finite energy states. In the case of harmonic potentials, these states are equidistant, i.e. $E_i = h\nu(n_i + 1/2), n_i = 0, 1, 2, \ldots$ where the energy levels are numbered as n_i. At n_i = 0, the potential energy has its lowest value, which is not the potential minimum energy (43)(44).

According to the selection rules, only transitions to the next energy level are allowed; therefore, molecules will absorb an amount of energy equal to hv. This rule is not inflexible and, occasionally, transitions of $2hv$, $3hv$, or higher are observed. These correspond to bands called overtones in an IR spectrum. They are of lower intensity than the fundamental vibration bands.

As mentioned above, infrared spectra cover the near infrared(0.75-3 μm), middle infrared (3-30 μm) and far infrared (30-300 μm) range. In this region, most molecules show absorption or emission bands arising from symmetry-allowed interaction with the radiation. The energy of the absorbed and emitted light is equivalent to the energy difference between the lowest vibrational states of the electronic ground state of a molecule.

Three types of instruments for IR absortion measurements are commonly available: dispersive spectrophotometers with a grid monochromator, Fourier thansform spectrometers employing an interferometer, and non-dispersive photometers using a filter or absorbing gas (typically used for analysis of atmospheric gases at specific wavelengths).

Until 1980s, the most widely used instruments for IR measurements were dispersive spectrometers. Nowadays, this type of instruments has been displaced by Fourier transform (FT) spectrometers because of their speed, reability, enhanced signal-to-noise ratio. Infrared spectrometers (Figure 2.19) usually combine a radiation source, collimator, fixed mirror, moving mirror, a sample holder, a device for spectral dispersion or selection of radiation (beam splitter), and a radiation detector, all connected to appropiate recording and evaluation facilities. An ideal spectrometer records completely resolved spectra with a maximum signal-to-noise ratio. It requires a minimum amount of sample which is measured nondestructively in a minimum time, and it provides facilities for storing and evaluating the spectra. FTIR spectrometers can be single-beam or double-beam instruments. A typical procedure for determining transmittance or absorbance with this type of instrument is to first obtain a reference interferogram by scanning a reference (usually air) twenty or thirty times coadding the data, and storing the results in the computer. A sample is inserted in the radiation path and the process repeated. The ratio of the sample to reference spectral data is, then, computed to obtain the transmittance at various frequencies.

Infrared spectroscopy (IR) has long been used to determine molecular structures and to identify unknown compounds. IR data have been used to obtain information about the

chemical composition, configuration, and crystallinity of polymeric and biological materials (43). In particular, FTIR spectroscopy is a versatile spectroscopic technique for analyzing protein structure in solution, in aggregates and inclusion bodies. Most IR studies focus on the characterization of protein secondary structures by using absorption bands reflecting the motions of peptide groups. Infrared spectra of proteins may be obtained either in the solid state or in solution. The vibrational spectra of proteins exhibit several relatively intense peaks which shift in wavenumber and intensity from one sample to another. There are several prominent bands for the study of polypeptides and proteins; however in this study, we will focused partularly on the amide bands, which are of particular interest for the study of protein conformation: the amide I, between 1680 and 1600 cm^{-1}, is mainly associated with the stretching vibration of the C=O bond; amide II, found between 1580 and 1480 cm^{-1}, and amide III band, observed between 1300 and 1200 cm^{-1}, are both associated with coupled C-N stretching and N-H bending vibrations of the peptide groups, respectively. These bands are conformationally sensitive, and their position may be attributed to a dominat protein conformation, that is, α-helix, parallel and antiparallel β-sheets, turns or random coil (38)(42). In particular, the following vibrational frequencies had been assigned to: 1654 cm^{-1} for α-helix; (1624, 1631, 1637, and 1675 cm^{-1} for β-sheets; 1663, 1670, 1683, 1688, and 1694 cm^{-1} for turns; and 1645 cm^{-1} for other structures (43)(46)-(48). The relative amounts of the four secondary structures are determined by the relative areas under the band peaks.

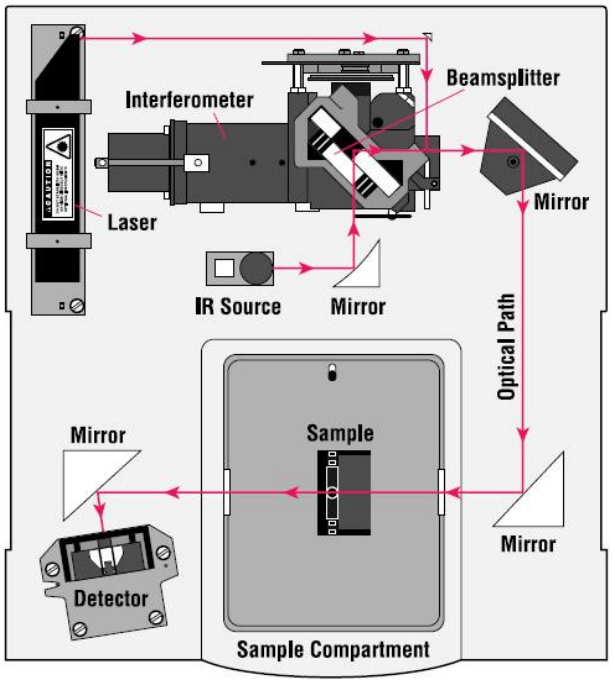

Figure 2.19. Scheme of a FTIR instrument.

2.9.- Rheology

Rheology involves the study of the deformation and flow of matter due to compressive stresses acting on a material. Particularly, it refers to the behaviour of materials when a mechanical force is applied on. Rheology includes three main concepts such as *force*, *deformation* and *time*. Irreversible flows, reversible elastic deformations or their combination (viscoelasticity) can, therefore, model and describe a rheological phenomenon under certain assumptions. The type of deformation depends on the state of matter; for example, gases and liquids will flow when a force is applied, whilst solids will deform by a fixed amount and, then, back to their original shape when the force is removed. In the case of polymers, the rheological and mechanical properties affect the polymers molecular properties, such as their molecular weight, molecular weight distribution, conformation, architecture and crystallinity (49)(50).

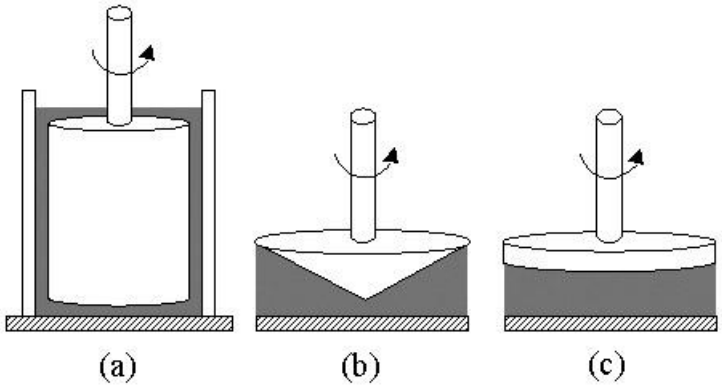

Figure2.20 Schematic diagram of basic tool geometries for a rotational rheometer: a) concentric cylinder, b) cone and plate, c) parallel plate (50).

A typical rheometer measures the velocity of displacement of the moving surface and the force exerted on one of the surfaces. Most rheometers are based on rotary motion and use one of the three following geometries (Figure 2.20): concentric cylinder, cone and plate, and parallel disk. In most cases the same rotary instrument can use all three of these flow geometries. To generate the needed motion, they typically use actuators like a hydraulic piston or ball screws found in standard tensile testing machines for solids. Solenoids or other electromechanical actuator are often used for small amplitudes and low forces. There are two basic designs of rheometers: controlled stress ones, where the stress is applied electrically via a motor measuring the strain; and controlled strain instruments, in which a strain is imposed and the stress is computed from the deformation of a calibrated spring system (50).

2.9.1.- Viscoelasticity

Many materials can be classified as solid or fluids, displaying elastic and viscous behaviour respectively. Viscoelastic materials such as polymers combine the characteristics of both elastic and viscous materials depending on the experimental time scale. Application of a stress of relatively long duration may cause some flow and irrecoverable deformation, while a rapid shearing would induce an elastic response in some polymeric fluids. Then, a classification of these materials should include a consideration of the timescale of the measurement relative to the characteristic time of the material. This ratio is given by the Deborah number (D_e): when D_e is 1 the material will display both viscous and elastic behaviour and is described as viscoelastic, whilst, for D_e » 1 and D_e « 1 the material has solid-like and viscous-like behaviour, respectively (49)(50).

Pure elastic solid behaviour may be exemplified by a Hookean spring, and pure viscous flow can be exemplified by the behaviour of a dashpot, which is essentially a piston moving in a cylinder of Newtonian fluid. Nevertheless, the viscoelasticity cannot be described accurately by neither spring nor dashpot alone, but a combination of both. In this way, several mechanical models have been developed to describe the viscoelastic response of a given material. All of these mechanical models are, then, supported on the combination of these two simple elements (spring and dashpot), which represented the elastic behaviour of a solid body, and the viscous flow for a liquid, respectively. Among all models, Maxwell's and Kelvin-Voigt's models are the most frequently used (Figure 2.21) (50).

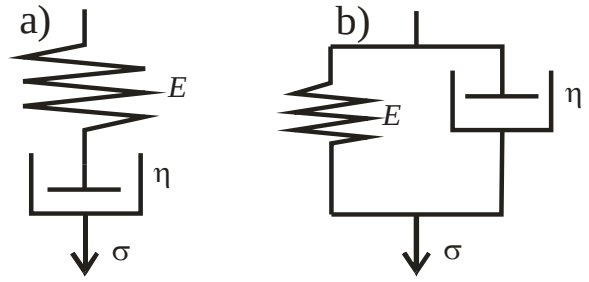

Figure 2.21. a) Maxwell's and b) Voigt's models.

The use of mechanical models such as the spring and dashpot as analogues of the behaviour of real materials enables us to describe very complex experimental behaviours using a simple combination of models. The uses of models to represent a wide range of deformation are not restricted to the application of shear stress; however, in this section, we will focus on the shear properties of the material (1).

To overcome the poor description of real polymeric materials by either the spring or the dashpot, Maxwell suggested a simple series combination of both elements (Figure 2.21a). Because the material possesses the ability to flow, some inertial relaxation will occur and less force will be required upon time to sustain the deformation. The goal in the Maxwell's model is to calculate how the stress varies with time, or expressing the stress in terms of the constant strain to describe the time-dependent modulus. Let us consider in the Maxwell's model, in which one spring is attached to one dashpot, as shown in Figure 2.21a. When a force is acting on the spring downward at $t = 0$ (in one dimensional flow), the stress-strain relation for the spring (Hookean material) may be described by (50):

$$\sigma = \gamma G \tag{2.33}$$

where σ is the applied stress, γ is the strain, and G the elastic modulus. Conversely, the stress response of the dashpot (a purely viscous Newtonian fluid) to an applied deformation rate may be described as:

$$\sigma = \eta \dot{\gamma} \tag{2.34}$$

where $\dot{\gamma} = d\gamma/dt$ is the strain rate and η, defines the viscous response of the dashpot with Newtonian behaviour. In other words, the spring purely exhibits an elastic effect (as a Hookean solid) and the dashpot exhibits purely a viscous effect (as a viscous fluid).

In the Maxwell's element, both the spring and the dashpot support the same stress and, therefore:

$$\sigma = \sigma_{el} + \sigma_{vis} \tag{2.35}$$

where σ_{el} and σ_{vis} are the stresses on the spring and dashpot, respectively. However, the overall strain and the strain rates are the sum of the elemental strain and strain rates, respectively, that is:

$$\gamma = \gamma_{el} + \gamma_{vis} \tag{2.36}$$

or

$$\dot{\gamma} = \dot{\gamma_{el}} + \dot{\gamma_{vis}} \quad 2.37$$

where $\dot{\gamma}_{tot}$ is the total strain rate, while $\dot{\gamma_{el}}$ and $\dot{\gamma_{vis}}$ are the strain rates of the spring and dashpot, respectively. Therefore, the total strain of the spring and dashpot at any time t is the sum of that of the spring and of the dashpot. Then, for a Maxwell's model the strain rates can be written as:

$$\dot{\gamma} = \dot{\sigma}/G + \sigma/\eta \quad 2.38$$

By rheometry we can be measure the response of a material to an oscillating stress or strain, so it is considered as mechanical spectroscopy. When a sample is constrained in, for example, a cone and plate assembly, an oscillating strain at a given frequency can be applied to the sample. After an initial start-up period due to a transient sample state a stress develops in direct response to the applied strain. If the strain has an oscillating value with time the stress must also be oscillating. We can represent these two wave forms as in Figure 2.22. The elastic and viscous effects are out of phase one each other by some angle δ (1).

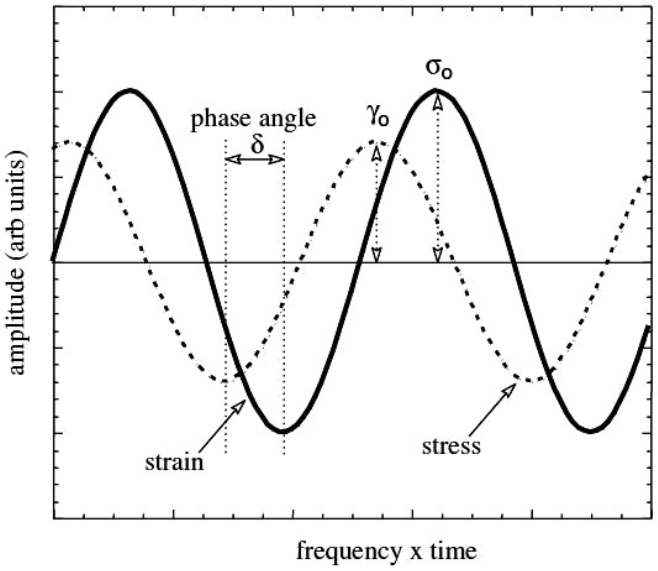

Figure 2.22. An oscillating strain and the stress response for a viscoelastic material.

All the information about the response of the sample at this frequency is contained within these wave forms. However, this information is not in a particularly tractable form. What we would really prefer is to have a few representative terms such as the relaxation time and

elasticity or viscosity of the sample in order to characterize its material properties. In order to obtain this information some mathematical manipulation is required. Two key features can be utilized. The first feature is the maximum stress, σ, divided by the maximum strain, γ, which is constant for a given frequency ω. This ratio is called the complex modulus G^*:

$$|G^*(\omega)| = {}^{\sigma}/_{\gamma} \qquad 2.39$$

ω is the radial frequency, which is $2\pi f$, where f is the applied frequency measured in Hz. The other feature constant with time at any given frequency is δ, the phase difference (expressed in radians). These two values, G^* and δ, are characteristic of the material. It is straightforward to visualise the situation where an elastic solid is placed in a cone and plate geometry. When a tangential displacement is applied to the lower plate a strain in the sample is produced. That displacement is transmitted directly through the sample. The upper cone will react proportionally to the applied strain to give a stress response. An oscillating strain will give an oscillating stress response that is in phase with the strain, so δ will be zero. However, if we have a Newtonian liquid, the peak stress will be out of phase by $\pi/2$ rad as the peak stress is proportional to the strain rate. So, it follows that if we have a viscoelastic material some energy is stored and some dissipated, and the stored contribution will be in phase whilst the dissipated or loss contribution will be out of phase respect to the applied strain.

In order to describe the material properties as a function of frequency we need to use the constitutive equation 2.30. This equation describes the relation between the stress and the strain. However, it is most convenient to express the applied sinusoidal wave in the exponential form of the complex number notation:

$$\gamma^* = \gamma_0 e^{i\omega t};\ \dot{\gamma}^* = i\omega\gamma_0 e^{i\omega t} = i\omega\gamma^* \qquad 2.40$$

Now, the stress response lags by the phase angle δ:

$$\sigma^* = \sigma_0 e^{i(\omega t+\delta)};\ \dot{\sigma}^* = i\omega\sigma_0 e^{i(\omega t+\delta)} = i\omega\sigma^* \qquad 2.41$$

So, substituting the complex stress and strain into the constitutive equation for a Maxwell fluid the resulting relation is given by:

$$\dot{\gamma}^* = {\dot{\sigma}^*}/{G} + {\sigma^*}/{\eta} \quad 2.42$$

Using equations 2.40 and 2.41 in equation 2.42 and rearranging we have:

$${\gamma^*}/{G\sigma^*} = 1 + {G}/{i\omega\eta} \quad 2.43$$

Thus, arrangement of this expression gives the complex modulus and frequency:

$${G}/{G^*(\omega)} = 1 + {1}/{i\omega\tau} \quad 2.44$$

or:

$$G^*(\omega) = G\left(\frac{i\omega\tau}{1+i\omega\tau}\right) \quad 2.45$$

where $\tau = G/\eta$ is the characteristic relaxation time. This expression describes the variation of the complex modulus with frequency for the Maxwell model. It is normal to separate the real and imaginary components of this expression. This is achieved by multiplying by $(1 - i\omega\tau)$ to give:

$$G^*(\omega) = G'(\omega) - iG''(\omega) = G\frac{(\omega\tau)^2}{1+(\omega\tau)^2} + iG\frac{\omega\tau}{1+(\omega\tau)^2} \quad 2.46$$

where $G'(\omega)$ is an in phase elastic modulus with energy storage in the periodic deformation, and is called the dynamic storage modulus. $G''(\omega)$ is an out of phase elastic modulus associate with the energy dissipation as heat, and is called the dynamic loss modulus. Then:

$$G'(\omega)G\frac{(\omega\tau)^2}{1+(\omega\tau)^2} \quad 2.47$$

$$G''(\omega) = G\frac{\omega\tau}{1+(\omega\tau)^2} \quad 2.48$$

These expressions describe the frequency dependence of the stress with respect to the strain.

It is normal to represent them as two moduli that determine the component of stress in phase with the applied strain (storage modulus) and the component out of phase by 90^0. In an experiment, the amplitudes of the oscillation input (γ_0) and output (σ_0), and the phase angle (δ) are measured. Therefore, each oscillatory shear flow measured at a given ω provides two independent quantities, amplitude ratio and phase angle:

$$|G^*(i\omega)| = \sigma_0/\gamma_0 = \left[\left(G'(\omega)\right)^2 + \left(G''(\omega)\right)^2\right]^{1/2} \quad 2.49$$

$$\tan\delta = G''(\omega)/G'(\omega) \quad 2.50$$

The storage and loss moduli are subtle descriptions of the material properties of the system. These two properties are related to the phase angle and complex modulus. These are both functions of the applied frequency and represent an alternative description of the system.

$$G'^{(\omega)} = G^*(\omega)\cos\delta, \qquad G''^{(\omega)} = G^*(\omega)\sin\delta \quad 2.51$$

The phase angle changes with the frequency, from 90 degrees at low frequency, to 0 degrees at the high frequency limit; thus, as the frequency increases the sample becomes more elastic, and the phase difference between the stress and the strain reduces.

2.10.- X-ray diffraction

X-ray diffraction (XRD) is a versatile, powerful and non destructive technique that reveals detailed information about the chemical crystallographic structure of natural and manufactured materials. Diffraction effects are observed when an electromagnetic radiation impinges on periodic structures with geometrical variations on the length scale of the radiation wavelength. The inter-atomic distances in crystal and molecules is around to 0.15 – 0.5 nm, which correspond in the electromagnetic spectrum with the wavelength of X-rays, having photon energies between 3 and 8 keV (3).

There are three different types of interactions between X-rays and matter. First, the photoionization, where electrons may be liberated from their bound atomic states during the process, and which falls into the group of inelastic processes. In addition, other inelastic

scattering process that incoming X-ray beams may undergo upon interaction with matter is the energy transfer to an electron but, in this case, without a release of the electron from the atom (phenomenon known as Compton scattering). Finally, X-rays may be elastically scattered by electrons, process known as Thomson scattering. In this process, the electron oscillates at the frequency of the incoming beam so the wavelength of the scattered radiation is conserved.

There are many theories and equations to correlate the diffraction pattern and the material structure. The Bragg law is a simple way to describe the diffraction of X-rays by a crystal. In Figure 2.23a, the incident X-rays reach the crystal planes with an incident angle θ and are diffracted at an angle θ. The diffraction peak is observed when the Bragg condition is satisfied (3)(51):

$$n\lambda = 2d \sin\theta \qquad 2.52$$

where λ is the wavelength of the incident X-rays, d is the distance between each adjacent crystal plane (d-spacing), θ is the Bragg angle at which a diffraction peak is observed, and n (1, 2, ...) is an integer number, called the reflection order; this means that the Bragg condition can be satisfied by various X–ray wavelengths. The Bragg law gives a simple relationship between the diffraction pattern and the crystal structure, and many X-ray diffraction applications can be easily explained by this law.

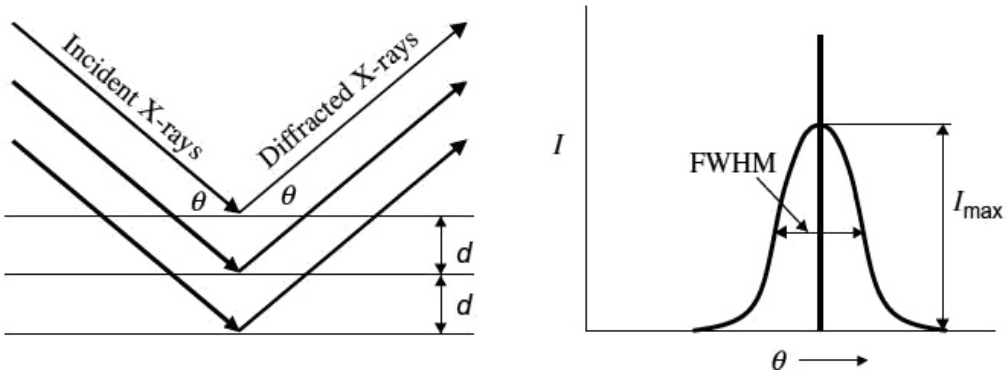

Figure 2.23. a) Incident and reflected X-rays form an angle θ which is symmetric to the crystal normal plane; b) The diffraction peak is observed at a Bragg angle θ (52).

In X-ray diffraction using a single wavelength, the Bragg equation is typically expressed with n = 1 for the first order of diffraction because higher order reflections can be considered as

resulting from different lattice planes. For instance, the second-order reflection from (*hkl*) planes is equivalent to the first-order reflection from (*2h, 2k, 2l*) planes. The diffraction peak is displayed as diffracted intensities at a range of 2θ angles. For perfect crystals, the peak is a delta function, the dark straight vertical line shown in Figure 2.23b (52).

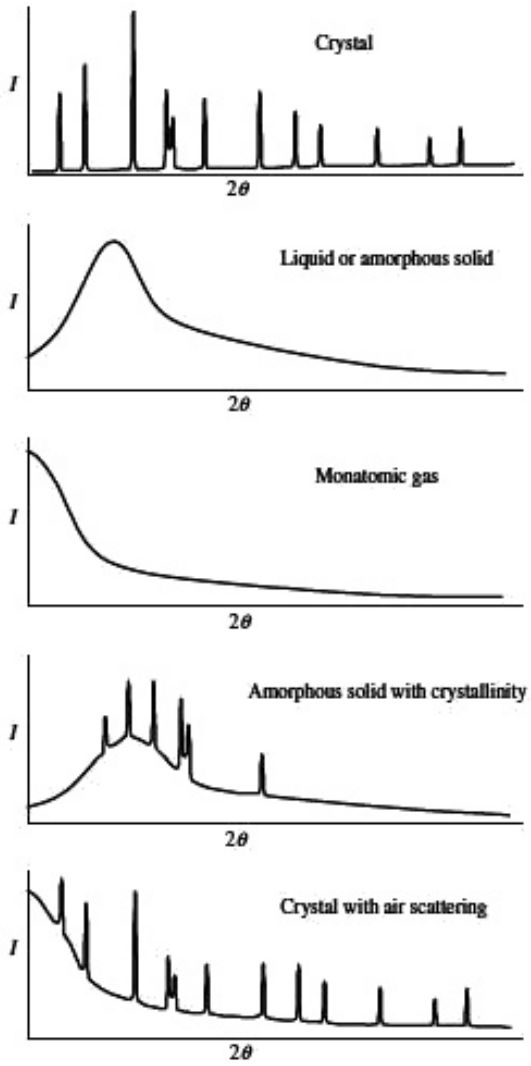

Figure 2.24. Diffraction patterns from crystalline solids, liquids, amorphous solids, and monoatomic gases as well as their mixtures (52).

A typical diffraction peak is a broadened peak displayed by the curved line in Figure 2.23b. The peak broadening can be due to many effects, including imperfect crystal conditions, such strain, mosaic structures, and finite sizes; ambient conditions, such as atomic thermal vibrations; and instrumental conditions, such as X-ray beam size, beam divergence, beam spectrum distribution, and detector resolution. The curved line gives a peak profile, which is the diffracted intensity distribution of the Bragg angle. The highest point on the curve gives the

maximum intensity of the peak, I_{max}. The width of the peak is typically measured by its full width at half maximum (FWHM). The total diffracted energy can be measured by the area under the peak, which is referred to as integrated intensity. The integrated intensity is a more consistent value for measuring the diffracted intensity of a reflection since it is less affected by all peak broadening factors (51)(52).

The Bragg diffraction condition is based on the existence of a long periodicity of crystalline materials. As mentioned above, X-rays diffraction can provide information on the atomic arrangement in material with long-range order, short-range order, or no order at all, like gases, liquid, and amorphous solids, and a material may have one or to be a mixture of the former atomic arrangement types. Figure 2.24 gives a schematic comparison of the diffraction patterns for crystalline solids, liquids, amorphous solids, and monatomic gases as well as their mixtures. The diffraction patterns shown in this Figure are displayed as diffracted intensity versus 2θ assuming that the diffracted intensity is a unique function of the diffraction angle. The diffraction pattern from crystals has many sharp peaks corresponding to various crystal planes based on the Bragg law. The peaks at low 2θ angles are from crystal planes of large d-spacing and, viceversa, at high 2θ angles. To satisfy the Bragg condition at all crystal planes, the crystal diffraction pattern is actually generated from polycrystalline materials or powder materials. Therefore, the diffraction pattern is also called powder diffraction pattern. A similar diffraction pattern can be collected with a single crystal if this has been rotated at various angles during data collection so that the Bragg law can be satisfied when the crystal is at the right orientation.

Both amorphous solid and liquid materials do not have the long-range order of crystals, but their atomic distances have a narrow distribution because of atoms are tightly packed. In this case, the intensity of the scattered X-rays forms one or two maxima with a very broad distribution in the 2θ range. The intensity *vs.* 2θ distribution, thus, reflects the distribution of the atomic distances. In the case of a gas there is no order at all, i.e. the atoms are distributed randomly in space. The scattering curve is featureless except that the scattered intensity drops continuously with the increase of 2θ. On the other hand, the diffraction pattern from a material containing both amorphous and crystalline features has a broad background from the amorphous phase and sharp peaks from the crystalline phase. For example, many polymer materials have an amorphous matrix with crystallized regions. The diffraction pattern may contain air-scattering background in addition to sharp diffraction peaks. The air-scattering can be generated from the incident beam or diffraction beam. If the air-scattering is not removed

by the diffractometer, the diffraction pattern contains a high background at low 2θ angle and the background gradually decreases with increasing 2θ angle (52).

On the other hand, X-ray diffraction phenomena can also be explained in reciprocal space by the reciprocal lattice and the Ewald sphere. Reciprocal lattice is a transformation of the crystal lattice in real space to reciprocal space. The shape and size of a unit cell in real space can be defined by three vectors, **a**, **b**, and **c,** all starting from any single lattice point. The unit cell of the corresponding reciprocal lattice is, then, given by three vectors **a***, **b***, and **c*** (also referred to as reciprocal lattice axes), and:

$$\begin{aligned} \boldsymbol{a}^* &= \frac{1}{V}(\boldsymbol{b} \times \boldsymbol{c}), \\ \boldsymbol{b}^* &= \frac{1}{V}(\boldsymbol{c} \times \boldsymbol{a}), \\ \boldsymbol{c}^* &= \frac{1}{V}(\boldsymbol{a} \times \boldsymbol{b}) \end{aligned} \qquad 2.53$$

where V is the volume of the crystal unit cell in the real space and

$$V = \boldsymbol{a} \cdot \boldsymbol{b} \times \boldsymbol{c} \qquad 2.54$$

Since each reciprocal lattice axis is the vector product of two lattice axes in real space, these are perpendicular to the plane defined by the two lattice axes. The original lattice axes and reciprocal lattice axes maintain the following relations:

$$\boldsymbol{a} \cdot \boldsymbol{a} * = \boldsymbol{b} \cdot \boldsymbol{b} * = \boldsymbol{c} \cdot \boldsymbol{c} * = \mathbf{1} \qquad 2.55$$

and

$$\boldsymbol{b} \cdot \boldsymbol{a}^* = \boldsymbol{c} \cdot \boldsymbol{a}^* = \boldsymbol{a} \cdot \boldsymbol{b}^* = \boldsymbol{c} \cdot \boldsymbol{b}^* = \boldsymbol{b} \cdot \boldsymbol{c}^* = \boldsymbol{a} \cdot \boldsymbol{c}^* = 0 \qquad 2.56$$

Figure 2.26 illustrate the relationship between the original lattice in real space and the reciprocal lattice. The unit cell of the original lattice is drawn in dotted lines. The three reciprocal lattice axes define a unit cell of the reciprocal lattice (solid lines). The origin of the reciprocal lattice axes, denoted by O, is the origin of the reciprocal lattice. The repeat

translation of the reciprocal lattice unit cell in three dimensions forms the complete reciprocal lattice. Except the origin, each lattice point is denoted by a set of three integers (*hkl*), which are the number of translations of the three reciprocal lattice axes, respectively, to reach the lattice point. In other words, the vector drawn from the origin of the lattice point (*hkl*) is given by:

$$\mathrm{H}_{hkl} = h\mathbf{a}^* + h\mathbf{b}^* + l\mathbf{c}^* \qquad 2.57$$

and the direction of the vector H_{hkl} is normal to the lattice planes (*hkl*) in real space. The magnitude of the vector H_{hkl} is given by the *d*-spacing of the (*hkl*) planes:

$$|\mathrm{H}_{hkl}| = 1/d_{hkl} \qquad 2.58$$

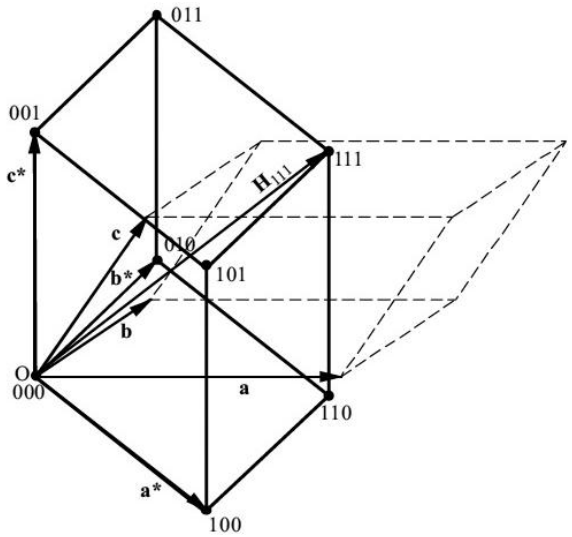

Figure 2.26. Relationship between the original lattice in real space and the reciprocal lattice (49).

Therefore, each point (*hkl*) in the reciprocal lattice represents a set of lattice planes (*hkl*) in the real space lattice. The position of the point in the reciprocal lattice defines the orientation and *d*-spacing of the lattice planes in the real space lattice. The farther away a reciprocal lattice point is from the origin, the smaller is the *d*-spacing of the corresponding lattice planes. For example, the reciprocal lattice point (111) represent the (111) lattice planes in the real space lattice, and the lattice vector is given by $\mathrm{H}_{111} = \mathbf{a}^* + \mathbf{b}^* + \mathbf{c}^*$ and $d_{111} = 1/|H_{111}| = 1/\mathbf{a}^* + \mathbf{b}^* + \mathbf{c}^*$.

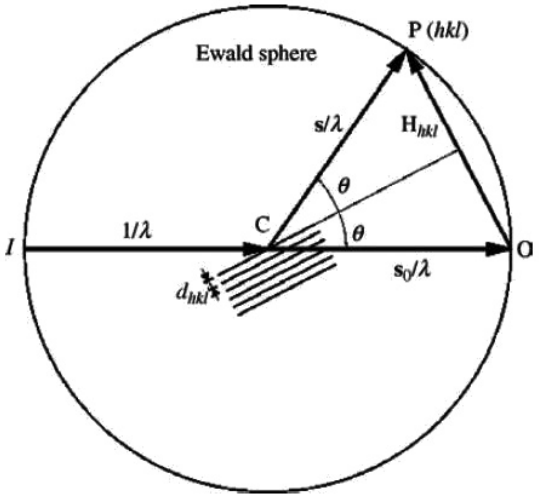

Figure 2.27. The Ewald sphere and Bragg condition in reciprocal space.

On the other hand, the relationship between the Bragg condition and the reciprocal lattice can be explained visually by the Ewald sphere, also referred as reflection sphere. Ewald came up with a geometrical construction to help the visualization of which Bragg planes are in the correct orientation to diffract. In Figure 2.27, the diffracting crystal is located in the center of the Ewald sphere, C. The radius of the Ewald sphere is defined as $1/\lambda$. The incident beam can be visualized as the vector from I to C, and the diffracted beam is the vector from C to P. Both the incident and diffracted beams form an angle θ from a set of crystal planes (hkl). The d-spacing of the crystal planes is d_{hkl} In the Ewald sphere; both incident beam vector s_0/λ and diffracted beam vector s/λ start at the poin C and end at the point O and P, respectively. The vector from O to P is the reciprocal lattice vector H_{hkl} and is perpendicular to the crystal planes. The three vectors have the following relationship:

$$\frac{s-s_0}{\lambda} = H_{hkl} = h\mathbf{a}^* + h\mathbf{b}^* + l\mathbf{c}^* \qquad 2.59$$

and their magnitude can be expressed based on the Bragg law as:

$$\frac{s-s_0}{\lambda} = \frac{2\sin\theta}{\lambda} = |H_{hkl}| = \frac{1}{d_{hkl}} \qquad 2.60$$

The point O is the origin of the reciprocal lattice, and the point P is the reciprocal point (hkl). The Bragg condition is satisfied only when the reciprocal lattice point falls on the Ewald sphere.

For a single crystal, the chance to have a reciprocal lattice point on the Ewald sphere is very small if the crystal orientation is fixed. Multiplying both ends of equation 2.59 by the three lattice axes in real space, respectively, the Laue equations are obtained:

$$\begin{aligned} \boldsymbol{a} \cdot (s - s_0) &= h\lambda \\ \boldsymbol{b} \cdot (s - s_0) &= k\lambda \\ \boldsymbol{c} \cdot (s - s_0) &= h\lambda \end{aligned} \qquad 2.61$$

The Laue equations establish that a periodic three-dimensional lattice produces diffraction maxima at specific angles depending on the incident beam direction and the wavelength. The Laue equations are suitable to describe the diffraction geometry of a single crystal. The Bragg law is more conveniently used for powder diffraction. Both the Bragg law and Laue equations define the diffraction condition in different formats.

On the other hand, the distance between the origin of the reciprocal lattice O and the lattice point P is reciprocal to the d-spacing. The largest possible magnitude of the reciprocal lattice vector is given by $2/\lambda$. This means that the smallest d-spacing satisfying the Bragg condition is $\lambda/2$. In powder X-ray diffraction, the random orientation of all crystallites can take all possible orientations assuming an infinite number of crystallites. The trace of the reciprocal lattice points from all crystallites can be considered as a series of spherical surfaces with origin O as the center point. Therefore, the condition to satisfy the Bragg law is only if the d-spacing is greater than half of the wavelength. In other words, the Bragg condition can be satisfied if a reciprocal lattice point falls in a sphere of 2λ from the origin O. This sphere is called the limiting sphere for powder diffraction.

X-ray diffraction systems have a variety of configurations and component options to fulfil requirements of different samples and applications. As shown in Figure 2.25, a typical XRD system normally consist of five basic components:

- The X-ray source produces X-rays with the required radiation energy, focal spot size, and intensity;
- The X-ray optics establish the primary X-ray beam to the required wavelength, beam focus size, beam profile, and divergence;
- The Goniometer and sample stage establish and tune the geometric relation between

primary beam, sample, and detector;

- The sample alignment and monitor assist users about sample positioning into the instrument and monitors the sample state and position;
- The area detector intercepts and records the scattering X-rays from a sample, and it saves and displays the diffraction pattern into a frame.

Each of the former basic components may have several options suitable for various application and functions. The whole system is controlled by a computer equipped with a software for instrument control, data acquisition and data analysis. In addition to the five basic components, there are some other accessories, such as a low and high-temperature stages, helium or vacuum beam path for SAXS, beam stop, and alignment and calibration fixtures.

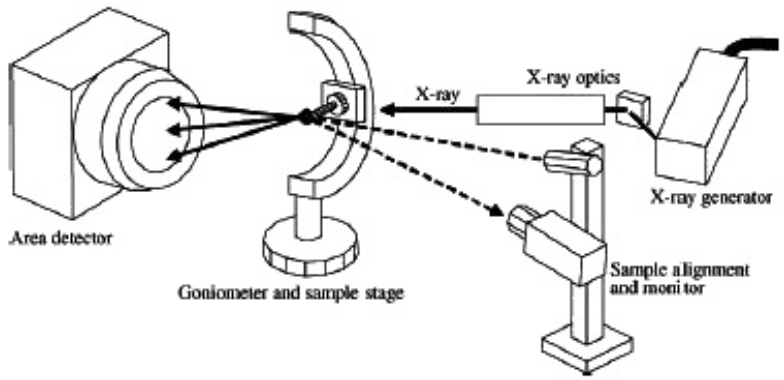

Figure 2.25. Scheme of a X-ray diffractometer.

2.11.- Additional experimental techniques used in fibrillogenesis studies

2.11.1.- UV-Vis absorption spectroscopy

Spectra are observed as the result of the energy exchange between a substance and the electromagnetic radiation. If the energy is absorbed by a substance from the radiation field, we have absorption spectra; if the energy is added to the radiation field, emission spectra are observed. An electromagnetic radiation may be characterized by the frequency ν, the wavelength λ, or the wave number υ. They are related as $\nu\lambda = c$, $1/\lambda = \upsilon$; where c is the velocity of light (39)(40)(53).

The three most important types of optical spectroscopies are ultraviolet and visible (UV-Vis), fluorescence and infrared (IR) spectroscopy. They differ only in the selection of the incident light wavelength. Both UV-Vis and fluorescence describe the phenomenon of electron

excitation; namely, a valance electron of a molecule is excited upon absorbing energy from the electromagnetic radiation and is, thereby, transferred from one energy level to other more energetic level. The spectra are electronic. In contrast, IR spectra describe the vibration of atoms (not electrons) around a chemical bond, as previously described in certain detail.

An electron transition consists of the promotion of an electron from a molecular orbital in the ground state to an unoccupied orbital by absorption of a photon. The molecule is, then, said to be in an excited state. Let us recall first the various types of molecular orbitals. A σ orbital can be formed either from two s atomic orbitals, from one s and one p, or from two p atomic orbitals having a collinear symmetry axis. The bond formed in this way is called a σ bond. A π orbital is formed from two *p* atomic orbitals overlapping laterally. The resulting bond is called a π bond. For example, in ethylene (CH_2=CH_2) the two carbon atoms are linked by one σ and one π bond. Absorption of appropriate energy can promote, for example, one of the π electrons to an anti-bonding orbital denoted by π^*. The transition is, then, called $\pi \rightarrow \pi^*$.

A molecule may also possess non-bonding electrons located on heteroatoms such oxygen or nitrogen. The corresponding molecular orbitals are called n orbitals. Promotion of a non-bonding electron to an anti-bonding orbital is possible, and the associated transition is denoted by $n \rightarrow \pi^*$. Hence, molecules containing a non-bonding electron, such as oxygen, nitrogen, sulphur, or halogens, often exhibit absorption in the UV region. To illustrate these energy levels, Figure 2.26 shows formaldehyde as an example with all their possible transitions. In particular, the $n \rightarrow \pi^*$ transition deserves further attention: upon excitation, an electron is removed from the oxygen atom and goes into the π^* orbital localized half on the carbon atom and half on the oxygen atom. The $n \rightarrow \pi^*$ excited state, thus, has a charge transfer character, as shown by the increase observed in the dipole moment regarding the ground state dipole moment of C=O (40)(53).

In summary, the electronic transitions observed in UV-Vis spectroscopy are $n \rightarrow \pi^*$, $\pi \rightarrow \pi^*$, $n \rightarrow \sigma^*$, $\pi \rightarrow \sigma^*$, $\sigma \rightarrow \pi^*$, and $\sigma \rightarrow \sigma^*$. The energy of these electronic transitions is, generally, in the following order: $n \rightarrow \pi^* < \pi \rightarrow \pi^* < n \rightarrow \sigma^* < \pi \rightarrow \sigma^* < \sigma \rightarrow \pi^* < \sigma \rightarrow \sigma^*$. Of the six transitions outlined, only the two lowest energetic ones ($n \rightarrow \pi^*$ and $\pi \rightarrow \pi^*$) are achieved by the energies available in the 200 to 800 nm. The last four types of electronic transitions required higher energy inputs, below 200 nm, corresponding to the far ultraviolet region of the electromagnetic spectrum. For instance, most $\sigma \rightarrow \sigma^*$ transitions for individual bonds take place below 200 nm and a compound containing only σ bonds is transparent (near

zero absorption) in the near-UV-Vis region. For example, methane (which has only C-H bonds) the transition $\sigma \rightarrow \sigma^*$ takes place at 125 nm.

In absorption and fluorescence spectroscopy, two important types of orbitals are considered: the Highest Occupied Molecular Orbitals (HOMO) and the Lowest Unoccupied Molecular Orbitals (LUMO). Both of these refer to the ground state of the molecule. For instance, in formaldehyde, the HOMO is the n orbital and the LUMO is the π^* orbital.

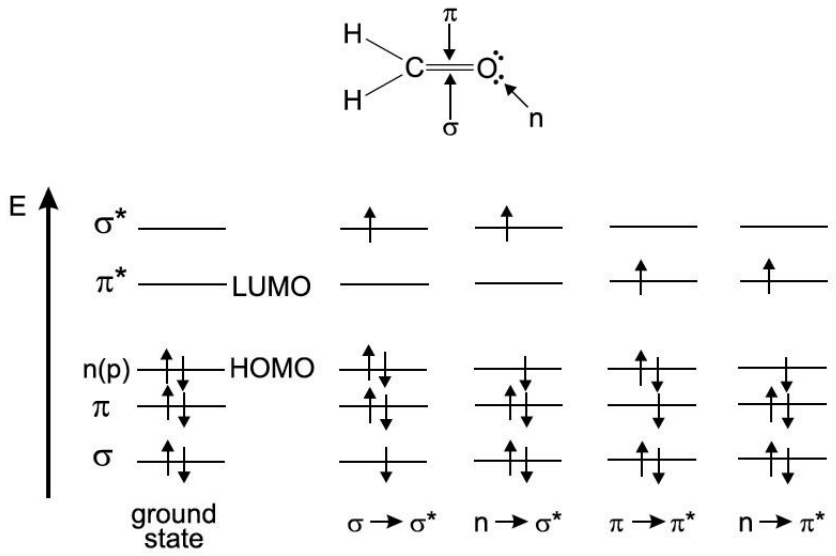

Figure 2.26. Energy levels of molecular orbitals in formaldehyde and possible electronic transitions (39).

When one of the two electrons of opposite spins (belonging to a molecular orbital of a molecule in the ground state) is promoted to a molecular orbital of higher energy, its spin is, in principle, unchanged so the total spin quantum number ($S = \sum s_i$ with $s_i = +\frac{1}{2}$ or $s_i = -\frac{1}{2}$) is zero. Because of the multiplicities of both the ground and excited states ($M = 2S + 1$) are equal to 1, both are called singlet states (usually denoted S_0 for the ground state) and S_1, S_2,... for the excited states (see Figure 2.27). The corresponding transition is called a singlet-singlet transition. A molecule in a singlet excited state may undergo conversion into a state where the promoted electron has changed its spin; therefore, there are two electrons with parallel spins, and the total spin quantum number is 1 and the multiplicity is 3. Such state is called a triplet state because it corresponds to three states of equal energy. According to Hund's rule, the triplet state has lower energy than the singlet state of the same configuration (39).

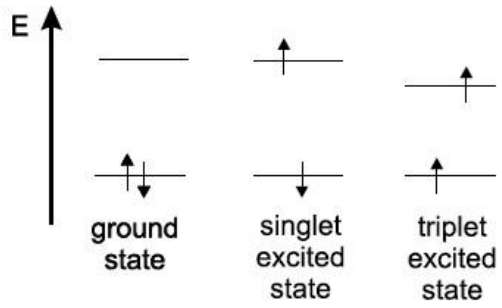

Figure 2.27. Distinction between singlet and triplet states.

An instrument for measuring the absorption of UV and visible radiation is built of one or more light sources, a wavelength selector, a sample container, radiation transducers, a signal processors and readout devices. Figure 2.28 shows a scheme of a single-beam instrument for absorption measurements. Single beam instruments vary widely in their complexity and performance characteristics. The simplest ones consist of a tungsten bulb as the source, a set glass filter for wavelength selection, a test tube for sample holders, a photovoltaic cell as the transducer, and an analogmeter as the readout device. Other sophisticated instruments have interchangeable tungsten and deuterium lamp sources, use a rectangular silica cell, and are equipped with a high-resolution grating monochromator with variable slit. Photomultiplier tubes are used as transducers, and the output is often digitalized, processed and stored in a computer so that it can be printer or plotted in several forms (54).

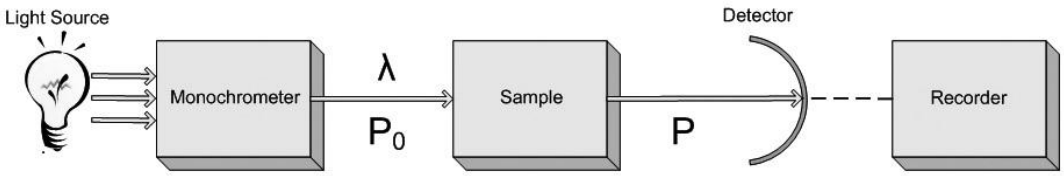

Figure 2.28. General scheme of a single-beam instrument for UV-Vis absorption measurements.

2.11.2.- Polarized light optical microscopy

Polarized light optical microscopy (POM) provides all the benefits of bright field microscopy and yet offers a wide range of information, which is simply not available with any other optical microscopy technique. POM can distinguish between isotropic and anisotropic materials. The technique exploits the optical properties of anisotropy to reveal detailed information about the structure and composition of materials.

Isotropic materials demonstrate the same optical properties in all directions of space. They have only one refractive index and no restriction on the vibration direction of light passing through them. In contrast, anisotropic materials have optical properties that vary with the orientation of the incident light. They shown a range of refractive indexes depending both on the light propagation direction through the sample and on the vibrational plane coordinates (phenomenon known as birefringence). Birefringence is the term used to indicate the ability of an anisotropic material to separate an incident ray into two rays, each polarized light ray travels at two different speeds. One of the resulting polarized rays travels through the sample with the same velocity in every direction and is termed the ordinary ray. The other ray travels with a velocity that is dependent upon the propagation direction within the anisotropic material. This light ray is termed the extraordinary ray. The two independent refractive indices of anisotropic sample are quantified in terms of their birefringence defined as: $B = |n_e - n_o|$, where n_e and n_o are the refractive indices of the extraordinary and ordinary rays, respectively. This expression is true for any part or fragment of anisotropic material except when light waves are propagated along the optical axis of the sample (55). The POM technique exploits the interference of the splitted light rays as they are re-united along the same optical path to extract information about these materials.

Birefringent specimens exhibit characteristic patterns and orientations of light and dark contrast features that vary, depending on the shape and geometry of the object (linear or elongate *vs.* spherical) and the molecular orientation. In the absence of a compensator, spherical objects with radially symmetric molecular structure exhibit a dark upright polarization cross superimposed on a disk composed of four bright quadrants (55).

POM is perhaps best known for its geological applications (primarily, for the study of minerals in rock-thin sections), but it can be used to study many other materials. These include minerals, composites, ceramics, fibers and polymers, and crystalline or highly ordered biological molecules such as DNA, protein, starch, wood and urea.

As commented in detail previously, light can be represented as a transverse electromagnetic wave made up of mutually perpendicular, fluctuating electric and magnetic fields. It means that, at any point of a light beam, the magnetic field is always perpendicular to the electric field, and oscillates in a plane perpendicular to the propagating direction of the light beam. In plane polarized light, the electric field vector oscillates along a straight line of the propagation light beam. Figure 2.29 shows a polarized light optical microscope configuration. In this

microscope, there are two polarized filters, the polarizer and the analyzer. The polarizer is situated below the specimen stage, and the analyzer is situated above the objectives and can be moved in and out of the light path as required. When both the analyzer and polarizer are in the optical path, in a crossed configuration, no light passes through the system and a dark field of view is present in the eyepieces.

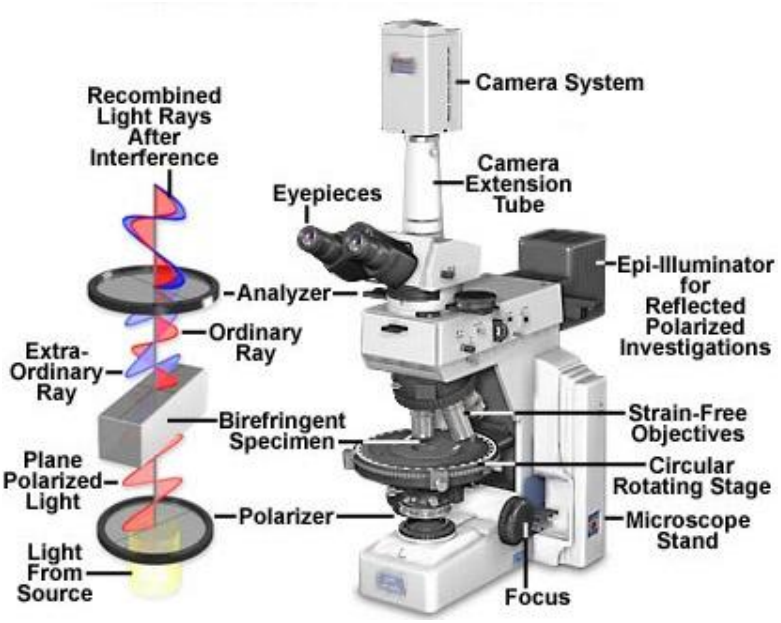

Figure 2.29. Polarized light optical microscope configuration.

2.11.3.- Emission spectroscopy

Inductively coupled plasma-atomic emission spectroscopy (ICP-AES) is a widespread technique for elemental analysis of a sample (56). In Figure 2.30, a scheme of an ICP-AES instrument is shown. A plasma source is used to make specific elements to emit light, after which a spectrometer separates this light in their characteristic wavelengths. This technique is especially suited for direct analysis of liquid samples. The sample solution is transformed into an aerosol by a nebuliser. Small droplets (1-10 µm) are transferred by an argon plasma. When the aerosol droplets enter the hot area of plasma, they are converted into salt particles. These salt particles are split into individual molecules that will subsequently fall apart to atoms and ions. In the plasma, even more energy is transferred to the atoms and ions, promoting the excitation of their electrons. When these excited atoms and ions back to a lower excitation state or to their ground state they will emit electromagnetic radiation in the ultra-violet/visible range of the spectrum. The classical approach for ICP-AES measurement is to collect and measure the emitted radiation radially, i.e. the optical axis is orthogonal to the central channel of the ICP. The limit of detection is in de order of ca. ng/ml.

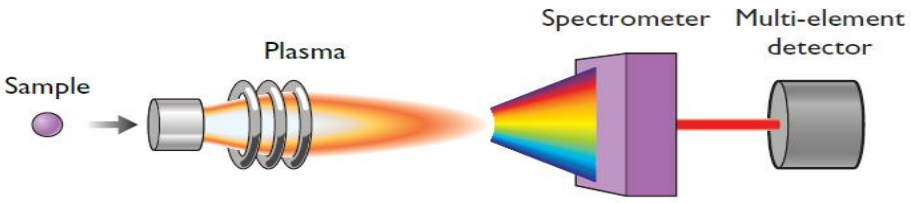

Figure 2.30. Scheme of an ICP-AES.

2.11.4.-Superconducting quantum interference device (SQUID)

SQUID is a sensitive device for measuring magnetic fields. SQUID magnetometers are used to characterize materials when the highest detection sensitivity over a broad temperatures range and application of magnetic fields up to several Tesla is needed. The main application of this instrument is the study of magnetic properties of materials by measuring the induced or remnant magnetic moment, usually as a function of applied magnetic field and temperature. A SQUID magnetometer combines several superconducting components, including the proper SQUID device, a superconducting magnet, detection coils, a flux transformer and superconducting shields. To make a measurement, a sample is first attached to a sample rod. The sample is then scanned through the center of a first-order or second-order superconducting gradiometer. The gradiometers form a closed flux transformer that is coupled to a SQUID. The shape and magnitude of the response curve can be then analyzed using a computer to obtain a corresponding magnetic moment (57).

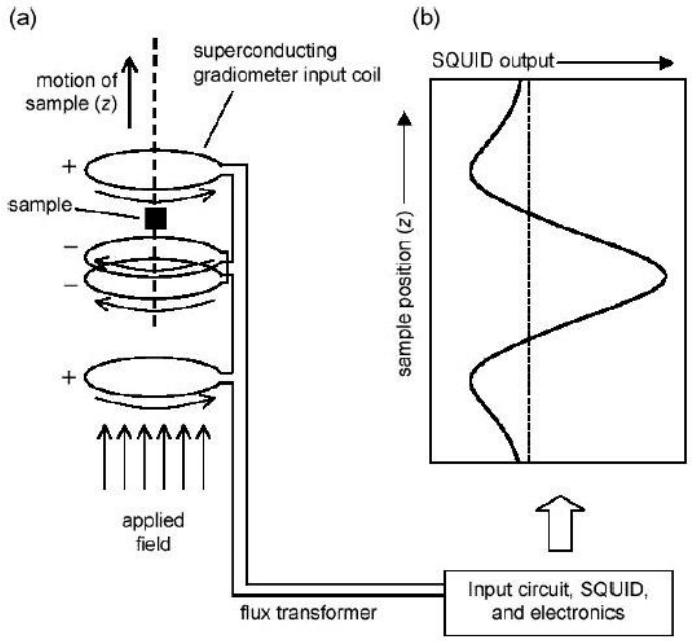

Figure 2.31. Scheme of a SQUID magnetometer (57).

In particular, we use SQUID to measure the magnetic properties of magnetic nanoparticles and hybrids. In this regard, magnetic nanoparticles show a wide variety of unusual magnetic properties as compared to the respective bulk materials. In a paramagnetic material, the thermal energy overcomes the coupling forces between neighbouring atoms above the Curie temperature, causing random fluctuations in the magnetization directions that result in a null overall magnetic moment. However, in superparamagnetic materials the fluctuations affect the direction of individual entire crystallites. The magnetic moments of individual crystallites compensate each other and the overall magnetic moment becomes null. When an external magnetic field is applied, the behaviour is similar to paramagnetic materials except that, instead of each individual atom being independently influenced by an external magnetic field, the magnetic moment of entire crystallites aligns with the magnetic field (Figure 2.32) (58)(59). For magnetic nanoparticles, superparamagnetism occurs in magnetic materials composed of very small crystallites (the threshold size depends on the nature of the material, i.e. Fe-based materials becomes superparamagnetic at sizes <25 nm).

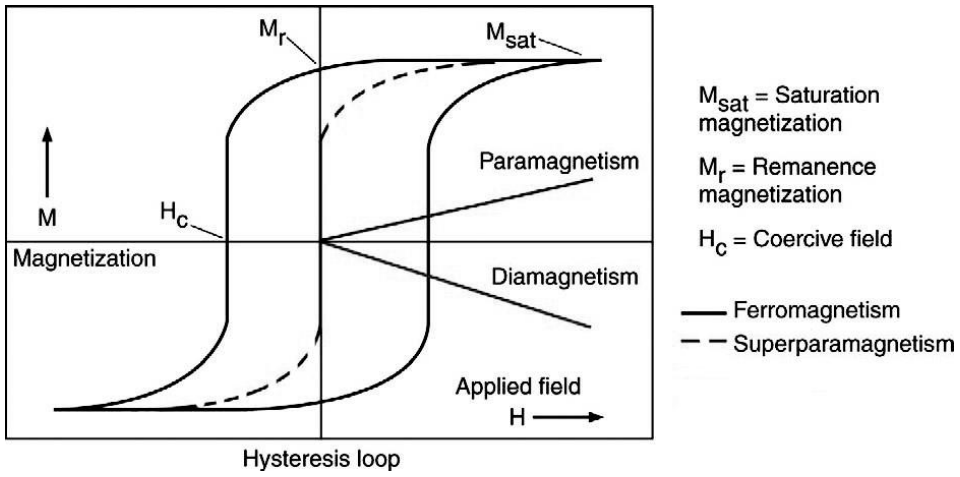

Figure 2.32. Hysteresis loops (magnetization *vs.* applied magnetic field) characteristic of ferromagnetic and superparamagnetic NPs. For comparison, *para-* and *diamagnetic* behavior are also shown. The Figure indicates the remanence, M_r, and coercive field, H_c, values (58).

The superparamagnetic relaxation in samples of magnetic nanoparticles is studied by measuring the zero-field cooled (ZFC) and field cooled (FC) magnetization curves. A ZFC magnetization curve is obtained by cooling the sample in zero applied magnetic field from a temperature at which the entire sample shows a superparamagnetic response. Then, a small field is applied and the magnetization of the sample is measured as a function of temperature during the heating process. The FC magnetization curve is measured as a function of the

increasing temperature after cooling the sample in the applied magnetic field (Figure 2.33). At temperatures well below the blocking temperature, the ZFC magnetization is small because the sample is not in thermal equilibrium, and the magnetization directions of the particles in a small applied field are mainly governed by the randomly oriented directions of magnetization. With temperature increases, the smaller particles become superparamagnetic, and the probability of finding a particle with magnetization directions close to that of the applied field increases, resulting in an increase in the magnetization. With further temperature increases, more and more particles become superparamagnetic, resulting in an increasing magnetization until the net effect of the thermal energy becomes dominant and involves a decrease in the magnetization value. In the FC state, the magnetization in the blocked state is preferably frozen in a direction close to that of applied field. Therefore, the magnetization is considerably larger than that in the ZFC state. The ZFC and the FC curves coincide above the bifurcation temperature, which is the temperature above which all particles are superparamagnetic (59).

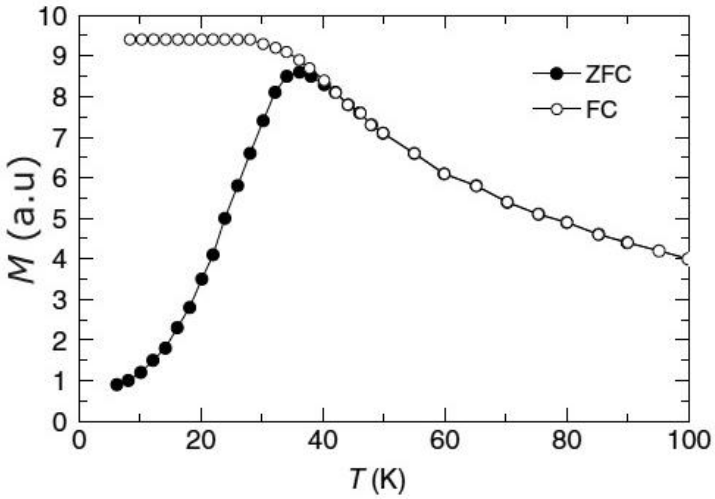

Figure 2.33. ZFC and FC magnetization curves measured on a ferrofluid material (59).

2.11.5.- Magnetic resonance imaging (MRI)

One of the most valuable and widely used imaging methods in medical diagnostic is the Magnetic Resonance Image (MRI). Though the diagnostic potential of conventional MRI is immense and a variety of different contrast models are well established, further improvements of the method have been pursued in last years by application of magnetic nanoparticles for contrast enhancement based on functional site specificity.

In MRI, the nuclear magnetic moment of protons is used as a sensitive probe of the chemical neighbourhood of protons in different tissues and organs of human body. Nuclear moments

are aligned by means of an external magnetic bias field (commonly in the range of 0.2-3 T) and the precession of the spins is excited by transverse RF pulses at a proton resonance frequency of about 42.58 MHz T^{-1}. After applying the pulse sequence, the induced magnetization decays and the longitudinal (T_1) and transverse (T_2) relaxation times of the precessing nuclear magnetic moments show tissue-specific differences that are used to generate the required image contrast. Imaging is performed by controlling external field gradients so that the resonance condition is fulfilled only in a restricted local region and, then, by scanning the resonant volume to be imaged. Magnetic response signals are detected by pick-up coils. In this way, the tissue-specific differences of the relaxation time T_1 and/or T_2 may be used for construction of the T_1 and T_2 weighted images showing optimal contrast of special tissue features. In practice, for optimization of tissue contrast a variety of different pulse sequences (e.g., the widely applied spin-echo methods) may be used (60)(61).

Generally, a magnetic resonance scanner is essentially defined by three hardware groups and their parameters: a) the main magnet with its homogeneity over imaging volume; b) the magnetic field gradient system with its linearity over the imaging volume; and c) the radiofrequency (RF) system with its RF signal homogeneity and signal sensitivity over the imaging volume. Whole-body MRI imposes very special demands on these system components (62)(63):

a) The main magnet. Magnetic resonance imaging requires a very strong magnetic field that has precisely the same magnitude and direction everywhere in the region we want to image. One of the key properties used to describe the quality of a MRI system is the uniformity, or homogeneity, of the applied magnetic field. For example, high-quality MRI systems made for clinical use in hospitals will have magnetic fields that vary less than 5 parts per million (ppm) over a 40 cm diameter spherical volume in the region desired for imaging.

b) The magnetic field gradient. As mentioned earlier, a key property of the static magnetic field of a MRI system is its homogeneity, but anything we place inside the magnetic field tends to change the magnetic field slightly. To make the magnetic field as uniform as possible and to compensate for changes caused by different objects in the field, we shim the field. Shimming is typically handled by placing small amounts of iron at specific locations within long trays that line the cylindrical magnetic field coil; or by several set of wire coils. Once the shimming is complete, the magnetic field is highly uniform over a central region where the imaging takes place.

c) The radio frequency system. Radio frequency systems suitable for MRI are characterized by RF excitation with homogeneous signals over an examination volume as large as possible. Here, it is important that the excitation flip angle remains as constant as feasible, as the image contrast is fundamentally influenced by this parameter.

Figure 2.34. A modern 9.4 Tesla MRI system (Bruker Biospin USR 94/20 instrument).

2.12.- Laboratory equipment.

Wilhelmy Plate method. Surface tensions (γ) were determined by the Wilhelmy plate method using a Krüss K12 surface tension equipment, equipped with a processor to acquire the data automatically. The equipment was connected to a circulating water bath to keep the temperature constant to within $\pm$ 0.01 ^{0}C.

Drop tensiometer. Surface tension measurements were also carried out in a Track tensiometer equipment (I.T. Concept, France) adapted to determine surface tension values in real time with an accuaracy of $\pm$0.1 mN/m. Interfacial tension and interfacial rheology estimations are based

on the digital profile of a drop image and the resolution of the Gauss-Laplace equation. Win Drop software (I.T. Concept, France) was used to obtain the surface tension values by means of the axisymetric drop shape analysis. For air-water interface, an air-bubble upward was formed at the tip of a U-shaped stainless steel needle (0.5 mm inner diameter) immersed in water bulk phase. On the contrary, chloroform bubble downward was formed at the tip of a straight stainless steel needle (0.5 mm inner diameter).

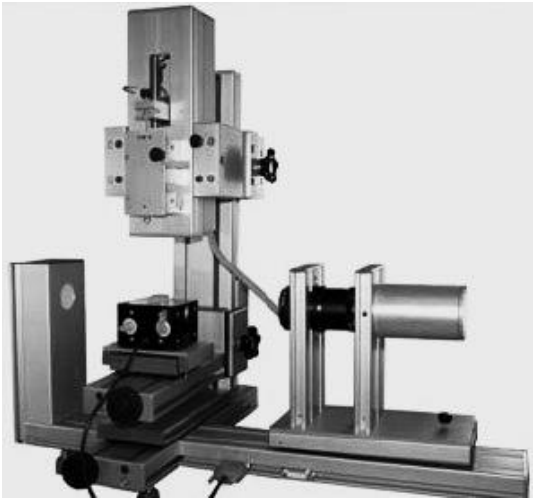

Langmuir-Blodgett trough. Surface-pressure isotherms were recorded in a Langmuir-Blodgett (LB) Teflon trough (model 611 from Nima Technologies, Ltc., Coventry, U.K.).

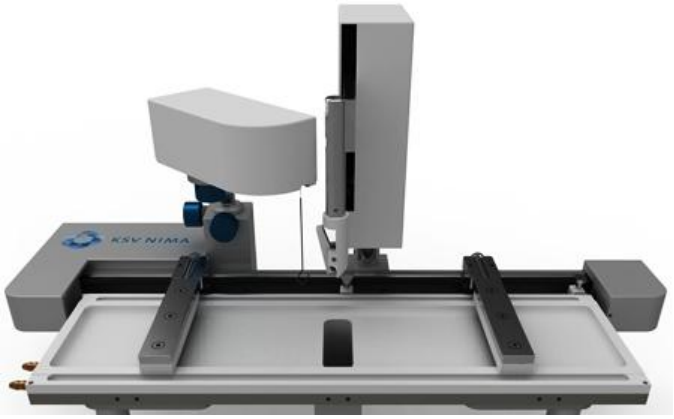

Atomic force microscopy. The AFM measurements were performed in a JEOl instruments (model JSPM-4210) in non-contact mode using nitride cantilevers NSC 15 from Micro Masch, USA (typical working frequency and spring constant of 325 kHz and 40 N/m, respectively).

Laser light scattering. Dynamic and static light scattering (DLS and (SLS) intensities were measured by means of an ALV-5000F (ALV-GmbH) instrument with vertically polarized incident light of wavelength λ= 488 nm supplied by a CW diode pumped Nd;YAG solid-state laser supplied by Coherent, Inc. and operated at 2 W.

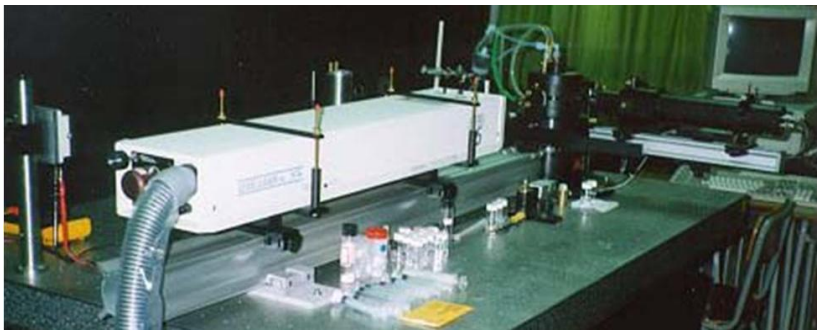

Polarized optical microscopy. POM experiments were made by using a Zeiss Axioplan optical microscope (Carl Zeiss Ltd., Welwyn Garden City, U.K.) A total magnification of either 50x or 100 X was used. A polarizer and analyzer were put in fixed position, orthogonal to one another for the cross-polarizer imaging. Images were taken using a Kodak digital camera mounted on the top of the microscope.

Laser confocal microscopy. Confocal microscopy was performed on a Leica TCS SP2 confocal system mounted on a Leica DM-IRE2 upright microscope, using a 40X objective. For fluorescence measurements, Thioflavin T was added to spherulitic samples and excited using the 458 nm line of an argon ion laser. Simultaneously, transmission images were obtained with crossed polarizers in place using the 633 nm line of a He-Ne laser.

Rheometry. The rheological properties of the samples were determined using a Bohlin CS10 rheometer with water bath temperature control. Coutte geometry (bob, 24.5 mm in diameter, 27 mm in height, cup, 26.5 in diameter, 29 mm in height) was used for fluid samples. Samples of very high modulus were investigated using cone and plate geometry (diameter 40 mm, angle 4^0). Frequency scans of storage (G') and lost (G'') moduli were recorded for selected copolymer concentrations and temperatures with the instrument in oscillatory shear mode and with the strain amplitude (A) maintained at a low value (A < 0.5 %) by means of auto-stress facility of the Bohlin software. This ensured that measurements of G' and G'' were in the linear viscoelastic region.

Transmission electron microscopy. TEM micrographs were acquired by using a Phillips CM-12 electron microscope operating at an accelerating voltage of 120 kV.

High resolution transmission electron microscopy and selected area electron diffraction. HR-TEM images and SAED patterns were obtained with a transmission electron microscope (Carl-Zeiss Libra 200 FE-EFTEM) operating at 200 kV.

Scanning electron microscopy. SEM micrographs were acquired by using a LEO-435 VP scanning electron microscope (Leica Microsystems Gmb H, Wetlar, Germany) operating at an accelerating voltage of 30 kV. Microanalysis of the scanning electron microscopy samples was performed.

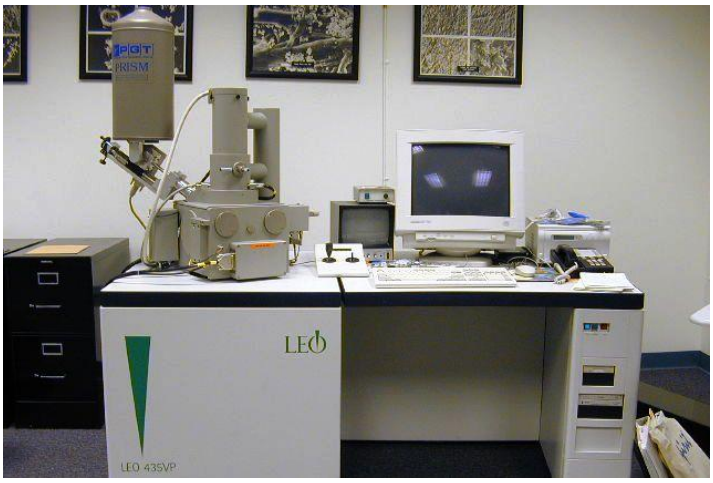

Fluorescence spectroscopy. Fluorescence was measured in a Cary Eclipse fluorescence spectrophotometer equipped with a temperature control device and a multicell sample holder (Varian instrument Inc.).

Ultraviolet-visible spectroscopy. UV-vis data were acquired by using a spectrophotometer DU series 640, Beckman Coulter, (Fullerton, CA) operating at 190-110 nm.

Far and near-ultraviolet circular dichroism spectroscopy. CD spectra were obtained using a JASCO-715 automatic recording spectropolarimeter (Jasco, Tokyo, Japan) with a JASCO PTC-343 Peltier-type thermostated cell holder. Quartz cuvettes with 0.2cm pathlength were used. CD spectra were recorded between 195 and 300 nm at 25 ^{0}C.

Fourier transform infrared spectroscopy. An FTIR spectrometer (model IFS-66V; Bruker) equipped with a horizontal ZnS ATR accessory. The spectra were obtained at a resolution of 2 cm^{-1} and 200 scans were accumulated to obtain a reasonable signal/noise ratio.

X-ray diffraction. XRD experiments were carried out using a Siemens D5005 rotating anode X-ray generator. Twin Göbel mirror were used to produce a well-collimated beam of Cu Kα radiation (λ = 1.5418 Å). XRD patterns were recorded with an imaging plate detector AXS F.Nr. J2-394.

Superconducting quantum interference device. Magnetic susceptibility measurements were carried out with a SQUID magnetometer (Quantum Design MPMS5, San Diego, CA).

Magnetic resonance measurements. Transverse and longitudinal relaxation times were measured at 9.4 T (400 MHz) with a Brucker Biospin USR 94/20 instrument (Ettlingen, Germany).

CHAPTER 3

Block copolymers

Contents

3.1.- Introduction

Block copolymers are a particular class of polymers that are included in a wide family of nanomaterials, known as soft materials. Independently of the synthetic procedure, block copolymers can simply be considered as being formed by two or more chemically homogeneous polymer fragments joined together by covalent bonds, which can be found in different positions along the polymeric chain (Figure 3.01) (64)(65). According to the number of the building units, these polymers can be denominated as diblock, triblock and multiblock copolymers. The molecular architecture of block copolymers can be as simple as a linear chain or more complex like the molecular architecture of star or graft copolymers, which can be controlled by means of the chemical synthetic procedures (9)(66)-(68).

Methodologies used in the synthesis of block copolymers allow designing any polymeric chain with specific properties and architectures. Generally, the structure of a block copolymer is composed of incompatible joint homopolymers. When a copolymer is molten, and subsequently left cool down slowly, the incompatibilities between constituent building blocks give rise to microphase separation, leading to the formation of ordered nanodomains. The covalent linkage between the different polymeric chains prevents the separation in macrodomains. The generation of these structural nanodomains is managed by the self-assembling process of homologous segments that compose the block copolymer. Also, such dimensional nanostructures depend on the volume fraction of blocks copolymer. Two competing effects govern the thermodynamics of block copolymer melts. At high

temperatures, the chains are mixed homogeneously, as in any polymer melt. As the temperature is reduced the tendency for the blocks to segregate is enhanced, i.e. the enthalpic process of demixing is favoured. However, this is necessary accompanied by a reduction in the entropy as the chain configuration becomes more constrained. The extent of segregation of the copolymer may be expressed using the reduced parameter χN. Here, χ is the Flory-Huggins interaction parameter, which contains a significant enthalpic contribution, and is governed by the incompatibility of the monomers; and N is the copolymer degree of polymerization, reflecting the N-dependent translational and configurational entropy. The transition from homogeneous melt of chains to heterogeneous melt of ordered microphase-separated domains occurs at a critical value of χN, depending on the composition of the copolymer (65).

In bulk, the minority block is segregated from the majority block forming regularly shaped and uniformly-spaced nanodomains. The shape of the segregated domains in a diblock is governed by the volume fraction of the minority block, f, and block incompability. Figure 3.1 shows the equilibrium morphologies documented for diblock copolymers as an example. At a volume fraction of ≈ 20 %, the minority block forms a body-centred cubic spherical phase in the matrix of the majority block. It changes to hexagonally packed cylinders at a volume fraction ≈ 30 %. Alternating lamellae are formed at approximately equal volume fractions for the two blocks. At a volume fraction of ≈ 38 %, the minority block forms bicontinuous structures at moderate and high incompatibility, respectively (64)(65)(69).

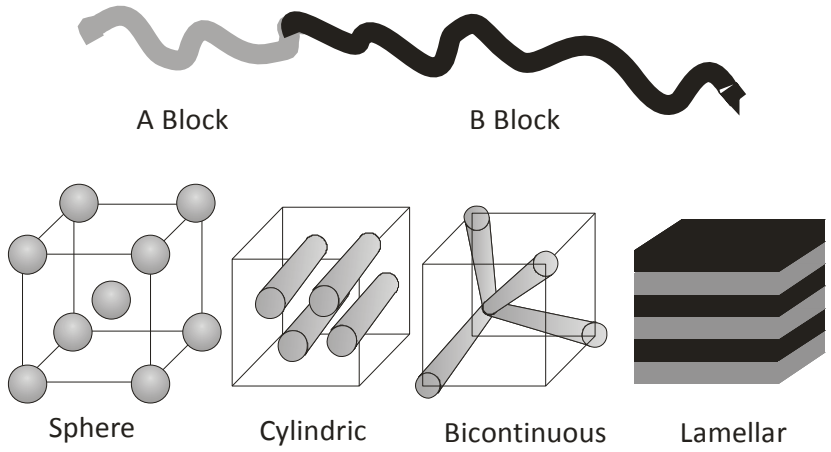

Figure 3.1. Regular structures in block copolymer leaded by theirs self-assembling.

The physical properties of copolymeric materials have been applied in a wide range of fields. For example, by decades copolymeric materials in solid state have been used as thermoplastic and elastomeric materials, foams, and glues owing to their high compatibility, sensitivity, and

resistance to external physical factors (65). On other hand, the auto-association properties of block copolymers in selective media allow the formation of structure-ordered aggregates, and, for that reason, this type of polymeric materials has been received special attention in last years for their used in high-nanotechnology applications, as shown below (8)(9).

3.2.- Behaviour of block copolymers in solution.

The hydrophilic and hydrophobic nature of amphiphilic block copolymer molecules lead to their self-assembly into a variety of structures in solution. There are two basic processes that characterize the phase behaviour of block copolymers in solution: micellization and gelation. Micellization occurs in dilute solution of block copolymers in a selective solvent at a fixed temperature above the cmc, as commented in more detail below. At higher copolymer concentrations, the micelles can order onto a lattice above a critical gel concentration (cgc). These regimes are illustrated in Figure 3.2.

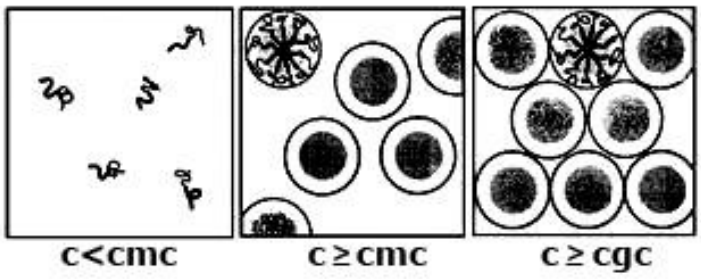

Figure 3.2 Illustration of cmc and cgc in ablock copolymer solution.

When a block copolymer is dissolved in a selective solvent, that is, a solvent which is good for one of the blocks and bad for the other one, the lyophobic part of the macromolecule tends to segregate and auto-associate with their neighbouring molecules, leading to the formation of stable aggregates with specific structures, in order to avoid the direct contact between solvent molecules with the insoluble copolymer block (70). The spontaneous aggregation of block copolymers is carried out either when the concentration of the macromolecule is near to their critical micellar concentration, or on the other hand, by changes in the solution temperature. In this case, the critical micellar temperature is reached. Both parameters are fundamental to characterize the association properties of a copolymer-solvent system (71). Despite the cmc does not correspond to a thermodynamic property of the system, it can simply be defined phenomenollogically as the concentration at which a sufficient number of micelles is formed to

be detected by a given method. Thermodynamically, for copolymers with a narrow block-length, the association process corresponds to equilibrium between molecules (unimers), *A*, and micelles, A_N, containing *N* molecules. This can be written as:

$$A \leftrightarrows (1/N)A_N, \qquad K_c = [A_N]_{eq}^{1/N}/[A]_{eq} \tag{3.1}$$

If the association number is large and independent of the temperature then $K_c \approx [A]^{-1}$ and the standart Gibbs energy of association is:

$$\Delta_{mic}G^0 = -RTlnK_c \approx RTln[A] \tag{3.2}$$

Under this condition, for molecules and micelles in equilibrium just above the cmc $\Delta_{mic}G^0 \approx RTln[cmc]$

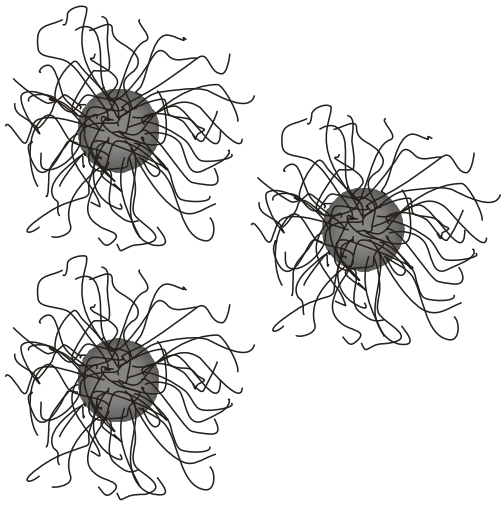

Figure 3.3. Schematic representation of block copolymer micelles in aqueous solution, dense hydrophobic core is constituted by the hydrophobic block, while the micellar shell is formed by the hydrophilic block.

The micellization process of amphiphilic block copolymers has been studied in a wide range of selective solvents: from water to organic polar solvents and non-polar solvents, as well as ecological solvents like supercritic fluids and ionic liquids (72). The simplest structural aggregates formed by block copolymer are called micelles, by the analogy that exists with the structure of common micelle formed by the convectional surfactants in aqueous media (Figure 3.3) (73).

In aqueous media, the micelle structure consists of a dense hydrophobic core surrounded by a hydrophilic shell which is exposed toward the bulk solvent phase in a spherical configuration; the micelles can change their size from 5 to some hundreds nanometers and can possess different geometries (spheres, worn-like, and so on) (74)-(78).

The various reported micellar-like morphologies are primarily a result of the inherent molecular curvature and how this influences the packing of the copolymer chains: specific self-assembled nanostructures can be targeted according to a dimensionless packing parameter, p, which is defined as $p = v/(a_0 l_c)$, where v is the volume of the hydrophobic chains, a_0 is the optimal area of the head group, and, l_c is the legth of the hydrophobic tail, as occurred for classical surfactants. Therefore, the packing parameter of a given molecule usually dictates its most likely self-assembled morphology. As a general rule, spherical polymeric micelles are favored when $p \leq 1/3$, cylindrical micelles when $1/3 \leq p \leq 1/2$, and enclosed membrane structures (vesicles, also known as polymersomes) when $1/2 \leq p \leq 1$.

Despite the structured aggregates from block copolymers formed in aqueous solution are similar to those produced by the self-assembly of small surfactant molecules such as lipids and detergents, the polymeric nature of the amphiphilic macromolecules provides new special properties to these structural complexes, as stability and functionality. In this way, their potential applications in different technological areas are largely increasing, including materials science, bioengineering, medicine, pharmaceutics industry, and ink and paint industry (70)(79).

3.3.- Mechanism of morphologic control and thermodynamic stability.

The conformation of the block copolymer chains depends on the interaction between chain segments and solvent molecules. In aqueous solution, the structure of the aggregates is governed by the balance of the interaction forces between the block copolymer molecules with water molecules, and by the intrachain interactions between the blocks which constitute the copolymer molecule (where the hydrophilic chain expands, avoiding unfavourable segment-segment interactions and the hydrophobic part contract to minimize the contact with solvent molecules).

It is possible to achieve a precise control of the size and shape of polymeric aggregates, and

subsequently, of their thermodynamic stability by modification of some factors such as block copolymer molecular weight, the relatively length of both hydrophobic and hydrophilic blocks, the chemical nature of the different monomer units and the architecture of the polymeric backbone. Firstly, this can be achieved by means of the block copolymer synthetic processes. However, the synthesis of block copolymers is time-consuming and expensive, disadvantages that have to be taken into account. A simpler alternative is the possibility of manipulating the block copolymer solution properties through the change of external parameters such as temperature, salinity, pH, addition of cosolvents… Under this context, it is possible to obtain different aggregate sizes or morphologies using the same block copolymer or the same family of copolymers. The morphology of the structured aggregates can be determined by a balance of different factors such as the solvent properties, the conformation of the hydrophobic chains into the micelle core, the repulsion between hydrophilic blocks into the micelle shell, and the surface tension between the micelle cores and the bulk solution (77)(78).

3.4.- Block copolymers of polyoxyalkylenes in aqueous solution.

The block copolymers of polyoxyalkylenes are composed of a hydrophilic block constituted by poly(ethylene oxide) (OCH_2CH_2 ethylene oxide unit, E) and by a second hydrophobic block that can be made of, for example, poly(propylene oxide) (P), poly(styrene oxide) (S), or poly(butylene oxide) (B), amongst others. In aqueous medium, polyoxyalkylene amphiphilic block copolymer contains both the hydrophilic and hydrophobic blocks that can associate to usually form spherical micelles in dilute aqueous solution. Increasing the concentration leads to the formation of lyotropic crystal mesophases (gels) where the structural objects are micelles, usually efficiently packed in a body-centered or face-centered cubic structure as a result of their interaction as hard spheres (80)(81).

For poly(oxyalkylenes) block copolymers, values of the cmc are affected by the variation of hydrophilic polyoxyethylene and hydrophobic block lengths. It is known that the dependence of the cmc on the number of E units in a copolymer is small unless the hydrophobic-block length is short. Indeed, when comparing results for two copolymers of nominally the same hydrophobic-block length, the effect of E-block length may well be less than the variation caused by the uncertainty in hydrophobic-block length. However, within a series of copolymers it is desirable to account for variation in E-block length. Taking as an example PE-PP-PE Pluronic block copolymers, micelle formation of this class of polymers in water is believed to

result from dehydratation of the hydrophobic block with increasing temperature, water being a selective solvent for PE. This explains why the solution properties of Pluronic polymers are strongly temperature-dependent. For most PE-PP-PE copolymers, the cmt increases with decreasing in copolymer concentration. The number of oxypropylene units has a strong effect on the micellization, copolymers with large hydrophobic PP block length forming micelles at much lower concentrations. Indeed, the cmc is found to decrease exponentially with the PP block length. On the other hand, the PE block has a smaller influence on the micellization. An increase in the number of PE units leads to small increases in the cmc and cmt values. The cmt and cmc decrease with increasing the total copolymer molecular weight, if comparisons are made for a constant PP/PE ratio. On the other hand, the large positive enthalpy of micellization, and the standard free energy of micellization observed on the self-assembly of PE-PP-PE demonstrate that the association process is entropy driven. Chain architecture has also a great influence on micelle formation. For example, the tendency for micellization of PP-PE-PP copolymer is reduced compared to a PE-PP-PE copolymer of the same composition.

3.5.- $E_{12}S_{10}$, $E_{10}S_{10}E_{10}$ and $E_{137}S_{18}E_{137}$ block copolymers

Our research group has been collaborating during last years with research groups of the School of Pharmacy and Pharmaceutical Sciences and the School of Chemistry of the University of Manchester in synthesizing block copolymers formed by ethylene oxide and styrene oxide blocks (81)-(83). In this regard, it has been previously demonstrated that the micellization process of diblock copolymers of this type has not cmt values. Moreover, they usually have small cmc values and micellization enthalpies ($\Delta_{mic}H$) as a consequence of the high hydrophobicity of the styrene oxide block. Triblock copolymers show cmc values higher than diblock ones for the same hydrophobic block length. On the other hand, the cmc values of the triblocks weakly depend of the hydrophilic block length.

Block copolymers studied in this work were: $E_{12}S_{10}$, $E_{10}S_{10}E_{10}$ and $E_{137}S_{18}E_{137}$, (where E represents the oxyethylene unit, S represents the oxystyrene unit, and the subscripts correspond to block lengths). These copolymers were synthesised by sequential anionic polymerisation of the two monomers, oxyethylene and oxystyrene. Oxyrane compounds are heterocyclic compounds constructed by two carbon atoms and one oxygen atom into the cyclic structure (Figure 3.4) (84).

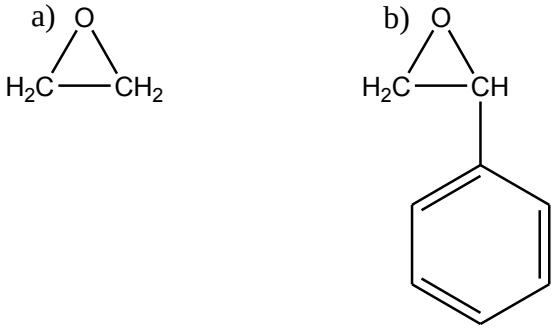

Figure 3.4. Oxyranes used in the synthesis of the block copolymers a) ethylene oxide and b) styrene oxide.

Anionic polymerization proceeds via organometallic sites, carbanions (or oxanions) with metallic counterions. Carbanions are nucleophiles; consequently, the monomers that can be polymerized by anionic polymerization are those bearing an electro-attractive substituent on the polymerizable double bound. Initiation of polymerization is accomplished by analogous low molecular weight organometallic compounds (initiators). A wide variety of initiators has been used so far in order to produce living polymers. Among them, the most widely used are organolithiums. The main requirement for employment of an organometallic compound as an anionic initiator is its rapid reaction with the monomer at the initiation step of the polymerization reaction and, specifically, with a reaction rate larger than that of the propagation step. This leads to the formation of polymers with narrow molecular weight distributions because all active sites start polymerizing the monomer almost at the same time. Propagation proceeds through nucleophilic attack of the carbanionic site onto a monomer molecule with reformation of the first anionic active center. The situation is similar in the case of the ring opening polymerization of cyclic monomers containing heteroatoms (oxyranes, lactones, siloxanes, etc.). Under appropriate experimental conditions, due to the absence of termination and chain transfer reactions, carbanions (or, in general, anionic sites) remain active after complete consumption of monomers, giving the possibility of block copolymer formation, in the simplest case, by introduction of a second monomer into the polymerization mixture. However, a variety of different synthetic strategies have been reported for the preparation of linear block copolymers by anionic polymerization.

As an example, in the polymerisation reaction of a monofunctional poly(oxyethylene) the addition of ethylene oxide (E) is initiated by a monofunctional alcohol (ROH), part of which is in the form of its alkali-metal salt (e.g., RO-K^+.) Initiation is instantaneous, and the subsequent reaction scheme is written:

slow propagation $MeE_mO\text{-}K^+ + E \longrightarrow MeE_{m+1}O\text{-}K^+$

fast equilibrium $MeE_mO\text{-}K^+ + MeE_nOH \rightleftharpoons MeE_mOH + MeE_nO\text{-}K^+$

where E_m represents a growing chain, the active centre is an ion pair, and the rapid equilibration ensures that all chains are equally likely to grow. This ideal scheme would produce polymers with M_n= (mass of E polymerised)/(moles of initiator used) and a Poisson distribution of chain lengths. In practice, the chain length distribution can be widened by a slow initiation. In the absence of termination, the system is living and is ideal for preparation of block copolymers. The same scheme applies to styrene oxide.

It is known that block poly(oxyalkylene) copolymers with hydrophobic blocks formed by propylene oxide or butylene oxide (either diblock or triblock architectures) have a spontaneous formation of spherical and cylindrical micelles in dilute aqueous solution. On the other hand, formation of vesicular structures for poly(oxyalkylene) block copolymers needs oftenly an energy supply via mechanical, sonochemical or electrical methods (85)(86). Nevertheless, it has been previously reported the spontaneous formation of vesicles (87)(88), where these types of structures are likely to form because of relatively large volume to length ratios of the hydrophobic block and the relative lengths of the poly(oxyethylene) blocks. In the case of block copolymers containing poly(oxystyrene) blocks as the hydrophobic block, the formation of elongated micelles has been unusual, whereas vesicle formation has not been yet reported.

CHAPTER 4

Papers on block copolymers

Contents

Self-Assembly Process of Different Poly(oxystyrene)-Poly(oxyethylene) Block Copolymers: Spontaneous Formation of Vesicular Structures and Elongated Micelles

Josué Juárez,[†] Pablo Taboada,*[,†] Miguel A. Valdez,[‡] and Víctor Mosquera[†]

Departamento de Investigación en Polímeros y Materiales y Departamento de Física, Universidad de Sonora, Sorales Resales y Transversal, 83000 Hermosillo Sonora, Mexico, and Laboratorio de Física de Coloides y Polímeros, Grupo de Sistemas Complejos, Departamento de Física de la Materia Condensada, Facultad de Física, Universidad de Santiago de Compostela, Spain

Received February 12, 2008. Revised Manuscript Received March 26, 2008

In the present work, we investigated the micellization, gelation, and structure of the aggregates of three poly(ethylene oxide)-polystyrene oxide block copolymers ($E_{12}S_{10}$, $E_{10}S_{10}E_{10}$, and $E_{137}S_{18}E_{137}$, where E denotes ethylene oxide and S styrene oxide and the subscripts the block length) in solution. Two of them have similar block lengths but different structures ($E_{12}S_{10}$ and $E_{10}S_{10}E_{10}$) and the other has longer blocks ($E_{137}S_{18}E_{137}$). For the first time, the spontaneous formation of vesicles by a poly(oxystyrene)-poly(oxyethylene) block copolymer is reported. These vesicular structures are present when copolymer $E_{12}S_{10}$ self-assembles in aqueous solution in coexistence with spherical micelles, as confirmed by the size distribution obtained by dynamic light scattering and pictures obtained by polarized optical microscopy, and transmission and cryo-scanning electron microscopies. Vesicle sizes vary between 60 and 500 nm. On the other hand, for copolymers $E_{10}S_{10}E_{10}$ and $E_{137}S_{18}E_{137}$, only one species is found in solution, which is assigned to elongated and spherical micelles, respectively. If we compare the high aggregation number derived by static light scattering for the triblock block copolymer micelles, with the maximum theoretical micellar dimensions compatible with a spherical geometry, we can see that the micellar geometry cannot be spherical but must be elongated. This is corroborated by transmission electron microscopy images. On the other hand, tube inversion was used to define the mobile−immobile (soft−hard gel) phase boundaries. To refine the phase diagram and observe the existence of additional phases, rheological measurements of copolymer $E_{137}S_{18}E_{137}$ were done. The results are in good agreement with previous values published for other polystyrene oxide-poly(ethylene oxide) block copolymers. In contrast, copolymers $E_{12}S_{10}$ and $E_{10}S_{10}E_{10}$ did not gel in the concentration range analyzed. Thus, only certain concentrations of copolymer $E_{10}S_{10}E_{10}$ were analyzed by rheometry, for which an upturn in the low-frequency range of the stress moduli was observed, denoting an evidence of an emerging slow process, which we assign to the first stages of formation of an elastic network.

Introduction

Block copolymers of hydrophilic poly(oxyethylene) (OCH_2CH_2, E = oxyethylene unit) and hydrophobic poly(oxystyrene) ($OCH_2CH(C_6H_5)$, S = oxyphenylethylene unit) are denoted as either E_mS_n, S_nE_m or $E_mS_nE_m$, $S_nE_mS_n$, depending on the sequence of polymerization or architecture, respectively. They associate to usually form spherical micelles in dilute aqueous solution.[1,2] Increases in concentration lead to the formation of lyotropic crystal mesophases (gels) where the structural objects are the micelles usually efficiently packed in a body-centered or face-centered cubic structure as a result of being effectively interacting as hard spheres.[3]

Aggregate morphology is determined primarily by a force balance among three contributions: the core-chain stretching, corona-chain repulsion, and interfacial tension between the core and the outside solution. Consequently, factors that influence the above balance can be used to control the aggregate architecture: polymer molecular weight, relative block lengths, hydrophobic block structure, solution conditions, and so forth. For a given value of the association number (N_w) for a poly(oxyalkylene) block copolymer, the average volume of a micelle core is readily estimated, and the corresponding spherical radius (r_c) can be compared with the length l (or half-length, $l/2$, in the case of triblock copolymers) of the extended hydrophobic blocks. With allowance made for a Poisson distribution of hydrophobic blocks, experience shows that spherical (or near-spherical) micelles will be formed if l ($l/2$ for triblock architecture) is approximately equal or greater than the value of r_c.[4,5] If this does not occur, other types of assemblies are observed under certain solution conditions. For example, a cylindrical geometry is expected as the solution temperature is increased because of an increase in the aggregation number derived from block copolymer dehydration:[6] the core blocks are stretched as the radius of a spherical micelle core is increased eventually to reach a point at which the enthalpy penalty forces the transition to a cylindrical geometry. Thus, formation of cylindrical micelles has been widely studied in block poly(oxyalkylene) copolymers with hydrophobic blocks

* Author to whom correspondence should be addressed. Telephone: 0034981563100, ext.: 14042. Fax: 0034981520676. E-mail: fmpablo@usc.es.
† Universidad de Santiago de Compostela.
‡ Universidad de Sonora.

(1) Crothers, M.; Attwood, D.; Collett, J. H.; Yang, Z.; Booth, C.; Taboada, P.; Mosquera, V.; Ricardo, N. P. S.; Martini, L. G. A. *Langmuir* **2002**, *18*, 8685–8691.
(2) Yang, Z.; Crothers, M.; Ricardo, N. M. P. S.; Chaibundit, C.; Taboada, P.; Mosquera, V.; Kelarakis, A.; Havredaki, V.; Martini, L.; Valder, C.; Collett, J. H.; Attwood, D.; Heatley, F.; Booth, C. *Langmuir* **2003**, *19*, 943–950.
(3) Castelletto, V.; Hamley, I. W.; Crothers, M.; Attwood, D.; Yang, Z.; Booth, C. *J. Macromol. Sci., Phys.* **2004**, *43*, 13–27.
(4) Taboada, P.; Velazquez, G.; Barbosa, S.; Castelletto, V.; Nixon, S. K.; Yang, Z.; Heatley, F.; Hamley, I. W.; Ashford, M.; Mosquera, V.; Attwood, D.; Booth, C. *Langmuir* **2005**, *21*, 5263–5271.
(5) Ricardo, N. M. P. S.; Pinho, M. E. N.; Yang, Z.; Attwood, D.; Booth, C. *Int. J. Pharm.* **2005**, *300*, 22–31.
(6) Booth, C.; Attwood, D. *Macromol. Rapid Commun.* **2000**, *21*, 501–527.

10.1021/la8004568 CCC: $40.75
Published on Web 06/12/2008

formed by propylene oxide[6–9] and butylene oxide[10–13] with diblock and triblock architectures. On the other hand, formation of vesicular structures for poly(oxyalkylene) block copolymers has often needed energy supply via mechanical, sonochemical, or electrical methods.[14,15] Nevertheless, some works have reported the spontaneous formation of vesicles, denoting that these types of structure are likely to form because of relatively large volume-to-length ratios of the hydrophobic block and the relative lengths of the poly(oxyethylene) blocks.[16–18]

In the case of block copolymers containing poly(oxystyrene) blocks, the formation of elongated micelles has been unusual, whereas vesicle formation has not been reported. Probably, neither the composition nor the solvent conditions of the analyzed poly(ethylene oxide)-polystyrene oxide block copolymers promote the clear formation of other aggregate structures than spherical micelles. Only Yang et al.[19] have compared the association number (N_w) of copolymer micelles of copolymers $E_{17}B_8$ and $E_{17}S_8$ and found that substitution of the B block by the S block brought about a large rise in N_w, which was larger than the theoretical increase expected for spherical micelles. They hypothesized that the difference in N_w between these two copolymers might be explained in terms of micelle elongation, but no direct measurements were done. Moreover, in a recent report Elsabahy et al.[20] studied the drug solubilization capacity and release kinetics in vitro of the anticancer drug docetaxel by poly(oxystyrene)-poly(oxyethylene) block copolymers. These authors have demonstrated the existence of an elongated structure of micelles formed by copolymers $E_{45}S_{15}$ and $E_{45}S_{26}$ by TEM. Nevertheless, these authors also pointed out the possible influence of residual styrene oxide homopolymer from the synthesis step dissolved in the micelle core to elongate the aggregate structure, as discussed earlier by Nagarajan.[21]

Thus, in the present work, we studied the self-assembly properties and the different resulting aggregate structures of three copolymers with poly(oxyethylene) and poly(oxystyrene) blocks ($E_{12}S_{10}$, $E_{10}S_{10}E_{10}$, and $E_{137}S_{18}E_{137}$), one diblock and two triblock copolymers, respectively, with very different volume-to-length ratios of the hydrophobic block and relative lengths of the poly(oxyethylene) blocks, which should help in controlling aggregate morphology. The study was conducted by using different techniques such as surface tension, light scattering, transmission and scanning electron microscopies, polarized optical microscopy, and rheology. In fact, for copolymer $E_{12}S_{10}$ coexistence of spherical micelles with vesicular structures is detected. To the best of our knowledge, the spontaneous formation of vesicles by a poly(oxystyrene)-poly(oxyethylene) block copolymers is reported for the first time. On the other hand, formation of elongated micelles upon self-assembly of copolymer $E_{10}S_{10}E_{10}$ in dilute solution is elucidated from light scattering and transmission electron techniques. In the case of copolymer $E_{137}S_{18}E_{137}$, typical spherical micelles are observed as expected. The micellization properties of the latter copolymer had been already partially studied previously, and the present study completes the gap.[22,23] Finally, comparison of the self-assembly properties of the present copolymers with structurally related poly(ethylene oxide)-propylene oxide and poly(ethylene oxide)-butylene oxide block copolymers is also made.

Table 1. Molecular Characteristics of the Copolymer [a]

	M_n/g mol^{-1} (NMR)	wt % S (NMR)	M_w/M_n (GPC)	M_w/g mol^{-1}
$E_{12}S_{10}$	1660	73	1.05	1760
$E_{10}S_{10}E_{10}$	1980	55	1.06	2130
$E_{137}S_{18}E_{137}$	14200	15	1.06	15100

[a] Estimated uncertainty: M_n to ±3%; wt % S to ±1%, M_w/M_n to ±0.01. M_w calculated from M_n and M_w/M_n.

Experimental Section

Materials. The synthesis of the copolymers was described previously in detail.[1,2] Table 1 shows the molecular characteristics of the copolymers. Water was double distilled and degassed before use.

Clouding. Solutions in small tubes (10 mm in diameter) were prepared by weighting copolymer and mixing with water in the mobile state before being stored at low temperature for several days ($T \approx 5$ °C). Tubes containing 0.5 cm^3 of solution were immersed in a water bath, which was heated at a heating/cooling rate of 0.2 °C min^{-1} from 5 to 90 °C. Clouding was detected by the eye. The tubes were also inverted to check the possibility of gel formation. The change from a mobile to an immobile system (or vice versa) was determined by inverting the tube at 1-min intervals.

Surface Tension Measurements. Surface tensions (γ) of the copolymers were measured by the Wilhelmy plate method using Krüss K-12 surface tension equipment, equipped with a processor to acquire the data automatically. The equipment was connected to a circulating water bath to keep the temperature constant at the corresponding temperature to within ±0.01 °C. The plate was cleaned by being washed with doubly distilled water followed by being heated in an alcohol flame. A copolymer stock solution was prepared with distilled water and diluted as required. For measurements, a solution was equilibrated at the proper temperature and the surface tension was recorded at 15-min intervals until a constant value was reached, a process that took 12−36 h depending on concentration. The accuracy of measurement was checked by frequent determination of the surface tension of pure water.

Light Scattering Measurements. Dynamic and static light scattering (DLS and SLS) intensities were measured for copolymer solutions at 20 and 50 °C for $E_{137}S_{18}E_{137}$ by means of an ALV-5000F (ALV-GmbH) instrument with vertically polarized incident light of wavelength $\lambda = 532$ nm supplied by a CW diode-pumped Nd; YAG solid-state laser supplied by Coherent, Inc. and operated at 400 mW. The intensity scale was calibrated against scattering from toluene. Measurements were made at the scattering angle, θ, of 90° to the incident beam. Solutions were equilibrated at each chosen temperature for 30 min before we made a measurement. Experiment duration was in the range 5−15 min, and each experiment was repeated two or more times. To eliminate dust, samples were filtered through Millipore Millex filters (Triton free, 0.45−0.8-μm porosity).

(7) Chu, B.; Zhou, Z. Physical Chemistry of Polyoxyalkylene Block Copolymer Surfactants. In *Nonionic Surfactants: Polyoxyalkylene Block Copolymers*; Nace, V. M., Ed.; Surfactant Science Series 60; Marcel Dekker: New York, 1996.
(8) Hvidt, S.; Jørgensen, E. B.; Brown, W.; Schillén, K. *J. Phys. Chem.* **1994**, *98*, 12320–12328.
(9) Gangaly, R.; Awal, V. K.; Hassan, P. A. *J. Colloid Interface Sci.* **2007**, *325*, 693–700.
(10) Kelarakis, A.; Havredaki, V.; Booth, C.; Nace, V. M. *Macromolecules* **2002**, *35*, 5591–5594.
(11) Chaibundit, C.; Ricardo, N. M. P. S.; Crothers, M.; Booth, C. *Langmuir* **2002**, *18*, 4277–4283.
(12) Li, H.; Yu, G.-E.; Price, C.; Booth, C.; Fairclough, J. P. A.; Ryan, A. J.; Mortensen, K. *Langmuir* **2003**, *19*, 1075–1081.
(13) Chaibundit, C.; Sumnatrakool, P.; Chinchew, S.; Kanatharana, P.; Tattershall, C. E.; Booth, C.; Yuan, X.-F. *J. Colloid Interface Sci.* **2005**, *283*, 544–554.
(14) Battaglia, G.; Ryan, A. J. *J. Am. Chem. Soc.* **2005**, *127*, 8757–8764.
(15) Zipfel, J.; Lindner, M.; Tsinou, M.; Alexandridis, P.; Richtering, W. *Langmuir* **1999**, *15*, 2599–2602.
(16) Battaglia, G.; Ryan, A. J. *Nature Mat.* **2005**, *4*, 869–876.
(17) Bryskhe, K.; Jansson, J.; Topgaard, D.; Schillén, K.; Olsson, U. *J. Phys. Chem. B* **2004**, *108*, 9710–9719.
(18) Harris, J. K.; Rose, G. D.; Bruening, M. L. *Langmuir* **2002**, *18*, 5337–5342.
(19) Yang, Z.; Crothers, M.; Attwood, D.; Collet, J. H.; Ricardo, N. P. S.; Martini, L. G. A.; Booth, C. *J. Colloid Interface Sci.* **2003**, *263*, 312–317.
(20) Elsabahy, M.; Perron, M.-E.; Bertrand, N.; Yu, G.-E.; Leroux, J.-C. *Biomacromolecules* **2007**, *8*, 2250–2257.
(21) Nagarajan, R. *Colloids Surf., B* **1999**, *16*, 55–72.
(22) Ricardo, N. M. P. S.; Chaibundit, C.; Yang, Z.; Attwood, D.; Booth, C. *Langmuir* **2006**, *22*, 1301–1306.
(23) Pinho, M. E. N.; Costa, F. M. L. L.; Filho, F. B. S.; Ricardo, N. M. P. S.; Yeates, S. G.; Attwood, D.; Booth, C. *Int. J. Pharm.* **2007**, *328*, 95–98.

The correlation functions from DLS were analyzed by the CONTIN method to obtain intensity distributions of decay rates (Γ).[24] The decay rate distributions gave distributions of apparent diffusion coefficient ($D_{app} = \Gamma/q^2$, $q = (4\pi n_s/\lambda)\sin(\theta/2)$, where n_s = refractive index of solvent), and integrating over the intensity distribution gave the intensity-weighted average of D_{app}. Values of the apparent hydrodynamic radius ($r_{h,app}$, radius of hydrodynamically equivalent hard sphere corresponding to D_{app}) were calculated from the Stokes−Einstein equation

$$r_{h,app} = kT/(6\pi\eta D_{app}) \quad (1)$$

where k is the Boltzmann constant and η is the viscosity of water at temperature T.

The basis for analysis of SLS was the Debye equation

$$K^* c/(I - I_s) = 1/M_w^{mic} + 2A_2c + \ldots \quad (2)$$

where I is intensity of light scattering from solution relative to that from toluene, I_s is the corresponding quantity for the solvent, c is the concentration (in g dm^{-3}), M_w^{mic} is the mass-average molar mass of the solute, A_2 is the second virial coefficient (higher coefficients being neglected), and K^* is the appropriate optical constant which includes the specific refractive index increment, dn/dc. Values of the specific refractive index increment, dn/dc, and its temperature increment were taken from previous reports.[1,2] The possible effect of the different refractive indices of the blocks on the derived molar masses of micelles has been found to be negligible.[25] Other quantities used were the Raleigh ratio of toluene for vertically polarized light, $R_v = 2.57 \times 10^{-5}[1 + 3.68 \times 10^{-3}(t - 25)]$ cm^{-1} (t in °C) and the refractive index of toluene, $n = 1.4969[1-5.7 \times 10^{-4}(t - 20)]$.[26]

Polarized Optical Microscopy (POM). POM experiments were made by using a Leica TCS-SP2 microscope equipped with cross polarizers in copolymer sample before being filtered. Samples after filtration did not allow measurements of the typical lamellae patterns because of insufficient instrument resolution.

Transmission Electron Microscopy (TEM). Samples for TEM were prepared by evaporation of a 2.5 g dm^{-3} aqueous micellized filtered copolymer solutions under air (with 0.8-μm pore filters). A drop of copolymer solution was placed on an electron microscope copper grid and stained with 2% (v/v) of phosphotungstic acid. After drying, electron micrographs of the sample were recorded with a Phillips CM-12 electron microscope.

Cryo-Scanning Electron Microscopy (Cryo-SEM). Cryo-SEM micrographs were acquired by using a JEOL JSM-6360LV microscope with accelerating voltage of 0.5−30 keV. Solutions were filtered and flash frozen in liquid ethane and stored in liquid nitrogen. They were transferred to a cryo preparation chamber at −90 °C and held at this temperature for 2 min in a vacuum to sublime the surface ice and sputter-coated with conductive chromium.

Rheometry. The rheological properties of the samples were determined using a Bohlin CS10 rheometer with water bath temperature control. Couette geometry (bob, 24.5 mm in diameter, 27 mm in height; cup, 26.5 mm in diameter, 29 mm in height) was used, with 2.5 cm^3 of sample being added to the cup in the mobile state. Samples of very high modulus were investigated using cone-and-plate geometry (diameter 40 mm, angle 4°). A solvent trap maintained a water-saturated atmosphere around the cells. Frequency scans of storage (G') and loss (G'') moduli were recorded for selected copolymer concentrations and temperatures with the instrument in oscillatory shear mode and with the strain amplitude (A) maintained at a low value ($A < 0.5\%$) by means of autostress facility of the Bohlin software. This ensured that measurements of G' and G'' were in the linear viscoelastic region. Temperature scans were recorded for selected copolymer concentrations at a frequency of 1 Hz. The samples were heated at ca. 0.5 °C in the range 5−80 °C. Measurements on solutions of low modulus ($G'' = 1-10$ Pa) which felt outside the range for satisfactory autostress feedback were rejected.

(24) Provencher, S. W. *Makromol. Chem.* **1979**, *180*, 201–209.
(25) Mai, S.-M.; Booth, C.; Kelarakis, A.; Havredaki, V.; Ryan, J. A. *Langmuir* **2000**, *16*, 1681–1688.
(26) (a) El-Kashef, H. *Rev. Sci. Instrum.* **1998**, *69*, 1243–1245. (b) Liu, T.; Schuch, H.; Gerst, M.; Chu, B. *Macromolecules* **1999**, *32*, 6031–6042. (c) The temperature dependence of the Raleigh ratio was not found in the literature and, as a working approximation, values of R_v for toluene were adjusted relative to those published for benzene. Gulari, E.; Chu, B.; Liu, T. Y. *Biopolymers* **1979**, *18*, 2943. The adjustment is small over the temperature range involved.

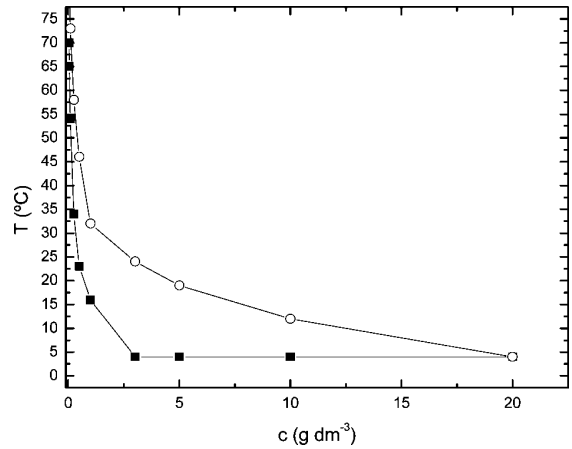

Figure 1. Temperatures at which turbidity was visually observed on heating dilute solutions of copolymers (■) $E_{12}S_{10}$ and (○) $E_{10}S_{10}E_{10}$. The lines are to guide the eye.

Table 2. Critical Micelle Concentration (cmc), Surface Excess Concentration (Γ_{max}), Minimum Area per Molecule (A_{min}), Gibbs Free Energy of Micelle Formation (ΔG°_{mic}), and Gibbs Free Energy of Adsorption (ΔG°_{ads}) of the Present Copolymers [a]

polymer	T (°C)	cmc (g dm^{-3})	Γ_{max} (10^{-6} mol m^{-2})	A_{min} (nm^2)
$E_{12}S_{10}$	15	0.006	0.97	1.7
$E_{10}S_{10}E_{10}$	15	0.012	0.91	1.8
$E_{137}S_{18}E_{137}$	15	0.017	0.40	4.1
	50	0.013	0.46	3.6

[a] Estimated uncertainties: cmc, Γ_{max}, A_{min} to ±10%.

Results

Clouding. Clouding temperatures obtained visually over a wide concentration range are plotted in Figure 1. The overall shape for copolymers $E_{12}S_{10}$ and $E_{10}S_{10}E_{10}$ is as expected for solutes with a lower critical solution temperature. Solutions of copolymer $E_{12}S_{10}$ were only transparent at very low concentration, and opacity increased in a narrow interval as the concentration increased. Copolymer $E_{10}S_{10}E_{10}$ solutions were clear in a wider temperature and concentration range. Meanwhile, solutions of copolymer $E_{137}S_{18}E_{137}$ remained clear to the eye in the whole temperature and concentration range analyzed. As described in subsequent sections, the solutions were formed by copolymer aggregates over the concentration range involved and the detailed shape of the cloud point curve for the former copolymers has to be discussed in that context. This reflects the different behavior of the three copolymers as will be commented in detail below. We return to this point after presentation of the light scattering results. On the other hand, gelation was only observed for copolymer $E_{137}S_{18}E_{137}$ at concentrations larger than 15% (w/v) with no lower temperature boundary.

Critical Micelle Concentration and Surface Properties of Copolymers. Surface tensions of solutions of samples corresponding to copolymers $E_{137}S_{18}E_{137}$, $E_{10}S_{10}E_{10}$, and $E_{12}S_{10}$ were investigated, as set out in Table 2. Plots of surface tension against log(concentration) are plotted in Figure 2. The concentration at

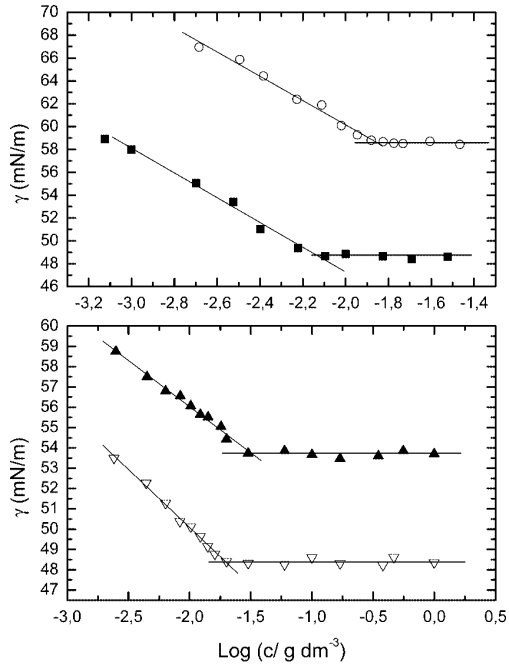

Figure 2. Surface tension (γ) vs logarithm of concentration (g dm^{-3}) of copolymers (○) $E_{10}S_{10}E_{10}$ and (■) $E_{12}S_{10}$ at 15 °C and $E_{137}S_{18}E_{137}$ at (▲) 15 and (▽) 50 °C in aqueous solution.

which the surface tension reached a steady value served to define the cmc. Representative values of the cmc and of the surface tension at the cmc (γ_{cmc}) are listed in Table 2. It can be observed that the triblock copolymers have higher cmc values than the diblock copolymer. The effect is originated by the entropy of the triblock chains constrained by two block junctions in the core−shell interface of the aggregate, compared with only one constrain for the diblock chain. The present values for solutions of copolymers $E_{137}S_{18}E_{137}$, $E_{10}S_{10}E_{10}$, and $E_{12}S_{10}$ at 15 °C are in good agreement with previously reported values for other diblock and triblock copolymers of ethylene oxide and styrene oxide.[27,28]

On the other hand, the surface excess concentration, Γ_{max}, and the minimum area per copolymer molecule, A_{min}, at the air/water interface were obtained using the surface tension measurements and the following equations:

$$\Gamma_{max} = -\frac{1}{RT}\left(\frac{\partial\gamma}{\partial \ln c}\right)_{T,p} \quad (3)$$

$$A_{min} = 1/N_A\Gamma_{max} \quad (4)$$

where R is the gas constant, N_A is Avogadro's number, and c is the copolymer concentration.

Because of their higher hydrophobicity, copolymers $E_{12}S_{10}$ and $E_{10}S_{10}E_{10}$ display a larger interface coverage than $E_{137}S_{18}E_{137}$, whose molecules also need more space to be accommodated because of the longer length.[28] On the other hand, for the triblock $E_{137}S_{18}E_{137}$ there is a decrease in the value of A as the temperature rises as a consequence of the increase in the thermal motions of the polymer chains and the dehydration of the hydrophilic blocks.[29,30]

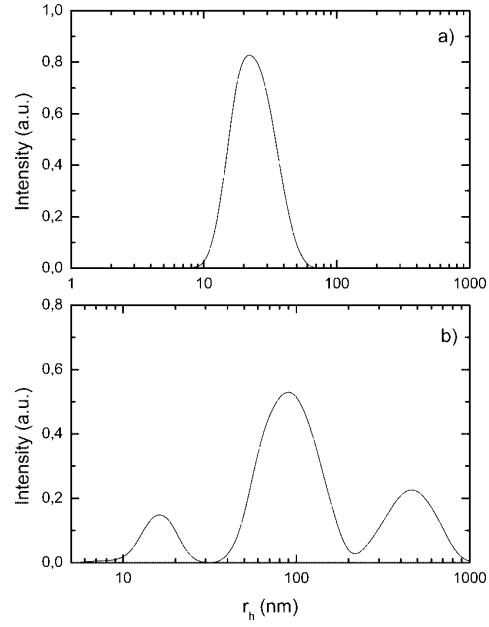

Figure 3. Intensity fraction distributions of the apparent hydrodynamic radius for (a) copolymer $E_{137}S_{18}E_{137}$ (60 g/dm^{-3} at 20 °C) and (b) copolymer $E_{12}S_{10}$ (2.5 g/dm^{-3} at 10 °C).

Vesicular Formation in Copolymer $E_{12}S_{10}$. Intensity fraction distributions of decay times for the three copolymers are shown in Figure 3. In the case of copolymers $E_{10}S_{10}E_{10}$ and $E_{137}S_{18}E_{137}$, the distribution contained one single peak (see Figure 3a for copolymer $E_{137}S_{18}E_{137}$ as an example). In contrast, three single narrow peaks were observed for copolymer $E_{12}S_{10}$ at suitable concentrations to be measured by DLS (Figure 3b). These peaks did not vary in a systematic way in the narrow copolymer concentration range analyzed (0.5−3 g dm^{-3}) provided that solutions were not completely clear (turbidity increased as the copolymer concentration rises), so a true hydrodynamic radius could not be obtained (plot not shown). Because of the translucent aspect of these solutions and to know if these solutions were isotropic or not, we analyzed some of the samples by POM. Surprisingly, the typical patterns displayed by spherical lamellae were observed for all the samples in the concentration range anlyzed[31] (Figure 4a).

In contrast, no presence of these patterns was observed for solutions of copolymer $E_{10}S_{10}E_{10}$ or copolymer $E_{137}S_{18}E_{137}$ in the concentration range analyzed, even in solutions not optically clear. The different sizes of the observed circular patterns in polarized spectroscopy denote the polydisperse size of the vesicles. It is necessary to note that samples for POM experiments were unfiltered samples provided that filtered ones did not allow accurate measurements because of instrument resolution. Thus, sizes of vesicles from POM are larger than those derived from electron microscopies (between 1 and 5 μm) and even more polydisperse. The presence of vesicular structures was further corroborated by TEM and cryo-SEM, as seen in Figure 4b,c, in this case using filtered solutions as for DLS. Despite the inherent problems of TEM due to solvent evaporation during sample preparation, which affects sizes and structures of nanostructures in solution, the coexistence of micelles with a mean size of ca.

(27) Booth, C.; Attwood, D.; Price, C. *Phys. Chem. Chem. Phys.* **2006**, *8*, 3612–3622.
(28) Barbosa, S.; Cheema, M. A.; Taboada, P.; Mosquera, V. *J. Phys. Chem. B* **2007**, *111*, 10920–10928.
(29) Kelarakis, A.; Havredaki, V.; Yu, G.-E.; Derici, L.; Booth, C. *Macromolecules* **1998**, *31*, 944–946.
(30) Sony, S. S.; Sastry, N. V.; George, J.; Bohidar, H. B. *Langmuir* **2003**, *19*, 4597–4603.
(31) Kunieda, H.; Nakamura, K.; Davis, H. T.; Evans, D. F. *Langmuir* **1991**, *7*, 1915–1921.

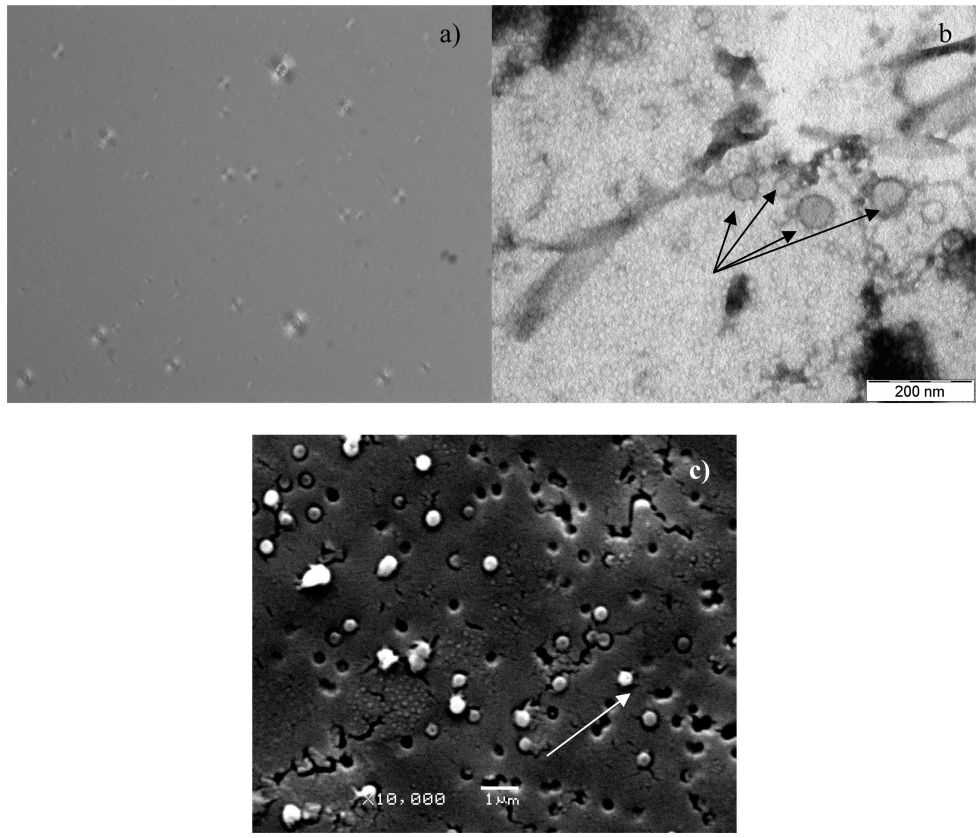

Figure 4. (a) POM image of vesicles formed by copolymer $E_{12}S_{10}$. Picture was taken at 100× magnification. (b) TEM images of vesicles (denoted with arrows) that coexist with smaller micelles. (c) Cryo-SEM picture of polymer vesicles of copolymer $E_{12}S_{10}$. The smallest vesicles are denoted with arrows.

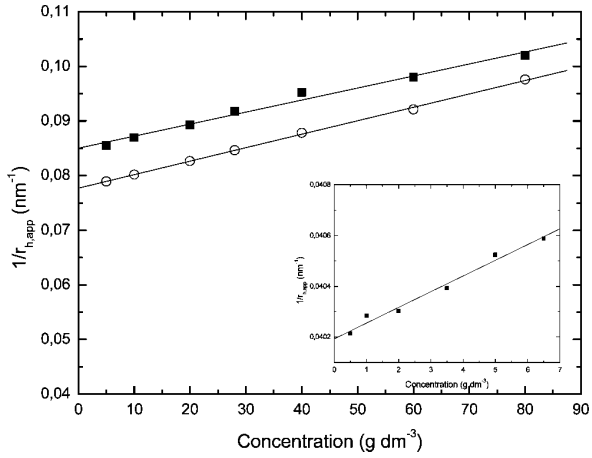

Figure 5. Concentration dependence of the reciprocal apparent hydrodynamic radii for micellar solutions of copolymers $E_{137}S_{18}E_{137}$ at (■) 15 and (○) 50 °C and copolymer $E_{10}S_{10}E_{10}$ at 15 °C (inset).

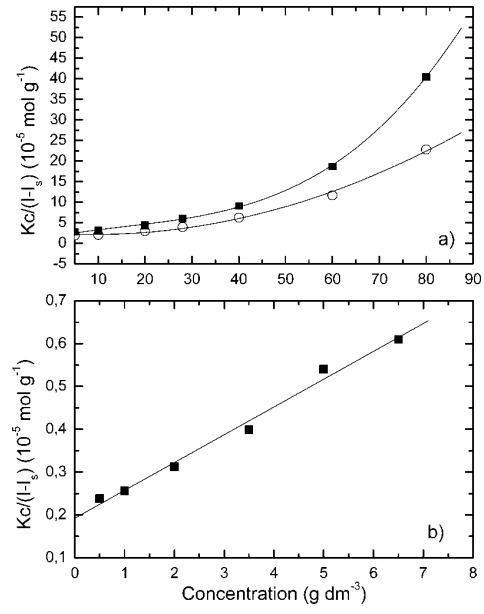

Figure 6. Debye plots for micellar solutions of (a) copolymer $E_{137}S_{18}E_{137}$ at (■) 15 and (○) 50 °C and (b) copolymer $E_{10}S_{10}E_{10}$ at 15 °C.

16 nm and some small vesicles of polydisperse size (mean size of ca. 65 nm; see arrows in Figure 4b) can be discerned. Cryo-SEM showed also the existence of larger vesicles (with sizes around ca. 400 nm) at more concentrated copolymer solutions, as seen in Figure 4c, which coexist with smaller vesicles of ca. 100 nm of diameter (see arrows). In this figure, pores created from vesicle disintegration during sample preparation can be also observed. Micelles were not seen because the equipment resolution was not sufficient. Then, comparing the size distributions derived from DLS with the sizes of the structures seen by TEM and SEM, we can assign the first peak of the DLS size

Table 3. Micellar and Hydration Properties of Block Copolymers $E_{12}S_{10}$, $E_{10}S_{10}E_{10}$, and $E_{137}S_{18}E_{137}$

polymer	T/°C	$A_2/10^{-4}$ mol g^{-2} cm^3	δ_t	$M_w^{mic}/10^5$ mol g^{-1}	r_h/nm	N_w	r_t/nm
$E_{10}S_{10}E_{10}$	15	4.5	1.0	4.7	20.2	202	21.5
$E_{137}S_{18}E_{137}$	15	0.2	5.8	4.8	12.9	34	9.9
	50	0.27	4.8	6.3	11.8	42	10.2

distribution of copolymer $E_{12}S_{10}$ to micelles provided that this species lies in the typical sizes of copolymer micelles (with an apparent radius of ca. 13 nm), whereas the other two peaks are assigned to polymer vesicles of different sizes. In this regard, differences in vesicle sizes between SEM, DLS, and TEM may arise from solvent evaporation in the latter technique, which dehydrates the polymer corona and shrinks the polymer structure. On the other hand, polymer solutions when measured by TEM showed the presence of polymer aggregated material, which may be composed of the largest vesicles as a consequence of the sample evaporation process since these were not observed by this technique (picture not shown).

Micellar Properties of Copolymers $E_{137}S_{18}E_{137}$ and $E_{10}S_{10}E_{10}$. *Hydrodynamic Radii.* Now we will focus on the micellar properties of copolymers $E_{137}S_{18}E_{137}$ and $E_{10}S_{10}E_{10}$. Plots of the reciprocal of the intensity average of $r_{h,app}$ (by using the Stokes−Einstein relation) are shown in Figure 5 for copolymers $E_{137}S_{18}E_{137}$ and $E_{10}S_{10}E_{10}$. The intercepts of these plots at $c = 0$ gave values of r_h. Note that through eq 1 the reciprocal of $r_{h,app}$ is proportional to $D_{app}/\eta T$ and thus compensated for changes in solvent viscosity and temperature. The positive slopes in this figure are consistent with these micelles acting effectively as hard spheres.[1] This behavior is usually accommodated by introducing a diffusion second virial coefficient (k_d) in the equation of the straight line

$$D_{app} = D(1 + k_d c + \dots) \quad (5)$$

The coefficient k_d is related to the thermodynamic second virial coefficient A_2 by[32]

$$k_d = 2A_2 M_w^{mic} - k_f - 2\upsilon \quad (6)$$

where k_f is the friction coefficient and υ is the specific volume of the micelles in solution. As seen from Figure 6, the positive term in eq 7 is dominant. Relating A_2 to the effective hard-sphere volume of the micelles, υ_{hs} ($A_2 = 4N_A\upsilon_{hs}/M_w^{2\,(mic)}$)[33] shows that the first term depends on the ratio υ_{hs}/M_w^{mic}. A_2 values (Table 3) are positive in agreement with the commented micellar behavior. On the other hand, the larger insensitivity of $1/r_{h,app}$ with changes in concentration of copolymer $E_{10}S_{10}E_{10}$ is associated to their higher molar masses and is a common feature observed for elongated micelles.[4,14]

Aggregation Numbers. As noted in the , the Debye equation (eq 2) is for nonideal dilute solution of particles that are small relative to the wavelength of the light. The Debye equation taken to the second term, A_2, could not be used to analyze the SLS data for copolymer $E_{137}S_{18}E_{137}$ as micellar interaction causes curvature of the Debye plot across the concentration range investigated (Figure 6). The fitting procedure used for these curves was based on scattering theory for hard spheres[34] whereby the interparticle interference factor (structure factor, S) in the scattering equation

$$K^* c/(I - I_s) = 1/SM_w^{mic} \quad (7)$$

was approximated by

$$1/S = [(1+2\phi)^2 - \phi^2(4\phi - \phi^2)](1-\phi)^{-4} \quad (8)$$

where ϕ is the volume fraction of equivalent uniform spheres. Values of ϕ were conveniently calculated from the volume fraction of copolymer in the system by applying a thermodynamc expansion factor $\delta_t = \upsilon_t/\upsilon_a$, where υ_t is the thermodynamic volume of a micelle (i.e., one-eighth of the volume, u, excluded by one micelle to another) and υ_a is the anhydrous volume of a micelle ($\upsilon_a = \upsilon M_w^{mic}/N_A$), where υ is the partial specific volume of the copolymer solute. The fitting parameter, δ_t, applies as an effective parameter for compact micelles irrespective of their exact structure. The method is equivalent to using the virial expansion for the structure factor of effective hard spheres taken to its seventh term[34] but requires just two adjustable parameters (i.e., M_w^{mic} and δ_t). Values of these two quantities are shown in Table 3. In addition, weight-average association numbers, N_w, of the copolymer micelles were calculated from the micellar molecular mass derived from the fitting procedure shown above and the weight-average molecular weight of the copolymer in the unimer state (i.e., $N_w = M_w(\text{micelle})/M_w(\text{molecule})$; Table 1). Values of the equivalent hard-sphere radius (the thermodynamic radius, r_t) calculated from the thermodynamic volume of the micelles (i.e., from $\upsilon_t = \delta_t\upsilon_a$) are also listed in Table 3. It is also clear that the effective hard-sphere radius, like the hydrodynamic radius, has a more direct relation to spherical micelles than to other shapes.

As expected, N_w values for copolymer $E_{137}S_{18}E_{137}$ slightly increase as the temperature rises since water becomes a poorer solvent for the poly(oxyethylene) blocks. This is consistent with the effect of temperature in micelles of other copoly(oxyalkylene)s.[28,35] In addition, present aggregation numbers are in agreement with previously reported ones for this copolymer at other temperatures.[23]

TEM imaging was undertaken to directly visualize the micelle shape. Copolymer $E_{137}S_{18}E_{137}$ formed nearly spherical micelles in solution (Figure 7a), whereas copolymer $E_{10}S_{10}E_{10}$ self-assembled into spheroidal aggregates (Figure 7b). Under TEM, the diameters of micelles were close to those obtained by DLS. The mean length of the major axis of the spheroids was ca. 22 nm. Nevertheless, one has to bear in mind that with TEM we image single particles whereas DLS gives an average size estimation, which is biased toward the larger-size end of the population distribution. In addition, it should be pointed out that r_h for elongated micelles derived from DLS is an effective value for "equivalent spheres", and hence r_h is not expected to equal the ellipsoid or cylinder radius.

Rheological Behavior. Solutions of copolymers $E_{10}S_{10}E_{10}$ and $E_{137}S_{18}E_{137}$ were analyzed to study their rheological behavior. Solutions of $E_{10}S_{10}E_{10}$ (0−50% (w/v)) were investigated for gel formation using tube inversion experiments. Immobility implies no detectable flow over a period of hours or days. To a good approximation, immobility in the test requires the gel to have a yield stress higher than 30 Pa.[36] Adopting the notation used by Hvidt et al.,[36–38] we refer to this immobile phase as "hard gel".

(32) Vink, H. *J. Chem. Soc., Faraday Trans. 1* **1985**, *81*, 1725–1730.
(33) Flory, P. J. *Principles of Polymer Chemistry*; Cornell University Press: Ithaca, NY, 1953.
(34) (a) Percus, J. K.; Yevick, G. J. J. *Phys. Rev.* **1958**, *110*, 1–13. (b) Vrij, A. *J. Chem. Phys.* **1978**, *69*, 1742–1747. (c) Carnahan, N. F.; Starling, K. E. *J. Chem. Phys.* **1969**, *51*, 635–636.
(35) Booth, C.; Attwood, D. *Macromol. Rapid Commun.* **2000**, *21*, 501–527.
(36) Hvidt, S.; Jørgensen, E. B.; Brown, W.; Schillén, K. *J. Phys. Chem.* **1994**, *98*, 12320–12328.
(37) Kelarakis, A.; Mingvanish, W.; Daniel, C.; Li, H.; Havredaki, V.; Heatley, F.; Booth, C.; Hamley, I. W. *Phys. Chem. Chem. Phys.* **2000**, *2*, 2755–2763.

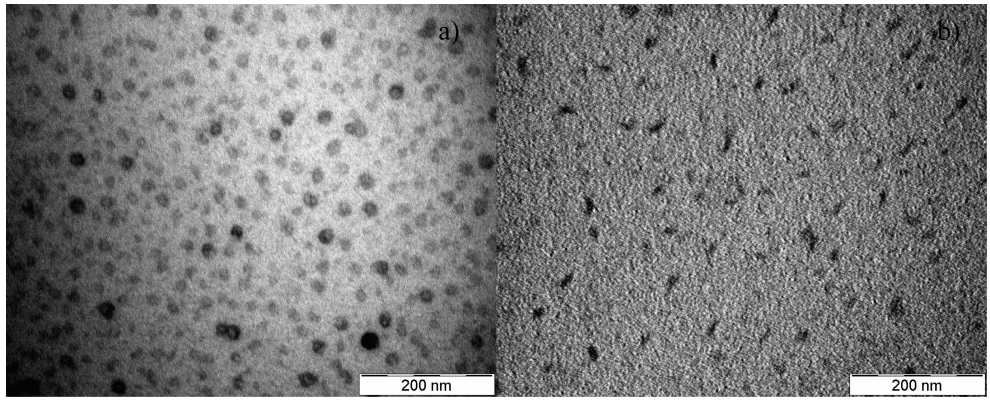

Figure 7. TEM micrograhs of micelles formed by copolymers (a) $E_{137}S_{18}E_{137}$ and (b) $E_{10}S_{10}E_{10}$.

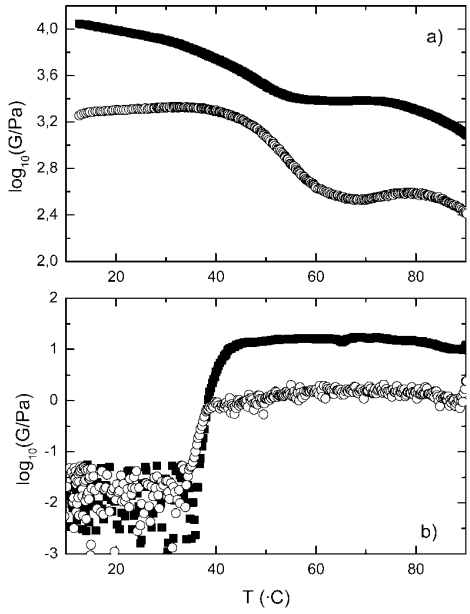

Figure 8. Aqueous solutions of copolymer $E_{137}S_{18}E_{137}$. (a) Temperature dependence of (■) storage (G') and (○) loss (G'') moduli for aqueous hard gel at 50% (w/v), frequency, $f = 1$ Hz, and strain amplitude, $A = 0.5\%$. (b) Temperature dependence of storage (G') (■), and loss (G''), (○), moduli at 10% (w/v), $f = 1$ Hz, and $A = 0.5\%$.

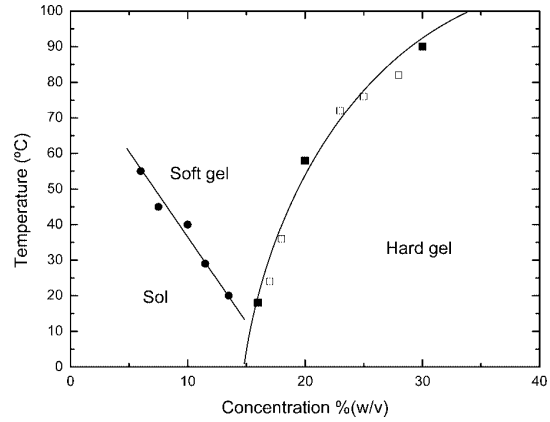

Figure 9. Phase diagram of copolymer $E_{137}S_{18}E_{137}$ from (□) tube inversion and (■, ●) rheology showing the sol, soft gel, and hard gel regions.

They have used yield stress (σ_y) and modulus (storage and loss, G' and G'') to define three convenient subdivisions of the range of behaviors observed: immobile hard gel (high σ_y and G', $G' > G''$), mobile soft gel (low σ_y and G', $G' > G''$), and mobile sol (null σ_y and very low G', $G' < G''$).

Temperature Dependence of Copolymer $E_{137}S_{18}E_{137}$. The sol-hard gel boundary was already determined by tube inversion and rheology previously,[39] but additional measurements were done to complete its phase diagram. Figure 8a shows an example of a temperature scan of the logarithm of the elastic modulus for a concentrated solution above the critical gel concentration (cgc) for this copolymer (19% (w/v), derived from the expression cgc $= 10^2\rho_a\phi_c/\delta_t$, where $\phi_c = 0.68$ is the volume fraction of spherical micelles packed in a body-centered structure.[39] On the basis of a critical value of $G'' = 1$ kPa for a hard gel, the 50% (w/v) copolymer solution is a hard gel in the whole range, with a maximum value of $G' \approx 16$ kPa, and $G' > G''$ throughout the whole experiment. In Figure 8b, a temperature scan of G' and G'' at a concentration below the hard-gel boundary (10% w/v) is also shown as an example. Other polymer concentrations in this region below the cgc display the same profile (not shown). Using the conditions described above, we found that at temperatures at which G' (1 Hz) exceeds 10 Pa the solutions are soft gels, otherwise sols.[36–38] As illustrated, within the region of raised modulus G' was higher than G'', which justifies the convenient term "soft gel" for the fluid to distinguish it from sol. A complete phase diagram of the regions of sol, soft gel, and hard gel defined by rheometry and tube inversion for copolymer $E_{137}S_{18}E_{137}$ is shown in Figure 9. These sol−gel diagrams follow the general pattern as those published previously for other EO/SO block copolymers.[1,2] The upper limit to the soft gel region for the copolymer is not reached within the temperature range investigated, consistent with the stability at high temperature of the hard gels of this copolymer.

Frequency Dependence of Copolymer $E_{137}S_{18}E_{137}$. To get a more detailed picture about the rheological behavior of both hard and soft gels, frequency scans of solution of $E_{137}S_{18}E_{137}$ block copolymer were performed. Figure 10a shows the frequency scan obtained for the 15% (w/v) solution of copolymer $E_{137}S_{18}E_{137}$ at 25 °C. This type of soft gel at temperatures and concentrations relatively near the hard-gel boundary can be assigned as defective versions of the cubic packed hard gels (i.e., small structured domains in an overall fluid matrix). These soft gels are

(38) Almgrem, M.; Brown, W.; Hvidt, S. *Colloid Polym. Sci.* **1995**, *273*, 2–15.
(39) Hamley, I. W.; Castelletto, V.; Ricardo, N. P. M. S.; Pinho, M. E. N.; Booth, C.; Attwood, D.; Yang, Z. *Polym. Int.* **2007**, *56*, 88–92.

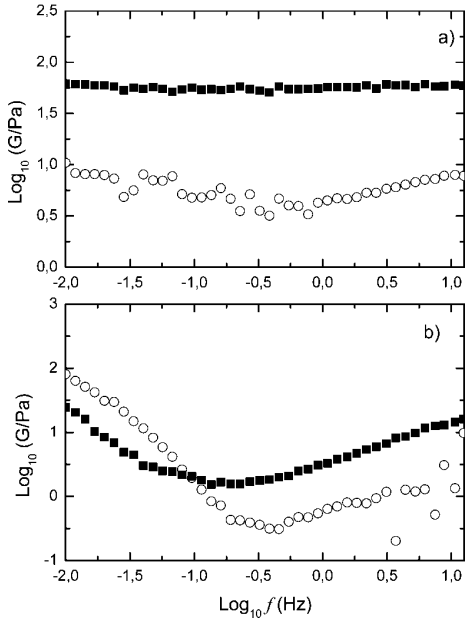

Figure 10. Frequency dependence of (●) storage and (○) loss moduli (log−log plot) for (a) 15% (w/v) aqueous solution of copolymer $E_{137}S_{18}E_{137}$ in the soft gel region and (b) 6% (w/v) aqueous solution of copolymer $E_{137}S_{18}E_{137}$ in the soft gel region at $T = 60$ °C.

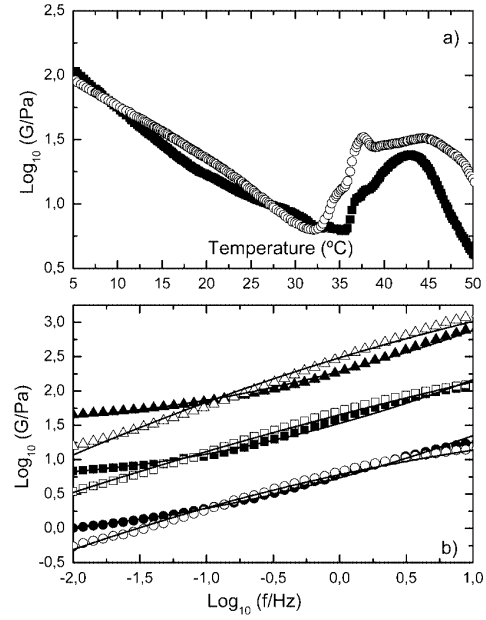

Figure 11. (a) Temperature dependence of (●) storage and (○) loss moduli (log−log plot) for a 20% (w/v) aqueous solution of copolymer $E_{10}S_{10}E_{10}$. (b) Frequency dependence of storage (close symbols) and loss moduli (open symbols) (log−log plot) for (●) 20, (■) 30, and (▲) 40% (w/v) aqueous solution of copolymer $E_{10}S_{10}E_{10}$ at 15 °C.

characterized by the almost constant value of log G', the minimum in log G'', and both moduli do not show a crossover point in the measured frequency range, all of which are characteristic of hard gels formed by cubic packing of spherical micelles,[40] although the modulus values are low compared to those of the hard gel ($G' \approx 70$ Pa and $G'' \approx 5$ Pa at $f = 1$ Hz, $A = 0.5\%$). Soft gels of this type have been also found for other $E_mS_nE_m$, E_mS_n,[28] and $E_mG_nE_m$[4] (where G = phenylglycidyl unit) copolymers studied by rheometry, and some E_mB_n copolymers using SAXS[41] and Pluronics using SANS.[42]

On the other hand, the scan obtained for a 6% (w/v) solution at 60 °C differs from that of Figure 10a (Figure 10b), having very low values of G' (e.g., $G' \approx 8$ Pa at $f = 1$ Hz, $A = 0.5\%$) and with a moduli crossover at low frequency, corresponding to a Maxwell fluid, at most, showing localized cubic order. This must be a consequence of the weak attraction of spherical micelles in water at temperatures where it is a poor solvent for the micelles. The transition from sol to soft gel may well occur when aggregates of spherical micelles reach the percolation threshold, yielding sufficient structure to cause the characteristic rheological effect. Soft gels of this type have been also identified in aqueous micellar solutions of a wide range of copolymers including other EO/SO copolymers,[1,2,28,40] as well as in $E_mP_nE_m$ (P = propylene oxide unit) by Hvidt and co-workers who ascribed the effect in certain systems to the intervention of the sphere-to-rod micellar transition,[36,38] and by Mallamace and co-workers who identified mechanisms of percolation and packing (structural-arrest), depending on temperature and concentration.[43,44]

Concentration and Temperature Dependence of Copolymer $E_{10}S_{10}E_{10}$. For copolymer $E_{10}S_{10}E_{10}$, gelation was not found in the concentration range analyzed. Concentrations in the range 5−30% (w/v) and temperatures in the range 10−45 °C were investigated despite the turbid solution, a signal that the phase-separation boundary was close, as will be commented below. For a given concentration of copolymer, the value of G' decreased with increasing temperature (Figure 11a), which is associated with the water becoming a worse solvent for poly(oxyethylene), resulting in a compression of the E-block corona and, thereby, a decrease in the effective volume fraction of micelles in the solution. The break in the curve of Figure 11a observed around 35 °C is related to solution-phase separation.

Frequency Dependence of Copolymer $E_{10}S_{10}E_{10}$. The frequency dependence of the modulus was determined for solutions of copolymer $E_{10}S_{10}E_{10}$ in the concentration range 5−40% (w/v) at 25 °C. Solutions were mobile fluids over the frequency range of our measurements. Typically, values of G'' exceeded those of G' over the accessible frequency range except at low frequencies (Figure 11b). The viscoelasticity of the solution was modeled by parallel Maxwell elements:

$$G' = (G_\infty \tau^2\omega^2)/(1 + \tau^2\omega^2) \quad (9a)$$

$$G'' = (G''\tau\omega)/(1 + \tau^2\omega^2) \quad (9b)$$

where G_∞ is the plateau value of G' at high frequency, τ is the relaxation time, and $\omega = 2\pi f$ (f in hertz). A good fit required the sum of several elements, but as illustrated in Figure 11b, the essential features of the rheology of the system could be reproduced using three elements, with characteristic relaxation times in the order of 0.02−0.03, 0.2−0.4, and 10−15 ms, respectively, for all the copolymer concentrations analyzed. The smallest time represents a fast process characteristic of a mobile fluid, whereas the slowest is assigned to an effect of intermicellar interaction between elongated micelles. The slight upturn in the scan at low frequency provided evidence of an emerging slow

(40) Li, H.; Yu, G.-E.; Price, C.; Booth, C.; Fairclough, J. P. A.; Ryan, A. J.; Mortensen, K. *Langmuir* **2003**, *19*, 1075–1081.
(41) Castelletto, V.; Caillet, C.; Fundin, J.; Hamley, I. W.; Yang, Z.; Kelarakis, A. *J. Chem. Phys.* **2002**, *116*, 10947–10958.
(42) Prud'homme, R. K.; Wu, G.; Schneider, D. K. *Langmuir* **1996**, *12*, 4651–4659.
(43) Lobry, L.; Micali, N.; Mallamace, M.; Liao, C.; Chen, S. H. *Phys. Rev. E* **1999**, *60*, 7076–7087.
(44) Chen, S. H.; Chen, W. R.; Mallamace, F. *Science* **2003**, *300*, 619–622.
(45) Antonietti, M.; Forster, S. *Adv. Mater.* **2003**, *15*, 1323–1333.

process, which we assign to the first stages of formation of an elastic network, and which gives rise to the formation of the soft gel.[13]

Discussion

As commented previously, it is assumed that the parameters that control the morphologies of the aggregates are mainly core chain stretching, interfacial tension, and corona repulsion. Consequently, factors that influence the above balance can be used to control the aggregate architecture: polymer molecular weight, relative block lengths, hydrophobic block structure, solution conditions, and so forth. Compared to the separated aggregation behavior of small and large colloidal spheres, micelles and vesicles may form in dilute solution of block copolymers.[45,46] In the classical and most simple description, the factor determining the shape of self-assembled amphiphilic structures is the size of the hydrophobic moiety to the hydrophilic part. In particular, the micellar structure formation can be described in terms of a critical packing factor, ϕ, defined as

$$\phi = \frac{V}{al} \tag{10}$$

where V is the hydrophobic volume in the micelle core, a is the cross-sectional area of the hydrophilic part, and l is the chain length.[47] This model hypothesizes that changes in the amphiphile geometry, reflected in changes in V, a, or l, affect the type of aggregate the amphiphile may form. At a ϕ value of 0.5, the model predicts formation of spherical lamellae. As the packing factor decreases, the extent of curvature increases, and the structure shape moves toward spherical micelle. Thus, in this work we prepare three different styrene oxide block copolymers with different relative block lengths and hydrophobe molecular volumes made by styrene oxide units. Since previously studied $E_{11}B_{11}$ and $E_{14}B_{10}$ were shown to form vesicles,[18] and provided that styrene oxide chain possess a larger volume than propylene oxide and butylene oxide units, we thought that copolymer $E_{12}S_{10}$ should possess a hydrophilic/hydrophobic block ratio and a sufficient hydrophobe volume (because of the presence of an aromatic ring in its structure) to form vesicles, as has been corroborated. In addition, the small size of the hydrophilic block should also favor vesicle formation provided that this is favored when the hydrophilic surface area (in our case the hydrophilic corona) decreases, as has been previously observed for structurally related poly(ethylene oxide)-poly(propylene oxide) and poly(ethylene oxide)-poly(butylene oxide) block copolymers.[17,18] On the other hand, structurally related block copolymer $E_{11}B_8$ (B = butylene oxide unit)[11] has been pointed out to undergo micelle elongation above 35 °C because of a severe increase in N_w and geometrical considerations. The same behavior has been claimed for copolymer $E_{17}S_{10}$, for which 20 °C was enough to greatly increase N_w.[19] Nevertheless, image or other suitable techniques were not used to detect the presence of other possible structures in both cases, mainly vesicles in contrast to copolymers $E_{11}B_{11}$ and $E_{14}B_{10}$ for which spontaneous vesicle formation has been demonstrated.[18]

On the other hand, the previous arguments would also explain why we did not find vesicular formation for the triblock $E_{10}S_{10}E_{10}$: this copolymer would behave as a diblock $E_{10}S_5$ because of the two core junctions in its structure, and not enough core volume and hydrophobic/hydrophilic ratio would be achieved to allow vesicle formation. Nevertheless, for this copolymer we found that its aggregates possess a spheroidal form, as seen by TEM, whereas for copolymer $E_{137}S_{18}E_{137}$ micellar spheres were observed. In fact, taking the length of an S unit to be 0.36 nm per chain unit,[33] the average length of the fully stretched S_{10} block is approximately 3.6 nm. As the central S block is looped in the micelle core for the triblock copolymer $E_{10}S_{10}E_{10}$, the effective length will be 1.8 nm. Consequently, this would be the maximum possible radius for an anhydrous core of a spherical micelle. This means that the maximum core volume would be 25 nm^3 and, given a liquid density at 15 °C of 1.15 g cm^{-3}, then the maximum aggregation number compatible with a spherical compact geometry would be ca. 15. Despite considering that (a) the S blocks possess Poisson distributions, as expected for an ideal polymerization of an alkylene oxide,[33] (b) the copolymer micelles possess water in the core associated with the hydroxyl end groups of the S blocks, as demonstrated recently,[48,49] and (c) the larger entropy penalty due to chain stretching, all of which should alleviate further the stretching restriction, the derived N_w value from SLS for these copolymer ($N_w = 202$) is incompatible with spherical micelles, which should be elongated, either spheroidal or wormlike. This is not the case for copolymer $E_{137}S_{18}E_{137}$, for which a maximum aggregation number of 71 is expected to be compatible with a spherical shape. In addition, the longer E blocks increase the hydrophilic surface area promoting spherical aggregates, as commented above. The difference in micelle geometry between copolymer $E_{137}S_{18}E_{137}$ and $E_{10}S_{10}E_{10}$ also provides an explanation for the different concentration dependences of the hydrodynamic radii and Debye functions illustrated in Figures 5 and 6, respectively. In this regard, the Debye function found for copolymer $E_{137}S_{18}E_{137}$ is typical of spherical copolymer micelles, with the curvature being a result of interference from micelles reducing the scattering intensity as concentration is increased. However, mass action ensures that elongated micelles of copolymer $E_{10}S_{10}E_{10}$ will increase in length as concentration is increased at a given temperature, an effect that progressively increases the scattering intensity and thus opposes the effect of micelle interaction. On the other hand, association numbers found for structurally related block copolymers with butylene oxide and styrene oxide and similar hydrophobic block length shows that, for example, copolymers $E_{13}B_{10}E_{13}$[50] (commercially available from Dow Chemical Co.) and $E_{16}B_{10}E_{16}$[51] do not form elongated micelles in the temperature range analyzed (up to 45 °C) since their aggregation numbers are sensibly lower than that obtained for copolymer $E_{10}S_{10}E_{10}$. Assuming a ratio of association numbers between poly(oxyethylene)-poly(oxystyrene) and poly(oxyethyelene)-poly(oxybutylene) copolymers of 3 ($N_{w,S}/N_{w,B} \approx 3:1$),[14] the association number 51 for $E_{16}B_{10}E_{16}$ would involve one of 153 for $E_{10}S_{10}E_{10}$, values well outside the range possible for spherical micelles, and smaller than the value found experimentally in the present work at 15 °C. In contrast, copolymer $E_{135}B_{20}E_{135}$ showed the formation of spherical micelles with an aggregation number of 17 at 25 °C,[22] as in the case of the closely related copolymer $E_{137}S_{18}E_{137}$ studied in the present work.

Finally, it has been shown[52] that a unifying rule for formation of polymersomes in water involves the necessity of a hydrophilic-to-total mass ratio 25% < $f_{hydrophilic}$ < 35%. Cylindrical shapes

(46) Yu, M.; Wang, H.; Zhou, X.; Yuan, P.; Yu, C. *J. Am. Chem. Soc.* **2007**, *129*, 14576–14577.
(47) Israelachvili, J. N. *Intermolecular and Surface Forces*; Academic Press: New York; 1992; pp 380–384.
(48) Kelarakis, A.; Mai, S.-M.; Havredaki, V.; Nace, V. M.; Booth, C. *Phys. Chem. Chem. Phys.* **2001**, *3*, 4037–4043.
(49) Castro, E.; Taboada, P.; Mosquera, V. *J. Phys. Chem. B* **2006**, *110*, 13113–13123.
(50) Yu, G.-E.; Yang, Y.-W.; Yang, Z.; Attwood, D.; Booth, C. *Langmuir* **1996**, *12*, 3404–3412.
(51) Yu, G.-E.; Li, H.; Price, C.; Booth, C. *Langmuir* **2002**, *18*, 7756–7758.
(52) Discher, D. E.; Eisenberg, A. *Science* **2002**, *297*, 967–973.

can be expected for 35% < $f_{hydrophilic}$ < 50%, spherical micelles for $f_{hydrophilic}$ < 45%, and inverted microstructures for $f_{hydrophilic}$ < 25%. Although sensitivities of these rules to chain chemistry and molecular weight have not been fully probed, the present analyzed copolymers seem to be in agreement with these.

Conclusions

We have analyzed the micellization, gelation, and structure of the aggregates of three poly(ethylene oxide)-polystyrene oxide block copolymers. Two of them have similar block length but different structures ($E_{12}S_{10}$, $E_{10}S_{10}E_{10}$), and the other has longer blocks ($E_{137}S_{18}E_{137}$). In this way, we can compare the effect of temperature and block length on the self-assembly properties. The values of the critical micelle concentration show that the short triblock copolymer has a cmc twice as large as that of the related diblock. The effect is originated by entropy of the triblock chains constrained by two block junctions in the core interface of the aggregate, compared with only one constraint for the diblock chain. Intensity fraction size distributions showed the existence of several species in solutions of copolymer $E_{12}S_{10}$ whereas only one for copolymers $E_{10}S_{10}E_{10}$ and $E_{137}S_{18}E_{137}$. Light scattering, polarized light microscopy, and transmission and cryo-scanning electron microscopies provided sufficient evidence to ensure the coexistence of micelles and polydisperse vesicles for the most concentrated samples of this copolymer (but even in the dilute regime). The size of these vesicular structures varies between 60 and 500 nm as shown by TEM, DLS, and cryo-SEM. The classical birefringent pattern of vesicles was observed by polarized light microscopy. On the other hand, the single size distribution observed for copolymers $E_{10}S_{10}E_{10}$ and $E_{137}S_{18}E_{137}$ was assigned to elongated and spherical micelles, respectively. This assignment was made in light of the high aggregation number derived for the former copolymer which is incompatible with a spherical geometry of the aggregated, as also corroborated by TEM. Tube inversion was used to define the mobile−immobile (soft−hard gel) phase boundaries. The phase diagram of copolymer $E_{137}S_{18}E_{137}$ was further completed to determine the sol−soft gel−hard gel boundaries. In contrast, copolymers $E_{12}S_{10}$ and $E_{10}S_{10}E_{10}$ did not gel in the concentration range analyzed. Only certain concentrations of copolymer $E_{10}S_{10}E_{10}$ were analyzed by rheometry, for which an upturn in the low-frequency range of the stress moduli was observed, denoting an evidence of an emerging slow process, which we assign to the first stages of formation of an elastic network.

Acknowledgment. We thank the Ministerio de Educación y Ciencia through projects MAT2007-61604 and Xunta de Galicia for financial support. J.J. thanks USC for his PhD fellowship, and E.C. thanks Xunta de Galicia for his "Anxeles Alvariño" research contract. We are really grateful to Profs. D. Attwood and C. Booth for providing several of the copolymer samples.

LA8004568

Surface Properties of Monolayers of Amphiphilic Poly(ethylene oxide)-Poly(styrene oxide) Block Copolymers

Josué Juárez,[†] Sonia Goy-López,[†] Adriana Cambón,[†] Miguel A. Valdez,[‡] Pablo Taboada,*[,†] and Víctor Mosquera[†]

Grupo de Física de Coloides y Polímeros, Departamento de Física de la Materia Condensada, Facultad de Física, Universidad de Santiago de Compostela, E-15782, Santiago de Compostela, Spain, and Departamento de Investigación en Polímeros y Materiales y Departamento de Física, Universidad de Sonora, Resales y Transversal, 83000 Hermosillo Sonora, Mexico

Received: May 31, 2010; Revised Manuscript Received: July 30, 2010

The surface properties of poly(styrene oxide)-poly(ethylene oxide) block copolymers $EO_{12}SO_{10}$, $EO_{10}SO_{10}EO_{10}$, and $EO_{137}SO_{18}EO_{137}$ at the air−water (a/w) and chloroform−water (c/w) interfaces have been analyzed by Tracker drop tensiometry, Langmuir film balance, and atomic force microscopy (AFM). The kinetic adsorptions for the block copolymer solutions at both interfaces were determined by the pendant drop technique. At the a/w, the polymer adsorption is reduced as the polymer hydrophobicity increases. Measurements of the interfacial rheological behavior of the copolymers showed that the adsorption layers at the a/w interface manifest obvious solid-like properties in the whole accessible frequency range, whereas a viscous fluid-like behavior is displayed at the c/w interface. The differences observed in the monolayer isotherms obtained for the three copolymers arose from their different hydrophobic/hydrophilic block ratios and block lengths. In this regard, copolymer $EO_{137}SO_{18}EO_{137}$ displays an adsorption isotherm with the four classical regions (pancake, mushroom, brush, and condensed states), whereas for $EO_{12}SO_{10}$ and $EO_{10}SO_{10}EO_{10}$ copolymers, only two regions were observed. The topographic images of copolymer films were obtained by AFM in noncontact mode. Surface circular micelles are observed at the two surface transfer pressures studied. A micelle size decrease and an increase in monolayer thickness are observed with an increase in transfer pressure. At the largest transfer pressure used, elongated aggregates were observed. Aggregation numbers derived from AFM pictures were in fair agreement with those obtained for micelles in solution, and they became larger as the SO weight fraction increases at a certain deposition pressure. This can be a consequence of stronger attractive interactions between the SO blocks to avoid contact with the solvent.

Introduction

Amphiphilic block copolymers are an important class of materials that have attracted considerable attention because of their outstanding solution properties, such as their self-assembly in the presence of a selective solvent or surface.[1] In particular, the interfacial properties of block copolymers have received great interest in the last years due to their role in the industrial and biological fields.[2−4] The ability of block copolymers to adsorb at an interface, modulate their properties, and even to self-assemble into well-defined nanoscale structures in two dimensions has led to their use in colloidal stability and coating processes,[5] as steric barriers at solid surfaces in medical devices to avoid undesired protein adhesion,[6] as stabilizers of liquid interfaces of foams[7] and emulsions[8] to prevent coalescence and flocculation, as templates for the rational design of large-scale nanometer architectures in thin film configurations,[9,10] and as precursors for nanoporous materials.[11]

The self-assembly behavior and physicochemical properties of diblock and triblock copolymers of polyoxyalkylenes in solution have been extensively studied.[12−21] Variation of hydrophobic monomer, block length, and architecture allows close control of their physicochemical properties. The most familiar copolymers of this type are those whose hydrophobic block is formed by units of oxypropylene ($-OCH_2CH(CH_3)$, denoted as PO), 1,2-oxybutylene ($-OCH_2CH(C_2H_5)$, denoted as BO), and oxyphenylethylene ($-OCH_2CH-(C_6H_5)$), prepared from styrene oxide (denoted as SO). These copolymers are already commercially available from BASF,[22] Dow Chemical Co.,[23] and Goldschimdt AG,[24] respectively. Nevertheless, the two-dimensional properties and aggregation of these classes of copolymers at the air/aqueous interface has been only extensively reported for poly(ethylene oxide)-poly(propylene oxide)-poly(ethylene oxide) (EO-PO-EO) block copolymers or Pluronics, the X-star shaped EO-PO-EO copolymers known as Tetronic copolymers (from BASF),[27,28] and poly(butylene oxide)-poly(ethylene oxide) block copolymers (BO-EO).[29] Very little or no report has been put into fundamentally understanding the 2-D dimensional behavior of poly(ethyelene oxide)-poly(styrene oxide) block copolymers at interfaces. Therefore, fundamental studies of SO-based block copolymers performed at either the air/water or the air/organic solvent interface can provide valuable information on their interfacial phase behavior to further guide their possible use in different biomedical and coating applications. To fill this gap, in the present work, we studied the surface behavior and surface properties of three poly(ethylene oxide)-poly(styrene oxide) block copolymers, $EO_{12}SO_{10}$, $EO_{10}SO_{10}EO_{10}$, and $EO_{137}SO_{18}EO_{137}$ (where the subscripts denote the respective block length) by dynamic

* To whom correspondence should be addressed. E-mail: pablo.taboada@usc.es. Tel: 0034981563100, ext 14042. Fax: 0034981520676.
[†] Universidad de Santiago de Compostela.
[‡] Universidad de Sonora.

10.1021/jp1049777
Published on Web 08/26/2010

TABLE 1: Molecular Characteristics of the Copolymers

	M_n[a]/g mol^{-1} (NMR)	wt % S[a] (NMR)	M_w/M_n[a] (GPC)	M_w/g mol^{-1}	cmc[b]/g dm^{-3}	$\Gamma^b_{max}/10^{-6}$ mol m^{-2}
$EO_{12}SO_{10}$	1660	73	1.05	1760	0.006	0.97
$EO_{10}SO_{10}EO_{10}$	1980	55	1.06	2130	0.012	0.91
$EO_{137}SO_{18}EO_{137}$	14 200	15	1.06	15 100	0.017	0.40

[a] Estimated uncertainty: M_n to ±3%; wt % S to ±1%, M_w/M_n to ±0.01. M_w calculated from M_n and M_w/M_n. [b] Data from ref 32 at 15 °C.

interfacial tension, dilatational rheology, Langmuir monolayers, and atomic force microscopy (AFM). The self-assembling properties and solubilization capacity of these copolymers in bulk aqueous solution were analyzed in recent studies,[30−32] in which the existence of vesicular structures (polymersomes), elongated micelles, and spherical micelles in bulk solution was reported for copolymers $EO_{12}SO_{10}$, $EO_{10}SO_{10}EO_{10}$, and $EO_{137}SO_{18}EO_{137}$, respectively. These block copolymers display different volume-to-length ratios of the hydrophobic block, relative lengths of the polyoxyethylene blocks, and polymer architectures, which enable analyzing the influence of these parameters on the block copolymer surface behavior. In this regard, due to its lengthy EO blocks and higher hydrophilicity (as denoted by its larger cmc values; see Table 1), copolymer $EO_{137}SO_{18}EO_{137}$ displays a clear and complete adsorption isotherm in which the different conformational states of the polymer chains ("pancake", "mushroom", and "brush" conformations) are observed, with a significant viscous fluid behavior and a spherical morphology of its aggregates at the surface film. In contrast, the surface pressures of $EO_{12}SO_{10}$ and $EO_{10}SO_{10}EO_{10}$ monolayers were measurable at a significantly smaller area per molecule, and only two different clear regions can be distinguished in their isotherms as a consequence of the reduction of the fractional interfacial area occupied by EO segments. In addition, copolymer $EO_{12}SO_{10}$ displays a clear rheological solid-like behavior and its organization in elongated structures similar to a string of beads upon self-assembly at the air−water (a/w) interface. Finally, a comparison of the surface behavior of these copolymers with that observed for structurally related polystyrene-poly(ethylene oxide) (PS-PEO) block copolymers is also established.[33,34]

Experimental Section

Materials. Copolymers $EO_{12}SO_{10}$, $EO_{10}SO_{10}EO_{10}$, and $EO_{137}SO_{18}EO_{137}$ were prepared by sequential oxyanionic polymerization of styrene oxide, followed by ethylene oxide, starting from a monofunctional or difunctional initiator to form the hydrophobic block as described in detail by Crothers et al.[35] Table 1 shows the molecular characteristics, critical micellar concentrations (cmc), and surface excess concentrations (Γ_{max}) of the copolymers. Water was double-distilled and degassed before used.

Dynamic Interfacial Tension and Dilatational Rheology Measurements. Pendant bubble tensiometry was used to determine the dynamic interfacial tension and the interfacial dilatational rheology at two different interfaces: air−water (a/w) and chloroform−water (c/w) interfaces. The bubble was formed at the tip of a U-shaped stainless steel needle (0.5 mm inner diameter) immersed in an aqueous block copolymer solution of the desired concentration, with the air bubble upward for the (a/w) interface, whereas downward for the (c/w) interface. Measurements were carried out in a Track tensiometer equipment (I.T. Concept, France) adapted to determine surface tension values in real time with an accuracy of ±0.1 mN/m. Interfacial tension and interfacial rheology estimations are based on the digital profile of a drop image and the resolution of the Gauss−Laplace equation. Win Drop software (I.T. Concept, France) was used to obtain the surface tension values by means of the axisymetric drop shape analysis.

The aqueous solutions concentrations of the $EO_{12}SO_{10}$, $EO_{10}SO_{10}EO_{10}$, and $EO_{137}SO_{18}EO_{137}$ block copolymers were prepared at a constant concentration of 2×10^{-3} mg/mL, below their respective cmc values. At the (a/w) interface, the analysis of the interfacial tension (γ) measurements was followed in a relative short time (2000 s) after the bubble was formed, and the dilatational elastic storage (E') and loss (E'') moduli were determined after 2000 s using a frequency sweep of 3.14, 2.09, 1.04, 0.52, 0.31, 0.15, 0.078, and 0.039 rad/s. All measurements were carried out in a time interval of 400 s using a 10% amplitude oscillation of the maximum volume drop. On the other hand, experimental data of interfacial tension, γ, at the chloroform−water interface were followed for 180 s, and after this time, volume oscillations to the stabilized pendant drop volume were applied. Storage, E', and loss, E'', moduli were determined in this way.

Briefly, the analysis of the viscoelastic properties of the absorbed layer was performed by means of a sinusoidal deformation of the drop area, A, at a defined frequency, ω, produced by the Tracker tensiometer at a time t. Calculus of the complex dilatational elasticity modulus $E(\omega)$ is determined by

$$E(\omega) = -A\frac{dy}{dA} \tag{1}$$

This can also be defined as a complex function, which can be written as

$$E(\omega) = E'(\omega) + iE''(\omega) \tag{2}$$

where E' and E'' correspond to the storage and the loss moduli, respectively, by analogy with 3-D rheology. Assuming that the mechanical properties of the adsorbed layer follow a Maxwell model behavior, the storage and loss moduli can be written as follows

$$E'(\omega) = \sum_i E_{0i}\frac{(\omega/\omega_{0i})^2}{1 + (\omega/\omega_{0i})^2} \tag{3}$$

$$E''(\omega) = \sum_i E_{0i}\frac{(\omega/\omega_{0i})}{1 + (\omega/\omega_{0i})^2} \tag{4}$$

where E_{0i} and ω_{0i} ($\omega_{0i} = 2\pi/\tau_{0i}$) are the corresponding weights of the ith relaxation element to the total elasticity modulus E_0 and the characteristic relaxation frequency, respectively; τ_{0i} is the characteristic relaxation time of the Maxwell model.

Adsorption Isotherms. Surface−pressure isotherms were recorded for monolayers spread from chloroform solutions (1 mg/mL) onto a nanopure-quality water subphase in a Langmuir−Blodgett (LB) Teflon trough (model 611 from Nima Technologies Ltc., Coventry, U.K.). Volumes ranging from 10 to 50 μL of either $EO_{12}SO_{10}$, $EO_{10}SO_{10}EO_{10}$, or $EO_{137}SO_{18}EO_{137}$ block copolymer solutions (1 mg/mL) were spread dropwise on a Millipore water subphase with a Hamilton microsyringe. To ensure complete evaporation of the solvent, a time lag of

15 min was applied between the deposition of the copolymer and the beginning of compression of the spread molecules. After chloroform was evaporated, the surface area was compressed by Teflon barriers at a rate of 5 mm·min^{-1}. The temperature was kept constant at 25 °C with a water bath, and all experiments were carried out inside a dust-free glass box. The surface pressure was measured using a Platinum Wilhelmy plate located midway between the two barriers and oriented perpendicular to them, that is, parallel to the direction of the barrier movement. The complete system was operated on an antivibration table. On the other hand, Langmuir films were transferred onto a freshly cleaved mica substrate for imaging. After spreading the chloroform solutions, again at least 15 min was allowed for solvent evaporation. The barriers were then compressed to the targeted surface pressures, 5 and 11 mN/m, respectively, at a speed of 5 mm/min. Once the targeted surface pressure was reached and stable, the cleaved mica was lifted up at a speed of 1 mm/min. Film transfer ratios of 0.95−1.0 were obtained. The resulting films were individually stored at room temperature in clean closed vials.

Atomic Force Microscopy. AFM images of block copolymer monolayers were performed on freshly cleaved mica substrates. The measurements were performed in a JEOL instrument (model JSPM 4210) in noncontact mode using nitride cantilevers NSC15 from MicroMasch, U.S.A. (typical working frequency and spring constant of 325 kHz and 40 N/m, respectively). The AFM samples were dried in air or under a nitrogen flow when required. Control samples (freshly cleaved mica and buffer solution) were also investigated to exclude possible artifacts. Topography and phase-shift data were collected in the trace and retrace direction of the raster, respectively. The offset point was adapted accordingly to the roughness of the sample. The scan size was usually 500 nm (aspect ratio, 1 × 1), with a sample line of 256 points and a step size of 1 μm. The scan rate was tuned proportionally to the area scanned and kept within the 0.35−2 Hz range. Each sample was imaged several times at different locations on the substrate to ensure reproducibility. In all cases, the imaging of LB films was performed far from the edge of the glass substrate to minimize local effects caused by turbulent water flow at the boundary and meniscus effects during transfer. Diameters and heights of copolymer aggregates were determined by sectional analysis taken from the average of several sections through the aggregates.

Results and Discussion

Some molecular characteristics of the investigated block copolymers $EO_{12}SO_{10}$, $EO_{10}SO_{10}EO_{10}$, and $EO_{137}SO_{18}EO_{137}$ are shown in Table 1. As expected, the two triblock copolymers have higher cmc values than the diblock. This effect originates from the entropy of the triblock chains constrained by two block junctions in the core−shell interface of the micelle compared to the only constrain for the diblock chain. The copolymers were chosen to form two pairs, one with similar-sized hydrophobic SO blocks but different polymer architectures ($EO_{12}SO_{10}$ and $EO_{10}SO_{10}EO_{10}$) and the other with completely different hydrophilic EO block lengths ($EO_{10}SO_{10}EO_{10}$ and $EO_{137}SO_{18}EO_{137}$) and relatively similar hydrophobic SO blocks. This was made with the purpose of comparing the relative importance of the polymer architecture and the hydrophilic/hydrophobic block ratio on both polymer adsorption and surface rheological behavior at the air/water and chloroform/water interfaces. In previous studies, the polymer architecture, the volume-to-length ratios of the hydrophobic block, and the relative lengths of the polyoxyethylene blocks were found to be helpful in controlling the micellar morphology of these copolymers.[32,36] In particular, the coexistence of spherical micelles with vesicles (polymersomes) was observed for copolymer $EO_{12}SO_{10}$; in contrast, the formation of elongated and spherical micelles for copolymers $EO_{10}SO_{10}EO_{10}$ and $EO_{137}SO_{18}EO_{137}$, respectively, was found upon their self-assembly.[32]

Dynamic Surface Tension

The surface tension of the copolymers as a function of time for copolymers $EO_{12}SO_{10}$, $EO_{10}SO_{10}EO_{10}$, and $EO_{137}SO_{18}EO_{137}$ at a concentration of 2×10^{-3} mg/mL is illustrated in Figure 1. The low concentration used allowed us to work in relative short time intervals to achieve a quasi-stabilization at both air−water (a/w) and chloroform−water (c/w) interfaces, and it also avoided complications associated with chloroform evaporation. Nevertheless, the true equilibrium state was not attained for any of the copolymers within 1 h of adsorption because the surface tension still continued to decrease slightly with time.

Usually, the dynamic surface tension curves can be divided in three stages: At relative low polymer concentrations, a quasi-plateau or a very slow decrease of $\gamma(t)$ can be distinguished at short times, which corresponds to the so-called lag phase. The postlag phase stage of the polymer adsorption process is characterized by a rapid decrease of $\gamma(t)$, which is associated with the increased number of copolymer molecules adsorbed at the interface and to conformational changes of the polymer chains adsorbed at the interface. In this stage, lateral interactions between adsorbed macromolecules stabilize the monolayer and the adsorption of the molecules continues to be controlled by macromolecule diffusion without appreciable desorption. Finally, the postlag stage transforms to the final (or last) adsorption phase, which is recognized by some slowing down of the interfacial tension decrease rate. At this stage, the dense adsorption layer exerts electrostatic and steric repulsion toward newly arrived macromolecules and hinders their adsorption at the interface.[37,38] Nevertheless, despite their hindrance, the interfacial tension tends to continuously decrease during this stage because of the high surface activity of the block copolymers.

In our case, initial γ values of 66.4, 64.5, and 57.1 mN/m were observed for copolymers $EO_{12}SO_{10}$, $EO_{10}SO_{10}EO_{10}$, and $EO_{137}SO_{18}EO_{137}$, respectively (see Figure 1a), as a consequence of the very rapid migration of copolymer molecules from the bulk solution to the a/w interface, giving rise to a block copolymer monolayer. For copolymer $EO_{137}SO_{18}EO_{137}$, we assume that the observed experimental data corresponds to the last part of the postlag time stage and the final polymeric adsorption stage. In contrast, for both $EO_{12}SO_{10}$ and $EO_{10}SO_{10}EO_{10}$, the curve profile can be divided in three stages after an almost instantaneous surface tension decrease. We will keep the same nomenclature (lag phase, postlag phase, and final adsorption phase) to define the regions in these curves despite that their true meaning corresponds to values departing from the surface tension value of pure water. For copolymer $EO_{12}SO_{10}$, the lag phase is longer, and the decrease of γ in the postlag phase is faster than for copolymer $EO_{10}SO_{10}EO_{10}$, probably as a result of its greater hydrophobicity. Similarly, a much larger EO block for copolymer $EO_{137}SO_{18}EO_{137}$ if compared to $EO_{10}SO_{10}EO_{10}$ results in a larger surface tension decrease in the very early stages of the adsorption process, which we attribute to an increased repulsion between the EO chains, giving rise to an enhancement of the surface pressure.

If the adsorption kinetics is controlled by the diffusion of macromolecules from the bulk solution to the interface, for

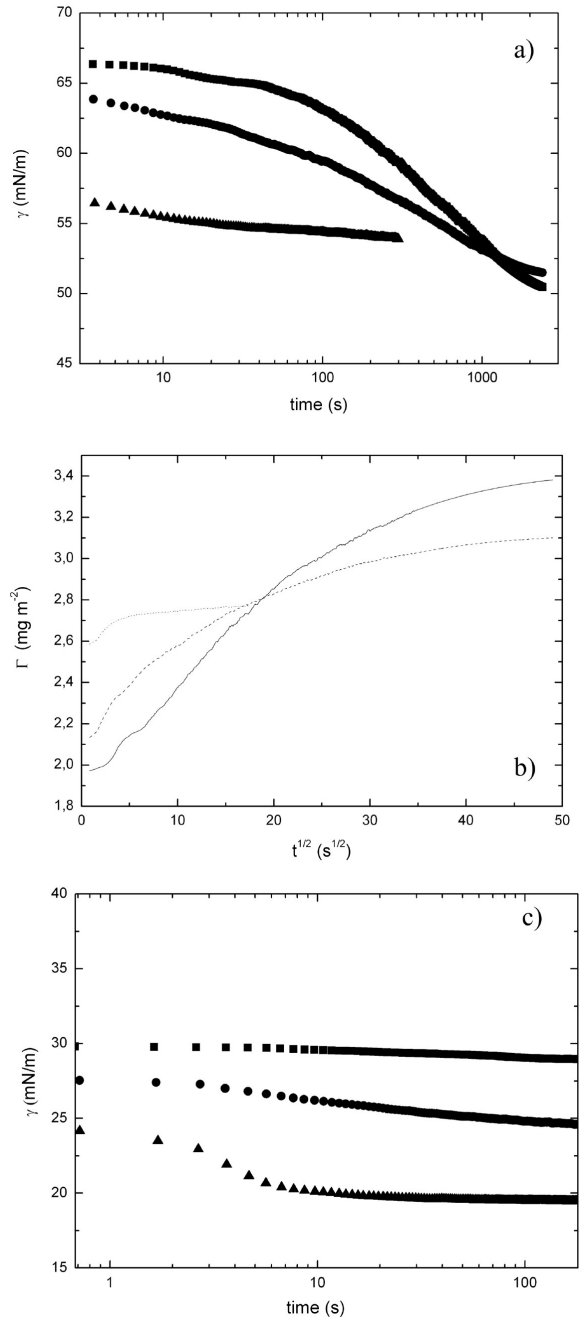

Figure 1. (a) Variation of surface tension, γ, with time at the air−water interface for copolymers (○) $EO_{12}SO_{10}$, (●) $EO_{10}SO_{10}EO_{10}$, and (▲) $EO_{137}SO_{18}EO_{137}$. (b) Variation of surface concentration, Γ, with time at the air−water interface for copolymers (—) $EO_{12}SO_{10}$, (•••••) $EO_{10}SO_{10}EO_{10}$, and (----) $EO_{137}SO_{18}EO_{137}$. (c) Variation of surface tension, γ, with time at the chloroform−water interface for copolymers (■) $EO_{12}SO_{10}$, (●) $EO_{10}SO_{10}EO_{10}$, and (▲) $EO_{137}SO_{18}EO_{137}$.

strongly adsorbing species, this is described by the Ward−Torday equation,[39] $\Gamma(t) = 2c_0(Dt/\pi)^{1/2}$, where c_0 is the polymer concentration and D the bulk diffusion coefficient. A diffusion-controlled adsorption mechanism will be expected to give a straight line in a plot of Γ versus $t^{1/2}$. In these experiments, the direct connection between Γ and t cannot be measured, but a measured value of Π may be converted to a relative value of Γ by using the scaling expression $\Pi \sim \Gamma^y$ and the calculated value of y from the adsorption isotherm experiments (see below). Figure 1b shows such a plot for the three copolymers. The proportionally constant was set equal to 1 $(m^2 \cdot mg^{-2})^y$ $mN \cdot m^{-1}$, which implies that the surface pressure is set to 1 $mN \cdot m^{-1}$ at a surface concentration of 1 $mg \cdot m^{-2}$. This value is typical for that found for many polymers.[40,41] From this figure, it can be observed that the expected straight line is quite steep at very short times, but a curvature in the plot is present at larger times. This may indicate that the diffusion-controlled adsorption process only operates during the first few seconds of the process and, then, is more likely controlled by a slow configurational change and reorientation of the polymer molecules at the surface. At this respect, a bimodal type of adsorption kinetics of Pluronic block copolymers, including initial diffusion, followed by an internal reorganization of the structure, was discussed recently.[42]

On the other hand, there was no measurable effect on the interfacial tension at the chloroform/water interface (c/w) due to the adsorption of copolymer $EO_{12}SO_{10}$ (see Figure 1c). This behavior might originate from the small amount of copolymer at the interface due to the slow diffusion of their chains to the interface in combination with a low bulk concentration. The slow diffusion can be associated with the fact that chloroform is a good solvent for both EO and SO blocks, and provided that copolymer $EO_{12}SO_{10}$ is very hydrophobic, the copolymer chains prefer being in the organic phase. This can be additionally corroborated with the progressively faster decrease observed in surface tension values at short times for the increasingly hydrophilic copolymers $EO_{10}SO_{10}EO_{10}$ and $EO_{137}SO_{18}EO_{137}$. This faster decrease also enables the development of a postlag phase for these copolymers. In fact, for the latter copolymer, the curve profile is very similar to that obtained at the a/w interface, although the absolute γ values are quite different as a result of the depression of interfacial tension due to the presence of chloroform.

Dilatational Rheology. Analysis of the frequency dependence of the dilational moduli allows us to get detailed information about the type of interactions existing between polymer chains located at the interface. Figure 2 shows the frequency dependence of storage, E', and loss, E'', dilatational moduli in semilogarithmic plots for the adsorbed layers of block copolymers $EO_{12}SO_{10}$, $EO_{10}SO_{10}EO_{10}$, and $EO_{137}SO_{18}EO_{137}$ at both the a/w and the c/w interfaces. The frequency dependence of both E' and E'' is generally believed to be caused by relaxation processes at the interface.[43,44] A satisfactory rheological description of the adsorption layers of macromolecules may be done by considering several characteristic relaxation frequencies (or relaxation times, τ), which are related to the adsorption−desorption exchange of polymer chains between the surface and the adjacent subinterface layer during dilatational perturbation and molecular reconformation of the adsorbed layer.[38] In this way, the frequency dependences of storage (E') and loss (E'') moduli were fitted to the sum of two Maxwell elements

$$E'(\omega) = E_{01}\frac{(\omega/\omega_{01})^2}{1 + (\omega/\omega_{01})^2} + E_{02}\frac{(\omega/\omega_{02})^2}{1 + (\omega/\omega_{02})^2} \quad (5)$$

$$E''(\omega) = E_{01}\frac{(\omega/\omega_{01})}{1 + (\omega/\omega_{01})^2} + E_{02}\frac{(\omega/\omega_{02})}{1 + (\omega/\omega_{02})^2} \quad (6)$$

where E' is related to lateral interactions between polymer segments at the interface plane and is relevant for the rigidity of interfacial film, whereas E'' is related to molecular reorga-

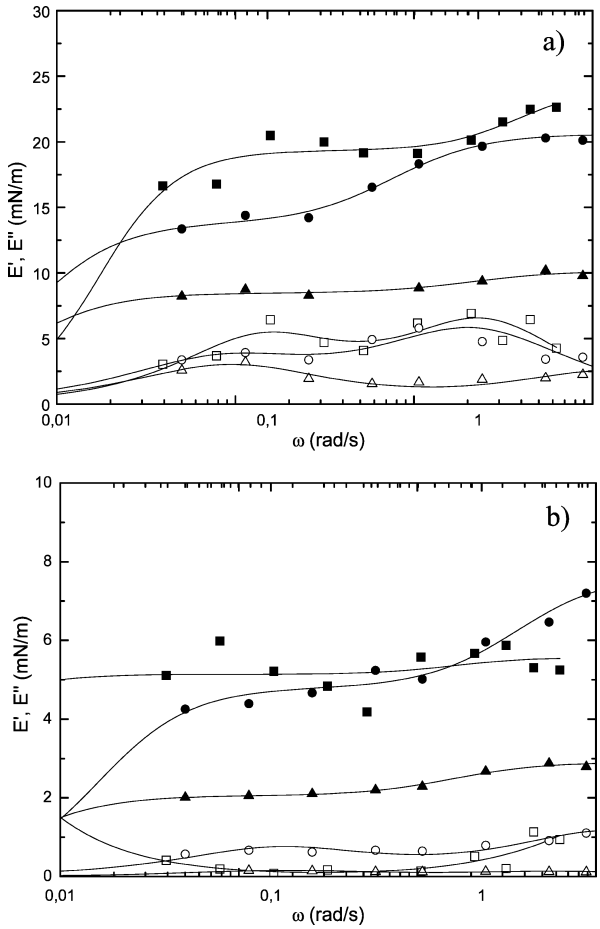

Figure 2. Storage, E' (closed symbols), and loss, E'' (open symbols), moduli as a function of frequency for copolymers (■) $EO_{12}SO_{10}$, (●) $EO_{10}SO_{10}EO_{10}$, and (▲) $EO_{137}SO_{18}EO_{137}$ at the (a) air−water and (b) chloroform−water interfaces.

nization processes, such as the expulsion of polymer chains from the interface upon compression and the interactions of polymer molecules with adjacent liquid molecules.[45] The first characteristic relaxation time, τ_{01}, is usually attributed to the adsorption−desorption exhange of molecules and polymer segments between the surface and the adjacent subsurface layer during dilatational perturbations of the interface; τ_{02} corresponds to slower reconformations of the adsorbed macromolecules inside the adsorption layer.

At the a/w interface, the adsorption layers manifest obvious solid-like properties in the whole accessible frequency range ($\omega = 0.039-3.14$ rad/s) with $E' > E''$, following the sequence $EO_{12}SO_{10} > EO_{10}SO_{10}EO_{10} > EO_{137}SO_{18}EO_{137}$, and with a low significance of dissipative processes during dilational deformations of these block copolymer layers. These values suggest a more fluid layer in the case of copolymer $EO_{137}SO_{18}EO_{137}$ as a consequence of its lower hydrophobicity (larger cmc) due to the presence of extended oxyethyelene chains. In contrast, copolymer $EO_{12}SO_{10}$ shows the most important solid-like behavior, which involves the formation of tightly packed copolymer chains at the interface to avoid contact between hydrophobic blocks and water. Molar copolymer concentration differences slightly affect the final dilatational moduli values (not shown). We also point out that the storage modulus E' slightly, but continuously, increases with frequency, whereas

TABLE 2: Characteristic Relaxation Times, τ_{01} and τ_{02}, and Characteristic Dilatational Moduli Weights of Each Relaxation Mode, E_{01} and E_{02}, of Copolymers $EO_{12}SO_{10}$, $EO_{10}SO_{10}EO_{10}$, and $EO_{137}SO_{18}EO_{137}$ at the Air−Water and Chloroform−Water Interfaces

	$\tau_{01}{}^a$/s	$\tau_{02}{}^a$/s	$E_{01}{}^a$/mN m^{-1}	$E_{02}{}^a$/mN m^{-1}
			air−water	
$EO_{12}SO_{10}$	3.2	48.0	4.9	19.3
$EO_{10}SO_{10}EO_{10}$	10.0	75.0	6.8	13.8
$EO_{137}SO_{18}EO_{137}$	6.6	81.1	1.7	8.5
			chloroform−water	
$EO_{12}SO_{10}$	56.3	5.7	5.6	0.3
$EO_{10}SO_{10}EO_{10}$	51.1	8.7	4.8	2.4
$EO_{137}SO_{18}EO_{137}$	75.9	7.1	2.1	0.9

[a] Estimated uncertainty: τ_{01}, τ_{01} to ±1%; E_{01}, E_{02} to ±0.01.

the loss modulus E'' is close to zero, in particular, for copolymer $EO_{137}SO_{18}EO_{137}$. This involves that the exchange processes between the surface layer and bulk solution are relatively important, and as the frequency becomes larger, the system does not have enough time to reach the equilibrium and returns most of the stored energy. Thus, the elasticity becomes larger. Otherwise, the time is not long enough to modify the interfacial concentration gradient through different relaxation processes at high oscillation frequencies. As a result, the dilational moduli increase with increasing oscillation frequencies. On the other hand, τ_{01} and τ_{02} values at the a/w interface for copolymers $EO_{12}SO_{10}$, $EO_{10}SO_{10}EO_{10}$, and $EO_{137}SO_{18}EO_{137}$ derived from the Maxwell modelization are displayed in Table 2. In particular, copolymer $EO_{12}SO_{10}$ possesses the shortest relaxation times τ_{01} and τ_{02}, which indicates the fastest adsorption−desorption exchange and a rapid molecular reorganization of the polymer chains adsorbed at the interface probably as a result of its lower molecular weight, diblock architecture, and larger hydrophobicity.

At the c/w interface, the profiles of the dilational rheology curves display similar behavior as at the a/w interface, although the absolute values of E_{01} and E_{02} are sensibly lower, particularly the former ones. For this reason, it seems that a viscous fluid-like behavior is displayed by the three copolymers at the c/w interface. Moreover, the values obtained for the characteristic relaxation times τ_{01} and intrinsic elasticity E_{01} decreased, whereas τ_{02} and E_{02} increased if compared to those obtained at the a/w interface; that is, a reverse behavior is found. This may point out that the copolymers have been weakly adsorbed at the c/w interface because copolymer molecules tend to stay at the chloroform phase because chloroform is a good solvent for both hydrophilic and hydrophobic copolymer blocks, as previously mentioned.

Adsorption Isotherms. Monolayers of $EO_{12}SO_{10}$, $EO_{10}SO_{10}EO_{10}$, and $EO_{137}SO_{18}EO_{137}$ block copolymers were spread on a Langmuir−Blodgett trough balance, and the $\Pi-A$ isotherms were obtained (see Figure 3a). In the present study, copolymer $EO_{137}SO_{18}EO_{137}$ displays a classical isotherm pattern divided in four regions. When no pressure is exerted, copolymer chains should lie on the interface with a flat ("pancake") conformation parallel to the surface plane.[46,47] The area occupied is a function of the number of SO and EO units. Roughly, the maximum cross-sectional area occupied by an EO unit is 13−16.5 Å^2[25] and that occupied by an SO unit can be taken similar as that of a PS unit (50 Å^2).[48] Once hydrated, the areas of EO and SO units increase by 8.5 Å^2 (a water molecule). Once the compression of the $EO_{137}SO_{18}EO_{137}$ monolayer began, the surface pressure gradually increased until reaching an area under compression of 7350 Å^2/molecule. This value agrees with the

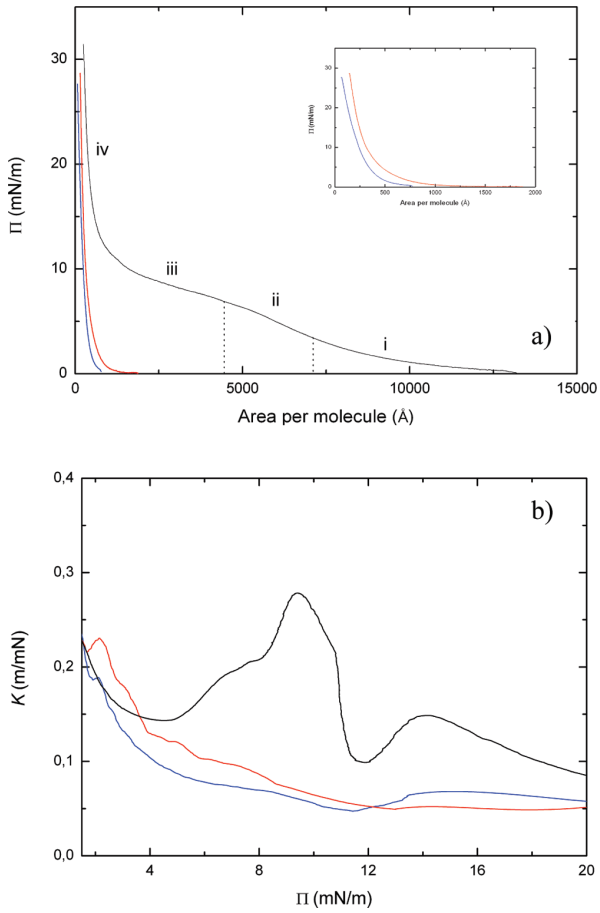

Figure 3. (a) Surface pressure, Π, isotherms for spread monolayers of copolymers (blue line) $EO_{12}SO_{10}$, (red line) $EO_{10}SO_{10}EO_{10}$, and (black line) $EO_{137}SO_{18}EO_{137}$. The inset is an enlargement of the isotherm corresconding to copolymers $EO_{12}SO_{10}$ and $EO_{10}SO_{10}EO_{10}$. (b) Compressibility, K, against surface pressure of spread monolayers of copolymers (red line) $EO_{12}SO_{10}$, (blue line) $EO_{10}SO_{10}EO_{10}$, and (black line) $EO_{137}SO_{18}EO_{137}$.

sum of the maximum transverse area occupied by all EO and SO units of copolymer $EO_{137}SO_{18}EO_{137}$. As the pressure increased, the hydrophobic SO blocks, initially on the air−water interface, were lifted away. The surface pressure at which this phenomenon occurs is usually very low owing to the weakness of the interaction between the aqueous medium and the hydrophobic groups[49] (Figure 3a, region ii). The 4800 Å^2/molecule area corresponds to an arrangement of the molecules that leads to an occupied area 35% lower than the original value. From 6.1 to 9.8 mN/m, another region of a lower slope appears due to a change in the copolymer conformation, which enables the penetration of the hydrophilic EO chains into the subphase: the copolymer adopts a "mushroom" conformation (Figure 3a, region iii). In this region, there is a slight increase in the surface pressure as the surface area is decreased, indicating that a true first-order transition does not occur. This "pseudoplateau" is interpreted as a rearrangement of the SO coils into "loops" within the monolayer regime and the immersion of more EO units in the aqueous subphase. The end of the pseudoplateau region correponds to an area of ∼1800 Å^2/molecule, which indicates that the vast majority of EO units is in the subphase. Isotherms of PS-PEO copolymers of different PEO lengths showed that the PEO block length largely influences in the character of this transition.[50] Further compression causes a rapid increase in surface pressure. Block copolymer molecules gradually become closer, the mobility of the blocks becomes restricted because of both space limitations and the increase in lateral interactions, and the copolymer molecules reorganize into a "brush conformation" (Figure 3a, region iv).[51−53] In the subphase, the EO chains entangle with neighboring copolymer molecules, whereas at the interface, the SO blocks can form loops and even are partially solubilized in the aqueous EO layer. If the area is further restricted, both hydrophilic and hydrophobic blocks become stretched (condensed state).[25] The extrapolation of the experimental data above this pressure indicates that the area occupied per molecule at the condensed state (A_L) is 276 Å^2.

In contrast, copolymers $EO_{12}SO_{10}$ and $EO_{10}SO_{10}EO_{10}$ exerted a relatively low resistance to compression at the largest and medium areas per molecule of their isotherms (see Figure 3a), as expected from their low molecular weight, shorter SO and EO segments, and fair aqueous solubility at low concentrations. The surface pressures of $EO_{12}SO_{10}$ and $EO_{10}SO_{10}EO_{10}$ monolayers were measurable at significantly smaller areas per molecule than for the $EO_{137}SO_{18}EO_{137}$ monolayer. Only two well-defined regions can be distinguished in their isotherms. When the area per molecule is large, the surface pressure slowly increases as the area decreases. Above 1 and 2 mN/m for $EO_{12}SO_{10}$ and $EO_{10}SO_{10}EO_{10}$, respectively, a very slight pseudoplateau might be depicted. This behavior arises from the increasing weight fraction of SO blocks at the interface, which reduces the fractional interfacial area occupied by EO segments. Above 3 and 5 mN/m, respectively, a sharp rise in the surface pressure occurs. This is consistent with a significant contribution from the SO domains, showing no plateau or pseudoplateau at 10 mN/m. In fact, the monolayers of both block copolymers can be considered as condensed-like films in comparison with that obtained for $EO_{137}SO_{18}EO_{137}$, which behaves as an expanded-like film.[53] The area occupied per molecule at the condensed state (A_L) is 167 Å^2 for $E_{12}S_{10}$ and 135 Å^2 for $EO_{10}SO_{10}EO_{10}$, respectively. These values are in fair agreement with the areas predicted from the number of SO units of $EO_{12}SO_{10}$ and $EO_{10}SO_{10}EO_{10}$, respectively, and support the fact that the interface is occupied only by SO blocks. This is also confirmed by the fact that, despite that the isotherms of the copolymers clearly differ in their shape at low surface pressures, they merge, becoming almost superimposable at large surface pressures.

On the other hand, the compressibility modulus ($K = -1/A \times (dA/d\pi)$) displays local maxima for every phase transition in the copolymers' monolayers. As shown in Figure 3b, several phase transitions located at ∼6.5, ∼9.5, and ∼14.0 m/Nm were found for copolymer $EO_{137}SO_{18}EO_{137}$. Those at ∼6.5 and ∼9.5 m/Nm are PEO-related phase transitions, which are a consequence of the penetration of PEO chains in the subphase, leaving the air−water interface to form a swollen three-dimensional structure in the aqueous phase (in particular, at ∼9.5 m/mN). After the latter peak, the subsequent minimum and additional maximum found at larger surface pressures is a result of the increasing repulsion between SO segments in the top layer and PEO segments in the subphase. This facilitates the desorption of SO blocks due to enhanced repulsions within the layer and the formation of loops and tails, which leads to a faster redistribution between the upper and lower regions of the layer. On the other hand, only slight maxima at ∼2.0 m/mN and a shoulder at ca. 6.0 m/mN are found for copolymers $EO_{12}SO_{10}$ and $EO_{10}SO_{10}EO_{10}$. The maximum can be related to a PEO phase transition, whereas the shoulder at 6.5 m/mN can resemble

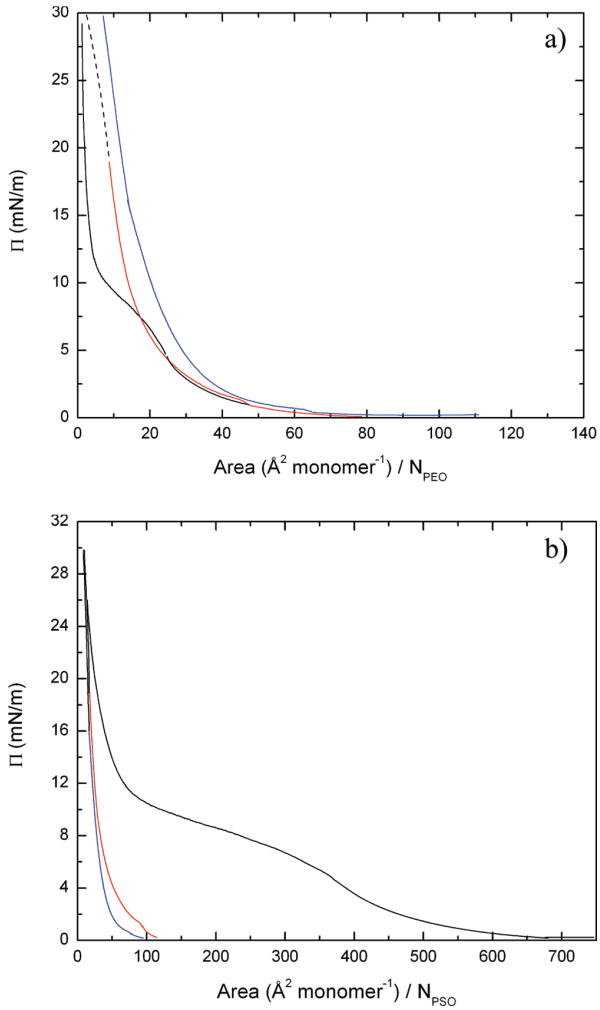

Figure 4. Surface pressure isotherms plotted with respect to (a) the average area per EO repeat unit and (b) the average area per SO repeat unit for copolymers (blue line) $EO_{12}SO_{10}$, (red line) $EO_{10}SO_{10}EO_{10}$, and (black line) $EO_{137}SO_{18}EO_{137}$.

some kind of structural rearrangement of SO blocks before complete film condensation. The absence of the transition at 9.5 m/Nm for both $EO_{12}SO_{10}$ and $EO_{10}SO_{10}EO_{10}$ is a consequence of their small PEO block length.

The effect of the polymer structure can be easily visualized by plotting the surface pressure as a function of the average surface area per monomer. Isotherms plotted with the molecular area normalized with respect to the number of EO and SO segments are shown in Figure 4a,b. Figure 4a demonstrates that all of the isotherms of the three copolymers fall on a single curve for surface areas corresponding to the semidilute regime. This indicates that the isotherm in this regime is mainly dependent on the EO block length. Beyond the pseudoplateau, all copolymers appear to be affected by the SO/EO ratio. In the semidilute regime, the Flory coefficient of the system can be obtained from the des Cloizeaux equation,[54] which describes the relationship between the surface pressure and the surface concentration (Γ) of a polymer by

$$\Pi = CA^{-y} = K\Gamma^{y} \text{ with } y = d\nu/(d\nu - 1) \qquad (7)$$

where C and K are proportionality constants, A is the molecular area, y is the scaling exponent, d is the geometrical dimension, and ν is the Flory coefficient used to express the radius of gyration in terms of molecular weight ($R_g \approx M^{\nu}$) and is a measure of the solvent quality.[55] For chains in good solvent conditions, the exponent ν is theoretically predicted to be 0.75 for a 2D self-avoiding walk and 0.6 for a 3D self-avoiding walk. Consequently, the theoretical exponent for the scaling of the surface pressure with the area per molecule is $y = 3$ for the 2D semidilute regime and $y = 2.25$ for the 3D semidilute regime. Plotting the variation of the surface pressure Π versus the inverse of the area per molecules $1/A$ on a double-logarithmic scale for the three different copolymers in the intermediate region between the dilute regime and the plateau, we have obtained y exponents of 2.28, 2.37, and 2.54 for $EO_{12}SO_{10}$, $EO_{10}SO_{10}EO_{10}$, and $EO_{137}SO_{18}EO_{137}$, respectively. This indicates that the chain conformation is almost a 3D interpenetrated layer for copolymers $EO_{12}SO_{10}$ and $EO_{10}SO_{10}EO_{10}$ and a intermediate between a purely 2D entangled layer and a 3D interpenetrated layer for copolymer $EO_{137}SO_{18}EO_{137}$, as also observed for different PSO-EO block copolymers.[56] From Figure 4b, the isotherms superimposed in the concentrated regime for the three block copolymers, which denotes that the isotherm shape is now determined by the SO chain length and SO/EO molar ratio.

Summarizing, if the SO block is short compared with the EO block, as in the case of copolymer $EO_{137}SO_{18}EO_{137}$, its role is limited to anchoring the EO chains at the air−water interface and it has no influence on the surface pressure isotherm or on the segment profile of the EO chains normal to the interface. But, as the SO block is repulsive to the EO block, as in the case of $EO_{12}SO_{10}$ and $EO_{10}SO_{10}EO_{10}$, this should modify the attractive nature of the interface for the EO and, therefore, the expected concentration profile for the EO chains, as also occurred for PS-EO and EO-PS-EO copolymers[34,47,49,57,58] and Pluronics[26] and Tetronics (four star-shaped ethylene oxide-propylene oxide block copolymers).[28] The balance between these opposite interactions will depend on the copolymer surface density, the SO block length, and the temperature.

AFM. Besides the isotherm data, detailed insight into the organization and morphology of the Langmuir−Blodgett monolayers should rely on the images of their corresponding films by AFM. We compare the morphologies of the three samples deposited at different pressures. Figure 5 shows AFM images of the block copolymer films on freshly cleaved mica obtained at 5 and 11 mN/m surface pressures. Aggregation was observed for all the copolymers investigated. The surface micelle assembly can take place (i) during the solvent evaporation step or (ii) during the LB tranfer. Nevertheless, dynamic light-scattering measurements (DLS, data not shown) of the three copolymers in chloroform did not show any evidence of micelle formation, which implies that the formation of EO-SO surface features in LB films are the result of spontaneous copolymer aggregation at the air−water interface rather than a transfer of micelles formed in the spreading solution.[59]

At a surface pressure of 5 mN/m, the AFM images of the block copolymers $EO_{12}SO_{10}$, $EO_{10}SO_{10}EO_{10}$, and $EO_{137}SO_{18}EO_{137}$ show the presence of spherical aggregates with diameters of 6.7 ± 0.4, 7.9 ± 0.2, and 9.1 ± 0.3 nm, respectively (Figure 5a,c,e; see Figure S1 in the Supporting Information for size distributions). The average height of the aggregates obtained at this surface pressure is 2.03 ± 0.01, 1.25 ± 0.01, and 1.52 ± 0.01 nm for $EO_{12}SO_{10}$, $EO_{10}SO_{10}EO_{10}$, and $EO_{137}SO_{18}EO_{137}$, respectively, so they can be identified as dots or circular micelles (see Figure 6 as an example and Figure S2 in the Supporting Informationfor height distributions). The difference in dot heights for the three copolymers is a consequence of the

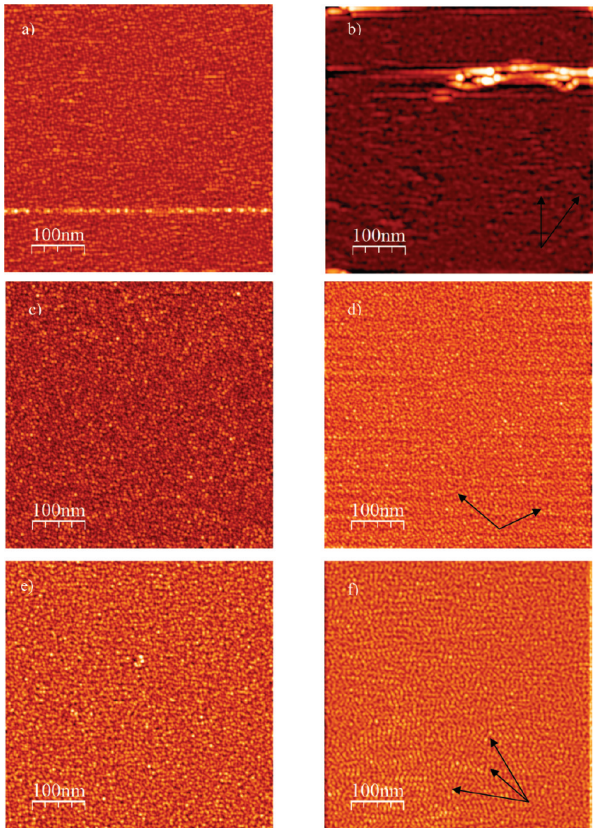

Figure 5. Typical AFM images of Langmuir−Blodgett films of the copolymers $EO_{12}SO_{10}$ (a, b), $EO_{137}SO_{18}EO_{137}$ (c, d), and $EO_{10}SO_{10}EO_{10}$ (e, f) at transfer surface pressures of 5 and 11 mN/m, respectively. Arrows denote some elongated polymer structures.

copolymer hydrophobicity and SO/EO ratio: Assuming that the length of an SO unit is 0.18 nm per chain unit,[60] the average length of the fully stretched SO_{10} and SO_{18} blocks would be 1.8 and 3.3 nm. As the central block is looped in the aggregate core in the case of the triblock copolymers, the effective length would be 0.9 and 1.7 nm, respectively. On comparison with the experimental values, the SO blocks of copolymers $EO_{12}SO_{10}$ and $EO_{10}SO_{10}EO_{10}$ display a more extended perpendicular configuration on the water surface ("brush" state) than for copolymer $EO_{137}SO_{18}EO_{137}$, for which a "mushroom" conformation is predominant, confirming the surface−pressure isotherm data.

When the transfer surface pressure rises to 11 mN/m, the height of the $EO_{12}SO_{10}$ layer largely increases up to 5.2 ± 0.01 nm, which suggests the formation of multilayers at the a/w interface. Formation of large aggregates is also observed as a consequence of micelle association. Part of these supra-aggregates display an elongated morphology, which seems to be composed of a string of beads, the beads being circular micelles in contact each other. Similar necklace-network strctures have been observed, for example, in Langmuir−Blodgett films of mixed PS and PS-P2VP (P2VP, poly(2-vinylpyridine)).[61] This large-scale aggregation pattern is observed, suggesting the possibility of a dewetting process, although we cannot neglect the possible influence of particle aggregation upon film drying. In the case of copolymers $EO_{10}SO_{10}EO_{10}$ and $EO_{137}SO_{18}EO_{137}$, the increase in film thickness increase upon transfer at 11 mN/m is less pronounced, with mean height values of 1.95 ± 0.01 and 3.90 ± 0.02 nm, respectively. These values point out that the SO blocks of both copolymers are in a full extended perpendicular configuration (brush state) at this transfer surface pressure. The average size of the aggregates is 7.2 ± 0.1, 5.6 ± 0.3, and 7.3 ± 0.1 nm for $EO_{12}SO_{10}$, $EO_{10}SO_{10}EO_{10}$, and $EO_{137}SO_{18}EO_{137}$, respectively, at this transfer pressure. Comparing these values with those measured at a surface pressure of 5 mN/m, we can assume that a compaction of the aggregates formed by copolymers $EO_{10}SO_{10}EO_{10}$ and $EO_{137}SO_{18}EO_{137}$ has occurred in order to accommodate all copolymer chains at the interface. Moreover, formation of elongated micelles is also observed at 11 mN/m for the former copolymers (see Figure 5d,f). In fact, elongated micelles in bulk solution have been previously found for copolymer $EO_{10}SO_{10}EO_{10}$, whereas for $EO_{137}SO_{18}EO_{137}$, only spherical micelles were detected.[32]

In contrast to what was found by Deveraux et al.[60] and Moffitt et al.[33] for PS-EO block copolymers, the deposition pressure influences the structure of the resulting copolymer surface aggregates. Furthermore, PS-EO copolymers show additional surface structures other than dots (elongated structures, lamellae...) when the EO weight contents are lower than 12%;[33] however, for SO-based copolymers, elongated structures are

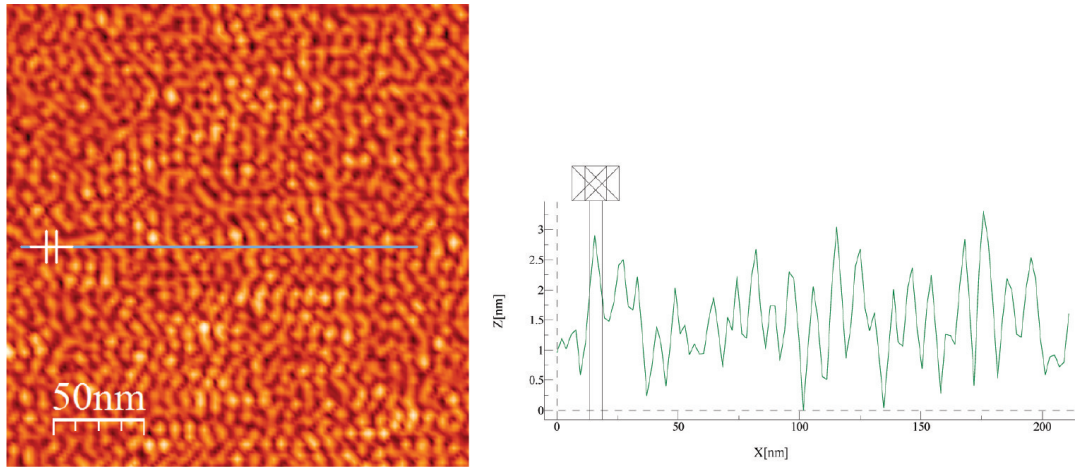

Figure 6. Determination of micelle size for copolymer $EO_{137}SO_{18}EO_{137}$ at a surface pressure of 11 mN/m through sectional analysis. *X* represents the aggregate diameter and *Z* the aggregate height.

TABLE 3: Aggregate Number, N_{agg}, for Surface Micelles of Copolymers $EO_{12}SO_{10}$, $EO_{10}SO_{10}EO_{10}$, and $EO_{137}SO_{18}EO_{137}$

	N_{agg}	
	5 mN/m	11 mN/m
$EO_{12}SO_{10}$	40	144
$EO_{10}SO_{10}EO_{10}$	29	68
$EO_{137}SO_{18}EO_{137}$	10	36

already observed at an EO content of 27% for copolymer $EO_{12}SO_{10}$. The lower glass transition temperature of SO (~40 °C) compared with that of a PS (~100 °C), which is thought to be associated with plasticization of water molecules associated with the ether oxygen of the SO units,[12] might involve a larger mobility of SO blocks in the aggregates, thus enabling a certain restructurization of the aggregates consisting of lateral interactions between SO segments of adjacent circular aggregates.

The aggregation number (N_{agg}) of the copolymer aggregates was evaluated from the AFM images in conjuction with the $\Pi-A$ isotherms. N_{agg} was determined by dividing the number of micelles per unit area by the molecular area from the $\Pi-A$ isotherms at the corresponding transfer pressure. The height profile of the micelles was generally found to be hemispheric with the condition used to scan the samples. From Table 3, it can be seen that N_{agg} increases with the increase of the SO weight fraction at a certain deposition pressure, which can be a consequence of stronger attractive interactions between the SO blocks to avoid contact with the solvent. Values of N_{agg} are in fair agreement with those obtained for micelles in solution.[32] The lower aggregation number of copolymer $EO_{137}SO_{18}EO_{137}$ may arise from the steric repulsion of EO chains at the interface due to the longer PEO blocks if compared to the other block copolymer. Moreover, N_{agg} for the corresponding samples tends to increase with the increase of the deposition pressure because further compression will provide enough energy to overcome repulsion between EO segments and form larger aggregates.

Conclusions

In summary, the spontaneous adsorption of block copolymers $EO_{12}SO_{10}$, $EO_{10}SO_{10}EO_{10}$, and $EO_{137}SO_{18}EO_{137}$ at the air−water interface is observed to be slowed down when the hydrophobicity of the molecule is increased. In contrast, at the chloroform−water interface, no measurable effect is observed for copolymer $EO_{12}SO_{10}$ due to the slow diffusion of its chains to the interface in combination with a low bulk concentration, the slow diffusion associated with the fact that chloroform is a good solvent for both EO and SO blocks. In addition, the adsorption layers at the a/w interface manifest obvious solid-like properties in the whole accessible frequency range with $E' > E''$, following the sequence $EO_{12}SO_{10} > EO_{10}SO_{10}EO_{10} > EO_{137}SO_{18}EO_{137}$, and with a low significance of dissipative processes. In contrast, a viscous fluid-like behavior is displayed by the three copolymers at the c/w interface. Copolymer $EO_{137}SO_{18}EO_{137}$ displays an adsorption isotherm with the four classical regions representing pancake, mushroom, brush, and condensed states, with the presence of a pseudoplateau attributed to the pancake-to-brush transition as EO chains submerge into the aqueous subphase. On the other hand, for $EO_{12}SO_{10}$ and $EO_{10}SO_{10}EO_{10}$ copolymers, only two regions are observed in their adsorption isotherms as a consequence of their low molecular weight, short SO and EO block lengths, and much larger SO/EO ratio. The latter involves the disappearance of the pseudoplateau region due to the decrease in the fractional interfacial area occupied by EO segments. Finally, surface circular micelles are observed by AFM pictures at two surface transfer pressures. A decrease in micelle size and an increase in monolayer thickness are observed with an increase in transfer pressure. In addition, at the largest transfer pressure, elongated micelles are observed. In the case of copolymer $EO_{12}SO_{10}$, association of micelles is also observed. Aggregation numbers derived from AFM images increase with the increase of the SO weight fraction at a certain deposition pressure, which can be a consequence of stronger attractive interactions between the SO blocks to avoid contact with the solvent. The lower aggregation number of copolymer $EO_{137}SO_{18}EO_{137}$ may arise from the steric repulsion of EO chains at the interface due to the longer PEO blocks if compared to the other block copolymer.

Acknowledgment. The authors thank the Ministerio de Ciencia e Innovación (MICINN) for research projects MAT 2007-6107 and Xunta de Galicia for additional financial support under project INCITE09206020PR. S.G.-L. thanks the MICINN for her FPI scholarship. The authors also thank Prof. D. Attwood and C. Booth for the generous gift of the copolymers.

Supporting Information Available: Size and height distributions of aggregates formed in Langmuir−Blodgett films of copolymers at surface pressures of 5 and 11 mN/M. This material is available free of charge via the Internet at http://pubs.acs.org.

References and Notes

(1) Edens, M. W. *Nonionic Surfactants, Polyoxyalkylene Block Copolymers*; Marcel Dekker: New York, 1996.
(2) Riess, G.; Cheymol, A.; Hoerner, P.; Krikorian, R. *Adv. Colloid Interface Sci.* **2004**, *108−109*, 43–48.
(3) Tao, Y.; Ma, B.; Segalman, R. A. *Macromolecules* **2008**, *41*, 7152–7159.
(4) Boudier, A.; Aubert-Pouëssel, A.; Gérardin, C.; Devoisselle, J. M.; Bégu, S. *Int. J. Pharm.* **2009**, *379*, 212–217.
(5) Gilcreest, V. P.; Dawson, K. A.; Gorelov, A. V. *J. Phys. Chem. B* **2006**, *110*, 21903–21910.
(6) George, P. A.; Donose, B. C.; Cooper-White, J. J. *Biomaterials* **2009**, *30*, 2449–2456.
(7) Sedev, R.; Jachimska, B.; Khristov, K.; Malysa, K.; Exrowa, D. *J. Dispersion Sci. Technol.* **1999**, *20*, 1759–1776.
(8) Alexandridis, P.; Lindman, B. *Amphiphilic Block Copolymers: Self-Assembly and Applications*; Elsevier Science: Amsterdam, 2000.
(9) Park, S.; Wang, J. W.; Kim, B.; Russell, T. P. *Nano Lett.* **2008**, *8*, 1667–1672.
(10) Park, S.; Kim, B.; Wang, J. W.; Russell, T. P. *Adv. Mater.* **2008**, *20*, 681–685.
(11) Hillmyer, H. A. *Adv. Polym. Sci.* **2005**, *190*, 137.
(12) Crothers, M.; Attwood, D.; Collet, J. H.; Yang, Z.; Booth, C.; Taboada, P.; Mosquera, V.; Ricardo, N. P. S.; Martini, L. G. A. *Langmuir* **2002**, *18*, 8685–8691.
(13) Yang, Z. M.; Crothers, M.; Ricardo, N. P. S.; Chaibundit, C.; Taboada, P.; Mosquera, V.; Kelarakis, A.; Havredaki, V.; Martini, L.; Valder, C.; Collett, J. H.; Attwood, D.; Heatley, F.; Booth, C. *Langmuir* **2003**, *19*, 943–950.
(14) Booth, C.; Attwood, D.; Price, C. *Phys. Chem. Chem. Phys.* **2006**, *8*, 3612–3622.
(15) Riess, G. *Prog. Polym. Sci.* **2003**, *28*, 1107–1170.
(16) Booth, C.; Attwood, D. *Macromol. Rapid Commun.* **2000**, *21*, 501–527.
(17) Gangaly, R.; Awal, V. K.; Hassan, P. A. *J. Colloid Interface Sci.* **2007**, *325*, 693–700.
(18) Battaglia, G.; Ryan, A. J. *J. Am. Chem. Soc.* **2005**, *127*, 8757–8764.
(19) Bryskhe, K.; Jansson, J.; Topgaard, D.; Schillén., K.; Olsson, U. *J. Phys. Chem. B* **2004**, *108*, 9710–9719.
(20) Chaibundit, C.; Sumanatrakool, P.; Chinchew, S.; Kanatharana, P.; Tattershall, C. E.; Booth, C.; Yuan, Y.-F. *J. Colloid Interface Sci.* **2005**, *283*, 544–554.
(21) Barbosa, S.; Cheema, M. A.; Taboada, P.; Mosquera, V. *J. Phys. Chem. B* **2007**, *111*, 10920–10928.
(22) Vaughn, T. G.; suter, H. R.; Lunsted, L. G.; Kramer, M. G. *J. Am. Oil Chem. Soc.* **1951**, *28*, 294.
(23) Nace, V. M. *J. Am. Oil Chem. Soc.* **1996**, *73*, 1–8.

(24) Fleute-Schlachter, I. Goldschmidt Industrial Specialties, Essen, Germany. Private communication.
(25) O′Connor, S. M.; Gehrke, S. H.; Retzinger, G. S. *Langmuir* **1999**, *15*, 2580–2585.
(26) Rippner Blomquist, B.; Wärnheim, T.; Claesson, P. M. *Langmuir* **2005**, *21*, 6373–6384.
(27) González-López, J.; Sandez-Macho, I.; Concheiro, A.; Alvarez-Lorenzo, C. *J. Phys. Chem. C* **2010**, *114*, 1181–1189.
(28) González-López, J.; Alvarez-Lorenzo, C.; Taboada, P.; Sosnik, A.; Sandez-Macho, I.; Concheiro, A. *Langmuir* **2008**, *24*, 10688–10697.
(29) Hodges, C. S.; Neville, F.; Konovalov, O.; Hammond, R. B.; Gidalevitz, D.; Hamley, I. W. *Langmuir* **2006**, *22*, 8821–8825.
(30) Ricardo, N. M. P. S.; Chaibundit, C.; Yang, Z.; Attwood, D.; Booth, C. *Langmuir* **2006**, *22*, 1301–1306.
(31) Pinho, M. E. N.; Costa, F. M. L. L.; Filho, F. B. S.; Ricardo, N. M. P. S.; Yeates, S. G.; Attwood, D.; Booth, C. *Int. J. Pharm.* **2007**, *328*, 95–98.
(32) Juárez, J.; Taboada, P.; Valdez, M. A.; Mosquera, V. *Langmuir* **2008**, *24*, 7107–7116.
(33) Cheyne, R. B.; Moffitt, M. G. *Langmuir* **2005**, *21*, 5453–5460.
(34) Deschênes, L.; Bousmina, M.; Ritcey, A. M. *Langmuir* **2008**, *24*, 3699–3708.
(35) Crothers, M.; Zhou, Z.; Ricardo, N. P. S.; Yang, Z.; Taboada, P.; Chaibundit, C.; Attwood, D.; Booth, C. *Int. J. Pharm.* **2005**, *293*, 91–100.
(36) Elsabahy, M.; Perron, M.-È.; Bertrand, N.; Yu, G.-e.; Leroux, J.-C. *Biomacromolecules* **2007**, *8*, 2250–2257.
(37) Babak, V. G.; Boury, F. *Colloids Surf., A* **2004**, *243*, 33–42.
(38) Babak, V. G.; Baros, F.; Boury, F.; Desbrières, J. *Colloids Surf., B* **2008**, *65*, 43–49.
(39) Ward, A. F. H.; Tordai, L. *J. Chem. Phys.* **1946**, *14*, 453–458.
(40) Hansen, F. K.; Myrvold, R. *J. Colloid Interface Sci.* **1995**, *176*, 498.
(41) Myrvold, R.; Hansen, F. K.; Balinov, B. *Colloids Surf., A* **1996**, *18*, 453.
(42) Muñoz, M. G.; Monroy, F.; Ortega, F.; Rubio, R. G.; Langevin, D. *Langmuir* **2000**, *16*, 1094–1101.
(43) Joos, P.; Fainerman, V. B. *Dynamic Surface Phenomena*; VSP: Utrecht, The Netherlands, 1999.
(44) Kopperud, H. B. M.; Hansen, F. K. *Macromolecules* **2001**, *34*, 5635–5643.
(45) Leiva, A.; Farias, A.; Gargallo, L.; Radic, D. *Eur. Polym. J.* **2008**, *44*, 2589–2598.
(46) Haefele, T.; Kita-Tokarczyk, K.; Meier, W. *Langmuir* **2006**, *22*, 1164–1172.
(47) Kiss, E.; Keszthelyi, T.; Kormany, G.; Hakkel, O. *Macromolecules* **2006**, *39*, 9375–9384.
(48) Elbolk, T. A.; Detellier, C. *J. Phys. Chem. Solids.* **2006**, *67*, 950–955.
(49) Hann, R. A. *Molecular Structure and Monolayer Properties. In Langmuir-Blodgett Films*; Roberts, G., Ed.; Plenum Press: New York, 1990; pp 18−23.
(50) Nivaggioli, T.; Tsao, B.; Alexandridis, P.; Hatton, A. T. *Langmuir* **1995**, *11*, 119–126.
(51) Chen, C.; Even, M. A.; Chen, Z. *Macromolecules* **2003**, *36*, 4478–4484.
(52) Chang, L.-C.; Lin, C. Y.; Kuo, M.-W.; Gau, C.-S. *J. Colloid Interface Sci.* **2005**, *285*, 640–652.
(53) Chang, L. C.; Chang, Y. Y.; Gau, C. S. *J. Colloid Interface Sci.* **2008**, *322*, 263–273.
(54) des Cloizeaux, J. *J. Phys. (Paris)* **1975**, *36*, 281–291.
(55) Vilanove, R.; Rondelez, F. *Phys. Rev. Lett.* **1980**, *45*, 1502.
(56) Faure, M. C.; Bassereau, P.; Lee, L. T.; Menelle, A.; Lheveder, C. *Macromolecules* **1999**, *32*, 8538–8550.
(57) Goncalves da Silva, A. M.; Simoes Gamboa, A. L.; Matinho, J. M. *Langmuir* **1998**, *14*, 5327–5330.
(58) Baker, S. M.; Leach, K. A.; Devereaux, C. E.; Gragson, D. E. *Macromolecules* **2000**, *33*, 5432–5436.
(59) Cox, J. K.; Yu, K.; Constantine, B.; Eisenberg, A.; Lennox, R. B. *Langmuir* **1999**, *15*, 7714–7718.
(60) Devereaux, C. A.; Baker, S. M. *Macromolecules* **2002**, *35*, 1921–1927.
(61) Wen, G.; Chung, B.; Chang, T. *Macromol. Rapid Commun.* **2008**, *29*, 1248–1253.

JP1049777

4.3.- Appended papers.

In the present work, the solution behaviour and surface adsorption properties of three different block copolymer ($E_{12}S_{10}$, $E_{10}S_{10}E_{10}$ and $E_{137}S_{18}E_{137}$), have been studied. These block copolymers display different volume-to-length ratios of the hydrophobic block and of relative lengths of the poly(oxyethylene) block ; and also polymer architecture may have an important role in controlling the morphology of polymeric aggregates and surface adsorption behaviour of these copolymers. To known the influence of such parameters, we studied the self-assembly properties and the different structural aggregates of the three copolymers in aqueous solution.

For copolymer $E_{12}S_{10}$, coexistence of spherical micelles with vesicular structures is detected. To the best of our knowledge, the spontaneous formation of vesicles by poly(oxystyrene)-poly(oxyethylene) block copolymers has been first reported here. On the other hand, formation of elongated micelles upon self-assembly of copolymer $E_{10}S_{10}E_{10}$ in dilute solution is elucidated from light scattering and transmission electron techniques. In the case of $E_{137}S_{18}E_{137}$, typical spherical micelles are observed, as expected. The micellization properties of the latter copolymer had been already partially studied previously (89)(90), and the present study completes this gap.

On the other hand, fundamental studies of polystyrene oxide-based block copolymers performed at either the air-water or the water-organic solvent interface can provide valuable information on their interfacial phase behaviour to further guide their possible use in different biomedical and coating applications. To fill this gap, in the present work, we studied the surface behaviour and surface properties of these three copolymers, $E_{12}S_{10}$, $E_{10}S_{10}E_{10}$ and $E_{137}S_{18}E_{137}$, by different techniques.

To do this work, different techniques such as surface tension, Langmuir-Blodgett through, drop tensiometry, light scattering, transmission and scanning electron microscopies (TEM and SEM), atomic force microscopy (AFM), polarized optical microscopy (POM) and rheometry were used.

4.3.1.- Relevant aspects

I. For $E_{12}S_{10}$ dilute solutions, the coexistence of spherical micelles with vesicular structures has been observed. In addition, the spontaneous formation of vesicles by poly(oxystyrene)-poly(oxyethylene) block copolymers is reported for the first time, as confirmed by light scattering, polarized light microscopy, and transmission and cryo-scanning electron microscopy data.

II. In dilute solution, the self-assembly of copolymer $E_{10}S_{10}E_{10}$ leads to the formation of elongated micelles as supported by light scattering and transmission electron techniques.

III. In the case of copolymer $E_{137}S_{18}E_{137}$, typical spherical micelles are observed. Tube inversion and rheological measurements were used to define the sol- soft- and gel-hard boundaries of this copolymer.

IV. $E_{12}S_{10}$ and $E_{10}S_{10}E_{10}$ copolymers did not form gels in the concentration range analysed. However, only certain concentrations of copolymer $E_{10}S_{10}E_{10}$ were analysed by rheometry. From experimental data, an upturn in the low-frequency range of the stress moduli was observed, denoting the existence of an emerging slow process, which was assigned to the formation of an elastic network.

V. Block copolymers $E_{12}S_{10}$, $E_{10}S_{10}E_{10}$ and $E_{137}S_{18}E_{137}$ showed spontaneous adsorption at the air-water interface, which slowed down when the hydrophobicity of the molecule was increased. In contrast, at the chloroform/water interface no measurable effect is observed for copolymer $E_{12}S_{10}$ due to the slow diffusion of its chains to the interface in combination with a low bulk concentration; this slow diffusion is associated with the fact that chloroform is a good solvent for both E and S blocks.

VI. Copolymer $E_{137}S_{18}E_{137}$ displays an adsorption isotherm with the four classical regions representing the pancake, mushroom, brush and condensed states; the presence of a pseudo-plateau is attributed to the pancake-to-brush transition as E chains submerge into the aqueous sub-phase. On the other hand, for $E_{12}S_{10}$ and $E_{10}S_{10}E_{10}$ copolymers only two regions are observed in their adsorption isotherms as a consequence of their low molecular weights, short S and E block lengths, and much larger S/E ratio. This involves the disappearance of the pseudo-plateau region due to the decrease in the fractional interfacial area occupied by EO segments.

VII. According to AFM images, circular micelles are observed on Langmuir-Blodgett films of the copolymers obtained at two surface transfer pressures. A decrease in micelle size and an

increase in monolayer thickness are observed with increases in transfer pressure. Aggregation numbers derived from AFM images increase with the increase of the S weight fraction at a certain deposition pressure, which can be a consequence of stronger attractive interactions between the S blocks to avoid contact with the solvent.

CHAPTER 5

Proteins

Contents

5.1.- Protein structure

From a chemical point of view, proteins are linear heteropolymers whose backbones are usually composed of almost 20 different monomers, as opposed to most synthetic polymers which are composed of one or few monomers. Whilst polymers have a large extended organization in aqueous solution, proteins fold as relatively small compacted structures. The spatial arrangement of atoms in a protein is called conformation. The possible conformations of a protein include any structural state which can achieve without breaking covalent bonds. A change in conformation could occur, for example, by rotation about single bonds. The conformations existing under a given set of conditions are usually those most thermodynamically stable, i.e. having the lowest Gibbs energy.

Four structural levels are frequently considered in protein architecture. The primary structure corresponds to the amino acid sequence. The secondary structure refers to the spatial arrangement of amino acid residues that are nearby in the sequence (for example, α-helix and β-sheet are elements of secondary structure). Tertiary structure refers to the spatial arrangement of amino acid residues that are far apart in the sequence and to the pattern of disulfide bonds. Finally, proteins containing more than one polypeptide chain exhibit a fourth level of structural organization (each polypeptide chain in such a protein is called a subunit). In this regard, quaternary structure refers to the spatial arrangement of subunits.

5.1.1.- Primary structure of the proteins

Proteins are linear polymers formed by the linkage of the carboxylic group of one amino acid to the amino group of another amino acid generating a peptide bond. The formation of a dipeptide from two amino acids is accompanied by the loss of a water molecule. A series of amino acids joined by peptide bonds form a polypeptide chain, and each amino acid unit in a polypeptide is called a residue. A polypeptide chain possesses polarity because its ends are different, with an amino group at one end and a carboxylic group at the other. By convention, the amino end is taken to be the start of the polypeptide chain, so the sequence of amino acids in a polypeptide chain is written starting with the amino-terminal residue (4).

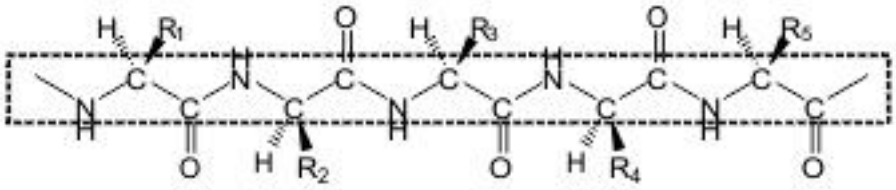

Figure 5.1 Polypeptide chain: structural constant backbone (inside the dotted squared box) and lateral side lateral chains, denoted by the letter R.

As mentioned before, proteins are built by a sequence of amino acids which are chemically connected by covalent bonds (peptide bond). A polypeptide chain is constituted of two parts: a main chain or backbone and a complementary one constituted by side lateral chains characteristic of each amino acid (Figure 5.1). The backbones possess a great ability to establish hydrogen bonds: each amino acid has a carboxylic group (-C=O), that is an acceptor of hydrogen bonds (except proline), and an amino group (-NH) which it is a donator of the hydrogen bonds. These functional groups mutually interact to provide stability to the biomacromolecule structure. Naturally, proteins are constituted by 20 different types of amino

acids whose lateral side chains change in size, form, charge, hydrophobic character and chemical reactivity.

5.1.2.- Secondary structure of the proteins.

The secondary structure of proteins depends on four factors: i) bond length and angles of peptidic bonds; ii) the coplanar arrangement of the substituted atoms in amide groups; iii) the hydrogen bonding between functional –NH and C=O groups in order to maintain structural stability; iv) the distance of the hydrogen bonds that can be formed (3). For instance, segments of polypeptide chains are in a coiled conformation due to intramolecular interaction, i.e. the atoms involved in amide groups must remain coplanar, and for maximal stability, each N-H group must be hydrogen bonded to a –CO and each -CO to a –NH. Under ideal conditions, functional groups (carboxylic and amine groups) of amino acids can form hydrogen bonds, with an energy of 5 kcal/mol. The polypeptide chains tend to adopt up to three different configurations that enable the formation of a maximum number of hydrogen bonds: alpha helix, beta sheet, turns or loops (Figure 5.2).

The alpha helix (α-helix) displays a cylindrical structure (Figure 5.2a) where the polypeptidic backbone possesses a helical conformation strongly folded into the internal cylindrical core. The side lateral chains are extended out of the helical distribution. The α-helix is stabilised by the hydrogen bonding along the principal backbone chain. Within this, the separation between the amino acids is close to 1.5 Å, and each complete helical turn has 3.6 amino acids (4)(91)(92). Alanine and leucine are strong helix favouring residues, while proline is rarely found in helices, because in its backbone nitrogen is not to available for the hydrogen bonding required for helix formation. The aromatic side chain of phenylalanine can sometimes participate in weakly polar interactions (4).

The beta sheet fold (β-sheet) differs markedly from the α-helix. A polypeptide chain, called a β-strand, in a β-sheet is almost fully extended rather than being tightly coiled as in the α-helix. (Figure 5.2b). The distance between adjacent amino acids along the β-strands is approximately 3.5 Å, in contrast with the distance of 1.5 Å along the α-helix. A β-sheet is formed by linking two or more β-strands by hydrogen bonds. Adjacent chains in β-sheets can run in opposite direction (antiparallel β-sheet) or in the same direction (parallel β-sheet). In the antiparallel arrangement, the –NH and the –CO groups of each amino acid are, respectively, hydrogen bonded to the –CO and the –NH groups of a partner on the adjacent chain. In the parallel arrangement, the –NH group is hydrogen bonded to the –CO group of one amino acid on the

adjacent strand, whereas the –CO group is hydrogen bonded to the –NH group on the amino acid two residues farther along the chain (4)(92).

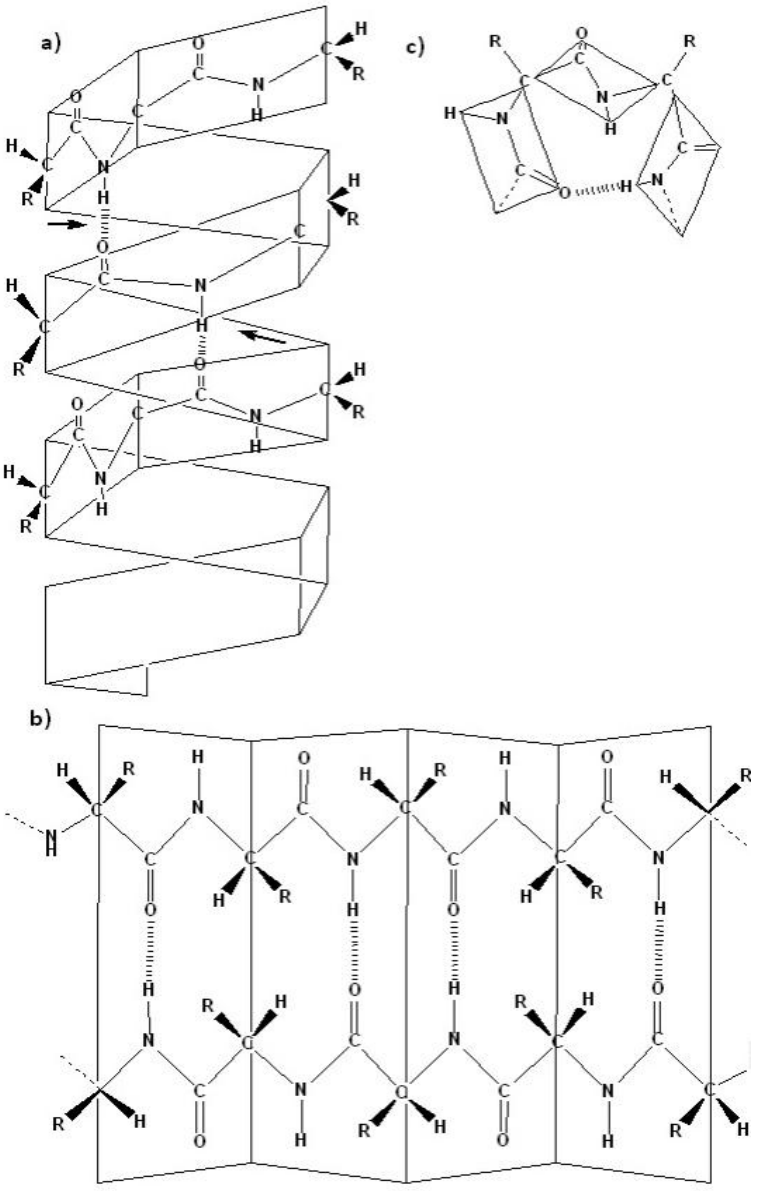

Figure 5.2 Secondary structures of the proteins a) α-helix, b) β-sheet and c) turns.

In proteins, the directional changes of the polypeptide chains are led by simple structural elements like inverse turn (Figure 5.2c), called β-turns or hairpin turns and loops. This structure stabilized abrupt direction changes of the polypeptide chains. Contrary to α-helix and β-sheet, turns and loops have no periodic structures (turns have a compact folded and usually rigid structure stabilized by hydrogen bonding, while loops have an extended and disorder structure without hydrogen bonds). These are the connecting elements that link successive runs of the α-helix or β-sheet conformations. Particularly, β-turns connect the ends of two

adjacent segments of an antiparallel β-sheet. The structure is a 180^0 turn involving four amino acid residues, with a carbonyl oxygen of the first residue forming a hydrogen bond with the amino-group hydrogen of the fourth. The peptide groups of the central two residues do not participate in any inter-residue hydrogen bonding (Gly and Pro residues often occur in β-turn, the former because it is small and flexible, the later because peptide bounds involving the amino nitrogen of proline readily assume cis configuration). Generally, β-turns are often localized near the surface of a protein, where the peptide groups of the central two amino acid residues in the turn can hydrogen-bonded with water. Hence, the secondary structures of proteins make reference to highly organized regular geometries. Turns and loops invariably lie on the surfaces of proteins and thus participate in interactions between proteins and other molecules (91)(92).

5.1.3.- Tertiary Structure of the proteins

The overall three-dimensional arrangement of atoms in a protein is referred to as the protein tertiary structure. Whereas the secondary structure refers to the spatial arrangement of amino acid residues that are adjacent in a segment of a polypeptide, tertiary structure includes longer-range aspects of the amino acid sequence. Amino acids that are far apart in the polypeptide sequence and are in different types of secondary structure may interact within the completely folded structure of a protein. In other words, tertiary structure emerges from the distribution of side chains of amino acid residues. Instead, the buried parts of proteins consist almost entirely of non-polar residues. On the other hand, charged residues usually are absent from the inside of proteins. However, both polar and non-polar residues can be found on the protein surface. In aqueous environment, protein folding is driven by the strong tendency of hydrophobic residues to be excluded from water (the system is thermodynamically stable when hydrophobic groups are clustered rather than extended into the aqueous surroundings). The polypeptide chain therefore folds so that its hydrophobic side chains are buried and its polar, charged chains are on the surface. Recall that many α-helix and β-strands are amphipatic since both secondary structures have a hydrophobic face, which points into the protein interior, and a more polar face, which points into solution. The buried domains in a hydrophobic environment are stabilized by hydrogen bonding, pairing all the amino and carboxylic groups. This pairing is neatly accomplished in an α-helix and β-sheet structures. Van der Waals interactions between tightly packed hydrocarbon side chains also contribute to the stability of the tertiary protein structure (4).

5.1.4.- Quaternary structure of the proteins

The quaternary structure refers to the association of several polypeptide chains (with tertiary structure) linked by weak forces. Amongst the forces stabilising the quaternary structure we find hydrogen bonding, hydrophobic interactions and cross-linking interactions like disulfide bridges and metal-ion ligation. At this structural level, the protein assemblies composed of more than one polypeptide chain are called oligomers, and each individual chain is called subunit.

5.2.- Protein aggregation

The timescale required to protein folding in biological systems is quickly enough to avoid a random mechanism for protein folding (93). As a general principle, the kinetic pathway of protein folding can be described as an ordered fold reaction. In this way, the folding of only very simple proteins has been determined at atomic level resolution to date (94), using biophysical and theoretical experiments as a sequential and highly cooperative reaction (95).

The concept of energy landscape is used to visualize the conformational space available to each individual polypeptide under a given condition. This theoretical formalism describes the progressive folding of polypeptide chains along their energetic structural evolution (the energy landscape) from an unfolded conformation to a compact native structure (Figure 5.3) (96). For small proteins, this landscape appears to be funnel-like and represent the evolutionary selection of a polypeptide sequence able to fold rapidly and reliably towards a unique native state. On the other hand, larger polypeptide sequences have rougher energy landscapes, in which there are present different populations of partially folded species that may be on- or off-pathway to the native fold. Characterizing the multitude of populated conformational states on this energy landscape is not only crucial for developing an understanding of the determinants of protein folding and function, but also contains crucial clues about side-reactions such as protein aggregation. Such characterization involves the knowledge of all structural, kinetic and thermodynamic properties of all conformations accessible to a given polypeptide sequence. However, it is necessary to develop analytical-high resolution tools capable to resolve the structural fast interconversion of the species involved, as well as the theoretical bases that permit to understand and interpret the obtained data (97).

5.2.1.- Unfolded state

Over the last decade, an enormous progress has been made in the description of the conformation of the unfolded states of polypeptide chains. These important species not only define the starting point for protein folding, but also have important roles in a variety of biological process. When described the unfolded state of a polypeptide sequence, the first idea in mind is a random coil structure, which lacks of specific inter-residue interactions between the lateral chains of the amino acid sequence. However, this viewpoint has moved over recent years as a result of the increasing number of detailed studies about the properties and structure of denatured states under different solution conditions (98). Current views consider that even in the presence of high denaturant concentrations, significant amounts of aliphatic and aromatic side chains present in the native state may persist, even when the secondary structure of the native state has been lost. On the other hand, under lesser harsh solution conditions, also some proteins can be unfolded in the absence of denaturant agents (for example, by mutating the sequence or changing the pH of the solution), the unfolded state has been shown to contain significant native-like interactions with substantial native and non-native side chain contacts which allow the existence of a residual structure. This residual structure in the unfolded state has not only been suggested to reduce the conformational search during protein folding, but also for some proteins may play a role in the onset of protein aggregation of unfolded polypeptide sequences (97)(99).

5.2.2.- Intermediate and transition state ensembles

The function of the intermediate states (populated partially-folded states) during protein folding has been a long-standing question. Supported by the observation that many small proteins fold with apparent two-state kinetics, folding intermediates were initially thought to be aberrant misfolds on the folding energy landscape, representing off-pathway species or kinetics traps. Nowadays, thanks to more powerful experimental methods (Foster resonance emission transfer fluorescence (FRET), fluorescent correlation spectroscopy or NMR spectroscopy, amongst others) protein folding studies have revealed that partially folded states are widely populated during the protein folding process, even in simplest proteins (97). In this regard, a model that involves transient intermediate states in equilibrium into the pathway of a given polypeptide chain has been suggested. Under this context, a polypeptide chain with high molecular weight may present many intermediate states, describing a roughness energy landscape for its particular folding pathway. For example, larger polypeptide chains have a higher tendency to collapse under specific solution conditions, leading to the formation of compact states, which can contain substantial native-like structure. Structural

reorganization as a consequence of inter-residue contact (including both native and non native-like interactions) of these compact states may involve high-energy barriers, leading to the transient population of partially intermediate states. Such species can be either productive for on-pathway folding until reaching the native state; or they can be trapped in such a manner that the native structure cannot be reached without substantial organizational events (off-pathway).

5.2.3.- Native state

Currently, it is known that the conformational states of proteins are structural dynamic processes, i.e. even at native conditions, structured proteins have access to a manifold of near-native conformations, in which protein native structures show fluctuations around the minimal energy conformation (100). Such structural movements are essential in order to encompass their function, such as enzyme catalysis or ligand binding, as well as site-to site communication within the globular protein fold or between proteins subunits.

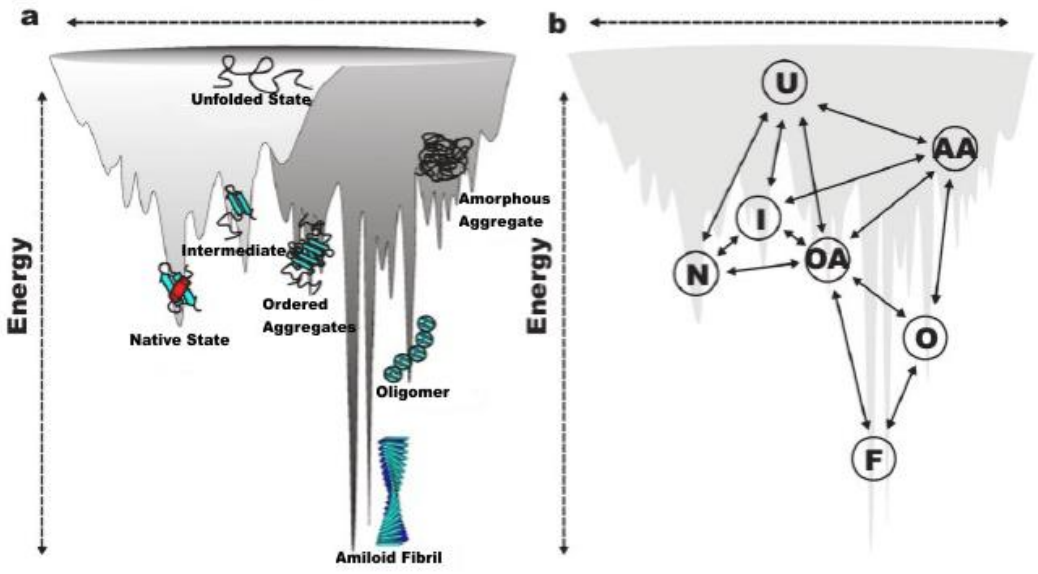

Figure 5.3 Schematic illustration of the energy landscape for protein folding and aggregation. a) The surface illustrates the roughness of the protein landscape, showing the multitude of conformational states available to a polypeptide chain. The conformational search of a single polypeptide chain to a functional monomer can be described in a simple folding funnel (light grey), intermolecular association increased the roughness of the energy landscape (dark grey), b) Proposed pathways related to the conformational states shown in a) populated on the combined folding and aggregation energy landscape (97).

5.2.4.- Energy landscape: protein aggregation

The schematic diagram in Figure 5.3 attempts to depict the complexity of the protein folding and aggregation energy landscapes as previously mentioned; at the same time, it makes an effort to illustrate the wide variety of different conformational states with minimum energies and the large diversity of folding pathways available for each polypeptide chain as it circumnavigates the landscape. Regarding the in-depth knowledge of the folding landscape of simple, single domain monomeric proteins, and the conformational states accessible to polypeptide oligomers, relatively little is understood. Energy minima on the aggregation side of the energy landscape might be poorly defined, as a result of broad ensembles of oligomeric states of similar energy that are rapidly interconverting, but could also be highly defined, as might be expected for higher order species such protofibrils or fibrils. For example, the energy minimum of mature amyloid fibrils might be deeper and sharper that those of native monomeric proteins, as suggested by the rigidity of the amyloid fold, as well as by the nucleation-dependent polymerisation mechanism (101). Here, however, even under the same solution conditions a multitude of fibril morphologies can be formed simultaneously, highlighting the complexity and multiplicity of the aggregation pathway (102)(103).

5.3.- Amyloid fibrils

Into the context of the energy landscape, the observation that virtually any protein sequence can form amyloid fibrils given the appropriate solution conditions led to the suggestion that the amyloid fold is the universal global free energy minimum of all polypeptide chains that may assemble by generic mechanisms governed by the physicochemical properties of the polypeptide chain.

5.3.1. Amyloid fibrils hallmarks

Amyloid comes from the Greek word amylon which means starch. Amyloid was coined initially in a botanical context by Scheiden (104). Virchow and others researches used the term amyloid into medicine to describe human pathogenic deposits that stain with sulphuric acid and iodine solution, similarly to starch staining. Although these deposits do not primarily consist of polysaccharides, they were found to be a proteinaceus, nowadays the definitions of amyloid fibrils depend on the context of their use. In pathological diagnosis, amyloid had been defined as extracellular deposits of proteins fibrils with a characteristic appearance in electron microscope, a typical X-ray diffraction pattern, and a strong affinity for Congo red dye (105).

In vivo, the self-assembly of proteins into highly ordered, β-sheet enriched, fibrillar, insoluble, supramolecular structures known as amyloid fibrils (or amyloid-like fibrils, term referring to protein fibrils that not associated with any disease) is linked to the onset of a growing number of human disorders, including Alzheirmer's, Parkinson's, Huntington´s diseases, spongiform encephalopathies, and type II diabetes mellitus. On the other hand, the controlled self-assembly of proteins and peptides into amyloid-like structures may constitute an attractive alternative to develop nanomaterials (106)(107).

Amyloid fibrils can be obtained *in vitro* through different ways by adjusting different external parameters as, for example, pH, ionic strength, and temperature, and cosolute or cosolvent additions. This means that the formation of amyloid-like conformations is not restricted to peptide chains of specific length or having a particular primary or secondary structure; this suggests that the conformational shift into β-sheet rich is energetically preferred. The characterization of the fibrillation process of proteins *in vitro* has largely been focused on biophysical characterization in order to determine the structure of the fibril, and on biochemical studies to get into the mechanism and kinetics of the process. Also, through techniques such X-ray diffraction, electron microscopy, and solid state NMR spectroscopy we now have a good understanding of the core architecture of individual fibrils too.

In general, amyloid fibrils possess distinct physical properties as: *i*) they are characterized by a cross-β sheet structure, where individual β-strands are perpendicular and each β-sheet is parallel to the fibril axis (Figure 5.4). The X-ray diffraction pattern shows two characteristic reflections at 4.7 Å and 10-11 Å, corresponding to the inter-strand and stacking distances between individual β-sheets, respectively; *ii*) amyloids bind to histological dyes such as Congo red (CR) and Thioflavin T (ThT). After binding to CR, an apple-green birefringence under cross-polarized light is observed. CR and ThT dyes, however, do not bind to monomeric proteins or peptides. These dyes fluoresce when they bind to β-sheet rich fibrils and are, therefore, useful for spectroscopic monitoring of fibril´s growth and kinetics; *iii*) under electron microscope (EM), amyloid fibrils appear to be few micrometers long, non-branched filaments, with 7-12 nm diameter. In a majority of cases, amyloids are composed of 2-4 protofilaments that are either helically twisted or laterally associated with each other forming higher order fibrils; *iv*) amyloids are resistant to heat, wide ranges of pH and proteases (107)-(113).

Over the past several years, soluble proteins and protein fragments self-assembled into amyloid aggregates have attracted the interest of researchers from diverse fields. From a

molecular medicine viewpoint, protein deposition is an undesired process associated with several human diseases. Hence, different questions must be arisen such as why self-association of a misfolded protein results in organ dysfunction and neurodegeneration?, what are the toxic species?, and whether aggregates of all proteins are toxic or not?. At the molecular level, fundamental research has been directed towards obtaining a rational understanding of the physico-chemical principles underlying protein misfolding and self-assembly. However, given the complexity of the molecular mechanisms driving amyloid aggregation, a frequently used strategy in the field consists of design polypeptide model systems to allow biophysical characterization and the study of their aggregation process (114)-(118). This strategy permits the analysis of the relationship between the amino acid sequence of the polypeptide chain and its structural stability during the conformational transition.

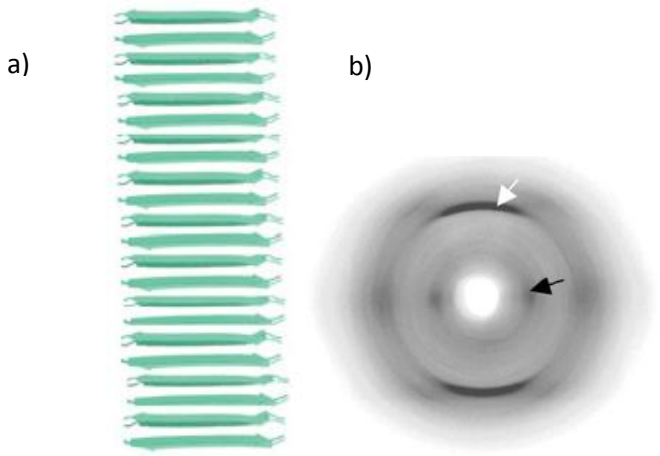

Figure 5.4 Schematic representation of an amyloid fibril structure: a) β-strands perpendicular to the fibre axis; the β-sheet structure arises from the hydrogen bonding between lateral side chains of amino acids; b) cross-β diffraction pattern observed in amyloid fibrils. Arrows indicate the positions of the cross-β reflection on the meridian at 4,7 Å (white) and on the equator at 10 Å (black) (112).

Several studies have shown that the destabilization of the polypeptide sequence *per se* is not enough to bring the self-assembly process up to form amyloid fibrils (119)(120). Additionally, the sudden conformational transition undergone by proteins in their native state to form amyloid fibrils rich in β-sheets is favoured only if the amino acid sequence increase its ability to form β-sheet structures. In most of these systems, the structural transitions from α-helix to β-structures are originated by applying external heat energy. This phenomenon involves a number of relatively weak non-covalent molecular forces: hydrophobic, electrostatic, and

hydrogen bonds mainly. Molecular simulations (109) demonstrated that hydrophobic interactions play an important role in promoting protein self-assembly. Meanwhile, for small peptides the β-sheet aggregates are stabilized by backbone hydrogen bonds, as well as by specific side-chain interactions such as hydrophobic stacking of polar side chains and electrostatic interaction.

5.3.2.- Kinetic fibril formation *in vitro*

The generic nature of the aggregation process has enabled extensive studies of the transition between soluble precursor states and insoluble amyloid fibril in vitro (121). The aggregation into amyloid structure of globular proteins has been shown to require a conformational transition process before reaching the amyloid fibre structure. To carry out this process, the native conformation of globular proteins usually must be destabilised by the addition of denaturants agents, low pH, high temperature, truncation/mutation and so (122)-(124). Specific protein destabilisation results in an increased population of partially folded conformations exposing aggregation-prone regions that are usually protected in the native state and, thus, enhancing the probability of non-native intermolecular interactions.

At present, the proposed models to describe the formation process of amyloid fibrils include monitoring the fibrillogenesis by high-resolution microscopic and spectroscopic tools, and by the binding of specific dyes to amyloid fibrils. The most common model for explaining the amyloid formation is the nucleation-dependent polymerization model. In such a model, the kinetic pathway from the native structure to amyloid fibrils occurs by a nucleation-aggregation process. The nucleation step (also known as lag phase) is the factor that determines the rate of amyloid formation by the slow generation of nuclei under successive thermodynamically unfavourable steps; these nuclei aggregate when a critical protein concentration value has been exceeded by a small amount; hence, the process is concentration-dependent. The lag phase precedes a period of exponential growth that corresponds to fibril elongation, characterised by a sudden fibre growth as a consequence of the addition of protein monomers or the association of other competent species; this step is called elongation phase. In contrast, another proposed model of fibrillogenesis is the “downhill polymerization” process, which consists of a continuum aggregate state without requiring a nucleation step. A relatively easy way to observe the fibrillation kinetics is by using an amyloid specific binding dye such Thioflavin T (ThT). ThT increases its fluorescence intensity upon binding to amyloid fibrils when using an excitation wavelength of 440 nm, and collecting the emission intensity at 480 nm. Figure 5.5 shown the kinetic formation of amyloid fibril followed by ThT binding. Figure 5.5 a)

shows the typical nucleation-dependent polymerization characterised by a sudden increase of of ThT fluorescence as a function time; once the lag phase is overcome (the lag phase is observed as the region where no appreciable changes in ThT fluorescence intensity take place). In contrast, with the non nucleation-dependent polymerization (downhill polymerization, Figure 5.5b) shows a marked and continuous ThT fluorescence intensity increase (125)-(129).

In vitro, the aggregation process of polypeptide chains into fibrillar structures can be also monitored by means of other analytical tools such as circular dichroism (CD), infrared spectroscopy (IR), nuclear magnetic resonance spectroscopy (NMR), light scattering, fluorescence spectroscopy (ThT), or imaging techniques such as TEM, SEM or AFM.

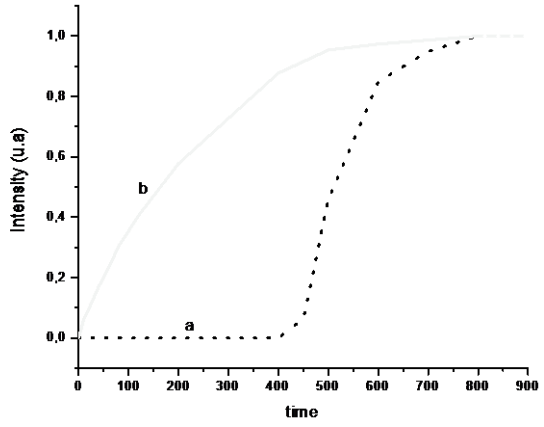

Figure 5.5 ThT fluorescence intensity as a function of time following a: a) nucleation-dependent polymerization, and b) a non-nucleation-dependent polymerization process.

5.4.- Human serum albumin (HSA)

HSA is a globular protein constituted by 585 amino acids in a single polypeptide chain with a molecular weight of 67,000 Da. Human serum albumin is the most abundant protein in blood plasma, it plays a special role in transporting endogenous and exogenous metabolites through the vascular system and also maintains the pH and osmotic pressure of plasma (130). The protein structure contains 17 disulfide bridges giving rigidity and stability to the protein structure. HSA has one free –SH group, which leads to protein dimerization and high order association. Accordingly to X-ray crystallography data, the secondary structure of HSA molecule is composed of 67% α-helix, no β-sheet, 10% turn, and 23% extended chain (131)(132). On the other hand, in agreement with CD spectroscopy data, the secondary

structure of HSA molecule at physiological solution conditions is composed of 67% α-helix, 5% β-sheet, 12% turn, and 17% extended chain (133). The three-dimensional configuration of serum albumin is divided into three major domains (labelled as I, I and III), and each domain are composed of two subdomains that possess common structural motifs, which are predominantly helical and cross-linked by the disulfide bridges (134)(135).

The HSA structure can be influenced by several factors as pH, temperature, cosolvents... It is known that HSA molecule shows a number of well-defined pH-dependent structural transitions, (Figure 5.6) (136): E form (below pH 2.7), F form (pH 2.7-4.3), N form (pH 4.3-8), B form (pH 8-10) and A form (over pH 10) (134)-(137). On the other hand, during its thermal unfolding process, three states can be distinguished: the native form, the reversible unfolded form (at ~65^{0}C) and the irreversible unfolded form (at ~74^{0}C) (120). Both unfolding processes give rise to aggregation-prone conformational changes of both secondary and tertiary structures, allowing the formation of amorphous aggregates, intermediate states, oligomers and amyloid fibrils.

Due to the physiological importance of human serum albumin as a carrier protein and blood pressure regulator and its propensity to easily aggregate in vitro, HSA has become a good model for protein aggregation studies. Moreover, as the phenomenon of protein aggregation appears to reflect certain generic “polymeric” features of proteins (138), the study of protein aggregation mechanisms in model systems is extremely useful to gain a better understanding about the molecular mechanisms of disease-associated amyloidogenesis.

In this way, in this work we show the propensity of HSA to form amyloid fibrils and other types of aggregates under different thermal and solvent conditions (changing the solution pH, solution ionic strength and solvent composition), allowing the modulation of electrostatic, hydrophobic and hydration interactions between protein molecules and aggregates (139)-(141). The kinetic aggregation, protein conformational changes upon self-assembly, and structure of the different intermediates on the fibrillation pathway were determined by means of ThT fluorescence and CR absorbance; far and near-UV-Vis CD; tryptophan fluorescence; Fourier transform infrared spectroscopy; X-ray diffraction; and TEM, SEM, AFM and optical microscopy. We have observed that the fibril formation is largely affected by electrostatic shielding: at physiological pH, fibrillation is progressively more efficient and faster in the presence of up to 50 mM NaCl; meanwhile, at larger salt concentrations, excessive charge shielding and further enhancement of the solution hydrophobicity might involve a change in

the energy landscape of the aggregation process, which makes the fibrillation process difficult. In contrast, under acidic conditions a continuous progressive enhancement of HSA fibrillation is observed as the electrolyte concentration in solution increases. Both the distinct protein ionization state and the initial structural states of the protein before incubation may be the origin of this behavior. According to ThT fluorescence data, the fibrillation kinetics of HSA does not show a lag phase except at pH 3.0 in the absence of added salt. The HSA fibrils obtained at the end of the fibrillation process show structural features typical of classical amyloid fibers, as denoted by XRD, CD and TEM techniques. Finally, we describe the physical and structural properties of additional supraself-assembled structures of HSA under solution conditions in which amyloid fibrils are formed. We have detected the formation of ordered aggregates of amyloid fibrils, i.e. spherulites, by means of polarized optical microscopy, laser confocal microscopy and TEM. These structures possess a radial arrangement of the fibrils around a disorganized protein core, and have sizes of several micrometers.

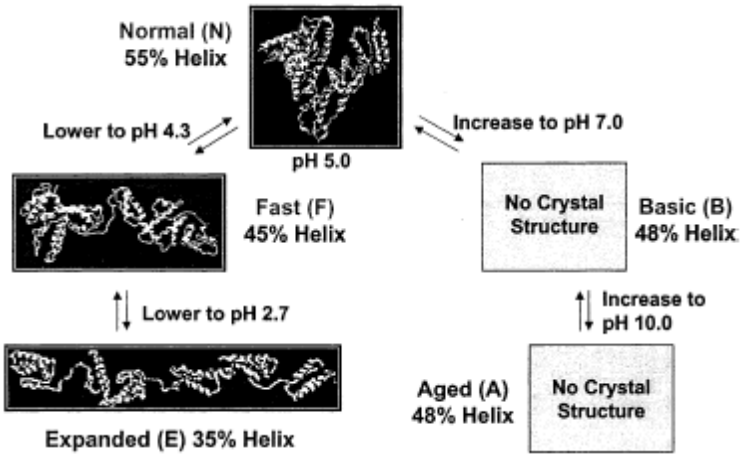

Figure 5.6 pH conditions and helical contents of the five organized forms of albumin including crystal structure of the N form, and the proposed configuration of the F and E forms (136).

5.5.- Amyloid fibrils as biomaterials

The bottom-up strategy takes advantage of the functionality of molecular materials and molecular recognition properties for self-assembly (142). The construction of functional nanomaterials and components through the bottom-up strategy has potential applications in different areas as electronics, tissue engineering, drug delivery, sensing… (143)(144). In this regard, self-assembly properties of biomacromolecules, as phospholipids, DNA, peptides, and proteins, can be an alternative for the obtention of new materials.

The physical and chemical properties of proteins are an attractive alternative for the construction of nanoestructured materials, providing an extraordinary array of functionalities that could be exploited in fields such as biomedicine, biotechnology, materials science, and nanotechnology (145). Protein amyloids are excellent candidates for the fabrication of molecular nanobiomaterials, such wires, layers, gels, scaffolds, templates, and liquid crystals, using the bottom-up strategy as a result of their outstanding physico-chemical properties (great stiffness, stable against heat and denaturants, resistant to proteases, amongst others) structural compatibility, nanoscale dimensions and efficient assembly into well-defined ultrastructures (146)(147).

On the other hand, metal nanoparticles (NP) have received considerable attention during last decade because of their particular optical, electronic, magnetic and catalytic properties and their important applications in many fields such as nanosensors, catalysis, biomedicine, biological, labelling, and surface-enhanced Raman scattering (SERS). To optimize and extend the applications of metal NPs, methods must be developed to control the assembly and organization of these nanomaterials. NPs in ordered arrays provide optical and electronic properties that are distinct compared to individual particles or disorganized macroscale agglomerations. In this way, the supramolecular structure of amyloid fibrils can be used to organize nanoparticles into predefined, topologically intricate nanostructures, or synthesize miscellaneous materials in order to control the properties of nanoparticle assemblies for potential applications in electronic, optical, and chemical devices. In particular, functionalizing one-dimensional (1D) supporting biomaterials with metal NPs that combine the properties of two functional materials, such as the high conductivity, surface area or the precise chemical functionality of the biotemplate, and the unique plasmonic or catalytic properties of the metal NPs widen their range of applications and, therefore, their important role in nanoscience and nanotechnology (148)-(151).

5.5.1 Hen egg-white lysozyme

Hen egg-white lysozyme (HEWL) is a relatively small globular, monomeric protein. HEWL consist of a polypeptide chain with 129 amino acid residues with four disulfide bonds, and it folds into two structural domains, the α and β ones. The α domain contains a core of hydrophobic side chains that are packed closely together (152); this domain consists of three long helices A (5-15), B (25-35) and C (89-99) (153). In contrast, the β domain of the protein does not display a similar hydrophobic core; instead, hydrogen bonds and a number of small hydrophobic clusters appear to be responsible for defining its tertiary fold, and there is also an

exposed loop region. The secondary structure of lysozyme dissolved in water is composed of 30% α-helix, 18% β-sheet, 22% turn, and 30% unordered structure (153)-(155). It has been also found that the HEWL easily forms amyloid fibrils under several denaturant solution conditions, such acidic conditions and elevated temperature (152)(155). In this regard, it has been proposed that fragment 57-107 is a highly amyloidogenic region, and probably the conversion to the β-sheet structure of the C subdomain is involved in the amyloid fibril formation rather than the other subdomains A and B (152)(153).

It is known that the proteins have multiple potential ion-binding sites within its aminoacid sequence; therefore, protein fibrils can be used in a metallization reaction under relative harsh conditions. In this regard, we take advantage about the spontaneous self-assembly of both HSA and HEWL into amyloid fibrils under fibrillation solution conditions, which enables the use of these fibrils as a template for the construction of 1-D hybrid material, in particular, gold and Fe_3O_4 nanowires. The inherent structural differences between HSA and HEWL fibrils, such as strength, length and stability make lysozyme (Lys) fibers (with widths of 4-10 nm, lengths 0.1-2 μm) most suitable for their use in the obtention of 1-D nanowires.

In this work, gold nanowires were obtained by seeded-growth process. The degree of metal coverage of the biotemplate was controlled by sequential addition of salt gold growth solutions. The hybrid metallic fibrils have been proved to be useful as catalytic substrates, providing a superior catalytical activity when they are incorporated in the reduction reaction of *p*-nitrophenol to p-aminophenol in the presence of $NaBH_4$. The reaction rates obtained were much larger than those reported for other gold hybrid materials such as Au nanoparticle networks, PAMAM-dendrimer-suported spherical nNPs, solid 1-D Au nanobelts, and nanorods, polymer micelles-supported Au NPs or 1-D assemblies of Au NPs (156)-(159). On the other hand, to obtain iron oxide wires, we *in situ* synthesize Fe_3O_4 NPs by precipitation in an alkaline medium by using the electrostatic interaction of iron ions (Fe^{+2} and Fe^{+3}) and the negative charged amino acid residues (mainly aspartic and glutamic acid) located on the protein fibril surfaces. Complete magnetic coating on the protein fibril surface was obtained by sequential nanoprecipitation *in situ* of Fe^{+2} and Fe^{+3} ions (1:2 molar ratio), in the presence of ammonium hydroxide (NH_4OH). Because of their large magnetic properties, the 1-dimensional magnetic nanowires can serve as efficient magnetic resonance image (MRI) contrast agents, with transverse relaxativities larger than those obtained previously for other 1-D nanostructures derived by alternative methods (160)-(162).

CHAPTER 6

Papers on amyloid fibrils

Contents

Existence of Different Structural Intermediates on the Fibrillation Pathway of Human Serum Albumin

Josué Juárez, Pablo Taboada,* and Víctor Mosquera
Grupo de Física de Coloides y Polímeros, Departamento de Física de la Materia Condensada, Facultad de Física, Universidad de Santiago de Compostela, Santiago de Compostela, Spain

ABSTRACT The fibrillation propensity of the multidomain protein human serum albumin (HSA) was analyzed under different solution conditions. The aggregation kinetics, protein conformational changes upon self-assembly, and structure of the different intermediates on the fibrillation pathway were determined by means of thioflavin T (ThT) fluorescence and Congo Red absorbance; far- and near-ultraviolet circular dichroism; tryptophan fluorescence; Fourier transform infrared spectroscopy; x-ray diffraction; and transmission electron, scanning electron, atomic force, and microscopies. HSA fibrillation extends over several days of incubation without the presence of a lag phase, except for HSA samples incubated at acidic pH and room temperature in the absence of electrolyte. The absence of a lag phase occurs if the initial aggregation is a downhill process that does not require a highly organized and unstable nucleus. The fibrillation process is accompanied by a progressive increase in the β-sheet (up to 26%) and unordered conformation at the expense of α-helical conformation, as revealed by ThT fluorescence and circular dichroism and Fourier transform infrared spectroscopies, but changes in the secondary structure contents depend on solution conditions. These changes also involve the presence of different structural intermediates in the aggregation pathway, such as oligomeric clusters (globules), bead-like structures, and ring-shaped aggregates. We suggest that fibril formation may take place through the role of association-competent oligomeric intermediates, resulting in a kinetic pathway via clustering of these oligomeric species to yield protofibrils and then fibrils. The resultant fibrils are elongated but curly, and differ in length depending on solution conditions. Under acidic conditions, circular fibrils are commonly observed if the fibrils are sufficiently flexible and long enough for the ends to find themselves regularly in close proximity to each other. These fibrils can be formed by an antiparallel arrangement of β-strands forming the β-sheet structure of the HSA fibrils as the most probable configuration. Very long incubation times lead to a more complex morphological variability of amyloid mature fibrils (i.e., long straight fibrils, flat-ribbon structures, laterally connected fibers, etc.). We also observed that mature straight fibrils can also grow by protein oligomers tending to align within the immediate vicinity of the fibers. This filament + monomers/oligomers scenario is an alternative pathway to the otherwise dominant filament + filament manner of the protein fibril's lateral growth. Conformational preferences for a certain pathway to become active may exist, and the influence of environmental conditions such as pH, temperature, and salt must be considered.

INTRODUCTION

β-Sheet-based assemblies have attracted much interest from multidisciplinary researchers because of their association with a variety of diseases and their emerging potential in material science and biotechnology (1,2). Protein misfolding and self-assembly into highly ordered β-sheet-rich fibrillar assemblies known as amyloid fibrils are common features of a growing class of systemic and neurodegenerative diseases, including Alzheimer's, Parkinson's, and Huntington's diseases; senile systemic amyloidoses; type II diabetes (3,4); and many others. The ability to fibrillate is independent of the original native structure of the protein, whose amino acid sequence primarily appears to play a key role in terms of filament arrangement (5), fibrillation kinetics (6), and overall yield and stability of the fibrils (7,8). Fibrillation originates under conditions in which proteins are partially destabilized or completely unfolded (9), and the formation of the amyloid fibrils reflects an alternative to the native packing conformational struggle of a polypeptide chain to 1), reduce its surface-accessible area; 2), saturate hydrogen bonding; and 3), reach an alternative ''nonnative'' global free energy minimum (10). Therefore, investigators have emphasized understanding and inhibiting amyloid formation more so than amyloid dissociation and clearance. Although the stability of β-sheet-rich amyloid fibrils against proteases, acids, and chemical denaturants has been shown, increasing evidence from human (11) and in vitro studies indicates that a dynamic structure exists within amyloid fibrils and suggests that the process of amyloid formation is reversible (12). These findings, along with the fact that strategies aimed at stabilizing amyloid fibrils and/or accelerating their clearance seem to reverse the disease phenotype (13,14), suggest that a detailed understanding of the formation, stability, and dynamic behavior of amyloid fibrils is critically important to the development of therapeutic strategies for amyloid diseases. Thus, the reversible untangling of amyloid architecture and intrafibrillar packing of the β-pleated sheets is a key issue to consider in designing inhibitors of fibrillar growth (15), and insights into the fibrillar assembly mechanisms may help elucidate the etiology of the ''prion diseases'', provided that the subtle structural differences underlying the puzzling phenomenon of ''prion strains'' can be understood (16).

Submitted September 30, 2008, and accepted for publication December 1, 2008.

*Correspondence: pablo.taboada@usc.es

Editor: Ruth Nussinov.

0006-3495/09/03/2353/18 $2.00

doi: 10.1016/j.bpj.2008.12.3901

Because of the physiological importance of human serum albumin (HSA) as a carrier protein and blood pressure regulator, and its propensity to easily aggregate in vitro, HSA has become a good model for protein aggregation studies. Moreover, as the phenomenon of protein aggregation appears to reflect certain generic ''polymeric'' features of proteins (17), studying mechanisms of protein aggregation in model systems is extremely useful for gaining a better understanding of the molecular mechanisms of disease-associated amyloidogenesis.

Under physiological conditions, HSA consists of 585 amino acids in a single polypeptide chain, with a globular structure composed of three main domains that are loosely joined together through physical forces and six subdomains that are wrapped by disulfide bonds. The protein contains 17 disulfide bridges and one free SH group, which facilitates dimerization and also influences higher-order association. Native HSA lacks any properties that suggest a predisposition to form amyloid fibrils, since most of its sequence (>60%) is arranged in an α-helix structure, with subsequent tightening of its structure through intramolecular interactions such as hydrogen bonds. Therefore, serum albumin aggregation is promoted under conditions that favor partly destabilized monomers and dimers, such as low pH, high temperature, and the presence of chemical denaturants (18). In a recent report (19), we showed that partially destabilized HSA molecules form amyloid-like fibrils and other types of aggregates under different solution conditions. These fibrils feature the structural characteristics of amyloids: x-ray diffraction (XRD) patterns, affinity to Congo Red (CR) and thioflavin T (ThT), birefringence, and high stability. We now extend that previous work to shed further light on the kinetics and hierarchical assembly of HSA fibril formation, linking the morphological structural transitions of aggregated protein intermediates to conformational events on protein structure as analyzed by means of different biophysical and spectroscopic methods. In this way, we present a systematic investigation of the relationship between protein conformation and the amyloid-like self-assembly pathway for HSA under different solution conditions. To this end, we incubated the protein under different thermal and solvent conditions and analyzed the protein conformation changes upon incubation. We additionally imaged different structural intermediates on the HSA fibrillation pathway depending on solution conditions. In this way, we sought to uncover the structural features underlying the formation of possibly cytotoxic HSA assemblies.

MATERIALS AND METHODS

Materials

HSA (70024-90-7), CR, and ThT were obtained from Sigma (St. Louis, MO) and used as received. All other chemicals were of the highest purity available.

Preparation of HSA solutions

Protein was used after further purification by liquid chromatography using a Superdex 75 column equilibrated with 0.01 M phosphate. Experiments were carried out using double-distilled, deionized, and degassed water. The buffer solutions used were glycine + HCl (I = 0.01 M) for pH 3.0, and sodium monophosphate-sodium diphosphate for pH 7.4 (I = 0.01 M), respectively. HSA was dissolved in each buffer solution to a final concentration of typically 20 mg/mL and dialyzed extensively against the proper buffer. Protein concentration was determined spectrophotometrically using a molar absorption coefficient of 35,219 M^{-1} cm^{-1} at 280 nm (20). Before incubation, the solution was filtered through a 0.2 μm filter into sterile test tubes. Samples were incubated at a specified temperature in a refluxed reactor. Samples were taken out at intervals and stored on ice before addition of CR or ThT.

Seeding solutions

To test whether seeding with preformed aggregates increases the rate of HSA aggregation under the different conditions in which fibrils are formed, a protein solution was incubated for 24 h and an aliquot that corresponded to 10% (w/w) of the total protein concentration was then added to a fresh protein solution.

CR binding

Changes in the absorbance of CR dye produced by binding onto HSA were measured in an ultraviolet-visible spectrophotometer (DU series 640; Beckman Coulter, Fullerton, CA) operating at 190–1100 nm. All measurements were made in the wavelength range of 220–500 nm in matched quartz cuvettes. Protein solutions were diluted 20- to 200-fold into a buffer solution with 5 μM of CR (Acros Organics, Geel, Belgium). Spectra in the presence of the dye were compared with those of the buffer containing CR in the absence of protein and also with those corresponding to the protein solution without dye.

ThT spectroscopy

Protein and ThT were dissolved in the proper buffer at a final protein/dye molar ratio of 50:1. Samples were continuously stirred during measurements. Fluorescence was measured in a Cary Eclipse fluorescence spectrophotometer equipped with a temperature control device and a multicell sample holder (Varian Instruments, Palo Alto, CA). Excitation and emission wavelengths were 450 and 482 nm, respectively. All intensities were background-corrected for the ThT fluorescence in the respective solvent without the protein.

Protein fluorescence

To examine the conformational variations around the Tryp residue of HSA, fluorescence emission spectra were recorded with a Cary Eclipse fluorescence spectrophotometer equipped with a temperature control device and a multicell sample holder (Varian Instruments). HSA samples were excited at 295 nm, which provides no excitation of tyrosine residues and, therefore does not cause emission or energy transfer to the lone side chain. Slit widths were typically 5 nm.

Circular dichroism

Far- and near-ultraviolet (UV) circular dichroism (CD) spectra were obtained using a JASCO-715 automatic recording spectropolarimeter (Jasco, Tokyo, Japan) with a JASCO PTC-343 Peltier-type thermostated cell holder. Quartz cuvettes with 0.2 cm pathlength were used. CD spectra were obtained from aliquots withdrawn from the aggregation mixtures at the indicated conditions and recorded between 195 and 300 nm at 25°C. The mean residue ellipticity θ (deg cm^2 $dmol^{-1}$) was calculated from the formula:

$\theta = (\theta_{obs}/10)(MRM/lc)$, where θ_{obs} is the observed ellipticity in deg, MRM is the mean residue molecular mass, l is the optical pathlength (in centimeters), and c is the protein concentration (in g mL^{-1}). To calculate the composition of the secondary structure of the protein, SELCON3, CONTIN, and DSST programs were used to analyze far-UV CD spectra. Final results were assumed when data generated from all programs showed convergence (21).

XRD

XRD experiments were carried out using a Siemens D5005 rotating anode x-ray generator. Twin Göbel mirrors were used to produce a well-collimated beam of CuKα radiation ($\lambda = 1.5418$ A). Samples were put into capillary with a diameter of 0.5 mm. X-ray diffraction patterns were recorded with an imaging plate detector (AXS F.Nr. J2-394).

Fourier transform infrared spectroscopy

Fourier transform infrared (FTIR) spectra of HSA in aqueous solutions were determined by using an FTIR spectrometer (model IFS-66v; Bruker) equipped with a horizontal ZnS ATR accessory. The spectra were obtained at a resolution of 2 cm^{-1} and generally 200 scans were accumulated to obtain a reasonable signal/noise ratio. Solvent spectra were also examined under the same accessory and instrument conditions. Each different sample spectrum was obtained by digitally subtracting the solvent spectrum from the corresponding sample spectrum. Each sample solution was repeated three times to ensure reproducibility and averaged to produce a single spectrum.

Transmission electron microscopy

For transmission electron microscopy (TEM), suspensions of HSA were applied to carbon-coated copper grids, blotted, washed, negatively stained with 2% (w/v) of phosphotungstic acid, air dried, and then examined with a Phillips CM-12 transmission electron microscope operating at an accelerating voltage of 120 kV. Samples were diluted 20- to 200-fold when necessary before deposition on the grids.

Scanning electron microscopy

Suspensions of HSA were applied to glass-coated stainless-steel grids, blotted, washed, air dried, and then examined with an LEO-435VP scanning electron microscope (Leica Microsystems GmbH, Wetlar, Germany) operating at an accelerating voltage of 30 kV. Samples were diluted 20- to 200-fold when necessary before deposition on the grids. Microanalysis of the scanning electron microscopy (SEM) samples was also performed to avoid the presence of impurities.

Atomic force microscopy

Atomic force microscopy (AFM) images were recorded in tapping mode by using a multimode SPM microscope equipped with a Nanoscope IIIa controller from Digital Instruments (Santa Barbara, CA). The microscope was coupled to an AS-12 resp. E-scanner and an Extender Electronics Module EX-II, which allows acquisition of phase images. The AFM probes were typically silicon SPM sensors (NCHR Nanosensors, Neuchatel, Switzerland). Immediately after incubation, the protein samples were diluted 20–400 times onto freshly cleaved muscovite mica (Sigma) attached to a magnetic steel disc that served as the sample holder. The abrupt dilution of the samples immediately quenched the concentration-dependent aggregation process. The AFM samples were dried on air or under nitrogen flow when required. Control samples (freshly cleaved mica, and mica and buffer solution) were also investigated with AFM to exclude possible artifacts. Height and phase-shift data were collected in the trace and the respective retrace direction of the raster. The scan rate was tuned proportionally to the area scanned and was kept within the 0.35–2 Hz range.

RESULTS

It is generally accepted that amyloid formation usually is a result of misfolded and partially unfolded states acting in competition with the normal folding pathways (22–24). The HSA molecule is known to undergo several well-organized changes during its conformation, usually under nonphysiological conditions, as follows:

1. The N-F transition between pH 5.0 and 3.5 involves the unfolding and separation of domain III without significantly affecting the rest of the protein molecule (25,26). The F form is characterized by a dramatic increase in viscosity, lower solubility, and a significant loss of helical content.
2. The F-E transition occurs between pH 3.5 and 1.2, and is accompanied by a further protein expansion with a loss of the intradomain helices of domain I. In addition, the E form involves an increase in protein intrinsic viscosity and a rise in the hydrodynamic axial ratio from ~4 to 9 (27).
3. The N-B transition occurs between pH 7.0 and 9.0, with a slight reduction in helical content affecting the two interdomain helices and a small increase in sheet structure (28).
4. In the presence of denaturant agents, such as urea, HSA shows a two-step, three-state transition with an intermediate (I) characterized by unfolding of the domain III and partial but significant loss of native conformation of domain I (29).

Therefore, an easy way to obtain at least partially denaturated states is to induce a temperature-induced or solvent-induced protein denaturation process through incubation. Thus, HSA was subjected to conditions previously found to be effective for protein aggregation, in particular those that induce amyloid-like fibril formation (19,30). HSA solutions were incubated at a concentration of 20 mg/mL in 0.01 M sodium phosphate buffer, pH 7.4, or 0.01 M glycine buffer, pH 3.0, in the presence of 0 or 50 mM of added NaCl at 25°C or 65°C for 15 days. We chose 65°C as the incubation temperature because HSA temperature-induced denaturation takes place through a two-state transition with a first melting temperature, T_m, of ~56°C and a second T_m of ~62°C (31,32) as a consequence of the sequential unfolding of the different domains of the protein, in particular, the IIA and IIIA subdomains. Moreover, as the pH becomes more acidic, T_m becomes lower. We confirmed these melting temperatures under our solution conditions by fluorescence spectroscopy, and the results were in close agreement with previously reported data (see Table S1 in the Supporting Material). Therefore, it can be inferred that aggregation is unfavorable below 65°C because protein folding competes with and suppresses amyloid formation. It is known that hydrogen bonding is weakened as temperature rises, but the hydrophobic interaction becomes strengthened (33). As the heating process continues, some of the cooperative hydrogen bonds

that stabilized helical structure begin to break and expose hydrophobic groups to the solvent, partially unfolding the protein structure, which favors aggregation.

Physiological conditions: kinetics and amyloid self-assembly of HSA

The propensity of protein solutions to form amyloid-like aggregates under physiological conditions was assessed by means of ThT fluorescence and CR absorbance measurements. These two dyes specifically bind to ordered β-sheet aggregates and, notably, to amyloid fibrils (34,35). Both assays are necessary because positive ThT binding sometimes does not occur with certain amyloid fibril systems (36). Before incubation, native HSA does not display a capacity to bind ThT. When incubated at physiological pH and room temperature, the fluorescence emission intensity for the protein at 482 nm is negligible, suggesting that HSA does not form amyloid fibrils or other types of fluorescent aggregates under these conditions. When the temperature is raised to 65°C, a time-dependent increase in fluorescence is observed (Fig. 1, *a* and *b*). The kinetics of HSA involved the continuous rising of ThT fluorescence during the early periods of the incubation procedure, and exhibited no discernible lag phase until a quasi-plateau region was attained in the timescale analyzed. The addition of electrolyte favors a faster formation of amyloid fibrils as a consequence of the screening of electrostatic repulsions between protein molecules (37). In fact, a gel phase can be observed after 4 days of incubation, which denotes an enhanced development of fibril formation because cross-links can be formed more easily, resulting in a lower critical percolation concentration.

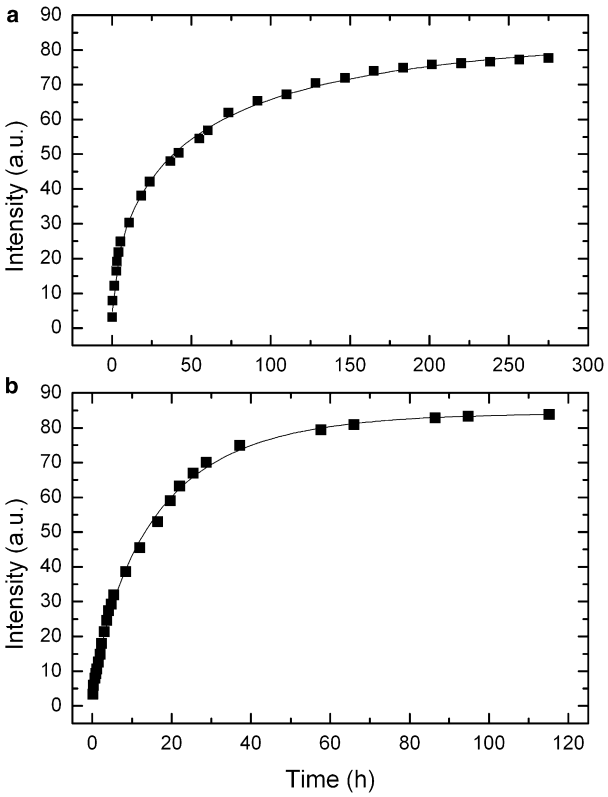

FIGURE 1 Time evolution of ThT fluorescence in HSA solutions incubated at 65°C at pH 7.4 in the (*a*) absence and (*b*) presence of 50 mM NaCl.

ThT fluorescence curves were fitted by means of nonlinear square curve-fitting to a stretched exponential function $F = F^{\infty} + \Delta F\exp(-[k_{sp}t]^n)$ to obtain information on the kinetics of amyloid formation. F, F^{∞}, and ΔF are the observed fluorescence intensity at time t, the final fluorescence intensity, and the fluorescence amplitude, respectively, and k_{sp} is the rate of spontaneous fibril formation. Although the interpretation of the parameters involved in this equation is not straightforward, these are useful for empiric descriptions of the complex reactions whose kinetics is not easily modeled (38,39). Values of k_{sp}, n, and ΔF determined in this way under the different conditions are shown in Table 1. Values of $n < 1$ indicated that the kinetics can be approximated to several exponential functions indicative of the existence of multiple events in the amyloid formation. Furthermore, larger k_{sp} values in the presence of electrolyte corroborate the more-efficient aggregation due to electrostatic screening under high ionic strength conditions.

CR absorption also corroborates the formation of amyloid fibrils, displaying a progressive red shift from 495 to ~530 nm of the differential absorption maximum at 65°C in both the absence and presence of added electrolyte, a typical feature of amyloid fibers (35). Since absorption of HSA alone after incubation contributes to only ~15% of the increase in CR absorption, the change in absorption is mainly caused by the formation of CR-binding species (see Fig. S1 in the Supporting Material).

Fibrillation is independent of seeding at physiological pH

Typical fibrillation processes involve a lag phase followed by a relatively rapid elongation phase that stabilizes when all

TABLE 1 Kinetic parameters of the self-assembly process of HSA solutions

	F^{∞}	ΔF	n	k_{sp} (h^{-1})
		pH 7.4		
65°C				
0 mM NaCl	85	83	0.56	0.019
50 mM NaCl	85	83	0.82	0.064
		pH 3.0		
25°C				
0 mM NaCl	10	8	1.34	0.007
50 mM Na Cl	13	11	1.57	0.007
65°C				
0 mM NaCl	8/30	6/22	1.25/3.6	0.144/0.005
50 mM NaCl	59	57	0.96	0.010

monomers have been incorporated into fibrils (40–42). In our case, the absence of a lag phase at pH 7.4 would suggest that nuclei are either formed very rapidly or the aggregation process we monitor is not a classical nucleation-based fibrillation. If nuclei consist of more than one molecule, their formation will be reduced if the HSA concentration is lowered. Nevertheless, when the protein concentration was decreased to 0.5 and 2 mg/mL at 65°C, we did not observe the appearance of a lag phase (figure not shown). In addition, another feature that confirms a continuous fibrillation process without a nucleation step is the absence of any remarkable effect on the fluorescence curves when protein seeds were added to protein solutions followed by subsequent incubation (see Fig. S2). The aggregation rate during the growth phase was unchanged by the addition of preformed aggregates and followed apparent first-order kinetics. These characteristics suggest that aggregation does not require nucleation, i.e., each protein monomer association step is bimolecular and effectively irreversible, and there is no energy barrier to aggregate growth. As discussed in detail below, TEM pictures showed the formation of spherical oligomers after very short incubation times. This usually occurs by a mechanism of classical coagulation, or downhill polymerization (43), that does not require a nucleation step.

Structural changes upon aggregation at physiological conditions: secondary structure

To gain insight into the structural protein modifications upon formation of amyloid-like aggregates, we recorded CD, FTIR, and tryptophan (Tryp) fluorescence spectra. As a supplement to ThT and CR assays, which provide information only about the formation of fibrillar protein assemblies, far-UV CD and FTIR data reveal the overall protein secondary structural composition and their evolution to form amyloid-like or amorphous aggregates. On the other hand, near-UV CD and Tryp fluorescence data denote changes in protein tertiary structure (for the latter technique, particularly in domain II of HSA).

Fig. 2, *a* and *b*, show far-UV CD spectra of HSA at pH 7.4 at 25°C and 65°C. The spectra at room temperature in the absence of added salt show two minima—one at 208 and other at 222 nm—characteristic of helical structure, which remains unmodified upon incubation. When electrolyte is present, a small decrease in ellipticity, [θ], occurs as a consequence of small changes in protein structure originating from the formation of some amorphous aggregates in solution, as shown in Fig. 2 *a*. In contrast, when the temperature is raised to 65°C, the minimum at 222 nm progressively disappears and [θ] at 208 nm also strongly reduces (Fig. 2 *b*). This indicates that high-temperature conditions spawn intermediates that are clearly less helical than the starting conformations. This change in CD spectra suggests the increment of either β-sheet or loop structures, as discussed in detail further below. The intensity loss of the 222 nm band indicates that the increase in random coil/β-sheet conformations is accompanied by a reduction in the α-helical content of the protein structure. At longer incubation times in the absence of added salt in solution (~72 h), the CD spectrum resembles that typical of proteins with high proportions of β-sheet structure, which are characterized by a minimum at ~215–220 nm and small [θ] values as a consequence of the presence of amyloid-like aggregates in solution. On the other hand, no significant changes in far-UV CD spectra are observed when electrolyte is added to solutions, except that the characteristic features of β-sheet structure are present at earlier incubation times at elevated temperature. A larger decrease in [θ] is also detected as a consequence of the increased number and size of scattering objects in solution, which agrees with the formation of a fibrillar gel upon longer incubation times.

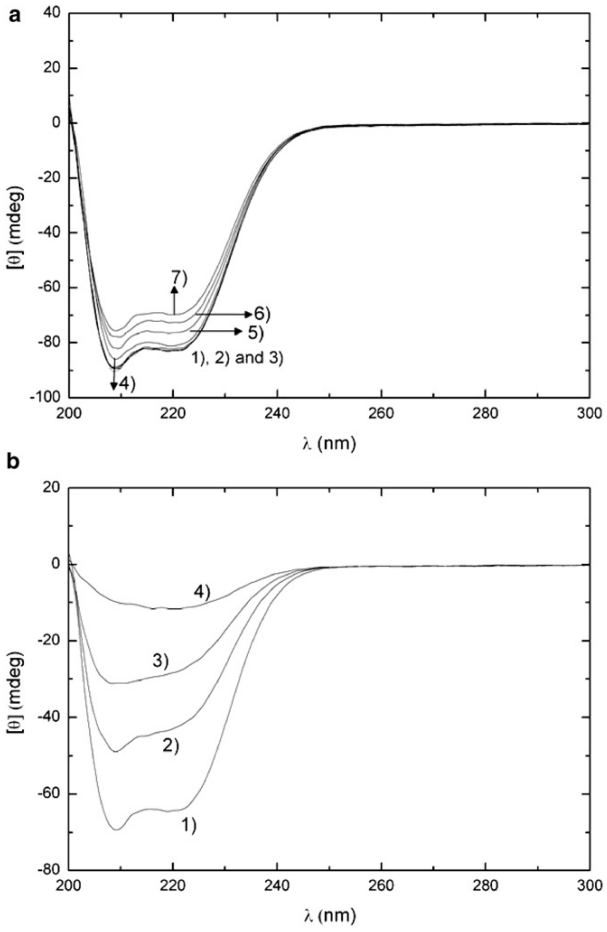

FIGURE 2 (*a*) Far-UV spectra of HSA solutions at 25°C in the presence of 50 mM NaCl at pH 7.4 at 1), 0 h; 2), 24 h; 3), 48 h; 4), 100 h; 5), 200 6), and 7), 250 h of incubation. (*b*) Far-UV spectra of HSA solutions at 65°C in the presence of 50 mM NaCl at 1), 0 h; 2), 12 h; 3), 24 h; and 4), 48 h of incubation.

Fig. 3 depicts the temporal evolution of the secondary structure composition as revealed by CD analysis (21). At pH 7.4 and room temperature, the initial α-helix content is ~59%, the β-sheet conformation is ~5%, the turn content

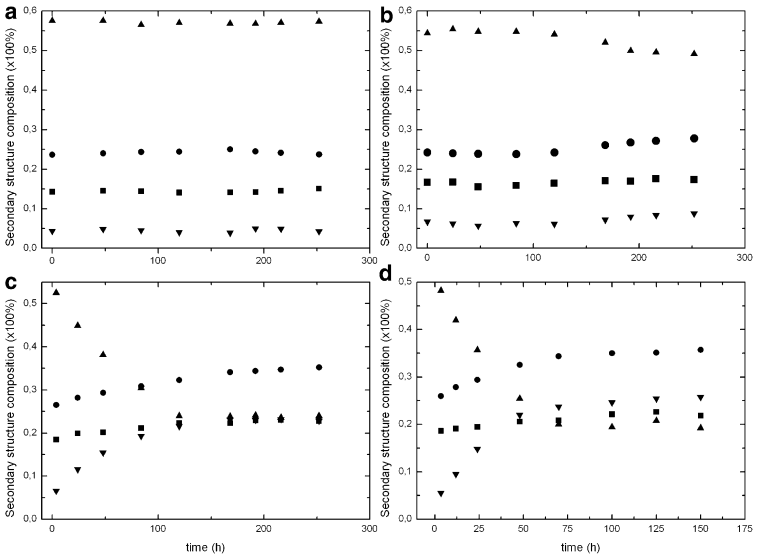

FIGURE 3 Time evolution of secondary structure compositions of HSA solutions at pH 7.4 at 25°C (*a* and *b*) or 65°C (*c* and *d*) in the absence and presence of 50 mM NaCl, respectively. (▲) α-helix, (■) β-turn, (●) unordered, and (▼) β-sheet conformations.

is ~13%, and the remaining random coil content is ~23%, in agreement with previous reports (25). In the presence of added electrolyte, no significant alterations in the structure compositions are observed upon incubation; the initial α-helix content is slightly reduced to ~55%, in contrast to a very small increase in turn and β-sheet conformations. After ~150 h of incubation, an additional slight decrease in α-helix is observed due to an enhancement of protein aggregation, i.e., the formation of a certain amount of protein aggregates is observed, which is a characteristic feature of globular proteins under high ionic strength conditions.

On the other hand, protein conformational compositions at 65°C after incubation indicate an increase in β-sheet conformation from ~5% to ~21% at the expense of the α-helix content (which diminishes from ~59% to ~20%) in the absence of electrolyte. This is also reflected by the decrease in the CD signal and the shift of the spectral minimum from 208 nm to longer wavelengths, as noted above. Coil and turn conformations also change through the incubation process, with values of ~27–34% and ~17–21%, respectively. The alteration in structure composition seems to be stronger when salt is added, due to electrostatic screening, which favors protein disruption and association by modifying the balance of interactions, with final β-sheet and α-helix contents of ~26% and ~19%, respectively (Fig. 3). Moreover, changes in secondary structure take place during the first part of the incubation process in both the absence (~90 h) and presence of electrolyte (~50 h), respectively, and occur more rapidly under the latter condition. At very long incubation times (>150 h) under high ionic strength conditions, the increased scattering from the fibrillar aggregates makes it difficult to estimate the secondary structure; thus, these results are not shown in Fig. 3.

FTIR spectra were recorded at the beginning and end of the incubation process by monitoring the observed changes in the shape and frequency of the amide I and II bands, and the results corroborated the CD data. Before incubation, two major absorption peaks in the spectral region of interest were observed: the amide I band at 1653 (1652) cm^{-1} and the amide II band at 1542 (1544) cm^{-1} in both the original and second derivative IR spectra, respectively. This indicates the predominant structural contribution of major α-helix and minor random coil structures, in agreement with CD data (44–46). For the amide I band (Fig. 4 *a*), a shoulder at ~1630 cm^{-1} can be also observed in the second derivative spectra that is related to intramolecular β-sheet structure. Additional peaks at ~1689 and 1514 cm^{-1} would correspond to β-turn and tyrosine absorption, respectively (45). All of these peaks were also observed in the presence of electrolyte at room temperature as

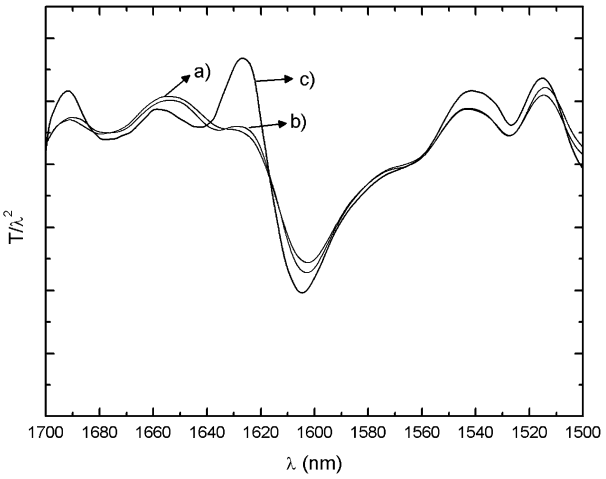

FIGURE 4 Second derivative of FTIR spectra at pH 7.4 of (*a*) native HSA at 25°C before incubation, (*b*) HSA at 25°C in the presence of 50 mM NaCl, and (*c*) HSA at 65°C in the absence of electrolyte.

incubation proceeded (Fig. 4 *b*), compatible with little changes in secondary structure composition, as noted above.

After incubation at 65°C, a red shift of the amide I band from 1652 to 1658 cm^{-1} and a blue shift of the amide II band to 1542 cm^{-1} in the second derivative spectrum are indicative of a certain increase of disordered structure, as revealed by far-UV CD (Fig. 4 *c*). The appearance of a well-defined peak around 1628 cm^{-1} (1626 cm^{-1} in the presence of added salt) points to a structural transformation from an intramolecular hydrogen-bonded β-sheet to an intermolecular hydrogen-bonded-β-sheet structure (47). The spectrum also shows a high-frequency component (~1692 cm^{-1}) that would suggest the presence of an antiparallel β-sheet (48). In addition, a little shoulder around 1534 cm^{-1} also was assigned to β-sheet after incubation at high temperature (49). The increase in the band associated with β-sheet in the FTIR spectra correlates well with the large changes in CD spectra. On the other hand, peak shifts are slightly more abrupt when electrolyte is present in solution because the aggregation is stronger (plot not shown). This leads to the formation of a fibrillar gel favored by the decrease in electrostatic repulsions and a change in the hydration layer surrounding the protein molecules that allows interfibrillar attachment.

Structural changes upon aggregation at physiological conditions: tertiary structure

At room temperature, the near-UV CD spectrum showed two minima at 262 and 268 nm and two shoulders around 275 and 285 nm, characteristic of disulphide and aromatic chromophores and the asymmetric environment of the latter (Fig. 5 *a*) (50). These features are significantly retained during incubation in the presence of electrolyte excess despite the formation of some amorphous aggregates in solution, as noted above (figure not shown). On the other hand, when the incubation temperature is raised to 65°C, important alterations in the near-UV CD spectra occur in both the absence and presence of electrolyte: ellipticity decreases, and the minima at 262 and 268 nm progressively disappear as incubation proceeds. In addition, a significant loss of fine structure detectable in the region of 270–295 nm also occurs. Nevertheless, these changes in near-UV CD data are less marked than in far-UV measurements because secondary structural changes are more sensitive to temperature than tertiary structural changes (51). These effects corroborate alterations in tertiary structure upon fibrillation conditions.

The behavior described by near-CD UV measurements is also supported by tryptophanyl fluorescence data. HSA has a single tryptophanyl residue, $Tryp^{214}$, located in domain II. A very small change in fluorescence emission occurs with incubation at room temperature in the presence of electrolyte, confirming the existence of little variations in tertiary structure, in agreement with previous data (not shown). In contrast, when the temperature is raised to 65°C, a 4 nm hypsochromic shift (from 341 to 337 nm) takes place accompanied by a reduction in fluorescence intensity: the domain II of HSA unfolds in such a way that the Trp^{214} residue of HSA located at the bottom of a 12 Å deep crevice (52) finds itself in a more hydrophobic environment (32). As incubation at elevated temperature proceeds, conversion of protein molecules to fibrils is accompanied by an additional burial of the Tryp residue, as indicated by the decrease of the Tryp fluorescence emission intensity (Fig. 5 *b*) and the further blue shift of the emission maximum from 337 to 333 nm (53). All of this points to the strong involvement of tertiary structure changes of domain II of HSA in the fibrillation mechanism. This change is enhanced and occurs more rapidly in the presence of added electrolyte, which confirms a larger structure alteration as a consequence of enhanced intermolecular interactions to give fibrillar assemblies. This also agrees with the increasing content of β-sheet conformation revealed by CD and FTIR measurements.

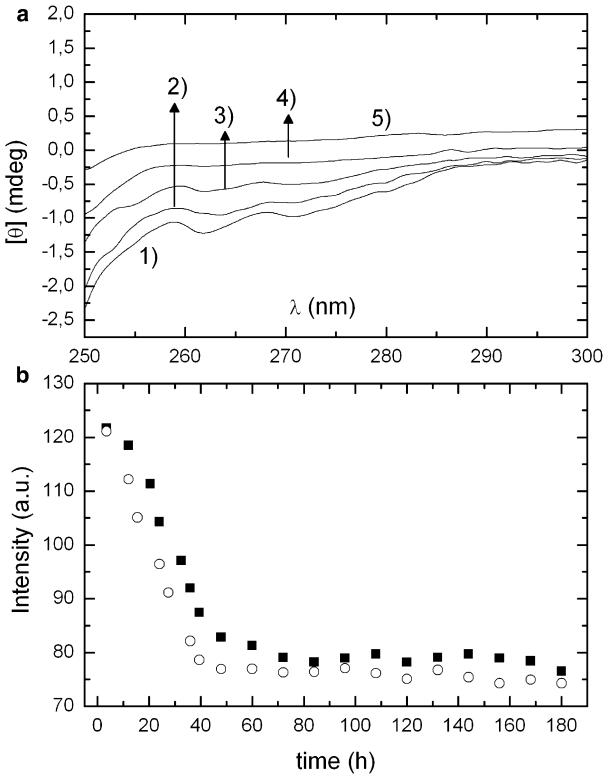

FIGURE 5 (*a*) Near-UV CD spectra of HSA solutions at pH 7.4 and 65°C in the absence of electrolyte at 1), 0 h; 2), 6 h; 3), 12 h; 4), 24 h; and 5), 48 h. (*b*) Time evolution of Trp fluorescence of HSA solutions at 65°C in the (■) absence and (○) presence of 50 mM NaCl.

In situ observation of fibrillar structures at physiological pH: TEM

TEM pictures were recorded at different stages of the incubation period for each of the conditions described above. Distinct time-dependent morphological stages can be

observed in these images. Thus, at room temperature neither fibrils nor other types of aggregates are detected, except for small amorphous protein clusters observed in the presence of electrolyte after a long incubation period (150 h), which possess a largely helical structure (Fig. 6 *a*). In contrast, when the temperature is raised to 65°C, fibril formation is observed. Electron microscopy indicates that aggregation leads first to a globular species that subsequently converts to fibrils with a curly morphology. The fibrillation pathway in the presence of electrolyte is very similar to that observed in its absence but it takes place in a shorter timescale, in agreement with previous results. Fig. 6, *b–j*, show electron micrographs of the sample heated at 65°C at different steps of the incubation period in the presence of 50 mM of electrolyte. The number and length of the fibrils has increased in relation to other structures, although several morphologies can be observed throughout incubation.

Small spherical clusters of ~20 nm formed by protein oligomers are observed (Fig. 6 *b*) at short incubation times (5 h). These aggregates present relatively few changes in their tertiary and secondary structures, as shown by CD and fluorescence data. With further incubation (Fig. 6 *c*, 15 h), a certain elongation of these spherical aggregates can be observed. This bead-like structure at short incubation times arises from what appears to be attractive interactions between spherical proteins aggregates, as shown in Fig. 6 *d-1* (see also Fig. S3), which may result in an increased exposure of hydrophobic residues, giving rise to more elongated structures. This elongation involves a conformational conversion of protein structure to consolidate the structure, and in all probability it implies changes in the hydrogen-bonding status (Fig. 6 *d-2*). This is in agreement with a further development in ThT fluorescence and decreases in both helical content and Tryp fluorescence at this incubation point, as shown previously. On the other hand, we did not find evidence of formation of elongated structures by longitudinal fusion of oligomers, as recently reported (54).

Bead-like structures progressively become more elongated upon incubation (35 h) due to mutual interactions between these structures and subsequent annealing, and convert into short protofibrils (Fig. 6 *e*), in agreement with a decrease in helical structure as revealed by CD. Alterations in the conformational structure of these oligomers and subsequent elongation via monomer addition may also be present; however, the TEM resolution did not allow us to confirm that. Several authors reported a tendency for these bead-like structures to transform into fibrillar structures at elevated temperatures caused by partial unfolding of the protein molecules and giving rise to conditions conductive to fibril formation (55–57).

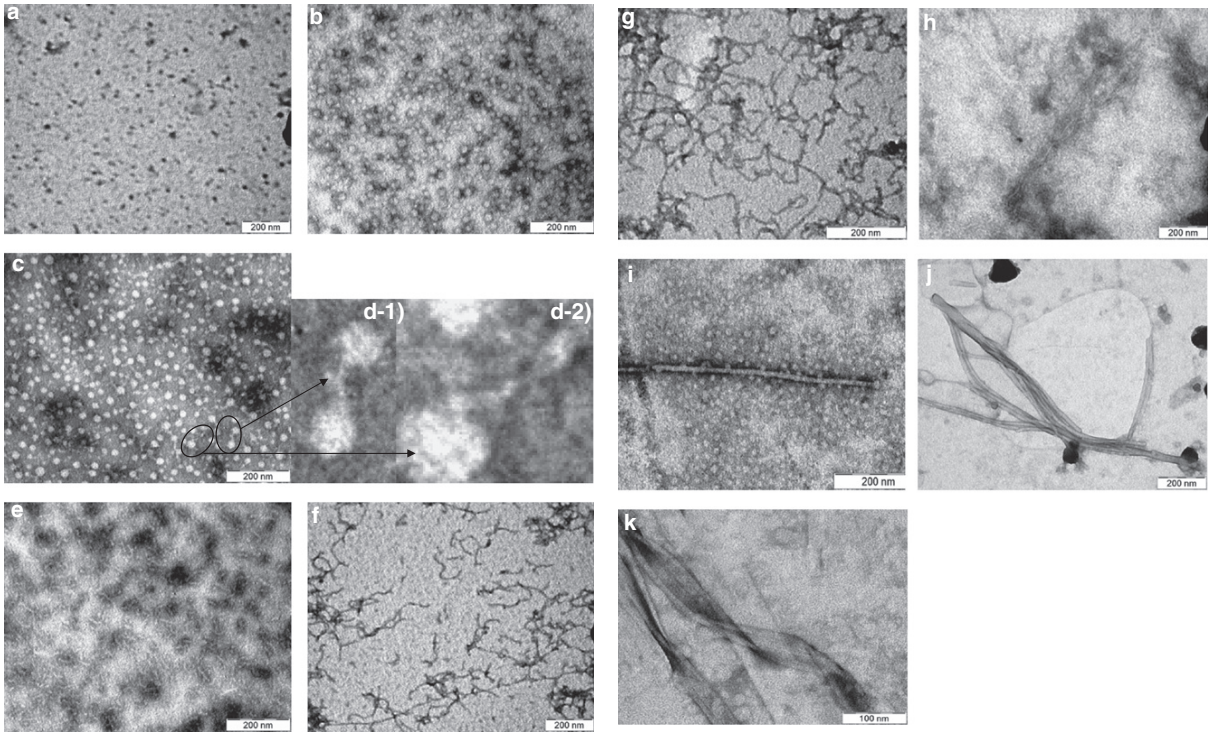

FIGURE 6 TEM pictures of the different stages of the HSA fibrillation process at pH 7.4: (*a*) at 25°C in the presence of 50 mM NaCl after 150 h of incubation, and at 65°C in the presence of 50 mM NaCl after (*b*) 5 h; (*c*) and (*d*) 15 h (part *d* shows the elongation of oligomers to give bead-like structures); (*e*) 35 h (where short protofibrils are observed); (*f*) 45 h; (*g*) 50 h (where long curly fibrils are seen); and (*h–k*) after 72 h. Part *i* shows the addition of oligomers to mature fibrils, *j* shows the association of mature fibrils in bundles, and *k* shows mature fibrils with ribbon-like structure.

Further incubation results in the presence of more fibrils, which increase in length as incubation proceeds (Fig. 6, *f* and *g*). After 2 days of incubation, numerous longer curly-branched and interconnected fibrils are present (Fig. 6 *g*), with lengths and widths characteristic of classical amyloid fibrils (i.e., between 0.5 and several micrometers in length and 9–10 nm in width (3,5,9)), as detected by TEM and AFM (see Fig. 6 *g* and Fig. S4). The appearance of this structure coincides well with the plateau region of ThT binding, the far UV-CD profiles characterized by minima around 215–220 nm, and the intermolecular β-sheet structure observed by FTIR. Most fibrils appear curly and interconnected, and some of them are even circular, as observed previously for other proteins, such as β_2 microglobulin (58) and α-crystallin (56).

If the incubation time is extended further (3 days), one can observe mature straight fibrils, which can be seen as a structural evolution of curly fibrils (Fig. 6 *h*). Mature fibrils are thicker and stiffer than single fibrils and seem to be formed by lateral (side-by-side) assembly of two or more individual filaments. These mature fibrils are less numerous in the absence of electrolyte because the electrostatic screening is lower, avoiding direct contact between constitutive fibrils. We have also observed that lateral interactions of single particles collaborate in growing these straight mature fibrils (57). Scrutiny of the protein aggregates indicates that HSA particles and clusters tend to align within the immediate vicinity of the fibers (Fig. 6 *i*), serving the single fiber as a lateral template or scaffold for small protein molecules, and would constitute a subcomponent in mature fibrils. It is worth mentioning that some fibril solutions when analyzed by SEM show the existence of very long fibers, exceeding 200 μm (see Fig. S5). We think that this effect may result from the air-drying process favoring attractive interactions between single fibers during the solvent removal.

In addition, a structural diversity of mature fibrils is noted: flat ribbons are observed in solution, as well as long, straight fibril ensembles (Fig. 6 *j*). This polymorphism may arise from variations in the quaternary structure, the manner in which protofilaments self-associate, or the protofilament substructure (e.g., in the details of hydrogen-bonding networks and side-chain packing) (59). Finally, one of the characteristic traits of the mature amyloid fibrils is their tendency to bend, twist, and agglomerate. Fig. 6 *k* shows laterally connected fibers that split over a certain distance or overlap each other. The extent and rate of this growth is dependent on solution conditions and lateral interactions between fibrils, which are responsible for the thickening of the mature fibrils and the formation of suprafibrillar aggregates. Thus, we conclude that pseudo-globular aggregates rearrange slowly to form linear, curly fibrils. These may be sufficient to produce a high-affinity template that is subsequently elongated by monomeric units or other fibrils, and can lead to the formation of ordered, straight, or ribbon-like fibrillar structures.

Fibril structure: XRD

The amyloid-like character of the fibrillar aggregates detected by TEM was confirmed by XRD. The XRD image of the HSA fibrils is shown in Fig. 7. Two strong reflections can be observed: a dominant sharp and intense reflection occurs at 4.8 Å, and one weaker, more diffuse, but still intense reflection is observed at ~11 Å. The 4.8 Å meridional reflection arises from the spacing between hydrogen-bonded individual strands in the β-sheet structure that lie perpendicular to the fibril axis, and the 11 Å equatorial reflection corresponds to the intersheet spacing, with the β-sheets stacked face to face to form the core structure of protofilaments (60,61). This indicates that fibrils possess a cross-β structure, one of the diagnostic hallmarks of amyloid structures.

Acidic conditions: kinetics and amyloid self-assembly of HSA

We next subjected HSA to acidic pH and assessed its propensity to form amyloid fibrils under such conditions in both the presence and absence of 50 mM NaCl. Increases in ThT fluorescence were observed at both 25°C and 65°C, although the increase was quite small at 25°C. This indicates the formation of a small amount of additional β-sheet conformation as a consequence of the formation of oligomeric aggregates, as will be shown below (Fig. 8). At 65°C, the increase in ThT fluorescence in the absence of electrolyte is lower than that obtained at physiological pH and extends over a larger period of time. This can be a result, on the one hand, of a lower capacity of fibrillation under these conditions (see below) or, on the other, to the presence of a lag phase if compared with solution to which electrolyte is added, as discussed further below. After a small increase in ThT fluorescence at relatively short incubation times, a plateau occurs at ~24–100 h, after which the ThT fluorescence starts to increase again. Thus, it

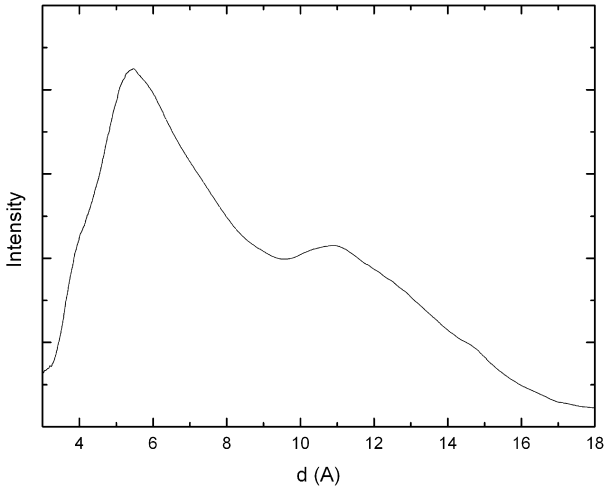

FIGURE 7 XRD pattern of HSA fibrils.

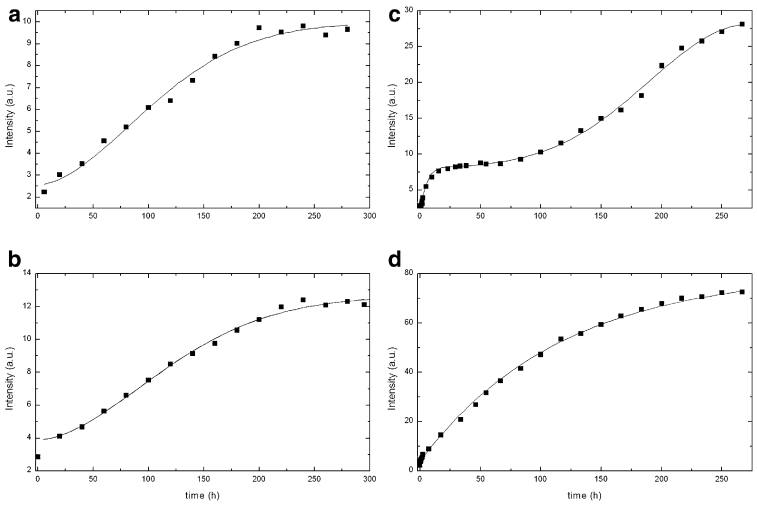

FIGURE 8 Time evolution of ThT fluorescence in HSA solutions incubated at pH 3.0 at 25°C (*a* and *b*) or 65°C (*c* and *d*) in the absence and presence of 50 mM NaCl, respectively.

is thought that under acidic conditions in the absence of electrolyte, oligomeric structures (protein clusters) are formed in a series of thermodynamically unfavorable assembly steps followed by a growth phase in which clusters are elongated by further addition of protein monomers and/or oligomers upon mutual interaction.

Fitting of the time ThT fluorescence evolution shows us that under acidic conditions, the self-assembly process becomes more cooperative, as indicated by the values of $n > 1$. This indicates the different nature of the self-assembly pathway of HSA under acidic conditions with respect to physiological pH, since interactions between protein molecules are modulated by changes in both the pH and the initial protein structure (62). In addition, the plot in the absence of electrolyte is fitted in two steps: 1), the fast formation of small clusters; and 2), the lag phase, which can originate from the necessity to reach a critical concentration of clusters for aggregation to continue. Probably, oligomeric species formed in very early stages of the aggregation process (whose existence is indicated by the slight increase of ThT fluorescence at very short incubation times) are more soluble under acidic conditions, and only after they achieve a critical concentration are they able to grow to generate larger aggregates (63). However, complete fibril formation can be achieved only in the presence of electrolyte.

Nucleation-dependent growth mechanism in acidic medium

To corroborate the origin of the plateau region in the absence of electrolyte at elevated temperature, we performed a seeding fibril growth under the conditions previously specified. When seeds are added to the protein solution, a continuous increase in ThT fluorescence is observed. This is the typical behavior observed for a nucleation-type growth mechanism and corroborates the existence of this lag phase (see Fig. S6). On the other hand, no changes are observed when protein seeds are added to a solution containing 50 mM NaCl. The difference between both solution conditions may arise from the greater hydrophobicity of oligomeric species formed during very earlier incubation stages in the presence of excess electrolyte. In its absence, electrostatic repulsion between oligomeric species seems to preclude for some time the formation of nuclei with a critical size to overcome the energy barrier that impedes aggregation.

Structural changes at acidic pH: secondary structure

At acidic pH and room temperature, both minima in $[\theta]$ at 208 and 222 nm are still present before incubation proceeds, which indicates an important retention of this type of structure, as previously described (25,64). During incubation, a slight decrease in $[\theta]$ is observed in both the absence and presence of added electrolyte, which is compatible with a small decrease in α-helices and the development of a small amount of β-sheet conformation due to the appearance of small amorphous aggregates in solution (figure not shown). In contrast, a shift of the 208 nm minimum to lower wavelengths takes place as incubation proceeds (0–200 h) at 65°C in the absence of electrolyte (Fig. 9 *a*). An increase in random coil structure (characterized by a single minimum below 200 nm) can account for this shift. Upon further incubation, an additional red shift occurs as a consequence of the increase of β-sheet structure in the aggregates formed, as also indicated by the increase in ThT fluorescence. The far-UV CD curves at 65°C in the presence of NaCl followed a trend similar to those obtained at physiological pH, although the ellipticity decrease is less severe at long incubation times as a consequence of a lower amount of scattered light from fibril aggregates (see Fig. 9 *b*). This confirms the lower fibrillar density under these conditions, which also precludes the formation of a fibrillar gel, in contrast to physiological conditions.

The secondary structure compositions in acidic solution at room temperature at the beginning of the incubation process

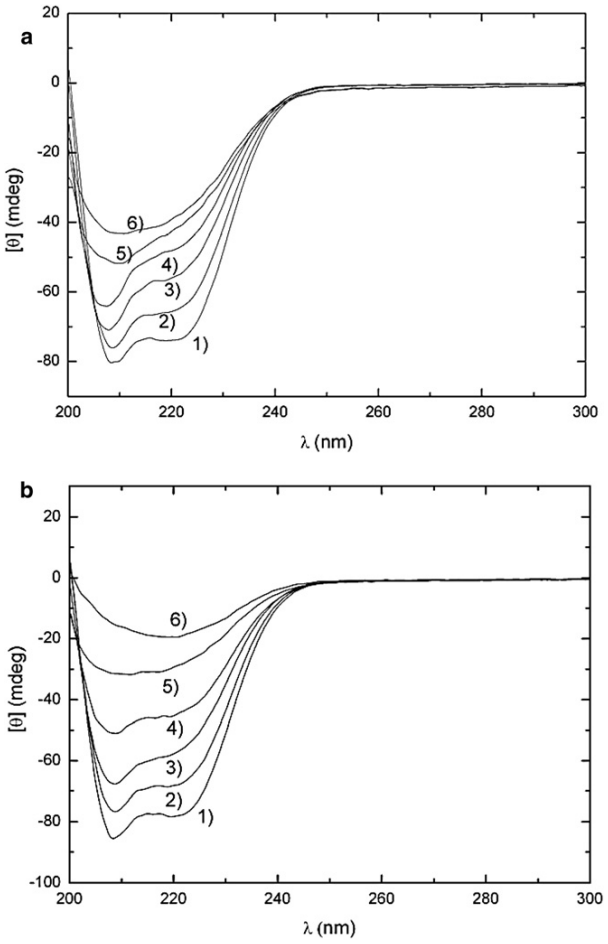

FIGURE 9 Far-UV spectra of HSA solutions at 65°C at pH 3.0 in (*a*) the absence of electrolyte at 1), 0 h; 2), 24 h; 3), 125 h; 4), 175 h; 5), 200 h; and 6), 250 h of incubation; and (*b*) the presence of 50 mM NaCl at 1), 0 h; 2), 15 h; 3), 48 h; 4), 100 h; 5), 150 h; and 6), 200 h of incubation.

indicate a reduction in α-helix conformation (~45%) and an increase in β-sheet, β-upturn, and coil contents (7%, 20%, and 28%, respectively), typical of the acid-expanded E-state of HSA (25) (Fig. 10). No significant changes were detected in structural composition during the incubation procedure at room temperature in either the absence or presence of added electrolyte up to 100 h incubation. At this stage, a slight increase in β-sheet and unordered conformations is observed for both solution conditions. In contrast, when the temperature is raised to 65°C, an important increase in β-sheets at the expense of helical conformation occurs as also observed at physiological pH. This is also accompanied by an increase in unordered conformation at early incubation times (0–150 h). The change in secondary structure occurs during a longer time interval (up to 9 days) in acidic solution. The final α-helix and β-sheet compositions are respectively 24% and 16% in the absence of electrolyte (17% and 21% in the presence of 50 mM NaCl), compared to 20% and 21% at neutral pH. This indicates small compositional changes in the resulting amyloid aggregates. The turn conformation also shows little changes throughout incubation.

FTIR experiments corroborate the structural changes undergone by the protein molecules as incubation proceeds at acidic conditions. Before incubation, the amide I band at 1650 cm^{-1} and the amide II band at 1542 cm^{-1} confirm that there is still a significant amount of α-helices. Incubation at room temperature under acidic conditions leads to a certain increase of the peak located at ~1627 nm, which corresponds to intramolecular β-sheet structure, in agreement with ThT fluorescence and CD data. On the other hand, after incubation at 65°C, a red shift of the amide I band from 1650 to 1656 cm^{-1} and a blue shift of the amide II band to 1540 cm^{-1} are indicative of an increased amount of disordered structure. In addition, the shift and further increase of the 1627 cm^{-1} peak to 1624 cm^{-1} also points to a structural transformation from an intramolecular hydrogen-bonded β-sheet to an intermolecular hydrogen-bonded β-sheet structure (46), as seen for physiological pH. Spectra also show a small high-frequency component (~1692 cm^{-1}) that would suggest the presence of antiparallel β-sheet (47) (see Fig. S7).

Structural changes at acidic pH: tertiary structure

When the pH is decreased, there is an increase in $[\theta]$ between 260 and 280 nm, and a slight decrease between 285 and 300 nm, denoting loss of tertiary structure. Nevertheless, there are still significant CD signals left, suggesting a remaining tertiary structure, in agreement with previous reports (25,65). These changes at acidic pH are related to structural rearrangements of all HSA domains. In particular, some increase in ellipticity below 295 nm takes place during incubation at room temperature, which points to little further tertiary structural changes as aggregation takes place; in particular, a loss of fine structure is detectable in the 270–295 nm region (see Fig. S8 *a*). At 65°C, changes in tertiary structure are more important; in particular, an almost complete absence of the minima is observed between 260 and 270 nm, indicating a further loss of asymmetry around disulfide bridges and/or aromatic residues as incubation proceeds. An additional loss of fine structure in the range of 280–295 nm, similar to that observed at physiological pH, is also detected (Fig. S8, *b* and *c*).

Upon incubation at acidic pH and room temperature, a certain decrease in the tryptophanyl fluorescence and a slight blue shift of the emission maximum occur between days 0 and 8 of incubation, which points to a certain internalization of Tryp to the nonpolar environment of domain II as a result of certain aggregation under these conditions (see Fig. S9). Because changes in far- and near-UV CD spectra are relatively small for this incubation period, this leads us to think that structural changes in domain II of HSA are involved in this aggregation process (66). At 65°C, the tryptophanyl residues are in a more solvent-exposed environment during the incubation because the fluorescence intensity abruptly decreases

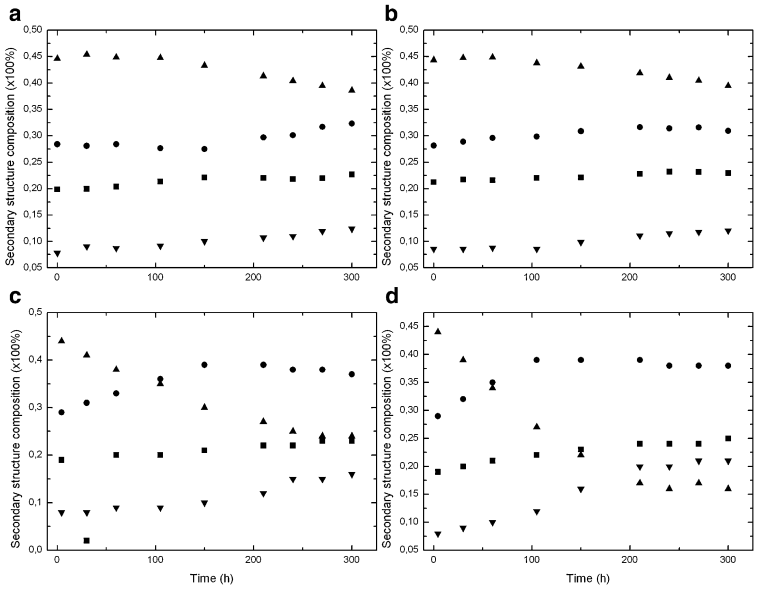

FIGURE 10 Time evolution of secondary structure compositions of HSA solutions at pH 3.0 at 25°C (*a* and *b*) or 65°C (*c* and *d*) in the absence and the presence of 50 mM NaCl, respectively. (▲) α-helix, (■) β-turn, (●) unordered, and (▼) β-sheet conformations.

during the first 4 days of incubation as a result of the sequential unfolding of domains I and II of HSA. This period of time is slightly shorter than at pH 7.4 (mainly in the presence of electrolyte excess) because the expanded E state already involves an important alteration in the tertiary structure.

In situ observation of fibrillar structures at acidic pH: TEM

HSA samples obtained at different incubation times were also subjected to TEM analysis under acidic conditions. At room temperature in the absence of salt, no aggregates were observed during the first 2 days of the incubation process. From the third day, the presence of small clusters (globules) of aggregated protein could be observed. These aggregates have a globular or spherical shape, not the regular fibrillar appearance associated with amyloid structures (see Fig. 11 *a*). In addition, less numerous, more elongated aggregates (20–30 nm long, 3–4 nm wide) can be also observed, and their population slightly increases as incubation proceeds. The formation of these types of aggregates is characterized by a decrease of helical structure accompanied by a slight rise in β-sheet and unordered conformations from CD measurements at long incubation times.

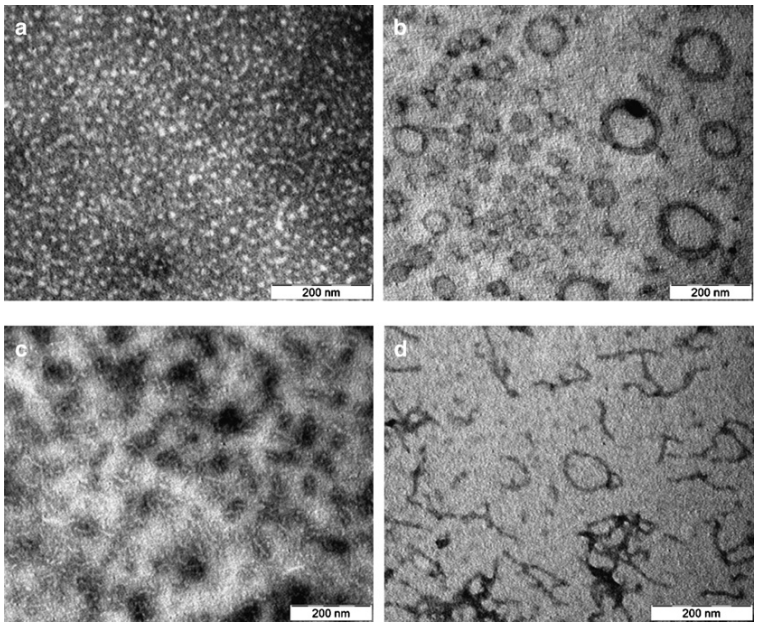

FIGURE 11 TEM pictures of the different stages of the HSA fibrillation process at pH 3.0 in the presence of 50 mM NaCl (*a*) at 25°C after 150 h of incubation, and at 65°C after (*b*) 24 h, (*c*) 150 h, and (*d*) 250 h of incubation in the presence of 50 mM NaCl.

When the temperature is raised to 65°C, fibril formation takes place in several steps. First, formation of quasi-spherical aggregates takes place under incubation times similar to those at pH 7.4, and these seem to be fairly soluble. On the other hand, we have found that a coexistence of spherical aggregates with circular ring-shaped particles of larger size (~100–300 nm) is observed at short incubation times (on the order of a few hours) in the presence of excess electrolyte (Fig. 11 *b*). These structures appear as a possible intermediate structural rearrangement of smaller protein aggregates before fibril formation facilitated by electrostatic screening. There is no evidence as to whether structural reorganization to form fibrils takes place within this type of aggregates, or whether dissociation of HSA molecules from these structures occurs. Based on our CD data, which indicate that a progressive gaining of β-sheet structure and unordered conformation at the expense of α-helices takes place in the first part of the incubation process, we suggest that only after a certain critical amount of β-sheet structure is reached inside these ring-shaped particles will short fibrils be formed in solution from decomposition of the former and become stable. Once sufficient molecules are present within the oligomer, reorganization steps become thermodynamically favorable as a result of an increase in the number of hydrogen bonds and other stabilizing interactions. Once fragments of highly ordered aggregates are present, the free energy for addition of monomeric molecules to a growing fibril will become more favorable. Similar circular ring-shaped structures have also been observed as a structural intermediate before the formation of amyloid fibrils in the self-assembly process of insulin (67), A$\beta_{17\text{-}42}$ peptide (68), A$\beta_{1\text{-}4}$ peptide, and HaPrP23-144 prion protein (69). In this case, the circular structures may incorporate into fibrils but also self-aggregate to form large, amorphous structures (57). Given the large structural differences between HSA insulin and A$\beta_{17\text{-}42}$ peptide, and their distinct propensity to form amyloid fibrils, it seems reasonable to think that these circular ring-shaped structures can be a sort of common structural intermediate of amyloid fibril formation under different solution conditions.

After longer incubation times (6 days) for HSA solutions in the absence of electrolyte at 65°C, small, well-defined, short protofibrils (~100 nm long and 3–4 nm wide) start to appear (Fig. 11 *c*). The corresponding CD spectrum shows a progressive increase in the proportion of β-structure at the expense of the helical one during incubation. In contrast, the presence of electrolyte involves an additional step: the formation of short curly fibers occurs in a broader incubation timescale than at physiological pH (Fig. 11 *d*); under further incubation, the fibrils appear to increase slightly in number and length. They range from ~100 nm to several hundred nanometers in length and 8 to 11 nm in width; thus, they are shorter on average than those obtained at physiological conditions but have the same average width. Closed fibril loops with diameters of ~100 nm were also frequently observed because the formed filaments can remain short and thin to enable them to bend and form closed rings, as also observed for β_2 microglobulin (58), α-crystallin (56), equine lysozyme (70), insulin (67), and α-synuclein (71). This fibrillar material appears similar to protofilaments observed in the early stages of other amyloidogenic systems, given the small length and the absence of higher-order structures.

DISCUSSION

The ability to form amyloid fibrils is a generic property of polypeptide chains, although the propensity of different regions of proteins to form such structures varies substantially (72). The properties of unfolded polypeptides, including their relative propensities for α- and β-structure, their intrinsic solubility, and the nature of the interactions within the resultant fibrillar structures, are likely to be particularly important determinants in their relative abilities to form fibrils. The conformation of the partially folded state is not by itself a critical feature of fibril formation; rather, it is suggested that the basis for amyloidogenesis is the presence of partially denaturation conditions that destabilize the native fold of the protein but do not preclude noncovalent interactions between the various groups within the protein. In our case, it appears necessary to destabilize HSA molecules and hence to generate a partially folded intermediate that can aggregate to form fibrils. Thus, one can readily atttain conditions in which such aggregation-prone intermediate states are significantly populated by lowering the pH or raising the temperature. ThT fluorescence, CR staining, XRD, and TEM pictures demonstrate the formation of amyloid-like structures under these conditions. The aggregation process is governed by the balance between attractive and repulsive interactions between protein molecules. Conformational changes induced by heat increase the number of hydrophobic residues exposed to the aqueous solvent. The exposure of these groups results in attractive hydrophobic interactions that play a dominant role in the aggregation process. Repulsive forces are induced by a surface charge that can be modulated by changes in pH, which controls the net charge of the protein, and by the ionic strength of the solvent, which controls the screening of electrostatic interactions (73).

Absence of a lag phase in HSA fibrillation process in most solution conditions

A first characteristic of the HSA fibrillation process is the absence of a lag phase, as previously observed for bovine serum albumin (BSA) (74) and acyl phosphatase (75) under all solutions conditions analyzed except for acidic pH at room temperature. This occurs if the initial aggregation is a downhill process that does not require a highly organized and unstable nucleus. This is supported by the fact that seeding of preformed aggregates does not accelerate the fibrillation process. In this regard, it has been suggested that large multidomain proteins like BSA are able to form

propagation-competent nucleus-like structures (oligomeric structures) (74). In our case, TEM pictures also show the formation of spherical oligomers upon very short incubation times, which occur by a means of classical coagulation mechanism. In contrast, the presence of a certain lag phase upon incubation in acidic medium at 65°C in the absence of electrolyte may well indicate that oligomeric aggregates need more time to develop and/or persist for longer times because of their enhanced solubility, so they need to reach a certain number or size to change the energy landscape of the system and promote further aggregation.

Existence of different intermediates on the HSA fibrillation pathway

On a macroscopic scale, the different steps in the fibril formation pattern, as observed by TEM, consist of the formation of nonfibrillar aggregates (oligomeric globules) and their subsequent elongation (bead-like structures and circular ring-shaped structures), and the development of protofilaments and their assembly in fibrils, which can rearrange in more complex structures. On a molecular level, CD and FTIR results show that HSA possesses native-like α-helical characteristics with residual β-sheet content before acidic or heat treatment.

In very early periods of incubation, HSA forms small, soluble, globular oligomers of mainly native-like molecules in acidic, physiological, and/or high-temperature conditions, with a progressive increase in β-sheet content and unordered conformation upon further incubation, as revealed by ThT fluorescence and far-UV CD. Thus, upon further incubation (5–50 h) at elevated temperature, the spectroscopic characteristics indicate losses of persistent tertiary structure along with unfolding of certain secondary structure to different extents depending on the solution conditions (acidic or physiological pH, added salt). Different conditions may cause different regions of the polypeptide chains that are relatively flexible and not involved in strong intramolecular interactions (76,77) to enhance the aggregation process, leading to an evolution of the previous globules into additional intermediate structures (bead-like structures and circular ring-shaped structures at physiological and acidic pH, respectively, with the latter found only at high ionic strength). Bead-like structures arise from what appears to be attractive interactions between globular protein oligomeric clusters, which may result from an increased exposure of hydrophobic residues, mainly in the presence of electrolyte. We found no evidence of formation of elongated structures by longitudinal fusion of oligomers. These bead-like structures progressively become more elongated upon incubation (35 h) due to mutual interactions between them and convert into protofibrils, in agreement with a decrease in helical structure as indicated by CD data. The decrease in diameter accompanying elongation may be explained on the basis of reorganization of structure, in particular of the β-strands. Several authors have also reported the tendency of these bead-like structures to transform into fibrillar structures at elevated temperatures caused by partial unfolding of the protein molecules and giving rise to conditions conducive to fibril formation (55–57), as shown in Fig. 6 *d*.

The combination of experimental observations described here indicates that the formation of fibrils from soluble HSA molecules proceeds in a series of stages, the first of which is effectively the presence of oligomeric globules. Thus, the role of association-competent oligomeric intermediates may result in a kinetic pathway via clustering of these oligomeric species, which can be rationalized in the light of colloid coagulation theory, i.e., the formation of a critical oligomer or an ensemble of critical oligomers and subsequent aggregation into bead-like structures, and then protofibrillar structures (78). The persistence of these spherical oligomers in solution coinciding with fibril assembly also supports the view that they may be ''on-pathway'' intermediates (see Fig. 6 and Fig. S10). Spherical oligomeric structures have been proposed to serve a key, on-pathway role in both the formation and elongation of amyloid fibrils of the Sup35 (79) and Ure2p yeast prion proteins (80).

In contrast, we speculate that the circular ring-shaped structures found in acidic medium at high ionic strength, which appear to be composed of two semicircular units, may come from bending and association of early-formed, short, bead-like structures due to a decrease in their solubility. This decrease would stem from the electrolyte concentration present in solution, which screens electrostatic interactions between aggregates. Once sufficient molecules are present within this type of intermediate structure, reorganization steps become thermodynamically favorable as a result of an increase in the number of hydrogen bonds and other stabilizing interactions. Once critical fragments of ordered aggregates are present (with a critical amount of β-sheet structure), the free energy for addition of monomeric molecules to a growing elongated structure becomes more favorable. In this way, short protofibrils will be formed in solution upon dissolution of the ring-shaped intermediate structures and will become stable. These intermediates are not observed by TEM once protofibrils start to be observed, which suggests that they may act as reservoirs of the initially very short protofibrils. However, a deeper structural analysis of this structural intermediate and its evolution to protofibrils is needed, and is currently under way. On the other hand, the fact that some elongated structures (but not fibrils) are formed in acidic pH at room temperature, in contrast to physiological medium, for which no aggregation is observed except for some amorphous aggregates, suggests that the charge distribution on the protein influences the propensity to form amyloid fibrils. The neutralization of negative charges at acidic pH may promote this elongation.

HSA fibrils are curly

The thermodynamic instability of prefibrillar aggregates causes them to evolve into more stable assemblies upon additional incubation (>75 h), eventually leading to the appearance

of stable fibrils, mainly at physiological conditions at elevated temperatures, where structural reorganization results in the large majority of hydrophobic groups being concealed from the solvent. This is corroborated by ThT fluorescence, far UV-CD, and FTIR spectra, which demonstrate that the major elements of ordered secondary structure are β-sheets, suggesting that the α-helical regions of the native protein have undergone significant structural changes. TEM pictures corroborate this picture, showing that the fibrils formed are mainly, narrow, branched, and elongated but curly, in contrast to the straight needle-like structures characteristic of bona fide fibrils. As incubation proceeds, these worm-like structures increase in length. These fibrils display the typical 4.8 Å peak indicating the typical interstrand distance of classical fibrils, and the 11 Å equatorial reflection corresponds to the intersheet spacing, with the β-sheets stacked face to face to form the core structure of protofilaments (81). Based on the CD and FTIR data, we speculate that these types of fibrils may be formed by a seam of β-sheet structure decorated by relatively disorganized α-helical structure, as previously observed for RNase A (82) or yeast Ure2p (83). In addition, an antiparallel arrangement of β-strands forming the β-sheet structure of the HSA fibrils seems to be the most probable configuration, as denoted by the band at ~1691–1693 cm^{-1} in the FTIR spectra. Curly aggregates have been also seen in other proteins, such as β_2 microglobulin (58) and α-crystallin (56). In addition, intramolecular end-to-end association of short individual filaments appears to be favorable, as TEM images reveal the presence of a substantial number of closed loops appearing to form spontaneously, mainly in the absence of electrolyte at acidic conditions. Qualitatively, the probability of a single fibril joining end-to-end to form a closed loop will be high if the fibril is sufficiently flexible and of appropriate length for the ends to find themselves regularly in close proximity to each other (84). Indeed, the results presented here exemplify the favorable nature of loop formation when such fibril morphologies are adopted. Loop formation was reported previously for other amyloid-forming systems (85,86).

On the other hand, it is interesting to note that a similar curly morphology for HSA can be achieved under different solution conditions: the single filament, in the form of both open flexible chains and closed loops, is observed at both physiological and acidic pH in the presence of electrolyte. Nevertheless, the rate and extent of aggregation depends on the solution conditions: the amount of formed fibrils and their length (larger at physiological conditions) favor interactions between early aggregates to form fibrils. This is revealed by the formation of a gel phase under suitable solution conditions.

Curly fibers can evolve into a suprafibrillar structure

Very long incubation times (>150 h) lead to a more complex morphological variability among amyloid fibrils (e.g., long straight fibrils, flat-ribbon structures, or laterally connected fibers). These compact, mature fibrillar assemblies formed at the endpoint of the aggregation process may result from an effort to minimize the exposure of hydrophobic residues, and are also likely to result in increased van der Waals interactions, leading to greater stability, as previously noted for β_2-microglobulin (87), α-synuclein (5), and insulin (88). A similar progression in structure from curly fibrils to mature straight fibers was also observed for Aβ-peptide (89) and insulin (90). In contrast, BSA fibrillation was shown to be halted at the early curly stage, despite the enormous structural similarities with HSA, since no further development in fibrillar structure over long timescales was observed (74). Mature fibrils are thicker and stiffer than single fibrils and appear to be formed by lateral (side-by-side) assembly of two or more individual filaments. Nevertheless, under physiological conditions, we observed that mature straight fibrils can also grow by swollen protein particles tending to align within the immediate vicinity of the fibers, as shown in Fig. 6 *i*, serving the single fiber as a lateral template or scaffold for small protein molecules, and would constitute a subcomponent in mature fibrils. Their population is dependent on solution conditions and lateral interactions between fibrils. This may be an additional pathway to the formation of mature fibrils via association of protofibrils. Conformational preferences for a certain pathway to become active may exist, and thus the influence of environmental conditions such as pH, temperature, and salt must be considered. Thus, it seems that a single filament may act as a ''lateral template'' or scaffold for small protein particles, which would constitute a neighboring subcord-like feature in the fiber shown in Fig. 6 *h*. This filament + monomers/oligomers scenario is an alternative pathway to the otherwise dominating filament + filament manner of the protein fibril's lateral growth, as has been also observed for insulin (57). AFM data recently reported by Green et al. (91) suggest that mature fibrils from human amylin are unlikely to be assembled by the lateral association of protofibrils.

It appears, therefore, that even for a homogeneous HSA sample undergoing uniform temperature or acidic treatment, there is still more than one mode of assembly of filaments (92). Such polymorphism may be caused by differences in the number of filaments assembled in the mature fibrils; however, it may also result from the incorporation in different regions of the sequence of the polypeptide chain with various types of fibrils. In addition, the differences between the populations of fibers clearly involve not only the rate of the aggregation process, but also the different quaternary folds. Although the different distribution profiles of the fibrillar features may still be explained in terms of kinetic effects (e.g., temperature may differently affect the kinetics at various stages of the assembly, effectively marginalizing certain sequential processes), high temperatures may also have a more direct effect on amyloidogenesis, for instance, by increasing the thermal energy of the interacting molecules

and hence causing the alignment of filaments to become less accurate. Such unspecific effects may contribute to morphological differences in any protein's amyloid samples induced at high temperature. In this regard, recent reports based on nuclear magnetic resonance showed that different fibril morphologies have different underlying secondary structures, and as such are likely produced by distinct independent assembly pathways (93,94).

A summary of the various fibril morphologies observed in this study is shown in Fig. 12 together with a schematic representation of the assembly process. We propose that at elevated temperature (except at pH 3.0 in the absence of electrolyte), HSA forms rapidly globular oligomers that upon mutual interaction evolve into more elongated structures (bead-like) that grow to protofibrils either by subsequent annealing of oligomers and/or protein monomers. Mature fibrils can be formed by lateral association of protofibrils or the addition of protein oligomers to the growing fibril, both at the ends of the fibril and by lateral fusion. Ring-like structures are present in acidic conditions at elevated temperature in the presence of electrolyte as an additional intermediate state formed by association of short bead-like structures, which disappears when protofibrils are observed in solution. Thus, we think that they may act as reservoirs of initially very short protofibrils.

CONCLUSIONS

We observed the formation of protofibrils, curly fibers, and mature fibrils by the protein HSA under different solution conditions. We analyzed the fibrillation process and the conformational changes associated with it by using different spectroscopic techniques, and confirmed the necessary development of β-sheet structure upon fibrillation. In addition, the shapes of the different structural intermediates and final products in the fibrillation process were observed by TEM, SEM, and AFM. The obtained fibrils show structural features typical of classical amyloid fibers, as denoted by XRD, CD, and fluorescence spectroscopies, and TEM. A model of fibril formation based on the elongation of protein oligomers through mutual interactions and subsequent annealing and growth is presented. Nevertheless, some differences in the fibrillation mechanism occur depending on the solution conditions; for example, ring-shaped structures are observed only as a structural intermediate under acidic conditions in the presence of added electrolyte.

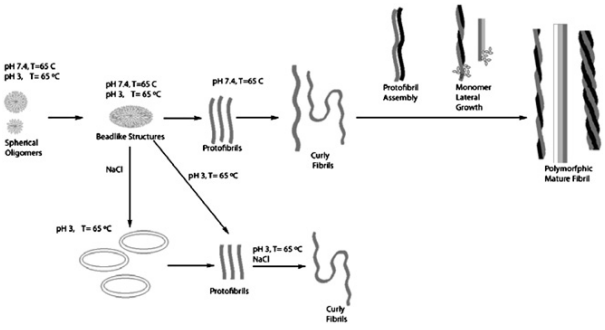

FIGURE 12 Mechanisms of fibril formation for HSA.

SUPPORTING MATERIAL

Ten figures and a table are available at http://www.biophysj.org/biophysj/supplemental/S0006-3495(09)00322-1.

We thank Dr. Eugenio Vázquez for his assistance with the CD measurements.

This study was supported by the Ministerio de Educación y Ciencia (project MAT-2007-61604).

REFERENCES

1. Reches, M., and E. Gazit. 2003. Casting metal nanowires within discrete self-assembled peptide nanotubes. *Science*. 300:625–627.
2. Rajagopal, K., and J. P. Schneider. 2004. Self-assembling peptides and proteins for nanotechnological applications. *Curr. Opin. Struct. Biol.* 14:480–486.
3. Stefani, M., and C. M. Dobson. 2003. Protein aggregation and aggregate toxicity: new insights into protein folding, misfolding diseases and biological evolution. *J. Mol. Med.* 81:678–699.
4. Soto, C., L. Estrada, and J. Castilla. 2006. Amyloids, prions and the inherent infectious nature of misfolded protein aggregates. *Trends Biochem. Sci.* 31:150–155.
5. Khurana, R., C. Ionescu-Zanetti, M. Pope, J. Li, L. Nelson, et al. 2003. A general mode for amyloid fibril assembly based on morphological studies using atomic force microscopy. *Biophys. J.* 85:1135–1144.
6. Chiti, F., M. Stefani, N. Taddei, G. Ramponi, and C. M. Dobson. 2003. Rationalization of the effects of mutations on peptide and protein aggregation rates. *Nature*. 424:805–808.
7. Williams, A. D., E. Portelius, I. Kheterpal, J. T. Guo, K. D. Cook, et al. 2004. Mapping a β amyloid fibril secondary structure using scanning proline mutagenesis. *J. Mol. Biol.* 335:833–842.
8. Hortscansky, P., T. Christopeit, V. Schroeckh, and M. Fändrich. 2005. Thermodynamic analysis of the aggregation propensity of oxidized Alzheimer's β-amyloid variants. *Protein Sci.* 14:2915–2918.
9. Fändrich, M., V. Forge, K. Buder, M. Kittler, C. M. Dobson, et al. 2003. Myoglobin forms amyloid fibrils by association of unfolded peptide segments. *Proc. Natl. Acad. Sci. USA*. 100:15463–15468.
10. Gazit, E. 2002. The "correctly folded" state of proteins: is it a metastable state? *Angew. Chem. Int. Ed. Engl.* 41:257–259.
11. Gillmore, J. D., A. J. Stangou, G. A. Tennet, D. R. Booth, J. O'Grady, et al. 2001. Clinical and biochemical outcome of hepatorenal transplantation for hereditary systemic amyloidosis associated with apolipoprotein AI Gly26Arg. *Transplantation*. 71:986–992.
12. Carulla, N., G. L. Caddy, D. R. May, J. Zurdo, M. Gairi, et al. 2005. Molecular recycling within amyloid fibrils. *Nature*. 436:554–558.
13. Pepys, M. B., J. Herbert, W. L. Hutchison, G. A. Tennent, H. J. Lachmann, et al. 2002. Targeted pharmacological depletion of serum amyloid P component for treatment of human amyloidosis. *Nature*. 417:254–259.
14. Janus, C., M. A. Chishti, and D. Westaway. 2000. Transgenic mouse models of Alzheimer's disease. *Biochim. Biophys. Acta*. 1502:63–75.
15. Cohen, F. E., and J. W. Kelly. 2003. Therapeutic approaches to protein-misfolding diseases. *Nature*. 426:905–909.
16. Tanaka, M., P. Chien, N. Narber, R. Cooke, and J. S. Weissman. 2004. Conformational variations in an infectious protein determine prion strain differences. *Nature*. 428:323–328.

17. Fändrich, M., and C. M. Dobson. 2002. The behavior of polyamino acids reveals an inverse side chain effect in amyloid structure formation. *EMBO J.* 21:5682–5690.

18. Gorinstein, S., A. Caspi, A. Rosen, I. Goshev, M. Zemser, et al. 2002. Structure characterization of human serum aproteins in solution and dry state. *J. Pept. Res.* 59:71–78.

19. Taboada, P., S. Barbosa, E. Castro, and V. Mosquera. 2006. Amyloid fibril formation and other aggregate species formed by human serum albumin association. *J. Phys. Chem. B.* 110:20733–20736.

20. Pace, C. N., F. Vajdos, L. Fee, G. Grimsley, and T. Gray. 1995. How to measure and predict the molar absorption coefficient of a protein. *Protein Sci.* 4:2411–2423.

21. Sreerama, N., and R. W. Woody. 2000. Estimation of protein secondary structure from circular dichroism spectra: comparison of CONTIN, SELCON, and CDSSTR methods with an expanded reference set. *Anal. Biochem.* 287:252–260.

22. Uversky, V. N., and A. L. Fink. 2004. Conformational constraints for amyloid fibrillation: the importance of being unfolded. *Biochim. Biophys. Acta.* 1698:131–153.

23. Calamai, M., F. Chiti, and C. M. Dobson. 2005. Amyloid fibril formation can proceed from different conformations of a partially unfolded protein. *Biophys. J.* 89:4201–4210.

24. Morel, B., S. Casares, and F. A. Conejo-Lara. 2006. Single mutation induces amyloid aggregation in the α-spectrin SH3 domain: analysis of the early stages of fibril formation. *J. Mol. Biol.* 356:453–468.

25. Dockal, M., D. C. Carter, and F. Rüker. 2000. Conformational transitions of the three recombinant domains of human serum albumin depending on pH. *J. Biol. Chem.* 275:3042–3050.

26. Peters, T. Jr., 1996. All About Albumin: Biochemistry, Genetics and Medical Application. Academic Press, New York.

27. Geisow, M. J., and G. H. Beaven. 1977. Physical and binding properties of large fragments of human serum albumin. *Biochem. J.* 165:477–484.

28. Khan, M. Y. 1986. Direct evidence for the involvement of domain III in the N-F transition of bovine serum albumin. *Biochem. J.* 236:307–310.

29. Ahmad, B., M. K. A. Khan, S. Haq, and R. H. Khan. 2004. Intermediate formation at lower urea concentration in 'B' isomer of human serum albumin: a case study using domain specific ligands. *Biochem. Biophys. Res. Commun.* 314:166–173.

30. Taboada, P., S. Barbosa, E. Castro, M. Gutiérrez-Pichel, and V. Mosquera. 2007. Effect of solvation on the structure conformation of human serum albumin in aqueous-alcohol mixed solvents. *Chem. Phys.* 340:59–68.

31. Farruggia, B., F. Rodriguez, R. Rigatuso, G. Fidelio, and G. Picó. 2001. The participation of human serum albumin domains in chemical and thermal unfolding. *J. Protein Chem.* 20:81–89.

32. Flora, K., J. D. Brennan, G. A. Baker, M. A. Doody, and F. V. Bright. 1998. Unfolding of acrylodan-labeled human serum albumin probed by steady-state and time resolved fluorescence methods. *Biophys. J.* 75:1084–1096.

33. Rader, A. J., B. M. Hespenheide, K. A. Kuhn, and M. F. Thorpe. 2002. Protein unfolding: rigidity lost. *Proc. Natl. Acad. Sci. USA.* 99: 3540–3545.

34. LeVine, H. 3rd., 1993. Thioflavine T interaction with synthetic Alzheimer's disease β-amyloid peptides: detection of amyloid aggregation in solution. *Protein Sci.* 2:404–410.

35. Klunk, W. E., J. W. Pettegrew, and D. J. Abraham. 1989. Quantitative evaluation of Congo Red binding to amyloid-like proteins with a β-pleated sheet conformation. *J. Histochem. Cytochem.* 37:1273–1281.

36. Khurana, R., C. Coleman, C. Ionescu-Zanetti, S. A. Carter, V. Krishna, et al. 2005. Mechanisms of thioflavin T binding to amyloid fibrils. *J. Struct. Biol.* 151:229–238.

37. Sagis, L. M. C., C. Veerman, and E. Van der Linden. 2004. Mesoscopic properties of semiflexible amyloid fibrils. *Langmuir.* 20:924–927.

38. Morozova-Roche, L. A., J. A. Jones, W. Noppe, and C. M. Dobson. 1999. Independent nucleation and heterogeneous assembly of structure during unfolding of equine lysozime. *J. Mol. Biol.* 289:1055–1073.

39. Jund, P., R. Jullien, and I. Campbell. 2001. Random walks on fractals and stretched exponential relaxation. *Phys. Rev. E.* 63:361311–361314.

40. Harper, J. D., and P. T. J. Landsbury. 1997. Models of amyloid seeding in Alzheimer's disease and scrapie: mechanistic truths and physiological consequences of the time-dependent solubility of amyloid proteins. *Annu. Rev. Biochem.* 66:385–407.

41. Lomakin, A., D. S. Chung, G. B. Benedek, D. A. Kirschner, and D. B. Teplow. 1996. On the nucleation and growth of amyloid β-protein fibrils: detection of nuclei and quantitation of rate constants. *Proc. Natl. Acad. Sci. USA.* 93:1125–1129.

42. Lomakin, A., D. B. Teplow, D. A. Kirschner, and G. B. Benedek. 1997. Kinetic theory of fibrillogenesis of amyloid β-protein. *Proc. Natl. Acad. Sci. USA.* 94:7942–7947.

43. Ferrone, F. 1999. Analysis of protein aggregation kinetics. *Methods Enzymol.* 309:256–274.

44. Susi, H., and D. M. Byler. 1983. Protein structure by Fourier transform infrared spectroscopy: second derivative spectra. *Biochem. Biophys. Res. Commun.* 115:391–397.

45. Lin, S. -Y., Y. -S. Wei, M. -J. Li, and S. -L. Wang. 2004. Effect of ethanol or/and captopril on the secondary structure of human serum albumin before and after protein binding. *Eur. J. Pharm. Biopharm.* 57:457–464.

46. Jackson, M., and H. H. Mantsch. 1995. The use and misuse of FTIR spectroscopy in the determination of protein structure. *Crit. Rev. Biochem. Mol. Biol.* 30:95–120.

47. Casal, H. L., U. Kohler, and H. H. Mantsch. 1988. Structural and conformational changes of β-lactoglobulin B: an infrared spectroscopy study of the effect of pH and temperature. *Biochim. Biophys. Acta.* 957:11–20.

48. Fabian, H., L. -P. Choo, G. I. Szendrei, M. Jackson, W. C. Halliday, et al. 1993. Infrared spectroscopic characterization of Alzheimer plaques. *Appl. Spectrosc.* 47:1513–1518.

49. Lin, S. -Y., Y. -S. Wei, M. -J. Li, and S. -L. Wang. 2004. Effect of ethanol or/and captopril on the secondary structure of human serum albumin before and after protein binding. *Spectrochim. Acta [A].* 60:3107–3111.

50. Uversky, V. N., N. V. Narizhneva, T. V. Ivanova, and A. Y. Tomashevski. 1997. Rigidity of human α-fetoprotein tertiary structure is under ligand control. *Biochemistry.* 494:13638–13645.

51. Muzammil, S., Y. Kumar, and S. Tayyab. 1999. Molten globule-like state of human serum albumin at low pH. *FEBS Lett.* 266:26–32.

52. Qiu, W., L. Zhang, O. Okobiah, Y. Yang, L. Wang, et al. 2006. Ultrafast solvation dynamics of human serum albumin: correlations with conformational transitions and site-selected recognition. *J. Phys. Chem. B.* 110:10540–10549.

53. Cowgill, R. W. 1968. Fluorescence and protein structure. XIV. Tyrosine fluorescence in helical muscle proteins. *Biochim. Biophys. Acta.* 161:431–438.

54. Shahi, P., R. Sharma, S. Sanger, I. Kumar, and R. S. Jolly. 2007. Formation of amyloid fibrils via longitudinal growth of oligomers. *Biochemistry.* 46:7365–7373.

55. Burgio, M. R., P. M. Bwennet, and J. F. Koretz. 2001. Heat-induced quaternary transitions in hetero- and homo-polymers of α-crystallin. *Mol. Vis.* 7:228–233.

56. Meehan, S., Y. Berry, B. Luisa, C. M. Dobson, J. A. Carver, et al. 2004. Amyloid fibril formation by lens crystallin proteins and its implications for cataract formation. *J. Biol. Chem.* 279:3413–3419.

57. Jansen, R., W. Dzwolak, and R. Winter. 2005. Amyloidogenic self-assembly of insulin aggregates probed by high resolution atomic force microscopy. *Biophys. J.* 88:1344–1353.

58. Radford, S. E., W. S. Gosal, and G. W. Platt. 2005. Towards an understanding of the structural molecular mechanism of β2-microglobulin amyloid formation *in vitro*. *Biochim. Biophys. Acta.* 1753:51–63.

59. Kodali, R., and R. Wetzel. 2007. Polymosphism in the intermediates and products of amyloid assembly. *Curr. Opin. Struct. Biol.* 17:48–57.

60. Sunde, M., and C. Blake. 1997. The structure of amyloid fibrils by electron microscopy and X-ray diffraction. *Adv. Protein Chem.* 50:123–159.

61. Bouchard, M., J. Zurdo, E. J. Nettleton, C. M. Dobson, and C. V. Robinson. 2000. Formation of insulin amyloid fibrils followed by FTIR simultaneously with CD and electron microscopy. *Protein Sci.* 9:1960–1967.

62. Vetri, V., F. Librizzi, M. Leone, and V. Militello. 2007. Thermal aggregation of bovine serum albumin at different pH: comparison with human serum albumin. *Eur. Biophys. J.* 36:717–725.

63. Bader, R., R. Bamford, J. Zurdo, B. F. Luisi, and C. M. Dobson. 2006. Probing the mechanism of amyloidogenesis through a tandem repeat of the PI3–SH3 domain suggests a generis model for protein aggregation and fibril formation. *J. Mol. Biol.* 356:189–208.

64. Shaw, A. K., and S. K. Pal. 2008. Spectroscopic studies on the effect of temperature on pH-induced folded states of human serum albumin. *J. Photochem. Photobiol. B.* 90:69–77.

65. Ahmad, B., S. Parveen, and R. H. Khan. 2006. Effect of albumin conformation on the binding of ciprofloxacin to human serum albumin: a novel approach directly assigning binding site. *Biomacromolecules.* 7:1350–1356.

66. Eftink, M. R., and C. A. Ghiron. 1976. Exposure of tryptophyl residues in proteins. Quantitative determination by fluorescence quenching studies. *Biochemistry.* 15:672–679.

67. Sibley, S. P., K. Sosinsky, L. E. Gulian, E. J. Gibbs, and R. F. Pasternack. 2008. Probing the mechanism of insulin aggregation with added metalloporphyrins. *Biochemistry.* 47:2858–2865.

68. Zheng, J., H. Jang, B. Ma, and R. Nussinov. 2008. Annular structures as intermediates in fibril formation of Alzheimer Aβ_{17-42}. *J. Phys. Chem. B.* 112:6856–6865.

69. Moore, R. E., S. F. Hayes, E. R. Fischer, and S. A. Priola. 2007. Amyloid formation via supramolecular peptide assemblies. *Biochemistry.* 46:7079–7087.

70. Malisauskas, M., V. Zamotin, J. Jass, W. Noppe, C. M. Dobson, et al. 2003. Amyloid protofilaments from the calcium-binding protein equine lysozyme: formation of ring and linear structures depends on pH and metal ion concentration. *J. Mol. Biol.* 330:879–890.

71. Lashuel, H. A., D. Hartley, B. M. Petre, T. Walz, and P. T. Lansbury Jr. 2002. Neurodegenerative disease: amyloid pores from pathogenic mutations. *Nature.* 418:291.

72. Jarrett, J. T., and P. T. Lansbury Jr. 1992. Amyloid fibril formation requires a chemically discriminating nucleation event—studies of an amyloidogenic sequence from the bacterial protein OSMB. *Biochemistry.* 31:12345–12352.

73. Lefebvre, J., D. Renard, and A. C. Sánchez-Gimeno. 1998. Structure and rheology of heat-set gels of globular proteins. I. Bovine serum albumin gels in isoelastic conditions. *Rheol. Acta.* 37:345–357.

74. Holm, N. K., S. K. Jespersen, L. V. Thomassen, T. Y. Wolff, P. Sehgal, et al. 2007. Aggregation and fibrillation of bovine serum albumin. *Biochim. Biophys. Acta.* 1774:1128–1138.

75. Chiti, F., P. Webster, N. Taddei, A. Clark, M. Stefani, et al. 1999. Designing conditions for *in vitro*, formation of amyloid protofilaments and fibrils. *Proc. Natl. Acad. Sci. USA.* 96:3590–3594.

76. Krishnan, R., and S. L. Lindquist. 2005. Structural insights into a yeast prion illuminate nucleation and strain diversity. *Nature.* 435:765–772.

77. Moraitakis, G., and J. M. Goodfellow. 2003. Simulations of human lysozime: probing the conformations triggering amyloidosis. *Biophys. J.* 84:2149–2158.

78. Modler, A. J., K. Gast, G. Lutsch, and G. Damaschun. 2003. Assembly of amyloid protofibrils via critical oligomers. A novel pathway of amyloid formation. *J. Mol. Biol.* 325:135–148.

79. Serio, T. R., A. G. Cashikar, A. S. Kowal, G. J. Sawicki, J. J. Moleshi, et al. 2000. Nucleated conformational conversion and the replication of conformational information by a prion determinant. *Science.* 289: 1317–1321.

80. Jiang, Y., H. Li, L. Zhu, J. M. Zhou, and S. Perrett. 2004. Amyloid nucleation and hierarchical assembly of Ure2p fibrils. Role of asparagines/glutamine repeat and nonrepeat regions of the prion domains. *J. Biol. Chem.* 279:3361–3369.

81. Makin, O. S., and L. C. Serpell. 2005. X-ray diffraction studies of amyloid structure. *Methods Mol. Biol.* 299:67–80.

82. Sambashivan, S., M. R. Liu, M. R. Sawaya, M. Gingery, and D. Eisenberg. 2005. Amyloid-like fibrils of ribonuclease A with three-dimensional domain-swapped and native-like structures. *Nature.* 437:266–269.

83. Ranson, N., T. Stromer, L. Bousset, R. Melki, and R. C. Serpell. 2006. Insights into the architecture of the Ure2p yeats protein assemblies from helical twisted fibrils. *Protein Sci.* 15:2481–2487.

84. Hatters, D. M., C. A. MacRails, R. Daniels, W. S. Gosal, N. H. Thomson, et al. 2003. The circularization of amyloid fibrils formed by apolipoprotein C–II. *Biophys. J.* 85:3979–3990.

85. Lashuel, H. A., and P. T. Lansbury Jr. 2006. Are amyloid diseases caused by protein aggregates that mimic bacterial pore-forming toxins? *Q. Rev. Biophys.* 39:167–201.

86. Meehan, S., T. P. J. Knowles, A. J. Baldwin, J. F. Smith, A. M. Squires, et al. 2007. Characterization of amyloid fibril formation by small heat-shock chaperone proteins human αA-, αB- and R120G αB-crystallins. *J. Mol. Biol.* 372:470–484.

87. Kad, N. M., S. L. Myers, D. P. Smith, S. E. Radford, and N. H. Thomson. 2003. Hierarchical assembly of β2-microglobulin amyloid in vitro revealed by atomic force microscopy. *J. Mol. Biol.* 330:785–797.

88. Khurana, R., J. L. Jimenez, E. J. Nettleton, M. Bouchard, C. V. Robinson, et al. 2002. The protofilament structure of insulin amyloid fibrils. *Proc. Natl. Acad. Sci. USA.* 99:9196–9201.

89. Otzen, D. E., and M. Oliveberg. 2004. Transient formation of nanocrytalline structures during fibrillation of an Alzheimer-like peptide. *Protein Sci.* 13:1417–1421.

90. Grudzielanek, S., V. Smirnovas, and R. Winter. 2006. Solvation-assisted pressure tuning of insulin fibrillation: from novel aggregation pathways to biotechnological applications. *J. Mol. Biol.* 356:497–506.

91. Green, J. D., C. Goldsbury, J. Kistler, G. K. Cooper, and U. Aebi. 2004. Human amylin oligomer growth and fibril elongation define two distinct phases in amyloid formation. *J. Biol. Chem.* 279:12206–12212.

92. Chamberlain, A. K., C. E. MacPhee, J. Zurdo, L. A. Morozova-Roche, H. A. O. Hill, et al. 2000. Ultrastructural organization of amyloid fibrils by atomic force microscopy. *Biophys. J.* 79:3282–3293.

93. Goldsbury, C. S., S. Wirtz, S. A. Müller, S. Sunderji, P. Wicki, et al. 2000. Studies on the in vitro assembly of Aβa-40: implications for the search for Aβ fibril formation inhibitors. *J. Struct. Biol.* 130: 217–231.

94. Petkova, A. T., R. D. Leapman, Z. Guo, W. M. Yau, M. P. Mattson, et al. 2005. Self-propagating, molecular-level polymorphism in Alzheimer's β-amyloid fibrils. *Science.* 307:262–265.

Influence of Electrostatic Interactions on the Fibrillation Process of Human Serum Albumin

Josué Juárez, Sonia Goy López, Adriana Cambón, Pablo Taboada,* and Víctor Mosquera

Grupo de Física de Coloides y Polímeros, Departamento de Física de la Materia Condensada, Facultad de Física, Universidad de Santiago de Compostela, E-15782, Santiago de Compostela, Spain

Received: March 12, 2009; Revised Manuscript Received: May 7, 2009

The fibrillation propensity of the multidomain protein human serum albumin (HSA) has been analyzed under physiological and acidic conditions at room and elevated temperatures with varying ionic strengths by different spectroscopic techniques. The kinetics of fibril formation under the different solution conditions and the structures of resulting fibrillar aggregates were also determined. In this way, we have observed that fibril formation is largely affected by electrostatic shielding: at physiological pH, fibrillation is progressively more efficient and faster in the presence of up to 50 mM NaCl; meanwhile, at larger salt concentrations, excessive shielding and further enhancement of the solution hydrophobicity might involve a change in the energy landscape of the aggregation process, which makes the fibrillation process difficult. In contrast, under acidic conditions, a continuous progressive enhancement of HSA fibrillation is observed as the electrolyte concentration in solution increases. Both the distinct ionization and initial structural states of the protein before incubation may be the origin of this behavior. CD, FT-IR, and tryptophan fluorescence spectra seem to confirm this picture by monitoring the structural changes in both protein tertiary and secondary structures along the fibrillation process. On the other hand, the fibrillation of HSA does not show a lag phase except at pH 3.0 in the absence of added salt. Finally, differences in the structure of the intermediates and resulting fibrils under the different conditions are also elucidated by TEM and FT-IR.

Introduction

Protein aggregation and, particularly, amyloid formation have received considerable interest in the fields of protein research and clinical medicine, since growing evidence has accumulated that these processes are likely to be key issues in the etiology of various medical disorders such as Alzheimer's, Parkinson's, Huntington's, and Creutzfeldt−Jakob diseases, type II diabetes, and cystic fibrosis among others. In fact, about 20 different known syndromes are associated with the formation of amyloid fibrils.[1−6] In addition, a number of nondisease associated proteins have also been found to be able to form ordered cytotoxic aggregates and amyloid fibrils *in vitro*.[7] On the other hand, the exceptional physical characteristics of the amyloidal protein state, such as its stability, mechanical strength, and resistance to degradation, imply that this type of structure possesses a range of potential technological applications in biotechnology and materials science.[8,9]

A consensus has emerged that the different processes of *in vivo* and *in vitro* aggregation might be linked by the implication of destabilized protein molecules that undergo non-native backbone-dominated self-assembly as a competing pathway to native functional folding.[10] However, both folding and protein aggregation are thought to underlie some common principles which aim at minimizing the Gibbs energy of destabilized protein states, such as the saturation of dangling hydrogen bonds,[11] the reduction of the solvent-accessible surface area, or the burial of hydrophobic residues.[12] In this way, globular proteins generally need to be destabilized (e.g., by mutation,[13,14] heat,[15,16] high pressure,[17,18] low pH,[19,20] or organic denaturant[7,15]) to aggregate rapidly, with fibril formation proceeding from extensively or partially unfolded states[3,21] or, in some cases, from native-like states in which unfolding may initially be limited and confined to local regions of the protein.[22,23]

The physiological importance of human serum albumin as a carrier protein and blood pressure regulator and its propensity to easily aggregate *in vitro* have become a good model for protein aggregation studies. As the phenomenon of protein aggregation appears to reflect certain generic "polymeric" features of proteins,[24] the studies of the mechanisms of protein aggregation on model systems are extremely useful for a better understanding of the molecular mechanisms of disease-associated amyloidogenesis. Since in living organisms the native environment of proteins is a complex composition of water, cosolvents, and cosolutes which affect the stability of the native protein fold,[25] experimental approaches to mimic various cellular environments *in vitro* to allow investigations on protein folding and aggregation often utilize the addition of cosolvents and cosolutes. Thereby, differences in the properties of the solvent might induce solvent-adapted structural "responses" of the aggregating protein. In particular, the importance of electrostatic interactions in the formation of amyloid fibrils[20,26,27] and the relevance of the total net charge on the protein to the fibril formation propensity have been pointed out.[26,27]

To put more light on this issue, in the present work we present a systematic study on the relationship between serum albumin amyloid-like fibrillation kinetics, fibrillation pathways, and the resulting aggregated protein structures under different conditions where the amyloid fibrils of this model protein were found by changing solution pH and solution ionic strength.[28,29] In this manner, a modulation of the electrostatic interactions between protein molecules and aggregates results in different balances of intermolecular forces between protein molecules, which involve changes in both protein aggregation and their kinetics. In this way, we have found large differences in the fibrillation

* Author to whom correspondence should be addressed. E-mail: pablo.taboada@usc.es. Telephone: 0034981563100, ext. 14042. Fax: 0034981520676.

10.1021/jp902224d CCC: $40.75
Published on Web 07/02/2009

kinetics of HSA and, as a result, different structural intermediates and fibrillation pathways. As well as that, differences in the resulting amyloid-like fibrils under the different solution conditions were also observed. It seems, then, that both pH and ionic strength play a key role in regulating the several steps which regulate HSA fibrillation.

Experimental Section

Materials. Human serum albumin (70024-90-7), Congo Red (CR), and Thioflavin T (ThT) were obtained from Sigma Chemical Co and used as received. All other chemicals were of the highest purity available.

Preparation of HSA Solutions. The buffer solutions used were glycine + HCl for pH 3.0 and sodium monophosphate-sodium diphosphate for pH 7.4, respectively. The buffers were prepared in different NaCl concentrations (0, 20, 50, 100, 150, and 250 mM NaCl). The HSA was dissolved in each buffer solution to a final concentration of typically 20 mg/mL, if not otherwise stated. Protein concentration was determined spectrophotometrically using a molar absorption coefficient of 35 219 M^{-1} cm^{-1} at 280 nm.[30] Before incubation, the solution was filtered through a 0.2 μm filter into sterile test tubes. Samples were incubated at a specified temperature in a refluxed reactor. Samples were taken out at intervals and stored on ice before adding CR or ThT.

Seeding Solutions. To test whether seeding with preformed aggregates increases the rate of HSA aggregation under the different conditions where fibrils are formed, a protein solution was incubated for 24−48 h and an aliquot that corresponded to 10% (w/w) of the total protein concentration was then added to a fresh protein solution.

Thioflavin T Spectroscopy. 50 μL aliquots of protein solution were withdrawn at different times and diluted 100 times with 4 mL of ThT solution in corresponding buffer (final ThT concentration 20 μM). Samples were continuously stirred during measurements. Fluorescence was measured in a Cary Eclipse fluorescence spectrophotometer equipped with a temperature control device and a multicell sample holder (Varian Instruments Inc.). Excitation and emission wavelengths were 450 and 482 nm, respectively. All intensities were background-corrected for the ThT-fluorescence in the respective buffer without the protein.

Congo Red Binding. Changes in the absorbance of Congo Red dye produced by binding to HSA were measured in a UV−vis spectrophotometer DU Series 640 (Beckman Instruments) operating from 190 to 1100 nm. All measurements were made in the wavelength range 200−600 nm in matched quartz cuvettes. Protein solutions were diluted 20−200-fold into a buffer solution with 5 μM Congo Red (Acros Organics, Geel, Belgium). Spectra in the presence of the dye were compared with that of the buffer containing Congo Red in the absence of protein, and also with that containing protein without dye.

Circular Dichroism (CD). Far-UV circular dichroism (CD) spectra were obtained using a JASCO-715 automatic recording spectropolarimeter with a JASCO PTC-343 Peltier-type thermostatted cell holder. Quartz cuvettes with 0.2 cm path length were used. CD spectra were obtained from aliquots withdrawn from the aggregation mixtures at the indicated conditions and incubation times, and recorded between 195 and 250 nm at 25 °C. The mean residue ellipticity θ (deg cm^2 $dmol^{-1}$) was calculated from the formula $\theta = (\theta_{obs}/10)(MRM/lc)$, where θ_{obs} is the observed ellipticity in deg, MRM is the mean residue molecular mass, l is the optical path-length (in cm), and c is the protein concentration (in g mL^{-1}). In order to calculate the composition of the secondary structure of the protein, SELCON3, CONTIN, and DSST programs were used to analyze far-UV CD spectra. Final results were assumed when data generated from all programs show convergence.[31]

Fourier Transform Infrared Spectroscopy (FT-IR). FT-IR spectra of HSA in aqueous solutions were determined by using a FT-IR spectrometer (model IFS-66v from Bruker) equipped with a horizontal ZnS ATR accessory. The spectra were obtained at a resolution of 2 cm^{-1}, and generally 200 scans were accumulated to get a reasonable signal-to-noise ratio. Solvent spectra were also examined in the same accessory and at the same instrument conditions. Each different sample spectrum was obtained by digitally subtracting the solvent spectrum from the corresponding sample spectrum. Each sample solution was repeated three times to ensure reproducibility and was averaged to produce a single spectrum.

Protein Fluorescence. To examine the conformational variations around the tryptophan residue of HSA, fluorescence emission spectra of HSA samples were excited at 295 nm, which provides no excitation of tyrosine residues, and therefore, neither emission nor energy transfer to the lone side chain takes place. Slit widths were typically 5 nm. The spectrophotometer used was a Cary Eclipse from Varian Instruments Inc.

Transmission Electron Microscopy (TEM). Suspensions of HSA were applied to carbon-coated copper grids, blotted, washed, negatively stained with 2% (w/v) of phosphotungstic acid, air-dried, and then examined with a Phillips CM-12 transmission electron microscope operating at an accelerating voltage of 120 kV. Samples were diluted between 20 and 200-fold where prior deposition on the grids was needed.

X-ray Diffraction. X-ray diffraction experiments were carried out using a Siemens D5005 rotating anode X-ray generator. Twin Göbel mirrors were used to produce a well-collimated beam of Cu Kα radiation (λ = 1.5418 A). Samples were put into capillaries with diameters of 0.5 mm. X-rays diffraction patterns were recorded with an AXS F.Nr. J2-394 imaging plate detector.

Results and Discussion

It has been previously reported that amyloid fibrils can also be formed *in vitro* from α-globular proteins such as myoglobin, ovoalbumin, bovine (BSA), and human (HSA) serum albumins,[4,32,33] for example. Similar to these proteins, native HSA also lacks any properties suggesting a predisposition to form amyloid fibrils, since most of its sequence (>60%) is arranged in an α-helix structure, with the subsequent tightening of its structure through intramolecular interactions such as hydrogen bonds. In this way, serum albumin aggregation is only promoted under conditions favoring partly destabilized monomers and dimers such as low pH, high temperatures, or the presence of chemical denaturants.[34] In a recent report,[28] we have shown that partially destabilized HSA molecules form amyloid-like fibrils and other types of aggregates under different solution conditions such as increasing the solution temperature and changing the solution pH.[28,35,36] Thus, HSA was subjected to conditions previously found to be effective for protein aggregation, in particular those inducing amyloid-like fibril formation but modifying the solution ionic strength in order to analyze its effects on the amyloid-like assembly pathway of this protein. Thus, we prepared HSA solutions at a concentration of 20 mg/mL in 0.01 M sodium phosphate buffer (pH 7.4) or 0.01 M glycine-HCl buffer (pH 3.0) in the presence of 0, 20, 50, 100, 150, and 250 mM NaCl at 25 or 65 °C followed by subsequent incubation for up to 15 days. HSA is in its native form (N) at pH 7.4, which is composed mostly of α-helix secondary structure. In contrast, HSA adopts

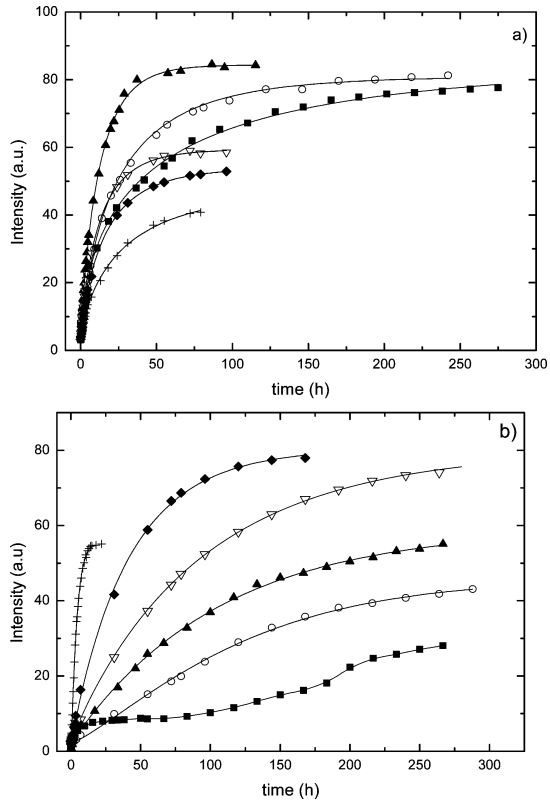

Figure 1. Time evolution of ThT fluorescence in HSA solutions incubated at 65 °C at (a) pH 7.4 and (b) pH 3.0 in the presence of (■) 0, (○) 20, (▲) 50, (▽) 100, (◆) 150, and (+) 250 mM NaCl.

an extended less-ordered configuration (E-state) below pH 3.5 with lesser helical content.[37−39] On the other hand, 65 °C was chosen as the incubation temperature, provided that HSA temperature-induced denaturation takes place through a two-state transition with a first melting temperature, T_m, of ∼56 °C and a second T_m of ∼62 °C[35,40,41] as a consequence of the sequential unfolding of the different domains of the protein, in particular IIA and IIIA subdomains: at 50 °C, a reversible separation of site I and II occurs; below 70 °C, the irreversible unfolding of site II is present, while increasing the temperature over 70 °C or higher results in the irreversible unfolding of site I.[42] Moreover, as the pH becomes more acidic, T_m becomes lower.[35]

Amyloid Formation Kinetics. When HSA solutions (20 mg/mL in the presence of 0, 20, 50, 100, 150, or 250 mM NaCl) were incubated at room temperature up to 300 h, the ThT fluorescence emission intensity was negligible at pH 7.4 whereas a slight increase was observed at pH 3.0 as a consequence of a little gain in β-sheet structure due to the formation of some oligomeric aggregates (data not shown). This suggests that HSA was not capable of forming amyloid fibrils or other types of aggregates with significant β-sheet structure under these conditions. In contrast, a time-dependent increase in ThT fluorescence is observed when the different HSA solutions were incubated at 65 °C (see Figure 1), in accordance with fibril formation. Congo Red (CR) absorption was also used to corroborate the formation of these fibrils in HSA solutions, which display a red-shift of the differential absorption maximum from 495 to ca. 530 nm at 65 °C (see Figure S1 as an example).

In general, the kinetics of HSA fibrillation under the present solution conditions at 65 °C involved the continuous rising of

TABLE 1: Kinetic Parameters of the Self-Assembly Process of HSA Solutions

pH	NaCl (mM)	ΔF	k_{sp} (h^{-1})	n
7.4	0	83	0.019	0.56
	20	82	0.040	0.70
	50	83	0.084	0.92
	100	57	0.068	0.80
	150	52	0.056	0.77
	250	46	0.034	0.70
3.0	0	6/22	0.144/0.005	1.25/3.60
	20	44	0.008	1.25
	50	57	0.010	0.96
	100	73	0.012	0.95
	150	77	0.024	0.93
	250	56	0.233	1.10

ThT fluorescence during the early periods of incubation until a quasi-plateau region was attained in the time scale analyzed, as occurred for different proteins such as BSA,[32] acylphosphatase,[7] or ovoalbumin,[33] and it exhibited no discernible lag phase. This absence may be related to the fact that the initial protein aggregation is a downhill process, which does not require a highly organized and stable nucleus. This was confirmed by the absence of any remarkable effect on the fluorescence curves when protein seeds are added to protein solutions followed by subsequent incubation (see Figure S2 in the Supporting Information). It has been suggested that large multidomain proteins such as BSA are able to form propagation-competent nucleus-like structures (oligomeric structures), since there is no energy barrier to impede aggregate growth.[32] As has been discussed in detail previously before,[32,36] HSA forms these oligomers upon very short incubation times, which usually occurs by a mechanism of classical coagulation or downhill polymerization.[44] Nevertheless, a different behavior was found at acidic pH in the absence of added electrolyte: After a small increase in ThT fluorescence at very short incubation times, there exists an almost plateau region (between 24 and 100 h approximately), from which the ThT fluorescence starts to increase again (see Figure 1b). This plateau region was identified as a lag phase, as confirmed by a fibril seeding growth process (see Figure S3 in the Supporting Information). This might well indicate that the formation of oligomeric structures might need more time to be developed and/or persist for longer times due to their enhanced solubility under acidic conditions in the absence of added salt, so oligomers need to reach a certain number/size to change the energy landscape of the system and promote further aggregation.

Figure 1 also shows that amyloid formation was favored and took place progressively quicker as the electrolyte concentration increased from 0 to 50 mM NaCl at pH 7.4 and at the whole concentration range studied at pH 3.0, as denoted by the increment in ThT fluorescence intensity and the subsequent presence of a plateau region at shorter incubation times. This points out that the increasing hydrophobicity originated from the screening of repulsive electrostatic interactions between protein molecules is capable of stabilizing the β-sheets.[36,45−48] In contrast, a progressive decrease in ThT fluorescence intensity is observed at electrolyte concentrations larger than 50 mM at physiological pH, with the plateau located at shorter incubation times. This decrease can be related to the formation of bundles of shorter fibrils and to the presence of amorphous aggregates (with larger α-helix and unordered conformation contents, as will be shown below), and is a consequence of an excessive shielding of intermolecular electrostatic forces, which is accompanied by an additional enhancement of the solution

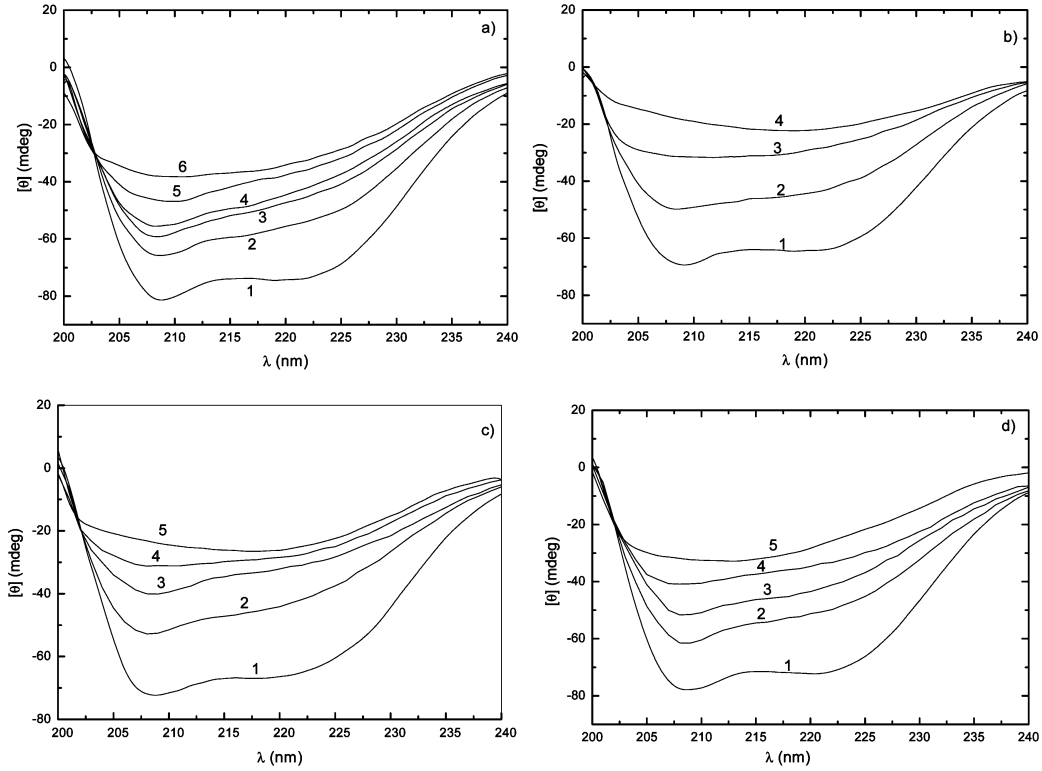

Figure 2. Far-UV spectra of HSA solutions at 65 °C and pH 7.4 in the presence of (a) 0, (b) 50, (c) 100, and (d) 150 mM NaCl at (1) 0 h, (2) 12 h, (3) 24 h, (4) 48, (5) 60 h, and (6) 72 h of incubation.

hydrophobicity through (a) a side-to-side adsorption between protein molecules and fibrils; (b) a reduction of the ThT fluorescence by blocking ThT binding sites on the fibrils due to a reduction in exposed surface area;[49] and (c) a lower fraction of formed fibrils due to an unsuitable energy balance to establish effective intermolecular interactions; that is, random aggregation is promoted, so there exists a change in the energy landscape of the protein fibrillation process.[50]

Differences in the trends observed between physiological and acidic conditions in the presence of electrolyte might arise from the fact that ordered aggregation of globular proteins requires partial unfolding of the native state,[21] which enables this precursor state to be populated and to expose aggregation-competent regions that are usually protected against intermolecular interactions in the native protein. However, these regions can be different and display different propensities to solvent exposition depending on solution conditions. Thus, although amyloid formation can occur, rates and extents of fibril formation, fibrillation pathways, and the structures of the resulting fibrils can be very diverse.[51,52] In this way, it seems that both the distinct ionization state of the protein and the different initial structural state at acidic conditions (expanded-E-state) may be the origin of the observed differences, which change the energy landscape of the aggregation process.

The time-dependence of the ThT fluorescence curves was fitted by nonlinear square curve-fitting to a stretched exponential function $F = F^{\infty} + \Delta F \exp(-[k_{sp}t]^n)$ in order to derive information on the amyloid kinetics formation. F, F^{∞}, and ΔF are the observed fluorescence intensity at time t, the final fluorescence intensity, and the fluorescence amplitude, respectively, and k_{sp} is the rate of spontaneous fibril formation. Values of k_{sp}, n, and ΔF are shown in Table 1. Values of n lower than 1 indicated that the kinetics can be approximated to several exponential functions indicative of the existence of multiple events in the amyloid formation. The increasing k_{sp} values as the electrolyte concentration goes up to 100 mM at physiological pH and at the whole concentration range under acidic conditions corroborate the more efficient aggregation due to electrostatic screening in the presence of added salt. However, under physiological conditions, progressively lower k_{sp} and n values are derived at larger ionic strengths (see Table 1), maybe as a predominance of fibril bundling and formation of amorphous aggregates over that of new fibrils, as commented before. This behavior is in contrast to that observed for other albumin proteins such as ovoalbumin and BSA, for which their fibrillation mechanisms and, thus, their aggregation rates were found not to be so strongly influenced by ionic strength if compared to that of HSA.[33] In particular, for ovolabumin, it was found that a continuous slight decrease in the rate of fibrillation takes place as the electrolyte concentration occurs, whereas for BSA the trend is similar to that of HSA, although less marked. Possibly, the subtle differences in the amino acid sequence between the proteins and in their structural conformation may account for these differences.

On the other hand, it is interesting to note that, after 3 days of incubation, most HSA solutions transformed into a gel-like state at elevated ionic strengths (between 100 and 250 mM). It is known that salt concentrations have an important role, not only favoring conformational transitions and intramolecular interactions in the protein but also enhancing protein−protein interactions leading to gelification.[48−50] In our case, these gels can be a consequence of a "correct" balance between electrostatic shielding and hydrophobic interactions which enables fibrils to interact in suitable relative orientations, as has been previously demonstrated for other proteins.[50] Nevertheless, these effects will be discussed in a forthcoming publication.

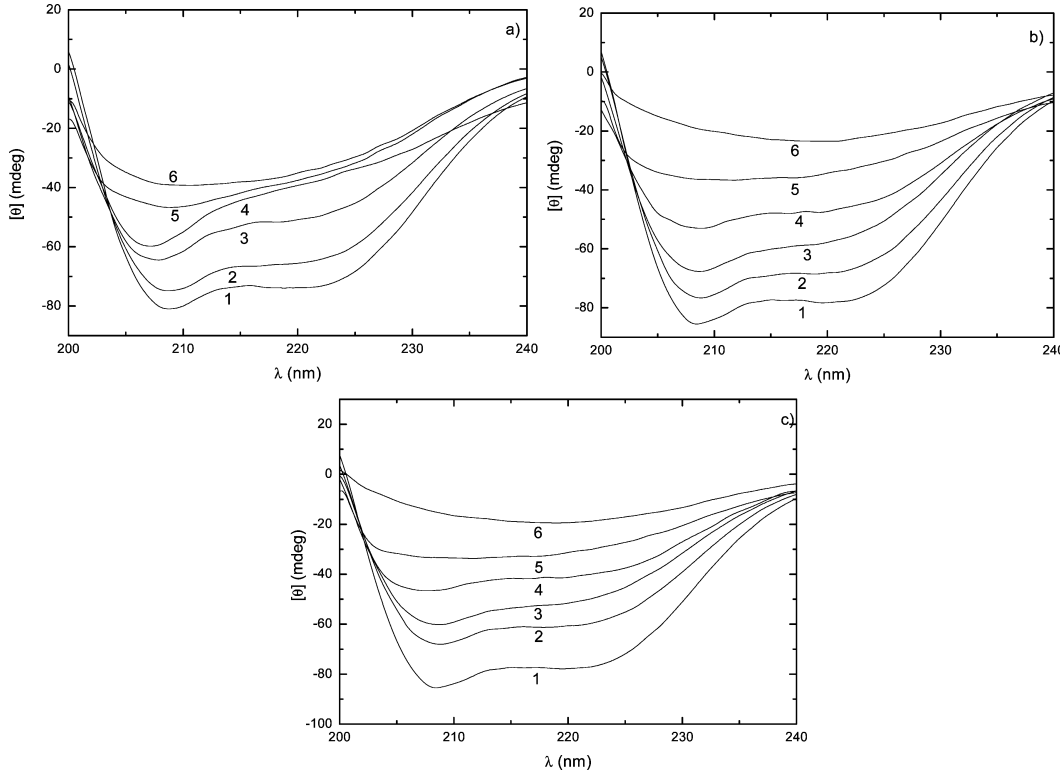

Figure 3. Far-UV spectra of HSA solutions at 65 °C and pH 3.0 in the presence of (a) 0, (b) 50, and (c) 150 mM NaCl at (1) 0 h, (2) 24 h, (3) 50 h, (4) 100 h, (5) 150 h, and (6) 250 h of incubation.

TABLE 2: Secondary Structure Variations (in %) on HSA Samples upon Incubation at 65° C under Different Solution pH Values and Electrolyte Concentrations

pH	NaCl (mM)	Δα-helix	Δβ-sheet	Δturn	Δ unordered
7.4	0	−35	16	8	11
	20	−37	18	9	12
	50	−42	21	10	11
	100	−39	16	9	14
	150	−37	15	8	16
	250	−33	11	7	19
3.0	0	−20	9	3	8
	20	−25	12	4	9
	50	−28	14	4	10
	100	−32	17	5	10
	150	−36	19	6	11
	250	−35	20	5	10

Structural Changes. To shed additional light on the differences of the amyloid-like formation of HSA in the presence of added salt at the different pH values, we recorded CD, FT-IR, and tryptophan (Trp) fluorescence spectra. The far-UV CD spectra of HSA solutions incubated at room temperature in the absence and the presence of electrolyte showed two minima at 208 and 222 nm, characteristic of a helical structure. At acidic pH, HSA molecules also preserve an important part of their α-helix structure upon incubation, as denoted by the presence of the minima at 208 and 222 nm. However, a slight decrease in ellipticity, [θ], is observed, which is compatible with a little decrease of α-helices due to the appearance of small amorphous aggregates in solution (not shown).

When HSA solutions were incubated at 65 °C, far-UV CD spectra showed a dramatic change in ellipticity throughout incubation. Figures 2 and 3 show CD spectra for HSA solutions at 65 °C in the presence of several NaCl concentrations at both pH 7.4 and 3.0, respectively. Under these conditions, the minimum at 222 nm progressively disappears while the negative band intensity at 208 nm is also reduced. All this indicates that high-temperature conditions spawn intermediates, which are clearly less helical than the starting conformations (a decrease in α-helix content is observed). Thus, these changes obtained in CD spectra suggest the increments of β-sheet and loop structures at longer incubation times (∼72 h and ∼150 h for pH 7.4 and 3.0, respectively), which resemble those typical of proteins with important proportions of β-sheet structure characterized by a minimum at ca. 215−220 nm and small [θ] values as a consequence of the presence of β-rich aggregates in solution, as can be observed, for example, in Figure 2b. Nevertheless, it is worth mentioning that the increasing number and size of large scattering objects such as fibrils in solution as the incubation proceeds involves the strong decrease in ellipticity, which makes it a little less clear the ellipticity minimum around 215−220 nm corresponding to β-sheet structures.

Changes in protein structure composition derived at the end of incubation at 65 °C were obtained from CD analysis[31] and are shown in Table 2. Data in this table are displayed as the difference (expressed in %) between the beginning and the end of the incubation process of protein structure composition (Δα-helix, Δβ-sheet, Δturn, and Δrandom coil conformation, respectively). The negative signs mean a decrease in the corresponding structure. At pH 7.4 and room temperature, the initial α-helix content is ∼59%, the β-sheet conformation is ∼5%, the turn content is ∼13%, and the remaining random coil content is ∼23%, in agreement with previous reports.[47] When HSA solutions were incubated at 65 °C, these showed important differences in the secondary structure compositions (see Table 2). The largest changes were observed in α-helix and β-sheet

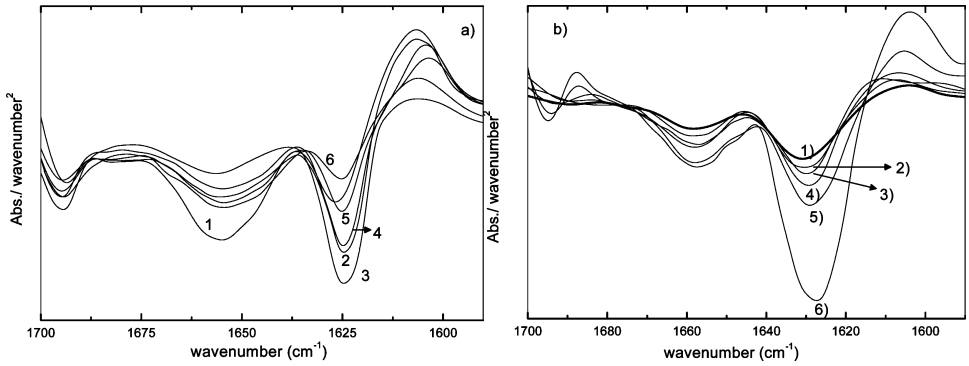

Figure 4. Second derivative of FT-IR spectra at 65 °C and (a) pH 7.4 and (b) pH 3.0 in the presence of (1) 0, (2) 20, (3) 50, (4) 100, (5) 150, and (6) 250 mM NaCl after incubation.

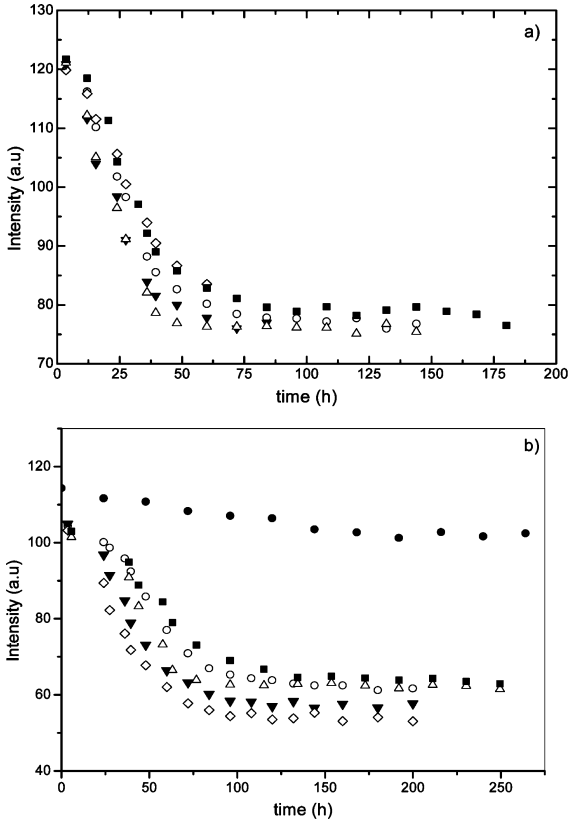

Figure 5. Time evolution of Trp fluorescence of HSA solutions upon incubation at (a) pH 7.4 and (b) pH 3.0 in the presence of (■) 0, (○) 20, (Δ) 50, (▼) 100, and (◇) 150 mM, and (●) at pH 3.0 and 25 °C in the presence of 50 mM NaCl.

contents, with the former mainly decreased to be converted into the β-sheet structure. Moreover, coil and turn conformations also change throughout the incubation process, increasing slightly their significance.

On the other hand, increases in the β-sheet content become more important as the electrolyte concentration increases, but only up to 50 mM NaCl at physiological conditions and in the whole concentration range at acidic pH, for which these variations were lighter. In this regard, fully mature amyloid fibrils could not be formed at low electrolyte concentrations at acidic pH, provided that effective interactions between β-strands are not allowed due to electrostatic repulsions: recent studies using hydrogen exchange and proteolysis have indicated a less-ordered structure for protofilaments compared with mature amyloid fibrils,[54,55] in agreement with their lower β-sheet content suggested by CD and ThT binding studies, as in the present study. On the other hand, certain recovery of α-helical content is observed at pH 7.4 at 150 and 250 mM NaCl concentrations, which agrees with the decrease in ThT fluorescence intensity observed at these concentrations, as commented previously.

FT-IR spectra recorded for HSA solutions under different conditions at the beginning and the end of the incubation process additionally corroborated ThT and CD data. Figure 4 shows the second derivative of the HSA solutions at 65 °C at pH 7.4 and pH 3.0 for different electrolyte concentrations. Following incubation at 65 °C, a red-shift from 1652 to 1658 cm^{-1} (see Figure S4 in the Supporting Information for the FT-IR spectrum of native HSA) and a decrease in intensity of the amide I band occur up to 50 mM NaCl at physiological conditions, which are indicative of the presence of a certain increase of disordered structure, as also seen by far-UV CD. For pH 3.0, this shift is more progressive along the whole added salt concentration range. The appearance of a well-defined peak around 1625 cm^{-1} points out a structural transformation to an intermolecular hydrogen-bonded-β-sheet structure,[56] which is a structural characteristic of the amyloid fibrils and is present at both pH values. The spectra also show a high frequency component (∼1693 cm^{-1}) at these electrolyte concentrations that would suggest the existence of a β-sheet in an antiparallel configuration.[57] The decrease of the peak intensity at 1657 cm^{-1} and the increase at 1625 cm^{-1} as the electrolyte concentration increases from 0 to 50 mM NaCl at pH 7.4 support that the major structural transition is from α-helix → β-sheet and that intermolecular interactions are favored at low and medium salt concentrations, in agreement with CD data. In contrast, the decrease in the band at 1625 cm^{-1} and the blue shift of the band at 1542 cm^{-1} (not shown) at larger electrolyte concentrations at this pH point out a lower β-sheet configuration and a further unordered conformation, which confirms that large electrolyte concentrations do not facilitate amyloid formation, in agreement with CD and ThT fluorescence data.

Tryptophanyl fluorescence data showed that when temperature is raised to 65 °C, a reduction in fluorescence intensity and a hypsochromic shift were observed, as noted in detail previously.[36] Nevertheless, we found that when incubation proceeds at electrolyte concentrations larger than 100 mM NaCl at pH 7.4, a slightly lower decrease in fluorescence intensity takes place, which agrees with the assumption that less ordered amyloid-like fibrils are formed under these solution conditions in coexistence with amorphous aggregates. In contrast, at acidic pH, the decrease in fluorescence is also slightly larger as the

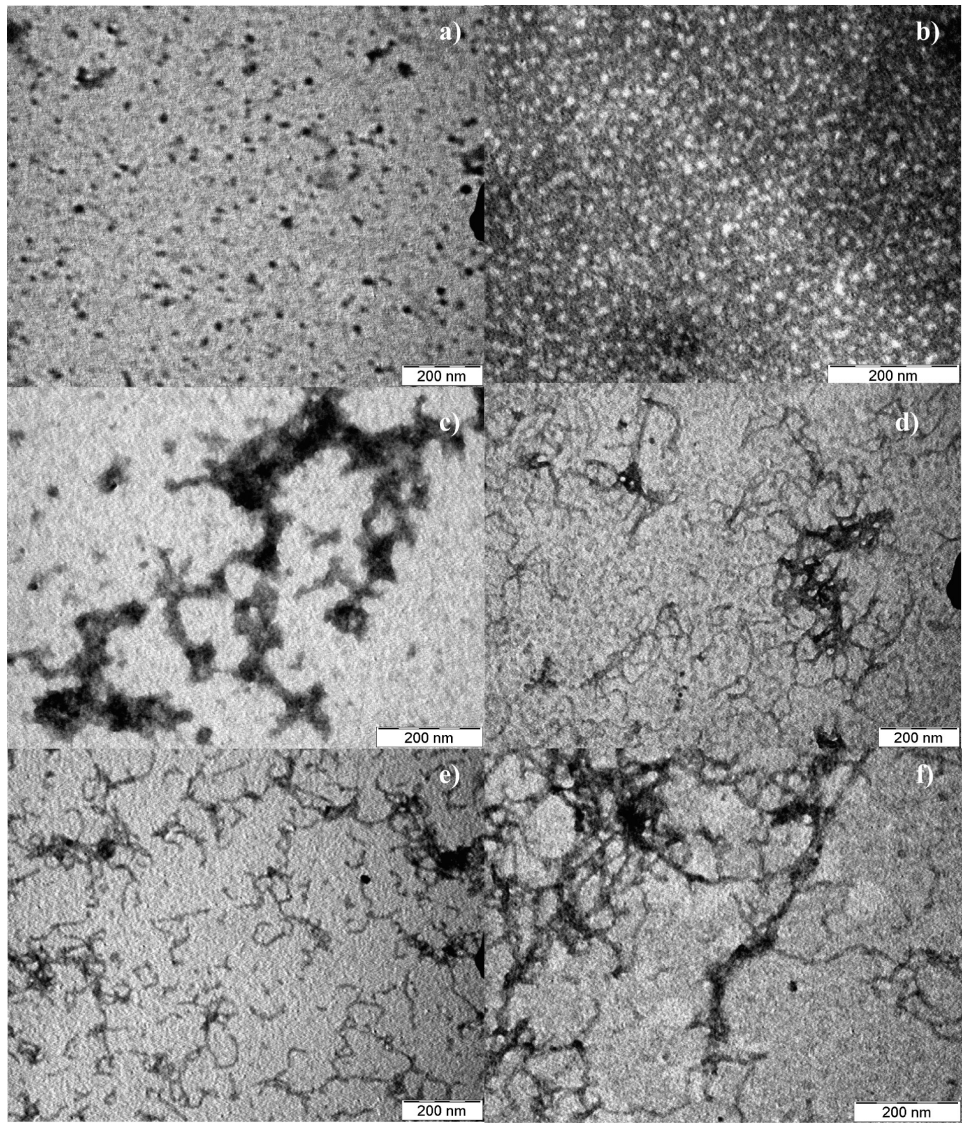

Figure 6. TEM pictures of the different stages of the HSA fibrillation process at 25 °C at pH 7.4: (a) in the presence of 50 mM NaCl after 150 h of incubation; (b) at pH 3.0 after 150 h of incubation in the absence of added salt; (c) at pH 7.4 at 65 °C in the presence of 150 mM NaCl after 50 h of incubation; (d) at pH 7.4 at 65 °C in the absence of added NaCl after 50 h of incubation; (e) at 65 °C at acidic pH in the presence of 100 mM after 150 h of incubation; (f) at 65 °C at acidic pH in the presence of 250 mM after 50 h of incubation.

added salt concentration increases, which denotes more important changes in tertiary structure (see Figure 5).

In Situ Observation of Protein Structures. TEM images were recorded at different stages during incubation under the different conditions described above to denote the possible differences existing between the aggregates as denoted previously. Distinct time-dependent morphological stages can be observed in these images. At room temperature, neither fibrils nor other type of aggregates are detected at the beginning of incubation. Only after some hours (24 h at pH 7.4, and 48 h at pH 3.0, respectively) are some spherical aggregates detected. These developed to amorphous clusters, which possess largely helical structure in the presence of electrolyte upon longer incubation (150 h), as seen in Figure 6a. In addition, at acidic pH, less numerous, more elongated aggregates can also be observed, with sizes of 20−30 nm in length and 3−4 nm in width, and their population slightly becomes more important as incubation proceeds and electrolyte concentration becomes larger (Figure 6b). The formation of these types of aggregates is characterized by a decrease of helical structure accompanied with a slight rise in β-sheet and unordered conformations at long incubation times, as seen from CD measurements.

In contrast, when temperature is raised to 65 °C, fibril formation is observed. Electron microscopy has pointed out that aggregation leads first to globular species, which subsequently convert to fibrils with a curly morphology via several structural intermediates, as has been previously discussed in detail.[36] X-ray diffraction data also confirms fibril formation (see Figure 7). Two strong reflections at 4.8 Å and 11 Å are observed in the X-ray image. The 4.8 Å meridional reflection arises from the spacing between hydrogen-bonded individual strands in the β-sheet structure that lie perpendicular to the fibril axis, and the 11 Å equatorial reflection corresponds to the intersheet spacing, with the β-sheets stacked face-to face to form the core structure

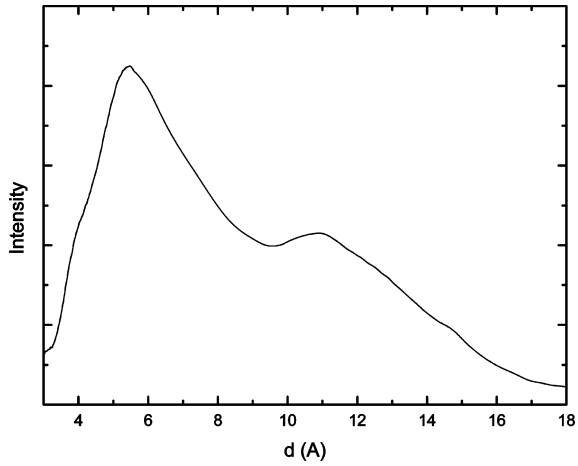

Figure 7. X-ray diffraction pattern of HSA fibrils at pH 7.4 and 65 °C.

of protofilaments.[58,59] This indicates that fibrils possess a cross-β structure, one of the diagnostic halfmarks of amyloid structures.

Nevertheless, the presence of larger concentrations of added electrolyte induces some changes in the structure of the resulting aggregates. In this way, at salt concentrations larger than 100 mM, we have detected that the resulting fibrils appear to be shorter and thicker, and coexist with amorphous material (see Figure 6c and d for comparison). Enhanced attractive interactions between structural intermediates such as beadlike structures and lateral protofibril previously observed can be the origin of these differences. Since electrolyte shields electrostatic repulsion between charged groups in the protein and between protein chains, the hydrophobic effect is progressively more important. Electrostatic shielding allows fibril bonding not only between fibril ends but also between axial sides of adjacent protofibrils and protein molecules, resulting in short and thicker fibrils. In particular, in the case when electrostatic shielding is so effective that protein association occurs before getting suitable relative orientations to give regular fibril assemblies, nonspecific aggregation may take place, leading to the formation of amorphous aggregates, provided that a suitable balance between interactions is necessary to completely stabilize the β-sheet structure.

On the other hand, at acidic conditions, the presence of increasing electrolyte concentrations allows further growth of the short protofibrils presented in solution at 48−96 h of incubation (depending on conditions), which do not develop otherwise. The corresponding CD spectrum shows a progressive increase in the proportion of the β-structure at the expense of the helical one during incubation. The presence of electrolyte concentrations larger than 50 mM involves other structural intermediates in the self-assembly process as ring-shaped structures, as seen before (see also Figure S5 in the Supporting Information).[36,60] Furthermore, as the added electrolyte concentration increases, there is an increase in size and a denser population of fibrils, in contrast to the behavior observed for physiological conditions (see Figure 6f): From the previously existing fibrils at low salt concentrations possessing sizes ranging from ∼100 nm to several hundred nanometers in length and 8−11 nm in width (shorter on average than those obtained at physiological conditions), which are composed of a seam of β-sheet structure decorated by relatively disorganized α-helical structure as occurred for Rnase[61] or yeast Ure2p,[62] it is possible to obtain larger and thicker curly fibrils at high electrolyte concentrations due to electrostatic screening, quite similar to those observed at pH 7 (Figure 6g).

Thus, it is interesting to note that a similar curly morphology for HSA fibrils can be achieved under the different solution conditions. Nevertheless, the rate and extent of aggregation depends on solution conditions. On the other hand, it is worth mentioning that, in contrast to HSA, BSA fibrillation has been shown to be halted at the early curly stage in spite of the enormous structural similarities with HSA, since no further development in fibrillar structure over long incubation times has been observed.[35] On the other hand, it was also noted that the formation of the mature fibrils in vitro is concomitant with gelation, as occurred in the present study.[63−65]

Conclusions

HSA has the ability to assemble into amyloid-like aggregates under different solution conditions, i.e., under both physiological and acidic pH at elevated temperature and different ionic strengths. However, the fibrillation process is strongly influenced by the latter parameter. In this way, we have analyzed the HSA fibrillation process and its kinetics by ThT fluorescence spectroscopy. We observed that, at physiological pH, fibrillation is progressively faster and more efficient in the presence of up to 50 mM NaCl due to electrostatic shielding. However, at higher salt concentrations, an excessive shielding and further enhancement of the solution hydrophobicity due to salt excess occurs, which induces a reduction of the ThT fluorescence by (a) decreasing the fraction of formed fibrils due to an unsuitable energy balance to establish effective intermolecular interactions, which favors random aggregation; (b) favoring side-to-side adsorption between protein molecules and fibrils, which leads to the formation fibril bundling, as observed by TEM; or (c) blocking the ThT binding sites on the fibrils due to a reduction in exposed surface area. Thus, there is a change in the energy landscape of the fibrillation process. CD, FT-IR, and Trp fluorescence spectra seem to confirm this picture by monitoring the structural changes in both tertiary and secondary structure along the fibrillation process. In this way, a reduction in β-sheet structure at large salt concentrations is also confirmed from the analysis of far-UV CD spectra. In contrast, under acidic conditions, a progressive enhancement of HSA fibrillation is observed as the electrolyte concentration in solution increases. Both the distinct ionization state and the different initial structural state of the protein at acidic conditions (expanded E-state) may be the origin of this behavior. On the other hand, we have noted that the fibrillation process of HSA does not show a lag-phase, except at acidic pH in the absence of added salt. This involves that the initial aggregation is a downhill process which does not require a highly organized and unstable nucleus, with a progressive increase of the β-sheet (up to 26%) and an unordered conformation at the expense of the α-helical conformation. Finally, the obtained fibrils show a curly morphology and differ in length depending on solution conditions. In fact, at acidic conditions, a progressive evolution of the resulting fibrils can be found from a seam of β-sheet structure decorated by relatively disorganized α-helical structure to highly structured fibrils, as found under physiological conditions, as derived from CD and FT-IR data.

Acknowledgment. The authors thank the Ministerio de Ciencia e Innovación for support via Project MAT-2007-61604. The authors also thank Dr. Eugenio Vázquez for his assistance with CD measurements.

Supporting Information Available: Figures showing a difference absorbance spectrum of Congo Red, time evolution

of ThT fluorescence, and FT-IR spectra of native HSA. This material is available free of charge via the Internet at http://pubs.acs.org.

References and Notes

(1) Van der Linden, E.; Venema, P. *Curr. Opin. Colloid Sci.* **2007**, *12*, 158.
(2) Shahi, P.; Sharma, R.; Sanger, S.; Kumar, I.; Jolly, R. S. *Biochemistry* **2007**, *46*, 7365.
(3) Dobson, C. M. *Nature* **2003**, *426*, 884.
(4) Fändrich, M. *Cell. Mol. Life Sci.* **2007**, *64*, 2066.
(5) Wang, W. *Int. J. Pharm.* **2005**, *289*, 1.
(6) Gazit, E. *FEBS J.* **2007**, *274*, 317.
(7) Chiti, F.; Webster, P.; Taddei, N.; Clark, A.; Stefani, M.; Ramponi, G.; Dobson, C. M. *Proc. Natl. Acad. Sci. U.S.A.* **1999**, *96*, 3590.
(8) Cherny, I.; Gazit, E. *Angew. Chem., Int. Ed.* **2008**, *48*, 4062.
(9) Gras, S. L.; Tickler, A. K.; Squieres, A. M.; Devlin, G. L.; Horton, M. A.; Dobson, C. M.; MacPhee, C. E. *Biomaterials* **2008**, *29*, 1553.
(10) Dobson, C. M. *Trends Biochem. Sci.* **1999**, *24*, 329.
(11) Thirumulai, D.; Klimov, D. K.; Dima, R. I. *Curr. Opin. Struct. Biol.* **2003**, *13*, 146.
(12) Qu, Y.; Bolen, C. L.; Bolen, D. W. *Proc. Natl. Acad. Sci. U.S.A.* **1998**, *95*, 9268.
(13) Chiti, F.; Taddei, N.; Bucciantini, M.; White, P.; Ramponi, G.; Dobson, C. M. *EMBO J.* **2000**, *19*, 1441.
(14) Niraula, T. N.; Haraoka, K.; Ando, Y.; Li, H.; Yamada, H.; Akasaka, K. *J. Mol. Biol.* **2002**, *320*, 333.
(15) Krebs, M. R.; Wilkins, D. K.; Chung, E. W.; Pikeathly, M. C.; Chamberlain, A. K.; Zurdo, J.; Robinson, C. V.; Dobson, C. M. *J. Mol. Biol.* **2000**, *300*, 541.
(16) Moraitakis, G.; Goodfellow, J. M. *Biophys. J.* **2003**, *84*, 2149.
(17) De Felice, F. G.; Vieira, M. N.; Meirelles, M. N.; Morozova-Roche, L. A.; Dobson, C. M.; Ferreira, S. T. *FASEB J.* **2004**, *18*, 1099.
(18) Ferrao-Gonzales, A. D.; Souto, S. O.; Silva, J. L.; Foguel, D. *Proc. Natl. Acad. Sci. U.S.A.* **2000**, *97*, 6445.
(19) Khurana, R.; Gillespie, J. R.; Talapatra, A.; Minert, L. J.; Ionescu-Zanetti, C.; Mollet, I.; Fink, A. L. *Biochemistry* **2001**, *40*, 3525.
(20) Zurdo, J.; Guijarro, J. I.; Jiménez, J. L.; Saibil, H. R.; Dobson, C. M. *J. Mol. Biol.* **2001**, *311*, 325.
(21) Uversky, V. N.; Fink, A. L. *Biochim. Biophys. Acta* **2004**, *1698*, 131.
(22) Plakoutsi, G.; Taddei, N.; Stefani, M.; Chiti, F. *J. Biol. Chem.* **2004**, *279*, 14111.
(23) Eakin, C. M.; Attenello, F. J.; Morgan, C. J.; Miranker, A. D. *Biochemistry* **2004**, *35*, 6470.
(24) Fändrich, M. C.; Dobson, C. M. *EMBO J.* **2002**, *21*, 5682.
(25) Timasheff, S. N. *Annu. Rev. Biophys. Biomol. Struct.* **1993**, *22*, 67.
(26) Hoyer, W.; Anthony, T.; Cherny, D.; Heim, G.; Jovin, T. M.; Subramaniam, V. *J. Mol. Biol.* **2002**, *322*, 383.
(27) Chiti, F.; Calamai, M.; Taddei, N.; Stefani, M.; Ramponi, G.; Dobson, C. M. *Proc. Natl. Acad. Sci.* **2002**, *99*, 16419.
(28) Taboada, P.; Barbosa, S.; Castro, E.; Mosquera, V. *J. Phys. Chem. B* **2006**, *110*, 20733.
(29) Taboada, P.; Barbosa, S.; Castro, E.; Gutiérrez-Pichel, M.; Mosquera, V. *Chem. Phys.* **2007**, *340*, 59.
(30) Pace, C. N.; Vajdos, F.; Fee, L.; Grimsley, G.; Gray, T. *Protein Sci.* **1995**, *4*, 2411.
(31) Sreerama, N.; Woody, R. W. *Anal. Biochem.* **2000**, *287*, 252.
(32) Holm, N. K.; Jespersen, S. K.; Thomassen, L. V.; Wolff, T. Y.; Sehgal, P.; Thomsen, L. A.; Christiansen, G.; Andersen, C. B.; Knudsen, A. D.; Otzen, D. E. *Biochim. Biophys. Acta* **2007**, *1774*, 1128.
(33) Pearce, F. G.; Mackintosh, S. H.; Gerrard, J. A. *J. Agric. Food Chem.* **2007**, *55*, 318.
(34) Gorinstein, S.; Caspi, A.; Rosen, A.; Goshev, I.; Zemser, M.; Weisz, M.; Añon, M. C.; Libman, I.; Lerner, H. T.; Trakhtenberg, S. *J. Peptide Res.* **2002**, *59*, 71.
(35) Juárez, J.; Taboada, P.; Mosquera, V. *Biophys. J.* **2009**, *96*, 2353.
(36) Sagis, L. M. C.; Veerman, C.; Van der Linden, E. *Langmuir* **2004**, *20*, 924.
(37) Shaw, A. K.; Pal, S. K. *J. Photochem. Photobiol. B* **2008**, *90*, 69.
(38) Muzammil, S.; Kumar, Y.; Tayyal, S. *Eur. J. Biochem.* **1999**, *266*, 26.
(39) Pereira, L. G. C.; Théodoly, O.; Blanch, H. W.; Radke, C. J. *Langmuir* **2003**, *19*, 2349.
(40) Farruggia, B.; Rodriguez, F.; Rigatuso, R.; Fidelio, G.; Picó, G. *J. Protein Chem.* **2001**, *20*, 81.
(41) Flora, K.; Brennan, J. D.; Baker, G. A.; Doody, M. A.; Brigth, F. V. *Biophys. J.* **1998**, *75*, 1084.
(42) Tavirani, M. R.; Moghaddamnia, S. H.; Ranjbar, B.; Amani, M.; Marashi, S. A. *J. Biochem. Mol. Biol.* **2006**, *39*, 530.
(43) Rader, A. J.; Hespenheide, B. M.; Kuhn, K. A.; Thorpe, M. F. *Proc. Natl. Acad. Sci U.S.A.* **2002**, *99*, 3540.
(44) Ferrone, F. *Methods Enzymol.* **1999**, *309*, 256.
(45) Lin, M.-S.; Chen, L.-Y.; Tsai, H.-T.; Wang, S. S.-S.; Chang, Y.; Higuchi, A.; Chen, W.-Y. *Langmuir* **2008**, *24*, 5802.
(46) Hills, R. D.; Brooks, C. L. *J. Mol. Biol.* **2007**, *368*, 894.
(47) Hong, Y.; Pritzker, M. D.; Legge, R. L.; Chen, P. *Colloids Surf., B* **2005**, *46*, 152.
(48) Fujiwara, S.; Matsumoto, F.; Yonezawa, Y. *J. Mol. Biol.* **2003**, *331*, 21.
(49) Sikkink, L. A.; Ramírez-Alvarado, M. *Biophys. Chem.* **2008**, *135*, 25.
(50) Zheng, J.; Jang, H.; Nussinov, R. *Biochemistry* **2008**, *47*, 2497.
(51) Cerda-Costa, N.; Esteras-Chopo, A.; Aviles, F. X.; Serrano, L.; Villegas, V. *J. Mol. Biol.* **2007**, *366*, 1351.
(52) Plakoutsi, G.; Bemporad, F.; Calamai, M.; Taddei, N.; Dobson, C. M.; Chiti, F. *J. Mol. Biol.* **2005**, *351*, 910.
(53) Sreerama, N.; Woody, R. W. *Protein Sci.* **2003**, *12*, 384.
(54) Kheterpal, I.; Chen, M.; Cook, K. D.; Wetzel, R. *J. Mol. Biol.* **2006**, *361*, 785.
(55) Myers, S. L.; Thomson, N. H.; Radford, S. E.; Ashcroft, A. E. *Rapid Commun. Mass Spectrom.* **2006**, *20*, 1628.
(56) Casal, H. L.; Kohler, U.; Mantsch, H. H. *Biochim. Biophys. Acta* **1988**, *957*, 11.
(57) Fabian, H.; Choo, L.-P.; Szendrei, G. I.; Jackson, M.; Halliday, W. C.; Otvos, L., Jr.; Mantsch, H. H. *Appl. Spectrosc.* **1993**, *47*, 1513.
(58) Sunde, M.; Blake, C. *Adv. Protein Chem.* **1997**, *50*, 123.
(59) Bouchard, M.; Zurdo, J.; Nettleton, E. J.; Dobson, C. M.; Robinson, C. V. *Protein Sci.* **2000**, *9*, 1960.
(60) Sibley, S. P.; Sosinsky, K.; Gulian, L. E.; Gibbs, E. J.; Pasternack, R. F. *Biochemistry* **2008**, *47*, 2858.
(61) Sambashivan, S.; Liu, M. R.; Sawaya, M. R.; Gingery, M.; Eisenberg, D. *Nature* **2005**, *437*, 266.
(62) Ranson, N.; Stromer, T.; Bousset, L.; Melki, R.; Serpell, R. C. *Protein Sci.* **2006**, *15*, 2481.
(63) Ramírez-Alvarado, M.; Merkel, J. S.; Regan, L. *Proc. Natl. Acad. Sci. U.S.A.* **2000**, *97*, 8979.
(64) Damaschun, G.; Damaschun, H.; Fabian, H.; Gast, K.; Krober, R.; Wieske, M.; et al. *Proteins: Struct., Funct., Genet.* **2000**, *39*, 204.
(65) Goda, S.; Takano, K.; Yamagata, Y.; Nagata, R.; Akutsu, H.; Maki, S.; et al. *Protein Sci.* **2000**, *9*, 369–375.

JP902224D

Additional Supra-Self-Assembly of Human Serum Albumin under Amyloid-Like-Forming Solution Conditions

Josué Juárez,[†] Pablo Taboada,*[,†] Sonia Goy-López,[†] Adriana Cambón,[†] Marie-Beatrice Madec,[‡] Stephen G. Yeates,[‡] and Víctor Mosquera[†]

Grupo de Física de Coloides y Polímeros, Departamento de Física de la Materia Condensada, Facultad de Física, Universidad de Santiago de Compostela, E-15782 Santiago de Compostela, Spain, and Organic Materials Innovation Center, School of Chemistry, University of Manchester, Manchester M13 9PL, United Kingdom

Received: May 5, 2009; Revised Manuscript Received: June 22, 2009

Protein aggregation has a multitude of consequences ranging from affecting protein expression to its implication in different diseases. Of recent interest is the specific form of aggregation leading to the formation of amyloid fibrils, structures associated with diseases such as Alzheimer's disease. These fibrils can further associate in other more complex structures such as fibrillar gels, plaques, or spherulitic structures. In the present work, we describe the physical and structural properties of additional supraself-assembled structures of human serum albumin under solution conditions in which amyloid-like fibrils are formed. We have detected the formation of ordered aggregates of amyloid fibrils, i.e., spherulites which possess a radial arrangement of the fibrils around a disorganized protein core and sizes of several micrometers by means of polarized optical microscopy, laser confocal microscopy, and transmission electron microscopy. These spherulites are detected both in solution and embedded in an isotropic matrix of fibrillar gels. In this regard, we have also noted the formation of protein gels when the protein concentration and/or ionic strength exceds a threshold value (the gelation point) as observed by rheometry. Fibrillar gels are formed through intermolecular nonspecific association of amyloid fibrils at a pH far away from the isolectric point of the protein where protein molecules seem to display a "solid-like" behavior due to the existence of non-DLVO (Derjaguin−Landau−Verwey−Overbeck) intermolecular repulsive forces. As the solution ionic strength increases, a coarsening of this type of gel is observed by environmental scanning microscopy. In contrast, at pH close to the protein isoelectric point, particulate gels are formed due to a faster aggregation process, which does not allow substantial structural reorganization to enable the formation of ordered structures. This behavior also additionally corroborates that the existence of particulates might also be a generic property of all polypeptide chains as amyloid fibril formation under suitable conditions.

Introduction

A number of neurodegenerative diseases have been related to protein aggregation and deposition in the form of amyloid fibrils, such as type II diabetes, Alzehimer's, Parkinson's, Huntington's, and prion diseases amongst others.[1−6] A wide range of proteins is known to misfold and aggregate in mildly or hard denaturating conditions as amyloid fibrils provided that the ability to fibrillate is independent of the original native structure of the protein, whose amino acid sequence primarily appears to play a key role in terms of filament arrangement,[7] fibrillation kinetics,[8] and overall yield and stability of the fibrils.[9,10] These fibrils have been found to be based on a common structural motif consisting of continuous intermolecular β-sheets which run along the fibril axis such that the individual β-strands are perpendicular to the fibril axis.[11]

Under certain conditions, protein fibrils can further associate either nonspecifically such as in fibrillar gels or plaques or in a more ordered fashion such as in spherulites.[12−18] It is known that fibrillar gels are formed by protein aggregation if the protein concentration exceeds a given critical value under conditions where protein molecules are partially denaturated (as at high temperatures) and electrically charged (this is, far away from their isolectric point) upon incubation, i.e., under conditions where fibrillation can occur. Nevertheless, the correspondence between fine strand gels and amyloid fibril structure was established recently.[19,20] In contrast, by decreasing the intermolecular repulsion through shifting the solution pH to values near the protein isoelectric point, or by increasing the solution ionic strength the gel networks are comprised of particulate aggregates.

On the other hand, for systems where fibrillar protein aggregates and gels are formed, the strands can further associate in a more ordered fashion such as spherulitic structures. These are characterized by the presence of anisotropic material ordered in a spherically symmetric way. This gives rise to the appearance of a Maltese cross extinction pattern when these structures are studied under a polarized light microscope, much in the same way as spherulites formed by synthetic polymers,[21,22] natural polymers, and biopolymers.[23−25] In solutions *in vitro*, spherulites have been reported for different synthetic and natural peptides,[17,26−30] and have also usually been associated to the amyloid-like formation pathways of several proteins such as β-lactoglobulin,[20,31,32] α-L-iduronidase,[33] lysozyme,[18] and insulin.[16,34] Spherulites were also found *in vivo* in Alzheimer's disease, Gerstmann−Straulsler−Scheinker dis-

* Author to whom correspondence should be addressed. E-mail: pablo.taboada@usc.es. Phone: 0034981563100, Ext. 14042. Fax: 0034981520676.
† Universidad de Santiago de Compostela.
‡ University of Manchester.

10.1021/jp904167e CCC: $40.75
Published on Web 08/14/2009

ease, Down's syndrome,[35] and in tumors.[36,37] Thus, the formation of fibrillar structures may not be the end of the aggregation process, and proper knowledge of the nature and structure of these supramolecular assemblies may have important implications in different fields such as medicine,[3,4,35−37] food industry,[38,39] or biomaterials.[40]

In recent reports,[41,42] we have shown that partially destabilized human serum albumin (HSA) molecules form amyloid-like fibrils under different solution conditions. These fibrils feature the structural characteristics for amyloids: X-ray diffraction patterns, affinity to Congo Red and Thioflavin T dyes, birefringence, and high stability. Nevertheless, different fibrillation pathways, fibrillation kinetics, and structural intermediates and morphological differences in the resulting fibrils were observed depending on the incubation conditions.[42]

In this paper, we extend our previous studies in order to explore the solution conditions which enable the formation of different supramolecular assemblies of HSA amyloid-like fibers, and the structure of these resulting assemblies. To do that, extensive incubation of HSA solutions of pH 2.5, 5.5, and 7.4 at elevated temperature and ionic strengths ranging from 0 to 250 mM NaCl was made, and the resulting protein assemblies were analyzed by optical, confocal, transmission electron, environmental scanning electron, and atomic force microscopies, rheometry, and attenuated reflectance Fourier transform infrared (ATR-FTIR) and fluorescence spectroscopies. We have observed that spherulitic formation takes place under conditions where amyloid fibrils were previously present. The spherulites possess a radial arrangement of the protein fibrils around a disorganized protein core and sizes of 5−50 μm. In addition, different types of gels were also obtained upon extensive incubation under different solution conditions, either with fibrillar or particulate structure. Fibrillar gels that form at a pH far from the isoeletric point of the protein display a "solid-like" behavior and are formed through intermolecular nonspecific association of amyloid fibrils. A coarsening of these gels occurs when the solution ionic strength increases. When the solution pH is close to the protein isoelectric point, particulate gels are formed. These originate from a faster protein aggregation which does not allow the necessary structural reorganization to enable the formation of more ordered structures.

Materials and Methods

Materials. Human serum albumin (70024-90-7) and Thioflavin T (ThT) were obtained from Sigma Chemical Co. and used as received. All other chemicals were of the highest purity available.

Preparation of HSA Solutions. Protein was used after further purification by liquid chromatography using a Superdex 75 column equilibrated with 0.01 M phosphate. Experiments were carried out using double distilled, deionized, and degassed water. The buffer solutions used were glycine + HCl (I = 0.01 M) for pH 2.5, sodium acetate−acetic acid for pH 5.5 (I = 0.01 M), and sodium monophosphate−sodium diphosphate for pH 7.4 (I = 0.01 M), respectively. HSA was dissolved in each buffer solution to a final concentration of typically 20 mg/mL if not otherwise stated, and dialyzed extensively against buffer solution. Protein concentration was determined spectrophotometrically, using a molar absorption coefficient of 35219 M^{-1} cm^{-1} at 280 nm.[43] Prior to incubation, solutions were filtered through a 0.2 μm filter into sterile test tubes. Samples were incubated at a specified temperature (65 °C) for up to 15 days in a refluxed reactor if not otherwise stated. Samples were taken out at intervals and stored on ice before adding ThT.

Polarized Optical Microscopy (POM). After incubation, aliquots of protein solutions were removed from the vials and put onto microscope slides. These were immediately studied using a Zeiss Axioplan optical microscope (Carl Zeiss Ltd., Welwyn Garden City, U.K.). A total magnification of either 50× or 100× was used. A polarizer and analyzer were put in fixed positions, orthogonal to one another for the cross-polarizer imaging. Images were taken using a Kodak digitial camera mounted on the top of the microscope. The size of the spherulites seen in the images was determined by calibrating with a scale bar of known dimensions and thereby quantifying the spatial resolution per pixel image.

Laser Confocal Microscopy. Confocal microscopy was performed on a Leica TCS SP2 confocal system mounted on a Leica DM-IRE2 upright microscope, using a 40× objective. For fluorescence measurements, Thioflavin T was added to spherulitic solutions and excited using the 458 nm line of an argon ion laser. Simultaneously, transmission images were obtained with crossed polarizers in place using the 633 nm line of a He−Ne laser.

Thioflavin T Spectroscopy. Protein and ThT were dissolved in proper buffer at a final protein−dye molar ratio of 50:1. Samples were continuously stirred during measurements. Fluorescence was measured in a Cary Eclipse fluorescence spectrophotometer equipped with a temperature control device and a multicell sample holder (Varian Instruments Inc.). Excitation and emission wavelengths were 450 and 482 nm, respectively. All intensities were background-corrected for the ThT fluorescence in the respective solvent without the protein. Data from at least three different separate experiments were averaged and normalized on a scale from 0 to 1.

Attenuated Total Reflectance Fourier Transform Infrared Spectroscopy (ATR-FTIR). ATR-FTIR spectra of HSA in aqueous solutions were determined by using a FTIR spectrometer (model IFS-66v from Bruker) equipped with a horizontal ZnS ATR accessory. The spectra were obtained at a resolution of 2 cm^{-1}, and generally 200 scans were accumulated to get a reasonable signal-to-noise ratio. Solvent spectra were also examined using the same accessory and instrument conditions. Each different sample spectrum was obtained by digitally subtracting the solvent spectrum from the corresponding sample spectrum. Each sample solution was repeated three times to ensure reproducibility and averaged to produce a single spectrum.

Transmission Electron Microscopy (TEM). Suspensions of HSA were applied to carbon-coated copper grids, blotted, washed, negatively stained with 2% (w/v) phosphotungstic acid, air-dried, and then examined with a Phillips CM-12 transmission electron microscope operating at an accelerating voltage of 120 kV. Samples were diluted between 20−200-fold and sonicated when needed prior to deposition on the grids.

Environmental Scanning Electron Microscopy (ESEM). Suspensions of HSA were applied to glass-coated stainless steel grids, blotted, washed, air-dried, and then examined with an LEO-435 VP scanning electron microscope (Leica Mycrosystems, Cambridge, U.K.) operating at an accelerating voltage of 20 kV. Samples were diluted when needed prior to deposition on the grids. Samples were left to equilibrate at 2 °C. A few drops of distilled and deionized water were place around the sample. The chamber was flooded repeatedly with water vapor and the pressure subsequently reduced to ∼5 Torr. Further decreases in pressure led to evaporation of water and drying of the samples.

Atomic Force Microscopy (AFM). AFM images were recorded in the tapping mode by using an AFM XE100

instrument (PSIA Inc., Seoul, Korea) equipped with a rigid silicon cantilever of nominal spring constant of about 40 mN/m and resonant frequency of 325 kHz. Immediately after incubation, protein samples were diluted 20−400 times onto freshly cleaved muscovite mica (from Sigma Chemical Co.) attached to a magnetic steel disk which served as a sample holder. The abrupt dilution of the samples immediately quenches the concentration-dependent aggregation process. The AFM samples were dried in air or under nitrogen flow when required. Control samples (freshly cleaved mica, mica and buffer solution) were also investigated with AFM to exclude possible artifacts. Topography and phase-shift data were collected in the trace and retrace direction of the raster, respectively. The offset point was adapted accordingly to the roughness of the sample. The scan rate was tuned proportionally to the area scanned and kept within 0.35−2 Hz range.

Rheometry. The rheological properties of the samples were determined using a Bohlin CS10 rheometer with water bath temperature control. Couette geometry (bob, 24.5 mm in diameter, 27 mm in height; cup, 26.5 mm in diameter, 29 mm in height) was used, with a 2.5 cm^3 sample being added to the cup in the mobile state. Samples of very high modulus were investigated using cone-and-plate geometry (diameter 40 mm, angle 4°). A solvent trap maintained a water-saturated atmosphere around the cells. Frequency scans of storage (G') and loss (G'') moduli were recorded for selected protein concentrations and temperatures with the instrument in the oscillatory shear mode and with the strain amplitude (A) maintained at a low value ($A < 0.5\%$) by means of the autostress facility of the Bohlin software. This ensured that measurements of G' and G'' were in the linear viscoelastic region. Measurements on solutions of low modulus ($G' = 1-10$ Pa) which fell outside the range for satisfactory autostress feedback were rejected.

Results and Discussion

Human serum albumin consists of 585 amino acids in a single polypeptide chain, with a globular structure composed of three main domains that are loosely joined together through physical forces and six subdomains that are wrapped by disulfide bonds. The protein contains 17 disulfide bridges and one free SH group. Most of the HSA sequence (>60%) is arranged in α-helix structure, with the subsequent tightening of its structure through intramolecular interactions such as hydrogen bonds. Nevertheless, amyloid-like formation of HSA has been reported under different solution conditions.[41,42] HSA fibril formation usually takes place in the absence of a lag phase, and the resulting fibrils share the common structural features of "true" amyloid fibrils, although their final morphology depends on the incubation conditions.[42]

Spherulite Formation and Characterization. The propensity for spherulite formation was investigated by using optical and confocal microscopy at pH 2.5, 5.5, and 7.4 at 65 °C upon incubation in the presence of NaCl in the range 0−250 mM. We have observed that spherulitic structures are found under conditions where HSA fibrils were previously detected,[42] that is, at physiological pH and under acidic conditions in the presence of the highest added salt concentrations (100−250 mM NaCl). Although data were not collected quantitatively, the highest density of spherulites was observed at pH 7.4 in the presence of 50 mM NaCl, and at acidic pH in the presence of 250 mM. This agrees with the maximum efficiency of fibril formation previously reported.[42] In this regard, it has been previously found[41] that at both physiological pH and temperature fibril formation is disfavored at high ionic strengths due to an excesive shielding of repulsive electrostatic forces, which involves an increase in rapid random protein aggregation. In contrast, under acidic conditions fibril formation is continuosly enhanced as the added salt concentration increases. This difference has been assigned to the different nature and structure of the protein precursor states, which leads to different fibrillation rates, fibril conversion extents, fibrillation pathways, and structures of resulting fibers.[44−46] In addition, no differences were observed between the spherulites obtained in the various samples studied regardless of the incubation conditions.

Analysis of the solutions at both pH 2.5 and 7.4 by polarized optical microscopy allowed us to observe the presence of classical Maltese cross extinction patterns (Figure 1a) as a key mark of the presence of spherulites. This type of pattern was not observed at pH 5.5. The observed spherulites possess sizes ranging from 5 to 50 μm. In addition, the test tubes when placed between crossed polarizers showed birefrigence from spherulites in the samples (not shown). Spherulitic structures are detected both in solution prior to gelification and embedded in an isotropic gel matrix after gelification. It should also be noted that nonspherulitic areas of the sample, which may contain fibrils not assembled into spherulites, are not visibly birefringent, indicating that polypeptide chains in this region are unoriented. Similar spherulitic occurrences in protein gels were also found, for example, for whey proteins,[47] β-lactoglobulin,[29,30] and insulin.[32,33]

To confirm that the spherulites contain amyloid fibrils, they were imaged by confocal microscopy using ThT as the fluorescent dye, whose fluorescence is known to increase markedly upong binding to amyloid fibrils.[48] In confocal mode, the fluorescence emission was observed to come from the spherulites (Figure 1b), which confirms they are composed of amyloid fibers.[49] Confocal microscopy in transmission mode resulted in an image similar to that obtained with an optical microscope (Figure 1c), clearly displaying the presence of spherulites as Maltese cross patterns of comparable sizes to those observed by optical miscroscopy. The nonordered and nonfluorescent core is probably due to nonpenetration of ThT. As this core is present even after extensive incubation in the presence of the dye, a more feasible explanation is the absence of significant amounts of amyloid material in this core, that is, it is formed before spherulitic growth takes place due to an interplay between amyloid fibrillation and protein random aggregation.[16] Aliquots of spherulitic solutions were also added to solutions containing ThT. The enhanced fluorescence relative to solutions of ThT and ThT containing freshly dissolved HSA additionally proved the presence of amyloid structures forming the spherulites (see Figure 1d).

To reveal the orientation of the fibrils within the spherulites, insertion of a waveplate at 45° angle to the cross polars provided confirmation of this radial arrangement (see inset in Figure 1a). The four quadrants in the spherulites are now colored. The appearance of the blue color indicates that the fast optical axis of the spherulites is aligned with the fast optical axis of the wave retardation plate.[34] The slow direction within the spherulite is the radial direction and, therefore, indicates that the fibrils lie radially within the spherulites, as seen previously for other proteins such as β-lactoglobulin,[20,31,32] α-L-iduronidase,[33] lysozyme,[18] and insulin.[16,34] Figure 1e shows that out from the core the radially oriented internal structure appears to be strands of fibril bundles (because individual fibrils are too narrow to be seen optically) with slight curvature to their orientation and without obvious branching. This is particularly viewable at the

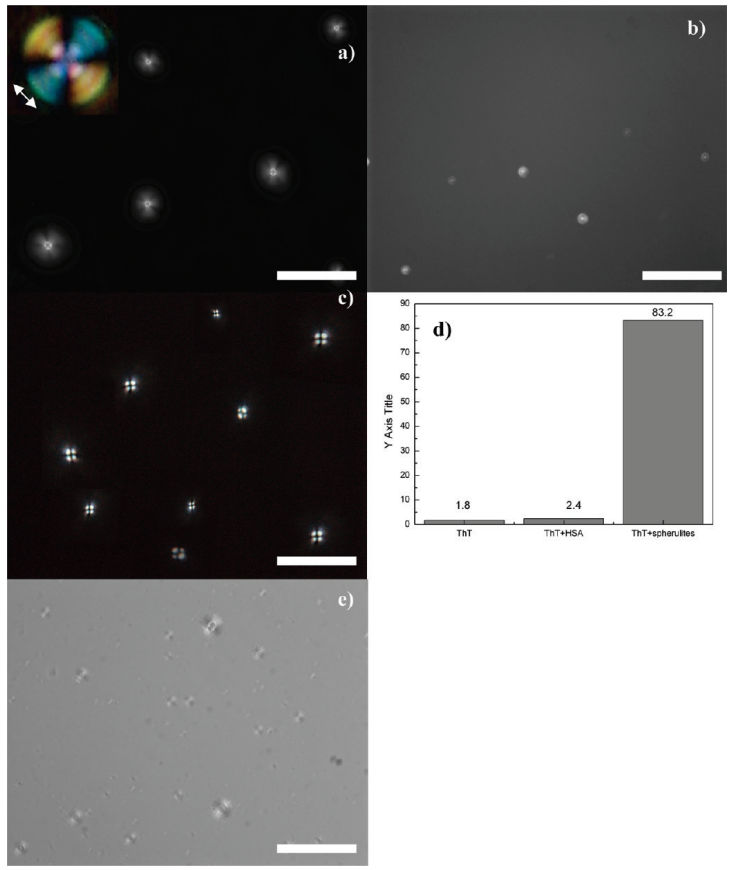

Figure 1. (a) Optical microscopy images of grown spherulites of HSA at pH 7.4 in the absence of added NaCl at 65 °C after 72 h of incubation under cross-polarizers. The inset indicates the radial arrangement of fibrils through insertion of a waveplate at 45° between the polarizers. (b) Fluorescence image in the confocal mode of spherulites using ThT as a probe. (c) Confocal image in the transmission mode of spherulites between cross-polarizers. (d) ThT fluorescence upon incubation in a solution without HSA, containing native HSA and containing spherulites. (e) Optical microscopy image of HSA spherulites without polarizers. Scale bars are (a) 50, (b) 200, and (c and e) 100 μm.

outer edges of the spherulites, where the fibril bundles are slightly separated from one another.

The spherical morphology of spherulites was also observed by ESEM (see Figure 2), with sizes similar to those derived from optical and confocal microscopy. Their surface appears to have a texture on the length scale of several micrometers but shows no obvious orientational order. Some cracks on the particle surface appeared as a consequence of the dehydration process in ESEM. Unfortunately, we could not observe if the spherulites formed display a radial internal order, since internal cracking of spherulitic structures was not achieved.

Direct measurement of spherulitic solutions was not posible by TEM provided that a film was formed on the grids which do not allow visualization. In this way, dilution and sonication of the spherulitic solutions were performed in order to investigate the samples by TEM. This treatment resulted in the disruption of the spherulites and the appearance of amyloid-like fibril structures, as seen in Figure 2d. This fact further confirms that spherulites are mainly composed of amyloid fibrils.

Gel Formation and Characterization. Prolonged incubation of solutions containing 0.3 mM HSA (or 0.8 mM where corresponds) at either pH 7.4, 5.5 or 2.5 at 65 °C in the presence of different amounts of added salt leads to the formation of gels. In this work, we have only analyzed solution conditions previously studied for amyloid fibril formation.[41,42] Significant differences were observed in the association properties of the different protein solutions. In this way, we have observed that at pH 7.4 and 5.5 gels were formed at electrolyte concentrations larger than 20 mM with gelation times decreasing from several days to hours as the solution ionic strength increases (or the protein concentration rises). On the other hand, under acidic conditions gels were only formed at the highest electrolyte concentration analyzed, 250 mM NaCl at 0.3 mM HSA. In general, it seems that gel formation is favored by the screening of electrostatic interactions between protein molecules, which favors protein aggregation.[45,46] Nevertheless, protein interactions at acidic pH are weaker than those at physiological pH due to the initial different conformational state of the protein (Expanded-E state under acidic conditions), which imparts a larger solubility to the acid-denaturated protein molecules as a result of electrostatic repulsion between them due to an increase of surface-charged groups.

Figure 3a shows cure curves (G', the storage modulus, versus time) for gelling HSA solutions at pH 7.4, 5.5, and 2.5 in the presence of 100 mM NaCl at 65 °C. To follow the protein gelation in a suitable time scale for the experiment, we increased the protein concentration up to 0.8 mM. The obtained cure data are typical of a sol−gel transition of biopolymer solutions: The elastic component of the shear modulus starts small but undergoes a sudden increase at a critical time and, then, ultimately almost levels off at longer times. For pH 7.4 and 2.5, the behavior is similar to that expected for a strongly gelling

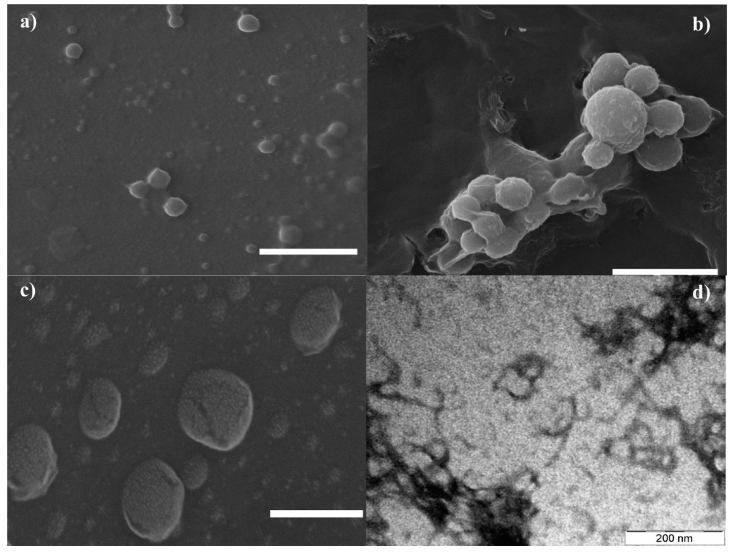

Figure 2. (a−c) ESEM images of different HSA spherulites incubated at pH 7.4 at 65 °C in the absence of added electrolyte along dehydration. Progressive dehydration allows a better visualization of the spherulites. In part c, some surface cracking can be observed. The scale bars are 200, 100, and 50 μm in parts a, b, and c, respectively. (d) TEM image of HSA fibrils obtained after disruption of grown spherulites by extensive sonication.

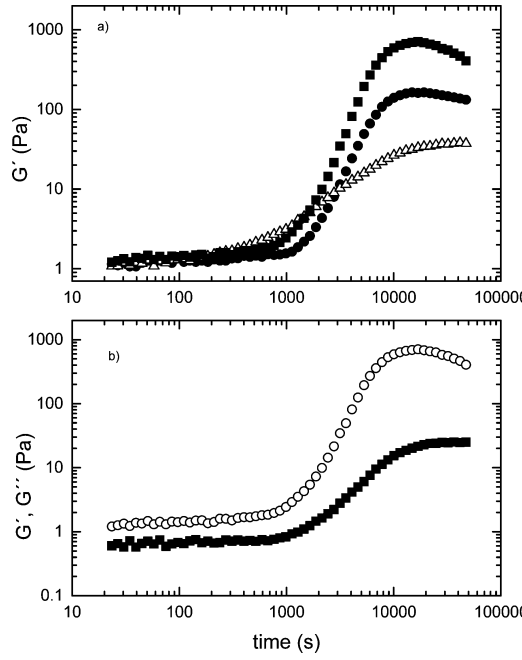

Figure 3. (a) G' versus time (cure data) for a 0.8 mM HSA solution heated at 65 °C at pH (■) 7.4, (●) 2.5, and (△) 5.5 in the presence of 100 mM NaCl. (b) Time evolution of storage (G', ○) and loss (G'', ■) moduli of a 0.8 mM HSA solution heated at 65 °C and pH 7.4 in the presence of 100 mM NaCl.

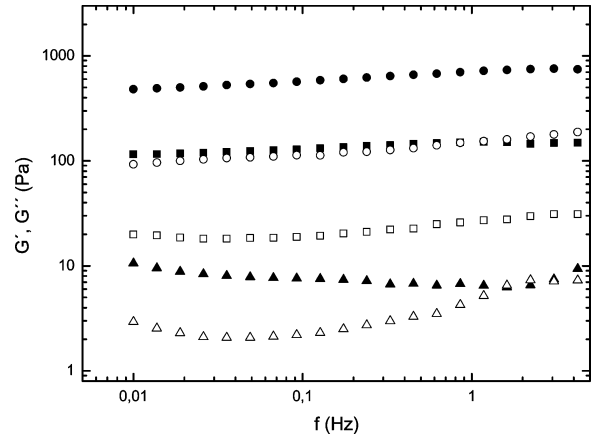

Figure 4. Frequency depedence of the storage (G', closed symbols) and loss (G'', open symbols) moduli of a 0.8 mM HSA solution at pH (●) 7.4, (■) 2.5, and (▲) 5.5 in the presence of 100 mM NaCl at 65 °C.

biopolymer solution, with the divergence between G' and G'' becoming larger with time and $G'' < G'$. Another feature of these cure curves is the "dip-down" in the modulus at long times, which may be indicative of slippage of the gel samples.[13] Interestingly, G', though small initially at both pHs, was larger than G'' (the loss modulus) even before the gelling point (see Figure 3b as an example). This "solid-like" behavior of the starting protein solutions has been ascribed to colloid-like structuring in the pregel solution due to nonclassical DLVO forces.[50,51] This is indicative of a different self-assembly mechanism and/or kinetics if compared to what was observed at pH 5.5, for which $G'' > G'$ at short incubation times. At the latter pH, faster aggregation takes place since enhanced protein/protein interactions are favored due to the proximity of the solution pH to the protein isoelectric point. It has been pointed out that rapid formation of an appreciable amount of intermolecular β-sheets favored by protein/protein interactions[52] involves very compact structures which precipitate, thereby limiting the amount of protein available to form protein/water networks necessary for robust gel formation[53] as in the present case. This fact is also corroborated comparing the lower G' values at pH 5.5 to those obtained at pH 7.4 and 2.5.

Figure 4 shows the corresponding frequency spectrum of G' and G'' for the gels after completion of the cure experiment. Samples at pH 2.5 and 7.4 show typical gel spectra. G' is

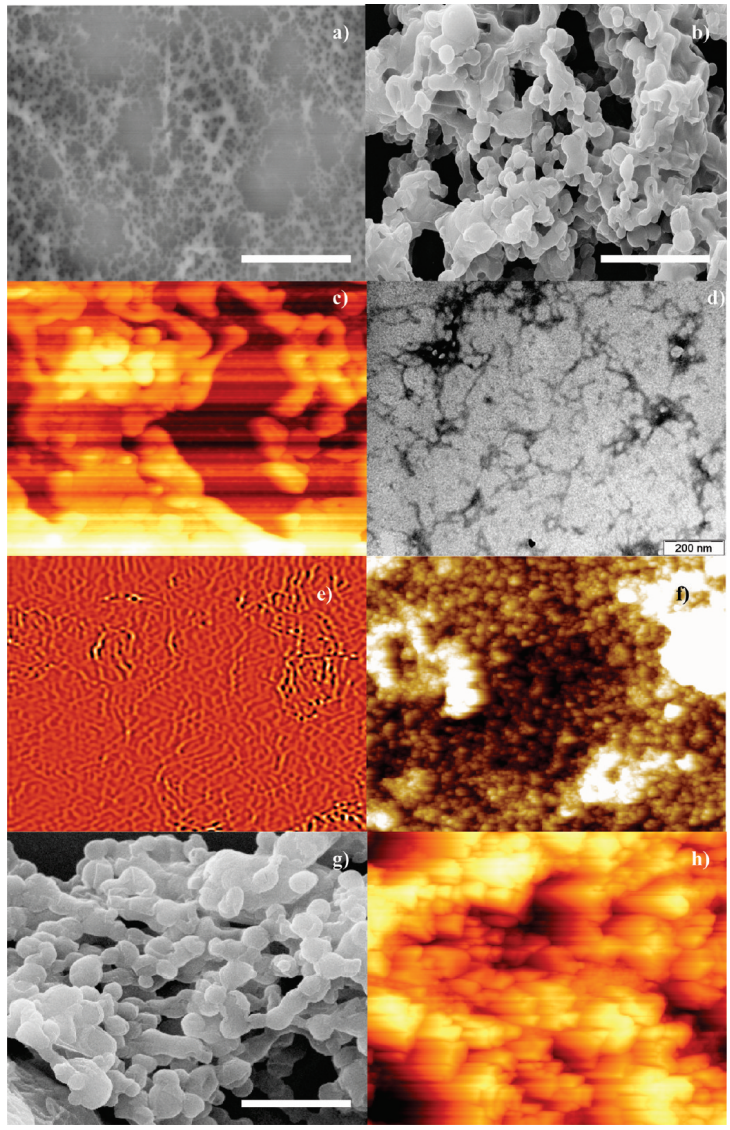

Figure 5. (a and b) ESEM and (c) AFM images showing progressive coarsening of fibril strands of HSA gels after incubation at 65 °C at pH 7.4 in the presence of 20, 100, and 250 mM NaCl, respectively (scale bars in parts a and b are 10 and 5 μm, respectively; AFM image size is 5 μm $\times$ 5 μm). (d) TEM and (e) AFM images of fibrils from coarsed HSA gels after disruption by dilution and sonication at physiological pH (AFM image size is 5 μm $\times$ 5 μm). (f and h) AFM and (g) ESEM images of particulate gels of HSA at pH 5.5 after incubation at 65 °C in the presence of 20 (f and g) and 150 mM NaCl (h) (scale bar in part g is 2 μm; AFM image size is 5 μm $\times$ 5 μm).

essentially frequency-independent, so we can assert that the storage moduli will have a finite value at very long times (low frequencies); i.e., it confirms the solid-like properties consistent with the development of a network, as previously commented. On the other hand, G' values at physiological pH are larger than those at acidic pH, which denotes the formation of a stiffer gel. This is also supported by the essentially frequency-independent behavior of G'' at pH 7.4. In contrast, under acidic conditions, a slight minimum in G'' can be observed, which becomes much more intense at pH 5.5. This minimum at pH 5.5 can be assigned to molecular packing,[54] and is in agreement with the lower G' values, the frequency-dependent behavior, and the particulate structure of the gels formed at this pH, as seen below.

Figure 5 shows ESEM and AFM images of the gels formed at pH 7.4, 5.5, and 2.5 at different ionic strengths. For physiological conditions after incubation at 65 °C in the presence of 20 mM NaCl, a fibrillar gel formed by fine strands can be observed (Figure 5a). These strands are formed by interconnected amyloid-like fibrils as denoted by the cross-β pattern derived from XRD analysis (see Figure S1 in the Supporting Information), and in agreement with the rheology data. Moreover, upon strong dilution and sonication the strands dissociate into fibrils which showed a predominant curly morphology, as observed previously for HSA[42] and other proteins such as β_2 microglobulin,[55] α-crystallin,[56] or bovine serum albumin (BSA).[57] Nevertheless, some mature straight fibrils and ribbon-like structures could also be observed (see Figure S2 in the Supporting Information).

When the ionic strength is increased at pH 7.4 up to 250 mM NaCl, a coarsening of the gel is progressively observed,

with the presence of relatively long, large, and thick aggregates which seem to be composed, at least partially, of globular aggregates (Figure 5b and c). Additionally, the size of the elementary particles appeared to be larger than those formed at lower added salt concentrations. A similar picture was observed for the gel formed at acidic pH (not shown). Therefore, a transition from fine-stranded to coarse gels with increasing ionic strength seems to be caused mainly by kinetic effects without accompanying fundamental changes in aggregation mechanisms.[58] After extensive dilution and sonication, rupture of these types of aggregates in a variety of fibrillar structures rather than in smaller spherical aggregates was observed by TEM and AFM (see Figure 5d and e), as seen in previous studies.[59] The length of the fibrils varies between 0.1 and 1−2 μm with a thickness of 15−30 nm.

In contrast, at pH 5.5 a network of quasipherical protein aggregates surrounded by liquid is formed; i.e., we observed a particulate gel (see Figure 5f−h). The particle size varies between ∼300 and ∼500 nm, which increases as the ionic strength increases. This leads to fused long and thick aggregates possibly composed of several particulates. In this regard, it has been speculated that intermolecular disulfide bonding is involved in connecting protein molecules within the particulates and that the connections among them is a nonspecific physical cross-linking without any specific connective sites.[58,60] ESEM also indicates that an amount of residual monomeric protein was left in the solutions (Figure 5g) and deposited between the particulates. This gives the appearance of connected particulates and, sometimes, apparently amorphous films. As commented above, shifting the pH toward the isoelectric point decreases the intermolecular electrostatic repulsion. This implies that aggregation becomes faster, preventing the formation of highly ordered nanostructures such as amyloid-like fibrils, but globular shapes are formed.

Thus, it seems that the gelation of HSA is also pH-dependent and the structures which form the gel depend on the solution conditions. In this regard, in a recent report the capability of several proteins such as β-lactoglobulin, BSA, insulin, and lysozyme among others to form either fibrillar or particulate gels under partially denaturing conditions but at different pHs has been confirmed.[61] This suggests that the formation of particulates can be a generic property of all polypeptide chains like amyloid fibrillation is. In this way, the results reported in this work support this view.

Finally, in order to investigate the internal structure of the fibrillar and particulate gels, attenuated total reflectance Fourier transform infrared spectroscopy (ATR-FTIR) measurements were made. All spectra were well resolved with clearly distinguishable secondary structure signatures. In this way, before incubation two major bands peaks in the second derivative IR spectra in the spectral region of interest were observed at pH 7.4: the amide I band at 1652 cm^{-1} and the amide II band at 1544 cm^{-1}. This indicates the predominant structural contribution of major α-helix and minor random coil structures.[62,63] For the amide I band (see Figure 6a), a shoulder at ca. 1630 cm^{-1} can also be observed in the second derivative spectra, which is related to a low intramolecular β-sheet content. Additional peaks at ca. 1689 and 1514 cm^{-1} would correspond to β-turn and tyrosine absorption, respectively.[63] As the pH is lowered, the remaining presence of the amide I and II bands confirms that there is still a significant amount of α-helices, even at the most acidic pH (see Figure 6a).

Following incubation at 65 °C and formation of the gel at pH 7.4, a red-shift of the amide I band from 1652 to 1658 cm^{-1}

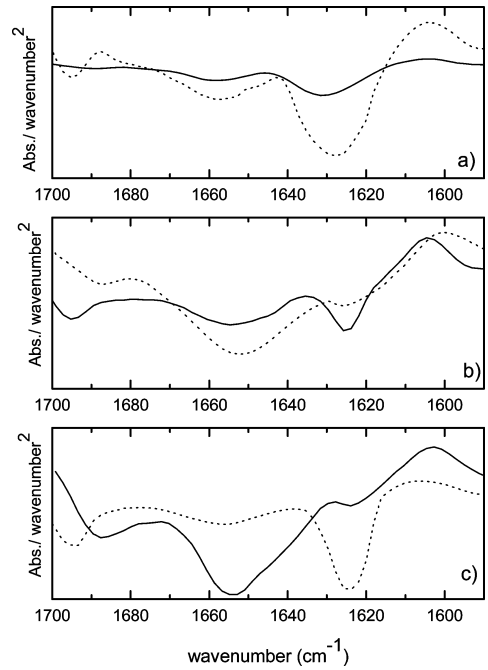

Figure 6. Second derivative of FTIR spectra of HSA samples formed at (a) pH 2.5, (b) pH 5.5, and (c) pH 7.4 in the presence of 50 mM NaCl (—) before and (•••) after incubation and gelation at 65 °C.

(1650 to 1656 cm^{-1} at acidic pH) and a blue-shift of the amide II band to 1542 cm^{-1} (1540 cm^{-1} for pH 2.5) is indicative of a certain increase of disordered structure (see Figure 6b). The appearance of a well-defined peak around 1625 cm^{-1} (1624 cm^{-1} for pH 2.5) points to a structural transformation from an intramolecular hydrogen-bonded β-sheet to an intermolecular hydrogen-bonded-β-sheet structure,[64] which is a structural characteristic of the amyloid fibrils. The spectrum also shows a high frequency component (∼1693 cm^{-1}) that would suggest the presence of an antiparallel β-sheet.[65] In addition, a small shoulder around 1534 cm^{-1} was also assigned to a β-sheet.[66]

In the case of particulate gels formed under incubation at 65 °C at pH 5.5, we could also observe a decrease and shift to 1657 cm^{-1} of the amide I band and an increase in the content of β-sheet conformation. This is indicated by the enhancement of the intensity and further shift of the band positioned around 1626 cm^{-1}, in agreement with previous reports (see Figure 6c).[61,67,68] In addition, the proportion of β-sheet content is lower than that at pH 7.4 and 2.5. This corroborates that the aggregation near the protein isoelectric point takes place faster and nonspecifically which decreases the likehood of substantial structural rearrangements during the aggregation process. In contrast, amyloid fibrils and fibrillar gels resulted from partially highly charged unfolded states,[41,42] which involve long-range repulsion and slow aggregation occurring only when substantial structural reorganization allows the formation of a favorable structure, the cross-β structure. In fact, when excess electrolyte is added, aggregation becomes faster and the proportion of β-sheet structure decreases due to an enhancement of the aggregation rates.[46]

Conclusions

In this work, we have described the existence of suprafibrillar assemblies formed by the protein human serum

albumin under different solution conditions: spherulites and fibrillar gels. Under conditions where amyloid-like fibrils for this protein were previously detected, that is, upon incubation at 65 °C at both acidic and physiological pH in the presence of different amounts of added electrolyte, spherulite formation was detected. Within spherulites, fibrils display a radial arrangement around a disoganized protein core with sizes of several micrometers, as revealed by POM and confocal microscopy. The spherulites are detected both in solution and embedded in an isotropic matrix of a fibrillar gel. Upon extensive incubation under increasingly added electrolyte and/or protein concentration, gels are formed. Under conditions where the protein is electrically charged, fibrillar gels were observed. In contrast, at a pH close to the protein isolectric point, particulate gels were observed. Fibrillar gels are formed through intermolecular nonspecific association of amyloid fibrils at a pH far away from the isolectric point of the protein, as observed by TEM, AFM, and ATR-FTIR. For these types of gels, the protein molecules seem to display a "solid-like" behavior due to the existence of non-DLVO intermolecular repulsive forces, as observed by rheometry. As the solution ionic strength increases, a coarsening of this type of gels is observed as seen by AFM, with a decrease in the elastic response. In contrast, at pH 5.5, particulate gels are present as a consequence of a faster protein aggregation which does not allow the necessary structural reorganization to enable the formation of more ordered structures such as fibrils, as observed by their shorter gelation times and the frequency-dependent behavior of the loss modulus. On the other hand, the formation of particulate gels with HSA also confirms the possibility that this type of structure may be a generic property of the polypeptide chains under suitable solution conditions.

Acknowledgment. Authors thank Ministerio de Educación y Ciencia by project MAT-2007-61604 and Xunta de Galicia for financial support.

Supporting Information Available: XRD fibril diffraction pattern and TEM pictures of mature fibrils. This material is available free of charge via the Internet at http://pubs.acs.org.

References and Notes

(1) Hady, J.; Selkoe, D. *Science* **2002**, *297*, 353–356.
(2) Dobson, C. M. *Nature* **2003**, *426*, 884–890.
(3) Stefani, M.; Dobson, C. M. *J. Mol. Med.* **2003**, *81*, 678–699.
(4) Lansbury, P. T., Jr. *Nat. Med.* **2004**, *10*, 13709–13715.
(5) Mattson, M. P. *Nature* **2004**, *430*, 631–639.
(6) Soto, C.; Estrada, L.; Castilla, J. *Trends Biochem. Sci.* **2006**, *31*, 150–155.
(7) Khurana, R.; Ionescu-Zanetti, C.; Pope, M.; Li, J.; Nelson, M.; Ramírez- Alvarado, L.; Regan, L.; Fink, A. L.; Carter, S. A. *Biophys. J.* **2003**, *85*, 1135–1144.
(8) Chiti, F.; Stefani, M.; Taddei, N.; Ramponi, G.; Dobson, C. M. *Nature* **2003**, *424*, 805–808.
(9) Williams, A. D.; Portelius, E.; Kheterpal, I.; Guo, J. T.; Cook, K. D.; Xu, Y.; Wetzel, R. *J. Mol. Biol.* **2004**, *335*, 833–842.
(10) Hortscansky, P.; Christopeit, T.; Schroeckh, V.; Fändrich, M. *Protein Sci.* **2005**, *14*, 2915–2918.
(11) Lashuel, H. A.; LaBrenz, S. R.; Woo, L.; Serpell, L. C.; Kelly, J. W. *J. Am. Chem. Soc.* **2000**, *122*, 5262–5277.
(12) Uversky, V. N.; Segel, D. J.; Doniach, S.; Fink, A. L. *Proc. Natl. Acad. Sci. U.S.A.* **1998**, *95*, 5480–5483.
(13) Gosal, W. S.; Clark, A. H.; Ross-Murphy, S. B. *Biomacromolecules* **2004**, *2*, 2048–2419.
(14) Sipe, J. D. *Annu. Rev. Biochem.* **1992**, *61*, 947–975.
(15) Manuelidis, L.; Fritch, W.; Xi, Y.-G. *Science* **1997**, *277*, 94–98.
(16) Krebs, M. R. H.; Bromley, E. H. C.; Rogers, S. S.; Donald, A. M. *Biophys. J.* **2005**, *88*, 2013–2021.
(17) Ban, T.; Morigaki, K.; Yagi, H.; Kawasaki, T.; Kobayashi, A.; Yuba, S.; Naiki, H.; Goto, Y. *J. Biol. Chem.* **2006**, *281*, 33677–33683.
(18) Heijna, M. C. R.; Telen, M. J.; van Enckevort, W. J. P.; Vlieg, E. *J. Phys. Chem. B* **2007**, *111*, 1567–1573.
(19) Gosal, W. S.; Ross-Murphy, S. B. *Curr. Opin. Colloid Interface Sci.* **2000**, *5*, 188–194.
(20) Bromley, E. H. C.; Krebs, M. R. H.; Donald, A. M. *Faraday Discuss.* **2005**, *128*, 13–27.
(21) Bassett, D. C. *J. Macromol. Sci. Phys.* **2003**, *42*, 227–256.
(22) Magill, J. H. *J. Mater. Sci.* **2001**, *36*, 3143–3164.
(23) Murray, S. B.; Neville, A. C. *Int. J. Biol. Macromol.* **1997**, *20*, 123–130.
(24) Murray, S. B.; Neville, A. C. *Int. J. Biol. Macromol.* **1998**, *22*, 137–144.
(25) Rill, R. L. *Proc. Natl. Acad. Sci. U.S.A.* **1986**, *83*, 342–346.
(26) Fezoui, Y.; Hartley, D. M.; Walsh, D. M.; Selkoe, D. J.; Osterhout, J. J.; Teplow, D. B. *Nat. Struct. Biol.* **2000**, *7*, 1095–1099.
(27) Aggeli, A.; Bell, M.; Carric, L. M.; Fishwick, C. W. G.; Harding, R.; Mawer, P. J.; Radford, S. E.; Strong, A. E.; Boden, N. *J. Am. Chem. Soc.* **2003**, *125*, 9619–9628.
(28) Hamodrakas, S. J.; Hoenger, A.; Iconomidou, V. A. *J. Struct. Biol.* **2004**, *145*, 226–235.
(29) Lockwood, N. A.; van Tankeren, R.; Mayo, K. H. *Biomacromolecules* **2002**, *3*, 1225–1232.
(30) Westlind-Danielsson, A.; Arneup, G. *Biochemistry* **2001**, *40*, 14736–14743.
(31) Domike, K. R.; Donald, A. M. *Biomacromolecules* **2007**, *8*, 3930–3937.
(32) Castelletto, V.; Hamley, I. W. *Biomacromolecules* **2007**, *8*, 77–83.
(33) Ruth, L.; Eisenberg, D.; Neufeld, E. F. *Acta Crystallogr., Sect. D* **2000**, *56*, 524–528.
(34) Krebs, M. R. H.; MacPhee, C. E.; Miller, A. F.; Dunlop, I. E.; Dobson, C. M.; Donald, A. M. *Proc. Natl. Acad. Sci. U.S.A.* **2004**, *101*, 14420–14424.
(35) Jin, L.-W.; Claborn, K. A.; Kurimoto, M.; Geday, M. A.; Maezawa, I.; Sohraby, F.; Estrada, M.; Kaminsky, W.; Kahr, B. *Proc. Natl. Acad. Sci. U.S.A.* **2003**, *100*, 15294–15298.
(36) Taniyama, H.; Kitamura, A.; Kagawa, Y.; Hirayama, K.; yoshino, T.; Kamiya, S. *Vet. Pathol.* **2000**, *37*, 104–107.
(37) Acebo, E.; Mayorga, M.; Val-Bernal, J. F. *Pathology* **1999**, *31*, 8–11.
(38) Clark, A. H. G.; Kavanagh, G. M.; Ross-Murphy, S. B. *Food Hydrocolloids* **2001**, *15*, 383–400.
(39) de la Fuente, M. A.; Singh, H.; Hemar, Y. *Trends Food Sci. Technol.* **2002**, *13*, 262–274.
(40) Zhang, S. *Nat. Biotechnol.* **2003**, *21*, 1171–1178.
(41) Taboada, P.; Barbosa, S.; Castro, E.; Mosquera, V. *J. Phys. Chem. B* **2006**, *110*, 20733–20736.
(42) Juárez, J.; Taboada, P.; Mosquera, V. *Biophys. J.* **2009**, *96*, 2353–2370.
(43) Pace, C. N.; Vajdos, F.; Fee, L.; Grimsley, G.; Gray, T. *Protein Sci.* **1995**, *4*, 2411–2423.
(44) Bolder, S. G.; Hendrickx, H.; Sagis, L. M. C.; van der Linden, E. *J. Agric. Food Chem.* **2006**, *54*, 4229–4234.
(45) Juárez, J.; Taboada, P.; Mosquera, V. *J. Phys. Chem. B* **2009**, *113*, 10521–10529.
(46) Cerda-Costa, N.; Esteras-Chopo, A.; Aviles, F. X.; Serrano, L.; Villegas, V. *J. Mol. Biol.* **2007**, *366*, 1351–1363.
(47) Plakoutsi, G.; Bemporad, F.; Calamai, M.; Taddei, N.; Dobson, C. M.; Chiti, F. *J. Mol. Biol.* **2005**, *351*, 910–922.
(48) LeVine, H., III. *Protein Sci.* **1993**, *2*, 404–410.
(49) Krebs, M. R. H.; Bromley, E. H. C.; Donald, A. M. *J. Struct. Biol.* **2004**, *149*, 30–37.
(50) Tobitani, A.; Ross-Murphy, S. B. *Macromolecules* **1997**, *30*, 4845–4854.
(51) Ikeda, S.; Nishinari, K. *Food Hydrocolloids* **2001**, *15*, 401–406.
(52) Surel, O.; Famelart, M. H. *J. Dairy Res.* **2003**, *70*, 253–256.
(53) Saguer, F.; Fort, N.; Alvarez, P. A.; Sedman, J.; Ismail, A. A. *Food Hydrocolloids* **2008**, *22*, 459–467.
(54) Zhao, J.; Majumdar, B.; Schulz, M. F.; Bates, F. S.; Almdal, K.; Mortensen, K.; Hadjuk, D. A.; Gruner, S. M. *Macromolecules* **1996**, *29*, 1204–1215.
(55) Radford, S. E.; Gosal, W. S.; Platt, G. W. *Biochim. Biophys. Acta* **2005**, *1753*, 51–63.
(56) Meehan, S.; Berry, Y.; Luisa, B.; Dobson, C. M.; Carver, J. A.; MacPhee, C. E. *J. Biol. Chem.* **2004**, *279*, 3413–3419.
(57) Holm, N. K.; Jespersen, S. K.; Thomassen, L. V.; Wolff, T. Y.; Sehgal, P.; Thomsen, L. A.; Christiansen, G.; Andersen, C. B.; Knudsen, A. D.; Otzen, D. E. *Biochim. Biophys. Acta* **2007**, *1774*, 1128–1138.
(58) Ikeda, S.; Morris, V. J. *Biomacromolecules.* **2002**, *3*, 382–389.
(59) Calamai, M.; Canale, C.; Relini, A.; Stefani, M.; Chiti, F.; Dobson, C. M. *J. Mol. Biol.* **2005**, *346*, 603–616.

(60) Le Bon, C.; Nicolai, T.; Durand, D. *Macromolecules* **1999**, *32*, 6120–6127.

(61) Krebs, M. R. H.; Devlin, G. L.; Donald, A. M. *Biophys. J.* **2007**, *92*, 1336–1342.

(62) Susi, H.; Byler, D. M. *Biochem. Biophys. Res. Commun.* **1983**, *115*, 391–397.

(63) Lin, S.-Y.; Wei, Y.-S.; Li, M.-J.; Wang, S.-L. *Eur. J. Pharm. Biopharm.* **2004**, *57*, 457–464.

(64) Casal, H. L.; Kohler, U.; Mantsch, H. H. *Biochim. Biophys. Acta* **1988**, *957*, 11–20.

(65) Fabian, H.; Choo, L.-P; Szendrei, G. I.; Jackson, M.; Halliday, W. C.; Otvos, L., Jr.; Mantsch, H. H. *Appl. Spectrosc.* **1993**, *47*, 1513–1518.

(66) Lin, S.-Y.; Wei, Y.-S.; Li, M.-J.; Wang, S.-L. *Spectrochim. Acta, Part A* **2004**, *60*, 3107–3111.

(67) Ikeda, S.; Li-Chan, E. C. Y. *Food Hydrocolloids* **2004**, *18*, 489–498.

(68) Ikeda, S.; Nishinari, K. *Biopolymers* **2001**, *59*, 87–102.

JP904167E

Soft Matter

Dynamic Article Links ►

Cite this: DOI: 10.1039/c0xx00000x

www.rsc.org/xxxxxx

PAPER

Hydration effects on the fibrillation process of a globular protein: The case of human serum albumin.

Josué Juárez, Manuel Alatorre-Meda, Adriana Cambón, Antonio Topete, Silvia Barbosa, Pablo Taboada*, and Víctor Mosquera.

Received (in XXX, XXX) Xth XXXXXXXXX 200X, Accepted Xth XXXXXXXXX 200X
DOI: 10.1039/b000000x

In this work, we have studied the fibrillation process of human serum albumin (HSA) under different solution conditions. In particular, aggregation kinetics, fibril morphology, and composition structural changes were investigated at varying experimental conditions such as pH (2.0 and 7.4), temperature (at 25 and 65 ºC), and solvent polarity (ethanol/water mixtures, 10 – 90% v/v). The characterization was carried out by means of static and dynamic light scattering (SLS and DLS), ThT fluorescence, circular dichroism (CD) and Fourier Transform Infrared spectroscopies (FT-IR), and transmission electron microscopy (TEM). The aggregation process and the α-helix to β-sheet transitions were found to be favored by temperature and physiological pH. Also, pH was observed to influence both the fibrillation pathway and aggregation kinetics, changing from a classical fibrillation process with a lag phase under acidic conditions to a downhill polymerization process at physiological pH in the presence of the alcohol. Regarding protein structural composition, at room temperature and physiological pH ethanol was found to promote an α-helix to β-sheet conformational transition at intermediate alcohol concentrations, whereas at low and high ethanol contents α-helix prevailed as the predominant structure. Under acidic conditions, ethanol promotes an important fibrillation at high cosolvent concentrations due to screening of electric charges and a decrease in solvent polarity. On the other hand, important differences in the morphology of the resulting fibrils and aggregates are observed depending on the solution conditions. In particular, the formation of classical amyloid-like fibrils at physiological pH and high temperature are observed, in contrast to the usual curly morphology displayed by HSA fibrils under most of solution conditions. Although high temperature and pH are the main parameters influencing the protein structure destabilization and subsequent aggregation upon incubation, ethanol helps to regulate the hydrogen bonding, the attractive hydrophobic interactions, and the protein accessible surface area, thus, modifying packing constraints and the resulting aggregate morphologies.

Introduction

From a general perspective, amyloid fibril formation present pros and cons regarding different approaches such as human health or technological development. On one hand, amyloid fibrils are recognized as high-performance protein nanomaterials with a formidable rigidity;[1-2] on the other, amyloidosis, the clinical condition in which amyloid fibrils form from innocuous soluble proteins, has been found to be involved in diverse pathological responses as observed in various neurodegenerative disorders including Alzheimer's, Parkinson's, and prion diseases amongst others.[3-5] The elucidation of the underlying molecular mechanisms for fibril formation would result not only in the development of strategies for the treatment of amyloidosis-related disorders but also in the design of new biomaterials for future applications in the area of nanobiotechnology.

Concerning protein folding and its repercussion on amyloid fibril formation, it has been demonstrated that fibrillation may proceed from different protein conformations including completely/partially unfolded[6-11] or fully folded states,[12,13] although the essential nature of the resulting amyloid fibrils can be largely independent of the conformational properties of the soluble precursors.[6]

In living organisms, the native environment of proteins is a complex composition of water, cosolvents and cosolutes which affect the stability of the native protein fold.[14] In this way, different experimental approaches using the addition of cosolvents and cosolutes to mimic various cellular environments *in vitro* have provided further knowledge on protein folding and aggregation/fibrillation mechanisms.[15-20] Thereby, cosolvent-mediated systems have revealed that differences in solvent

Grupo de Física de Coloides y Polímeros, Departamento de Física de la Materia Condensada, Facultad de Física, Universidad de Santiago de Compostela, E-15782. Santiago de Compostela. Spain. pablo.taboada@usc.es

properties induce solvent-adapted structural "responses" of the aggregating protein, which leads to a structural diversity of the resulting aggregates/fibers.[21-23] In particular, alcohols are included among the most commonly studied cosolvents. Several studies have shown that the effects of alcohol on very different systems and processes such as the thermal denaturation of nucleic acids and proteins, protein folding, micellization of surfactant molecules, or the solubility of nonelectrolytes are strikingly similar.[24-26] Also, water/alcohol mixtures at moderately low pH values have been suggested as model systems for studying the joint action of the local decrease in both pH and dielectric constant on the protein structure near the membrane surface;[27-32] similarly, new ways of protein administration and delivery based on inhalation systems with non-aqueous solvents as suspension media also reinforce the necessity of clarifying how the presence of the solvent affects the protein conformation and biological activity.[24, 25]

From a thermodynamic standpoint, the protein accessible surface area (ASA), the solvent exposure of hydrophobic residues, and a solvophobic backbone[33] can be taken as barriers hampering protein-solvent interactions.[34] Therefore, the hierarchical assembly of amyloids can perfectly be understood as an alternative to the native packing conformational struggle of a polypeptide chain, reducing ASA and saturating hydrogen bonding, while a simultaneous decrease in the configurational entropy of the protein is offset by gains in solvent entropy. The role of hydrational forces in protein aggreation in vivo, while still poorly understood, may be instrumental in elucidating the molecular basis of amyloidosis and, as such, attracts considerable interest.[35] In this way, the propensity for amyloid formation in mixed solvents of different proteins as, for example, human serum albumin (HSA), hen egg white lysozyme, bovine β-lactoglobulin, histone H2A, insulin, and bovine trypsinogen amongst many others, has been characterized.[36-39] Amongst them, HSA has been proposed as a good model for protein aggregation studies[40-42] as a consequence of both its physiological implications as a carrier protein and blood pressure regulator, together with its propensity to easily aggregate *in vitro*. Previous reports have addressed the HSA fibrillation kinetics, fibrillation pathway, and intermediate and final protein aggregated structures under varying pH and ionic strength solution conditions.[40-42] However, a detailed characterization of the aggregation/fibril process and the structure of the resulting aggregates in mixed solvent solutions under varying external conditions is still lacked.

In the present work, we present a detailed study on the aggregation/fibrillation pathway of the protein human serum albumin (HSA) in water/ethanol mixed solvent solutions at varying pH and temperature conditions. This enables us to make a clear comparison between the fibrillation pathway and intermediate/final protein aggregates in the mixed solvent with those obtained in pure aqueous solution in order to define the role of hydrational forces on the protein fibrillation mechanism. In fact, changes on the fibrillation mechanism from a downhill to a nucleated-growth polymerization mechanism at acidic pH and high temperature solution conditions are confirmed. Overall, as a result of differences in packing depending on the solution condition, different structures for the resulting fibrils are observed, from classically thin and very long straight to shorter and more curly fibers. In this regard, it comes as no surprise that factors favoring or disfavoring exposure of solvophobic groups must affect thermodynamic preferences for particular conformations.

Materials and Methods

Materials.

Human serum albumin (70024-90-7), and Thioflavin T (ThT) were obtained from Sigma Chemical Co. ThT was used as received. All other chemicals were of the highest purity available.

Preparation of HSA solutions.

HSA was purified by liquid chromatography using a Superdex 75 column equilibrated with 0.01 M phosphate buffer before use. To prepare the protein solutions, increasing volumes of ethanol were added to 1.0 mL of HSA stock solution either at pH 7.4 (sodium monophosphate-sodium diphosphate buffer) or pH 2.0 (glycine + HCl buffer), to get the desired ethanol concentration in the mixed solvent. The final protein concentration in all cases was 10 mg/mL with ionic strength 10 mM. pH was kept constant by adding HCl or NaOH when needed. The protein concentration was determined spectrophotometrically, using a molar absorption coefficient of 35219 M^{-1} cm^{-1} at 280 nm.[43] Aliquots were added through an electronic disperser unit Dosimat Metrohm 765. Experiments were carried out using double distilled, deionized and degassed water. Before incubation, solutions were filtered through a 0.2 μm filter into sterile test tubes. Samples were incubated at a specified temperature in a refluxed reactor for 15-20 days as required.

Light Scattering.

DLS and SLS intensities were measured at 25 °C by means of an ALV-5000F (ALV-GmbH) instrument working with a vertically polarized incident light of wavelength λ = 488 nm supplied by a CW diode-pumped Nd; YAG solid-state laser supplied by Coherent, Inc. and operated at 400 mW. The intensity scale was calibrated against scattering from toluene. Measurements were carried out at a scattering angle θ = 90° to the incident beam. Solutions were equilibrated for 30 min before measurements to reach thermal stabilization. Experiment duration was in the range of 3-5 min, and each experiment was repeated two or more times. The correlation functions from DLS were analyzed using the CONTIN method to obtain intensity distributions of decay rates (Γ).[44] The decay rate distribution functions gave distributions of apparent diffusion coefficient ($D_{app} = \Gamma/q^2$, where the scattering vector $q = (4\pi n_S/\lambda)\sin(\theta/2)$, and n_S is the refractive index of solvent) and integrating over the intensity distribution gave the intensity-weighted average of D_{app}. Values of the apparent hydrodynamic radius ($r_{h,app}$, radius of hydrodynamically equivalent hard sphere corresponding to D_{app}) were calculated from the Stokes-Einstein equation:

$$r_{h,app} = kT/(6\pi\eta D_{app}) \quad (1)$$

where k is the Boltzmann constant and η is the viscosity of water at temperature T.

Thioflavin T spectroscopy.

Protein and ThT were dissolved in buffer at a final protein-dye molar ratio of 50:1. Samples were continuously stirred only during data acquisition intervals in order to avoid ThT deposition onto protein aggregates/fibrils. Fluorescence was measured in a Cary Eclipse fluorescence spectrophotometer equipped with a temperature controller and a multi-cell sample holder (Varian Instruments Inc.). Excitation and emission were at wavelengths of 450 and 482 nm, respectively. All intensities were background-corrected for the ThT-fluorescence in the respective solvent in the absence and presence of monomeric HSA at pH 7.4 and 2.0.

Circular Dichroism (CD).

Far-UV circular dichroism (CD) spectra were obtained using a JASCO-715 automatic recording spectropolarimeter with a JASCO PTC-343 Peltier-type thermostated cell holder. Quartz cuvettes with 0.2 cm pathlength were used. The protein concentration was reduced to 0.1 mg/mL in order to avoid light scattering effects as much as possible due to protein aggregation. CD spectra were obtained from aliquots withdrawn from the aggregation mixtures at the indicated conditions after incubation, and recorded at wavelengths between 195 and 300 nm at 25 ºC. The mean residue ellipticity θ (deg cm^2 dmol^{-1}) was calculated according to: $\theta=(\theta_{Obs}/10)/(MRM/lc)$, where θ_{obs} is the observed ellipticity (in deg), *MRM* is the mean residue molecular mass (in g mol^{-1}), l is the optical path-length (in cm), and c is the protein concentration (in g ml^{-1}). The secondary structure of the protein was calculated from far-UV CD spectra by running the SELCON3, CONTIN, and DSST programs within the DICHROWEB server.[45,46] Final results were assumed when data generated from all programs showed convergence.

Transmission electron microscopy (TEM).

HSA solutions were applied to carbon-coated copper grids, blotted, washed, negatively stained with 2% (w/v) of phosphotungstic acid, air dried, and then examined with a Phillips CM-12 transmission electron microscope operating at an accelerating voltage of 120 kV. Samples were diluted between 20-200-fold prior deposition onto the grids.

Results and Discussion

To induce HSA aggregation and subsequent amyloid formation we use 10 mg/mL HSA solutions at either pH 7.4 or pH 2.0 and ionic strength of 10 mM. At pH 7.4 the protein is in its native state whereas at pH 2.0 it is in its E-expanded one, which is characterized by a separation of domain III and a loss of the intradomain helices of domain I.[47] Monomer sizes and structural compositions were similar to those previously reported.[40] Samples were prepared by adding specified volumes of protein stock solutions and different amounts of ethanol, which has been shown to destabilize both the secondary and tertiary structures of HSA;[36] subsequently, samples were incubated at room or elevated temperature (65 ºC, above the melting temperature of HSA)[48,49] to induce further protein structural changes and aggregation.

Aggregate formation.

The formation of HSA aggregates and their aggregation kinetics were firstly analyzed by SLS. Figure 1 shows the time evolution of the scattered light intensity of HSA samples at varying pH, temperature and alcohol content conditions upon incubation. Different curve profiles are obtained depending on incubation conditions.

At physiological pH (Figure 1a-b), the plots reflect a quick increase in the scattered intensity at short incubation times, which denotes the fast formation of protein aggregates. SLS plot profiles suggest a mechanism of continuous protein aggregation (in particular, a continuous fibrillation process as later confirmed by ThT, CD and TEM data) without a nucleation step, as denoted the absence of a lag phase in the early periods of incubation (see inset in Figure 1a). In addition, the absence of a faster aggregation process when protein seeds (i.e. protein aggregates) are added to protein solutions followed by subsequent incubation, and the decrease in the aggregation rate if the starting protein concentration is lowered (see Figure S1 in ESI) further indicate that under the present conditions HSA aggregation occurs by means of a classical coagulation or downhill polymerization mechanism, i.e. each protein monomer association is bimolecular, effectively irreversible and thermodynamically favorable, so that there is no energy barrier to impede aggregate growth.[50] A similar behavior has been previously obtained in the absence of alcohol.[40-42,50,51] ThT fluorescence data confirmed similar trends as those observed by SLS (see Figure S2). High values of ThT fluorescence point to an important formation/gain of β-sheet structure along the protein aggregation process, which is a first evidence of the possible formation of HSA fibrils during the aggregation process,[37] as further confirmed below by CD and TEM techniques.

Also, under physiological conditions we observe that as the ethanol concentration increases up to 60% (v/v) the formation of more numerous and/or bulkier protein aggregates takes place as derived from both the increments in scattered intensities – proportional to protein concentration and molecular weight (Figure 1a,b), and the shifts of the aggregate size distributions to larger values (see Figure 2a-b below). The clustering of alcohol molecules and the enhancement of alcohol-water interactions at intermediate ethanol concentrations in the mixed solvent should modify the extent of protein hydration and molecular packing[53] as confirmed by CD and FT-IR below, favoring an enhanced protein aggregation. At larger alcohol concentrations (> 60% (v/v)), protein solutions became progressively turbid as a consequence of the formation of even larger aggregates,[52] which gradually precipitated (see below for further explanation).

Cite this: DOI: 10.1039/c0xx00000x

www.rsc.org/xxxxxx

PAPER

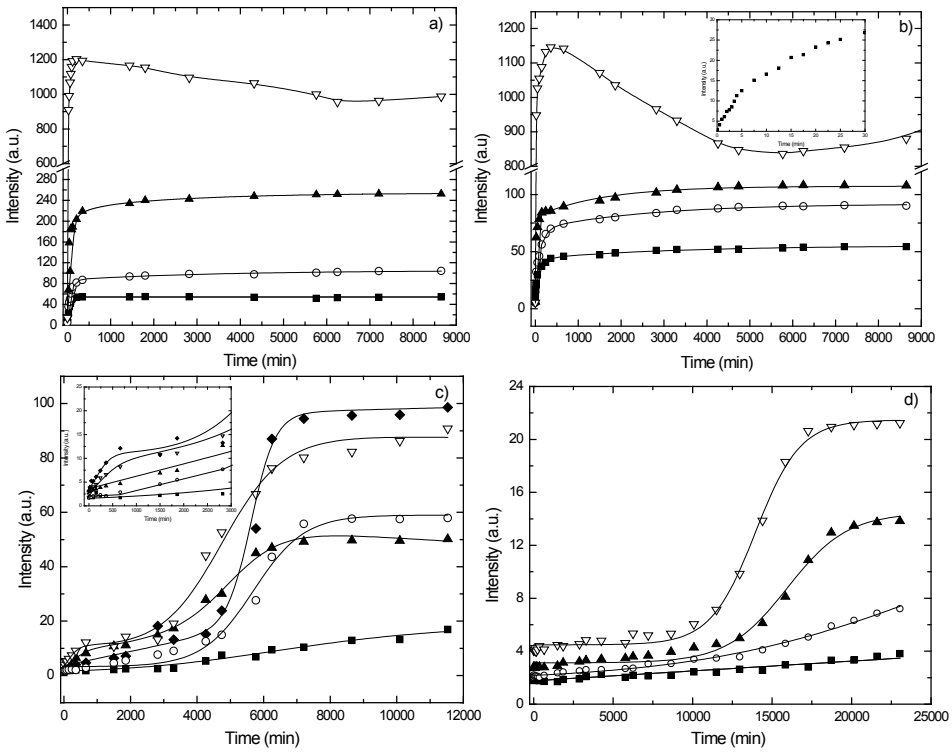

Figure 1: Time evolution of the scattered intensity of HSA solutions at a) pH 7.4 and 65 ºC, b) pH 7.4 and 25 ºC, c) pH 2.0 and 65 ºC, and d) pH 2.0 and 25 ºC under different concentrations of ethanol in the mixed solvent. In a), b) and d) ethanol concentrations are (■) 20, (○) 40, (▲) 60, and (▽) 80% (v/v). The enhanced scattered dispersion above 1000 a.u. at high alcohol concentrations in the mixed solvent is a consequence of the formation of big aggregates. In c) ethanol concentrations in the mixed solvent are (■) 20, (○) 40, (◆) 50, (▲) 60, and (▽) 80% (v/v). The inset in Figure 1b illustrates, as an example, the absence of a lag phase in the incubation of HSA at 25 ºC in the presence of 20% (v/v). The inset in Figure 1c illustrates the existence of the first step in the aggregation kinetics.

For samples incubated under acidic conditions (Figure 1c-d), the scattered intensity plot profiles depend on both alcohol content and temperature. HSA samples incubated at 25 ºC in the whole range of mixed solvent compositions and those incubated at 65 ºC at ethanol concentrations below 50% (v/v) gave rise to SLS plots with classical sigmoidal profile, i.e., there exists an initial lag phase in which the scattered intensity remains almost constant followed by a subsequent exponential phase which ends up in a final equilibrium region. These three stages correspond to the nucleation, elongation, and equilibrium phases.[54,55] The presence of a lag phase at acidic pH is related to the different initial structure of protein molecules in acidic solution, and to changes in the nature and strength of intermolecular interactions upon incubation, as previously stated in previous works.[41,42] This finding is additionally confirmed when a seeding growth process is performed, in which the lag phase is abolished (see Figure S3a).

On the other hand, for HSA samples at 65 ºC in the presence of alcohol concentrations between 50 and 90% (v/v), the formation of protein aggregates occurs in two well-differentiated steps: there exists a first short increase in the scattered intensity at very low incubation times followed by a quasi-plateau region; then, a second much stepper rise in a narrow time interval takes place until the final equilibrium region is reached. It has been previously demonstrated that this plot profile emerges when small oligomeric structures rapidly form,[40] which need more time to develop and/or persist for longer times due to their enhanced solubility under acidic conditions.[40-41] These species are water-soluble and, hence, only after achieving a critical concentration/size the energy landscape of the solution changes, i.e., the aggregation process becomes thermodynamically favorable enabling the evolvement of small oligomers to larger aggregates[56] as confirmed below by DLS data. Hence, the quasi-plateau region has been identified as a lag phase, as confirmed its suppression when a seeding fibril growth process is performed under the present solution conditions (see Figure S3b). It is also worth mentioning that the scattered intensities at equilibrium increases at ethanol concentrations between 0 and 50% (v/v), followed by a decrease between 50-70% (v/v), and by a new final increment (see Figure 1c). As confirmed by TEM and CD data

below, the first increase is related to the presence of progressively interconnected aggregates from the reduction in solvent polarity, which originates subtle changes in the protein secondary structure composition favoring the entanglement of protein aggregates. The subsequent intensity decrease at larger alcohol concentrations (> 50% v/v) originates from the formation of well-dispersed aggregates (short fibrils, see TEM pictures below) as a consequence of additional changes in protein secondary structure (as confirmed CD data below). The final scattered intensity increase at the largest ethanol contents arises from the presence of more numerous and longer aggregated structures in solution.

These observations are in contrast with the behavior observed at 25 ºC (see Figure 1d). For samples containing low ethanol contents, their low scattering intensity suggests that almost no aggregation occurs, whereas at higher ethanol contents (>40% v/v) the rise in the scattered intensity profile corroborates the presence of aggregates as a consequence of the screening of electrostatic repulsions between protein molecules as the solvent permittivity decreases. Additional confirmation is given by CD and ThT fluorescence data below.

On the other hand, comparison of scattered intensities at acidic and physiological pH shows the scattered intensity at the former pH is, in general, lower than that at the latter at the same mixed solvent conditions (see Figure 1). This is a consequence of the lowering of intermolecular interactions due to protonation of positively charged residues.[57] Also, when comparing the effect of temperature on the scattered intensity profiles, we can observe that incubation at 25 ºC involves a lower scattered intensity at both pH in the whole range of solvent compositions. It is known that hydrogen bonding is weakened as temperature rises, but hydrophobic interactions become strengthened.[58] As the heating process proceeds, destabilization of the protein helical structure of HSA occurs though hydrogen bonding weakening, as denoted by the loss of the minima at 208 and 222 nm typically assigned to α-helices in the HSA native state in the CD profiles of HSA samples at high temperature (see Figure 3); then, previously buried aminoacid residues can be now exposed to solvent as follows from changes in protein conformation from CD data (see below), which results more prone to aggregation as observed from the SLS data (and further confirmed by TEM pictures below).

Aggregation kinetics.

Data analysis of scattered intensity plots with a sigmoidal-like profile is consistent (also according to spectroscopy and TEM data), at a first approximation, with the following kinetic scheme:

$$M \leftrightarrow I \leftrightarrow \text{nucleus} \rightarrow \text{fibrils}$$

where M is the monomer and I is the intermediate. Thus, the scattered intensity as a function of time was fitted to the following equation:

$$Y = y_i + m_x y + \frac{y_f + m_f y}{1 + e^{-[(x-x_0)/\tau]}} \qquad (2)$$

where Y is the scattered intensity, x the time, and x_o is the time to reach 50% of maximal scattered intensity. Thus, the apparent rate constant, k_{app}, of fibril growth is given by $1/\tau$, and the lag time by $x_o - 2\tau$.[59] Lag times and apparent first-order rate constants were determined from curve fits and shown in Table S1 in ESI. In general, an increase in the alcohol concentration resulted in longer lag times and larger apparent rate constants. Also, the aggregation kinetics at physiological pH appears to be faster than under acidic conditions. This behavior is probably related to the existence of electrostatic repulsions between protein molecules and to an enhanced solubility of the initial protein clusters under acidic conditions. Finally, it is necessary to mention that two growth rates were obtained at high ethanol concentrations upon incubation at acidic conditions and 25 ºC. This fact is originated by the presence of intermediate oligomeric structures along the HSA aggregation pathway under these solution conditions, as discussed elsewhere.[40]

Aggregate size distribution.

Figure 2 shows some examples of population size distributions for samples incubated under the different solution conditions. At 65 ºC and physiological pH, two different populations are well differentiated and present under all mixed solvent compositions (Figure 2a): A peak at large sizes (ca. 400-1000 nm) assigned to protein aggregates, and other at smaller sizes (at ca. 20 to 40 nm) probably representing protein clusters/oligomers. Also, it is observed that a third population of aggregates with very large sizes (~ 20 μm) appears at an ethanol concentration of 80% (v/v). This feature confirms that supra-aggregation of protein aggregates is favored at high alcohol contents under the present conditions, in agreement with SLS data, and as further confirmed below by TEM pictures. For samples incubated at 25 ºC and physiological pH and at 65 ºC and pH 2.0 (Figure 2b-c), a progressive increase in the size of protein aggregates takes place as the ethanol concentration increases, as denoted by the existence of bimodal distributions. Only at intermediate ethanol concentrations the referred size increase involves the superimposition of population sizes corresponding to large protein aggregates and oligomeric structures, creating a wide population distribution (but still bimodal, as observed after deconvolution). In contrast, incubation at pH 2.0 and 25 ºC results in the simultaneous decrease of the peak height corresponding to the smallest sizes and the increase of that corresponding to the biggest ones. This fact indicates a progressive evolvement of protein monomers and small oligomeric structures to aggregates of larger sizes as the ethanol concentration in the mixed solvent increases (Figure 2d), corroborating SLS data.

Regarding the hydrodynamic radii derived from the size distributions depicted in Figure 2a-d, they can be grouped into three average values corresponding to $r_{h,app}$ of ca. 400-1000 nm, 20-50 nm, and 2-5 nm. At this point, it is necessary to remind that DLS sizes are obtained assuming a spherical shape, so these

Cite this: DOI: 10.1039/c0xx00000x

www.rsc.org/xxxxxx

PAPER

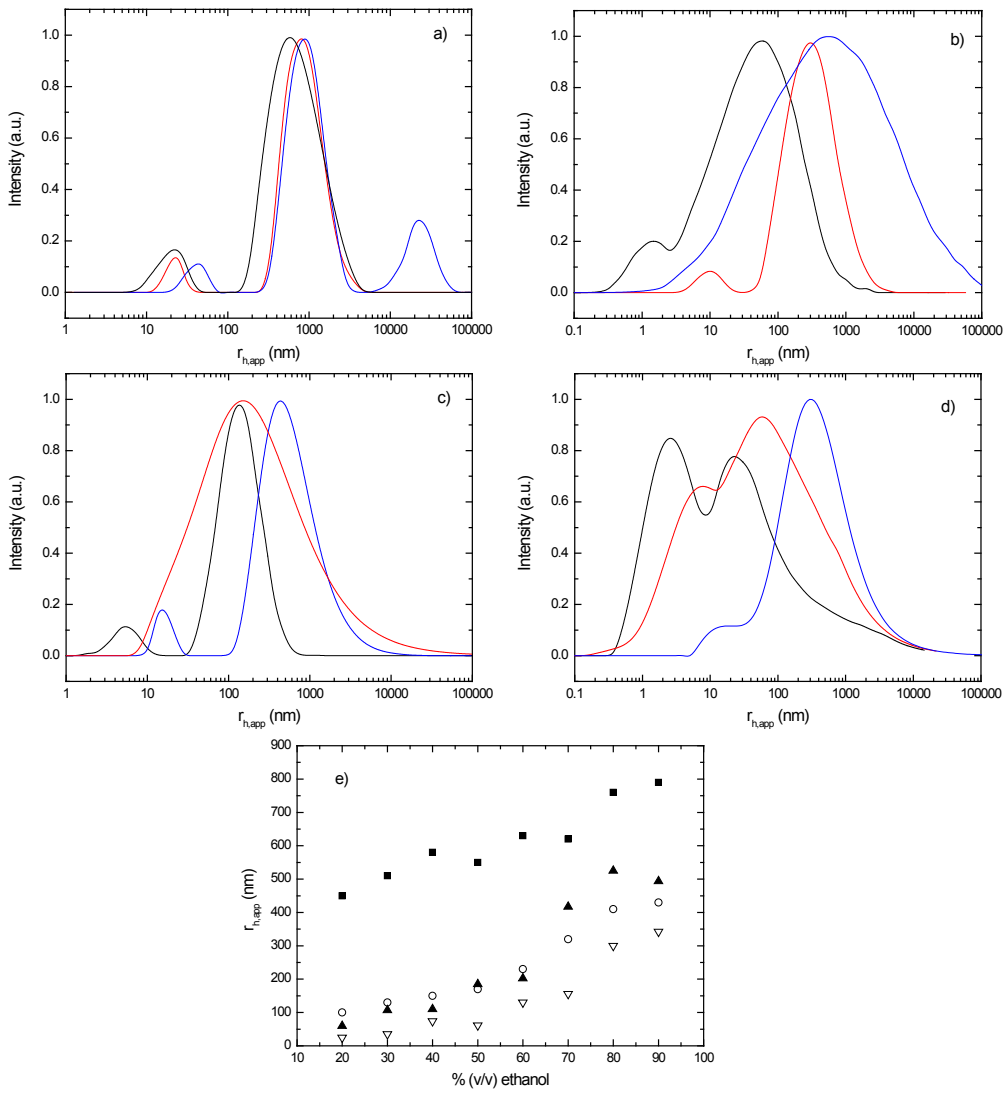

Figure 2: Selected size distributions derived from DLS data for HSA solutions incubated at pH 7.4 and a) 65ºC, and b) 25 ºC at ethanol concentrations of (—) 20, (—) 60, and (—) 80% (v/v), respectively; and at pH 2.0 and c) 65 ºC and d) 25 ºC at ethanol concentrations of (—) 20, (—) 50, and (—) 80% (v/v), respectively. Figure 2e shows the variation of the hydrodynamic radii of the main peak of the distribution with ethanol concentration after incubation at 65º C and (■) pH 7.4 and (○) 2.0, or at 25 ºC and (▲) pH 7.4 and (▽) 2.0.

are bare size estimations. In general, aggregates formed at physiological pH are bulkier if compared to those formed under acidic conditions, as plotted in Figure 2e. Structures with $r_{h,app}$ = 400-1000 nm constitute the main contribution to light scattering. As depicted in the TEM images shown below, *vide infra*, these can be associated with fibrillar conformations, in particular, assigned to the large axis of protein fibers. Those values of $r_{h,app}$ between 30-50 nm might have different interpretations depending on solution conditions: On one hand, at acidic pH and 25 ºC they correspond to oligomeric structures, which confirms the two-step aggregation process observed from SLS data under these conciditions; on the other, at high temperature conditions $r_{h,app}$ values might also include contributions from the fibrillar aggregates width. Finally, the smallest $r_{h,app}$ values around 2-5 nm fit fairly well with the estimated size of protein monomers.

Conformational structure changes along protein fibrillation.

To get further insight into the structural characterization of the resulting protein aggregates, CD, FT-IR and ThT fluorescence

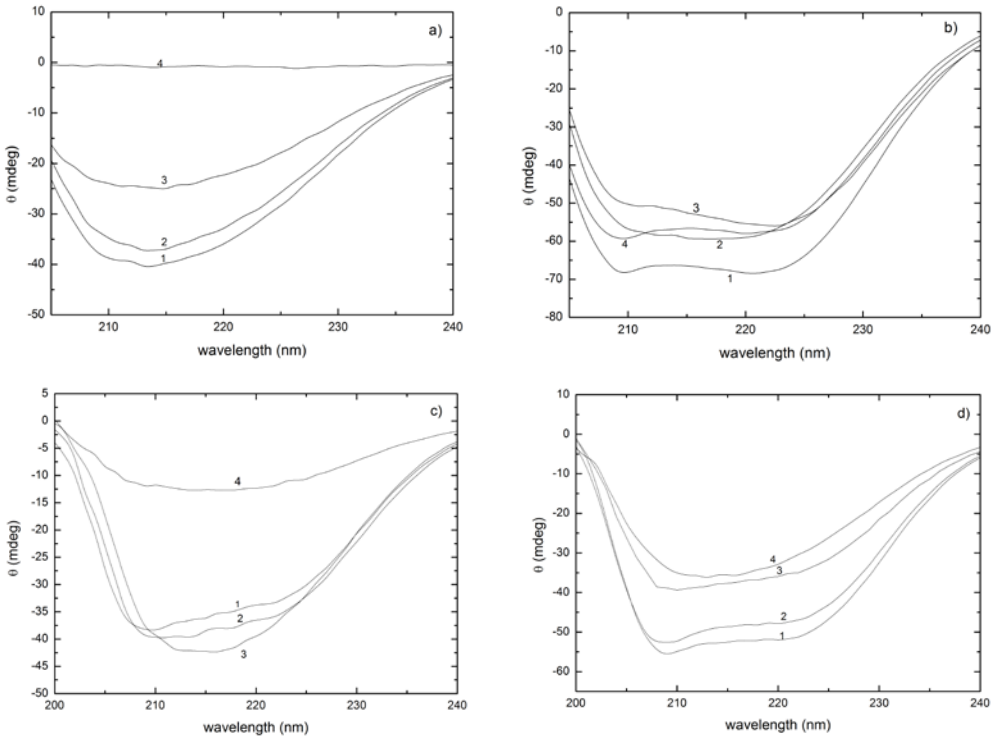

Figure 3: Selected far-UV spectra of HSA solutions after incubation at pH 7.4 at a) 65 ºC and b) 25 ºC; and at pH 2.0 at c) 65 ºC and d) 25 ºC at different ethanol concentrations in the mixed solvent: 1) 20, 2) 40, 3) 60, and 4) 80% (v/v).

experiments were performed. Figure 3 represents the far-UV CD spectra of HSA solutions at the different experimental conditions. When incubation is performed at high temperature and physiological pH (Figure 3a), a minimum at ca. 215 nm is observed in the whole range of solvent mixture compositions. This minimum denotes the predominant presence of β-sheet structure. The amount of α-helix conformation remains constant up to a 50% (v/v) alcohol concentration (see Table S2) and, then, it slightly decreases with an additional slight gain of β-sheets. At the largest ethanol concentrations (> 80% v/v), the reduction observed in ellipticity is related to light scattering caused by the presence of big aggregates in solution. These aggregates do not enable the obtention of reliable structural composition values. Upon incubation at pH 7.4 and 25 ºC (Figure 3b), a little increase in α-helical content is observed at ethanol concentrations below 30% (v/v) as a result of the weakening of hydrophobic interactions due to the presence of the cosolvent.[36] This fact results in the stabilization of the compact protein native structure and strengthens other interactions such as hydrogen bonding, stabilizing the secondary structure. Thus, alcohol acts as a "structure maker". At larger ethanol concentrations (30-60 % (v/v)) a simultaneous decrease in α-helix and an increase in β-sheet structures take place in a wider alcohol range as compared to non-buffered solutions[36], which is characterized by the absence of the minimum at 220-224 nm and the appearance of a new one at ca. 215 nm[60,61] (see Figure 3b). At ethanol contents higher than 60% (v/v), a progressive new increase in ellipticity at 222 nm and 208 nm occurs, which suggests the formation of non-native helical structure at the expense of β-sheet and unordered conformations. The loss of non-polar contacts at high ethanol concentrations appears to favor the formation of intramolecular hydrogen bonds responsible of the formation of new helices. This non-native α-helix structure is more prone to aggregation,[62] as denoted by the important increase in aggregate sizes previously observed in Figure 2.

Incubation at acidic pH and high temperature (Figure 3c) was found to involve an increasingly negative Cotton effect at 208 nm and the simultaneous decay in ellipticity at 222 nm. This suggests that, while ethanol induces disorder, some helical content is still retained. In fact, within the ethanol concentration range between 20-50% (v/v), the α-helix and unordered conformation contents slightly increase at the expense of β-sheets (see Table S2). The formation of this extra α-helix might arise from the disruption of long-range hydrophobic interactions due to the presence of alcohol molecules, which allows local helical conformation to provide a transient means of decreasing backbone solvation. At

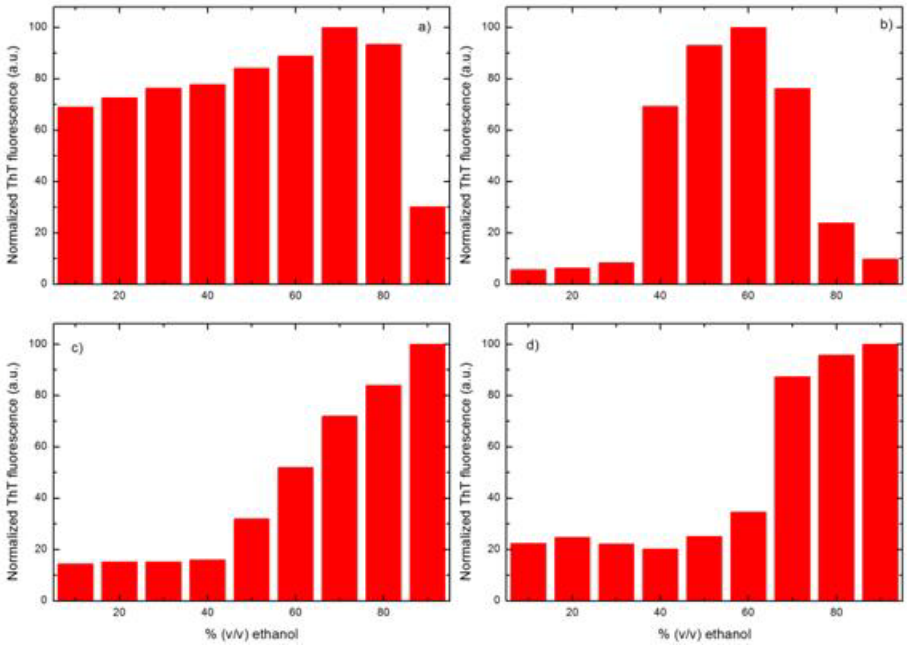

Figure 4: Normalized maximum ThT fluorescence intensities of HSA samples incubated at different ethanol concentrations in the mixed solvent at a) pH 7.4 and 65 ºC, b) pH 7.4 and 25 ºC, c) pH 2.0 and 65 ºC and d) pH 2.0 and 25 ºC. Normalization is made with respect to the maximum ThT fluorescence observed at pH 7.4 and 65 ºC.

ethanol concentrations larger than 50% (v/v) the β-sheet content increases, as denoted from the progressive shift of the minimum in CD spectra to 215 nm, which is characteristic of β-strand formation. In contrast, at acidic pH and 25 ºC (Figure 3d), the structural content of protein samples at ethanol concentrations lower than 60% (v/v) remains almost invariable. Since HSA molecules are in a starting acid-denaturated state, alcohol stabilizes the α-helix conformation of the acid-unfolded protein monomers by minimizing the exposure of the peptide backbone. In particular, at alcohol concentrations < 40% (v/v), intermolecular interactions are disfavored by suppression of the strong aggregate-stabilizing effect of negatively charged residues, still resulting in an effective electrostatic repulsion between positively charged chains. Hence, under these conditions alcohol stabilizes the molten-globule state of HSA during incubation, and only protein clusters can be formed.[63,64] The presence of these clusters, confirmed by the presence of a small peak at relatively low aggregate sizes (~20-30 nm) (see Figures 2d), implies some increase in light scattering from solution as shown previously and, thus, possibly originates the slight decrease in ellipticity observed in Figure 3d. Protein molecules experience additional structural rearrangements at ethanol concentrations between 50-90% (v/v) when the polarity of the medium is drastically changed. This involves a decrease in α-helix structure and formation of β-strands that, as observed from light scattering data, are prone to aggregate. FT-IR measurements corroborate the structural changes undergone by protein molecules depicted by CD data (for additional comments see ESI).

Although reliable in detecting β-strands and probing hydrogen bonding between them, CD and FT-IR spectroscopies fail to discriminate between amorphous and ordered aggregates. Since ThT dye strongly emits when bound to amyloid-like material rather than to amorphous aggregates, we conducted ThT fluorescence measurements of HSA samples under the different solution conditions in order to determine the presence of ordered aggregates (amyloid-like fibrils) in solution. Experimental data were background corrected for solvent and monomeric protein contributions and normalized to the largest value attained, i.e., at pH 7.4 and 65 ºC at 70 % (v/v) ethanol. Figure 4 confirms that β-sheet rich structures (fibrils as shown by TEM pictures below) are formed under all conditions except at acidic pH and 25 ºC at alcohol concentrations below 60% (v/v). At pH 7.4 and 65 ºC (Figure 4a), the amount of fibrils progressively increases up to an ethanol content of 70% (v/v), and then decreases. This decrease in ThT fluorescence can be associated with the presence of mature fibril association/aggregation, as confirmed by TEM (see below), which may reduce the protein exposed surface area and the number of available ThT binding sites.[65] In contrast, at acidic conditions (Figure 4c) the maximum level of fibril formation takes place at the largest ethanol concentrations (70-90% v/v). On the other hand, the temporal evolution of ThT binding confirms

Cite this: DOI: 10.1039/c0xx00000x

www.rsc.org/xxxxxx

PAPER

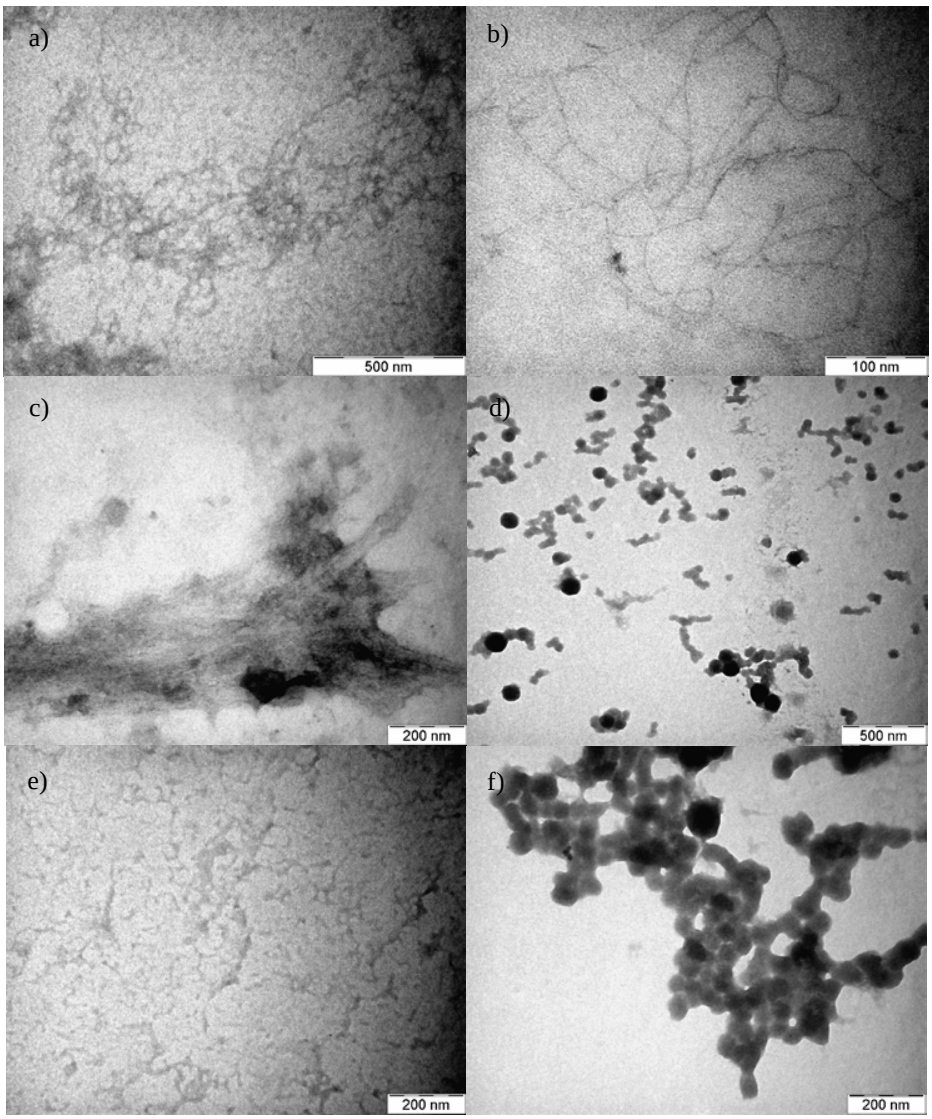

Figure 5: Selected TEM images of HSA samples incubated at pH 7.4 and a-c) 65 ºC, or d-f) 25 ºC at ethanol concentrations in the mixed solvent of a,d) 20, b,e) 60, c,f) 80% (v/v), respectively.

the trends previously observed from SLS kinetic data, although some differences at acidic and high temperature conditions are observed (see Figure S2 and further explanation in ESI).

Based on all the above findings, the combination of i) incubation at high temperature and ii) the presence of ethanol as a cosolvent in solution result in important variations of the protein structural content and subsequent strengthening of hydrophobic interactions between protein molecules. Incubation at high temperatures involves the denaturation of protein monomers due to the disruption of the structure of protein domains[48,49,63] while the presence of the cosolvent changes the solvent polarity and induces a further exposure of residues,[66] which enhances the internal degrees of freedom of side-chains.[67] Then, in most of the studied conditions, the cosolvent induces additional modifications in the starting protein structure, leading to a strong protein aggregation and fibril formation, but with differences in the packing mechanisms leading to fibril polymorphism, as will be shown below. All these facts become even clearer when comparing the secondary structure compositions here obtained with those measured under identical incubation conditions in the absence of alcohol.[36,40-42]

Aggregate morphology.

In order to determine the structural arrangement of protein aggregates and confirm the presence of amyloid-like fibrils, TEM images were obtained. Figures 5 and 6 show the structures of the different protein aggregates upon incubation under the different mixed solvent conditions.

Samples incubated at 65 ºC and physiological pH fibrillated in the whole range of alcohol concentrations analyzed (Figure 5a-c). However, remarkable differences in the structure of the resulting fibrils are observed if compared to those obtained in the absence of ethanol. In particular, for alcohol concentrations up to 70% (v/v) straight-several micrometers-long fibers with widths of ca. 10-12 nm are seen (Figure 5a,b). These fibrils are longer than those obtained in the absence of ethanol under similar conditions and do not possess the typically observed curly morphology of HSA fibrils;[40,68] In fact, they resemble those fibers obtained for classically amyloidogenic proteins such as α-synuclein,[69] insulin,[67] or lysozyme.[70] Probably, the larger β-sheet content which results from the combination of high temperature and alcohol-mixed solvent conditions during incubation favored the establishment of strong attractive interactions between protein monomers and a further exposition of their side chains to solvent. The reduction of the thermodynamic costs for the exposure of hydrophobic residues as the dielectric properties of the solvent approach to those of the bulk alcohol may be the origin for such behavior. Hence, this enables the possibility of a better packing of the protein strands inside the fibrils favoring an increase in fibril length. At larger ethanol contents (> 70% v/v), an important amount of thicker mature fibrils formed by lateral assembly (side by side) of two or more individual fibrils is observed. Moreover, very large aggregates composed of assembled fibrils are also seen (Figure 5c), which agrees with the decrease in ThT fluorescence and the existence of a third population distribution at very large sizes observed by DLS.

As observed from Figure 5d-f, incubation at room temperature and physiological pH involved the formation of protein globules (with sizes ranging from 15 to 60 nm), which seem to elongate at low alcohol content (< 30% v/v) as a consequence of the existence of attractive interactions between them (see Figure 5d). As ethanol concentration increases (up to 60% v/v) we observe the formation of curly fibrils with similar characteristic features (lengths between 0.2-1 μm, widths ranging between 8-15 nm, and a curly morphology) as those obtained upon incubation at high temperature in the absence of the alcohol (Figure 5e).[40] At larger ethanol contents (>60% v/v) fibrils progressively disappeared and large-elongated glomerular aggregates were observed. Considering CD, FTIR, and ThT fluorescence data obtained at this alcohol concentration range, we expect these aggregates to possess an increased level of α-helix content (Figure 5f) and recover the tertiary conformation.[36]

Under acidic conditions and 65 ºC, more curly fibrils are observed if compared with incubation at 25 ºC (see Figure 6a and d, for example). Also, the width and length of these fibrils are slightly larger than at room temperature. At intermediate ethanol contents, interconnected networks of elongated aggregates are observed (Figure 6b), which agrees with the increases in scattered light observed by SLS data. At large ethanol concentrations (> 60% v/v), single dispersed curly fibrils are again observed (Figure 6c), in agreement with the decrease in SLS intensities and conformational CD and FTIR data. On the other hand, at acidic pH and 25 ºC oligomeric partially-elongated structures with lengths of ca. 20-40 nm and widths of 3-4 nm are observed at ethanol concentrations between 0-40% (v/v), as seen in the absence of alcohol (see Figure 6d).[40] According to ThT and CD data, these structures are mainly composed of α-helix and unordered conformations. When larger amounts of ethanol are present in the solvent (>60% v/v), fibrils with a curly morphology are present (see Figures 6e,f). Under the present conditions, it seems the increasing amounts of ethanol induce an enlargement and fusion of oligomers as a result of additional intermolecular hydrophobic contacts between side chains, which favors the formation of β-strands and, hence, fibril formation.

Conclusions

In summary, from a general perspective, ordered aggregation of globular proteins requires partial unfolding of the native state.[71] This enables the globular precursor state to be populated and to expose aggregation-competent regions that are usually protected against intermolecular interactions in the native protein. However, these regions can be different and display distinct propensities to solvent exposition depending on solution conditions and, thus, different ability to fibrillate.[40,72] This seems to be the origin of the differences observed in the behavior of HSA samples incubated at physiological and acidic pH at the different solvent compositions. Under physiological pH ethanol is able to destabilize the protein secondary structure in most of the conditions, giving rise to an aggregation/fibrillation process. In contrast, under acidic conditions pH induces further structural changes in secondary structure favoring electrostatic repulsive interactions, which makes the protein molecules more soluble, disfavoring their aggregation to a great extent. Only when a cosolvent concentration threshold is reached does the fibrillation process start to be significant. Despite amyloid formation can occur under different solution conditions, rates and extents of fibril formation, fibrillation pathways, and the structures of resulting fibrils can be very diverse depending on solution conditions. Constraints due to electrostatic and hydrophobic interactions are, in this regard, important in that they govern the side-chain packing that controls stacking of β-sheets, favoring the formation of more classical amyloid-like fibrils at physiological pH and high temperature. The different modes of association under the present conditions are also dictated by the influence of solvent on hydrogen bonding within the β-sheets. At this respect, the distinct self-assembled motifs can be also a result of changes in the arrangement of β-strands within the β-sheets. This is clear from the different types of fibrillar structures observed under varying ethanol concentrations, in particular at physiological pH: from the classical curly geometry of HSA fibrils at low ethanol concentrations to the formation of long-straight fibrils which resemble those formed in originally disease-related proteins. Nevertheless, high temperature and physiological pH conditions are the main parameters influencing the protein structure destabilization and subsequent aggregation upon incubation, while ethanol aids to regulate hydrogen bonding, the attractive hydrophobic interactions, and the protein accessible surface area.

Cite this: DOI: 10.1039/c0xx00000x

www.rsc.org/xxxxxx

PAPER

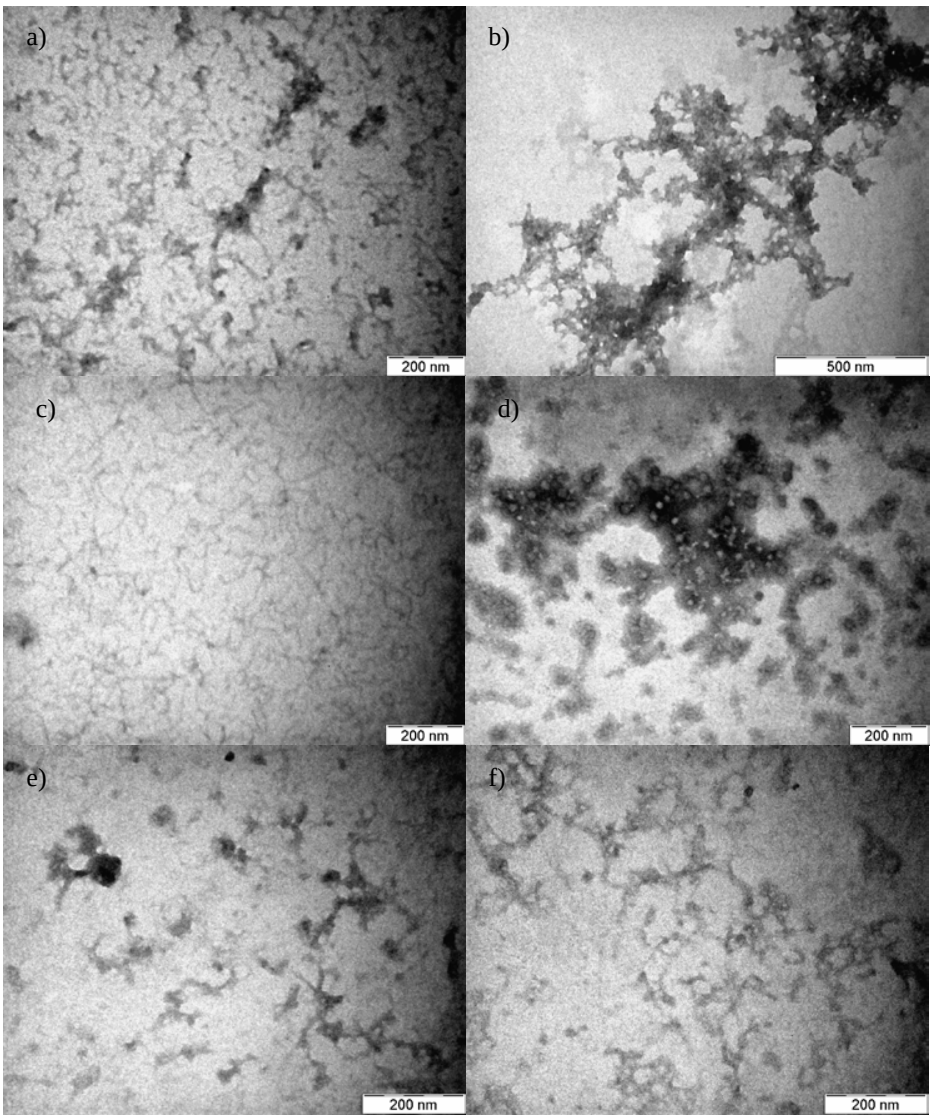

Figure 6: Selected TEM images of HSA samples incubated at pH 2.0 and a-c) 65 ºC, or d-f) at 25 ºC at ethanol concentrations in the mixed solvent of a,d) 20, b,e) 50, c,f) 80% (v/v), respectively.

The role of "fibril enhancer" of ethanol under most of the conditions is contrary to what is observed when already-formed fibrils are incubated in its presence. For example, it has been shown that insulin and β-lactoglobulin fibrils disassemble upon incubation in DMSO and ethanol, respectively, as a result of a weakening of hydrogen bonding inside the fibrils.[73,74] Thus, it appears that the solvent composition and the different initial state of the protein are responsible of the observed differences as a consequence of changes in the energy landscape of the aggregation process.

Acknowledgement. Authors thank Ministerio de Ciencia e Innovación (MICINN) for research project MAT 2010-17336, Xunta de Galicia for research project INCITE09206020PR and for European Regional Development Funds (research project 2010/50), and Fundación Ramón Areces for additional financial support.

Electronic Supplementary Information (ESI) available: Complementary seeding growth and concentration-dependent kinetic

studies, tables containing kinetic constants derived from SLS experiments and secondary structure compositions under the different solution conditions, FTIR spectra and discussion, and temporal evolution of ThT biding with subsequent discussion. See DOI: 10.1039/b000000x/

References

1. T. P. Knowles, A. W. Fitzpatrick, S. Meehan, H. R. Mott, M. Vendruscolo, C. M. Dobson, M. E. Welland, *Science* 2007, **318**, 1900-1903.
2. S. G. Zhang, *Nature Biotechnol.* 2003, **21**, 1171-1178.
3. A. T. Alexandrescu, *Protein Sci.* 2005, **14**, 1-12.
4. K. Lundmark, G. T. Westermark, A. Olsen, P. Westermark, *Proc. Natl. Acad. Sci. USA* 2005, **102**, 6098-6102.
5. M. B. Pepys, *Ann. Rev. Med.* 2006, **57**, 223-241.
6. M. Calamai, F. Chiti, C. M. Dobson, *Biophys. J.* 2005, **89**, 4201-4210.
7. B. A. Vernaglia, J. Huang, E. D. Clark, *Biomacromolecules* 2004, **5**, 1362-1370.
8. S. Goda, K. Takano, K. Yutani, Y. Yamagata, R. Nagata, H. Akutsu, S. Maki, K. Namba, *Protein Sci.* 2000, **9**, 369-375.
9. F. G. de Felice, M. N. N. Vieira, M. N. L. Meirelles, L. A. Morozova-Roche, C. M. Dobson, S. T. Ferreira, *FASEB J.* 2004, **18**, 1099-1101.
10. A. E. Cao, D. Y. Hu, L. H. Lai, *Protein Sci.* 2004, **13**, 319-324.
11. M. R. H. Krebs, D. K. Wilkins, E. W. Chung, M. C. Pitkeathly, A. K. Chamberlain, J. Zurdo, C. V. Robinson, C. M. Dobson, *J. Mol. Biol.* 2000, **300**, 541-549.
12. F. Bemporad, G. Calloni, S. Campioni, G. Plakoutsi, N. Taddei, F. Chiti, *Acc. Chem. Res.* 2006, **39**, 620-627.
13. G. Soldi, F. Bemporad, S. Torrassa, A. Relini, M. Ramazzotti, N. Taddei, F. Chiti, *Biophys. J.* 2005, **89**, 4234-4244.
14. S. N. Timasheff, *Ann. Rev. Biophys. Biomol. Struct.* 1993, **22**, 67-97.
15. W. Dzwolak, *Biochim. Biophys. Acta* 2006, **1764**, 470-480.
16. N. Rezaei-Ghaleh, M. Zweckstetter, D. Morshedi, A. Ebrahim-Habibi, M. Nemat-Gorgani, *Biopolymers* 2009, **91**, 28-36.
17. J. H. Lee, G. Bhak, S. G. Lee, S. R. Paik, *Biophys. J.* 2008, **95**, L16-L18.
18. M. Holley, C. Eginton, D. Schaefer, L. R. Brown, *Biochem. Biophys. Res. Comm.* 2008, **373**, 164-168.
19. V. Castelletto, I. W. Hamley, P. J. F. Harris, U. Olsson, N. J. Spencer, *Phys. Chem. B* 2009, **113**, 9978-9987.
20. I. W. Hamley, D. R. Nutt, G. D. Brown, J. F. Miravet, B. Escuder, F. Rodríguez-Llansola, *J. Phys. Chem. B* 2009, **114**, 940-951.
21. A. K. Paravastu, A. T. Petkova, R. Tycko, *Biophys. J.* 2006, **90**, 4618-4629.
22. W. Hoyer, T. Antony, D. Cherny, G. Heim, T. M. Jovin, V. Subramaniam, *J. Mol. Biol.* 2002, **322**, 383-393.
23. D. P. Smith, S. Jones, L. C. Serpell, M. Sunde, S. E. Radford, *J. Mol. Biol.* 2003, 330, **943**-954.
24. J. S. Patton, R. M. Platz, *Adv. Drug Delivery Rev.*1992, **8**, 179-196.
25. W. S. Choi, G. G. K. Murthy, D. A. Edwards, R. Langer, A. M. Klibanov, *Proc. Natl. Acad. Sci. USA* 2001, **98**, 11103-11107.
26. S. Cinelli, G. Onori, A. Santucci, *Colloids Surfaces A* 1999, **160**, 3-8.
27. V. E. Bychkova, O. B. Ptitsyn, *Biochem. Mol. Biol.* 1993, **4**, 133-163
28. O. B. Ptitsyn, V. E. Bychkova, V. N. Uversky, *Philos. Trans. Royal Soc. London B-Biol. Sci.* 1995, **348**, 35-41.
29. V. E. Bychkova, A. E. Dujsekina, S. I. Klenin, E. E. Tiktopulo, V. N. Uversky, O. B. Ptitsyn, *Biochemistry* 1996, 35, **19**, 6058-6063.
30. V. N. Uversky, N. V. Narizhneva, S. O. Kirschstein, S. Winter, G. Löber, *Folding Design* 1997, **2**, 163-172.
31. Y. O. Kamatari, T. Konno, M. Kataoka, K. Akasaka, *J. Mol. Biol.* 1996, **259**, 512-523.
32. N. V. Narizhneva, V. N. Uversky, *Protein Pept. Lett.* 1997, **4**, 243-249.
33. Y. X. Qu, C. L. Bolen, D. W. Bolen, *Proc. Natl. Acad. Sci. USA* 1998, **95**, 9268-9273.
34. S. N. Timasheff, *Proc. Natl. Acad. Sci. USA* 2002, **99**, 9721-9726.
35. D. Liu, T. Wyttenbach, C. J. Carpenter, M. T. Bowers, *J. Am. Chem. Soc.* 2004, **126**, 3261-3270.
36. P. Taboada, S. Barbosa, E. Castro, M. Gutiérrez-Pichel, V. Mosquera, *Chem. Phys.* 2007, **340**, 59-68.
37. P. Taboada, S. Barbosa, E. Castro, V. Mosquera, *J. Phys. Chem. B* 2006, **110**, 20733-20736.
38. Y. Aso, K. Shiraki, M. Takagi, *Biosci. Biotech. Biochem.* 2007, **71**, 1313-1321.
39. W. Dzwolak, S. Grudzielanek, V. Smirnovas, R. Ravindra, C. Nicolini, R. Jansen, A. Loksztejn, S. Porowski, R. Winter, *Biochemistry* 2005, **44**, 8948-8958.
40. J. Juárez, P. Taboada, V. Mosquera, *Biophys. J.* 2009, **96**, 2353-2370.
41. J. Juárez, S. Goy-López, A. Cambón, P. Taboada, V. Mosquera, *J. Phys. Chem. B* 2009, **113**, 10521-10529.
42. J. Juárez, P. Taboada, S. Goy-López, A. Cambón, M.-B. Madec, S. G. Yeates, V. Mosquera, *J. Phys. Chem. B* 2009, **113**, 12391-12399.
43. C. N. Pace, F. Vajdos, L. Fee, G. Grimsley, T. Gray, *Protein Sci.* 1995, **4**, 2411-2423.
44. S. W. Provencher, *Comp. Phys. Comm.* 1982, **27**, 213-227.
45. A. Lobley, L. Whitmore, B. A. Wallace, *Bioinformatics* 2002, **18**, 211-212.
46. L. Whitmore, B. A. Wallace, *Nucleic Acids Res.* 2004, **32**, W668-W673.
47. M. J. Geisow, G. H. Beaven, *Biochem. J.* 1977, **163**, 477-484.
48. B. Farruggia, F. Rodriguez, R. Rigatuso, G. Fidelio, G. Pico, *J. Protein Chem.* 2001, **20**, 81-89.
49. K. Flora, J. D. Brennan, G. A. Baker, M. A. Doody, F. V. Bright, *Biophys. J.* 1998, **75**, 1084-1096.
50. N. K. Holm, S. K. Jespersen, L. V. Thomassen, T. Y. Wolff, P. Sehgal, L. A. Thomsen, G. Christiansen, C. B. Andersen, A. D. Knudsen, D. E. Otzen, *Biochim. Biophys. Acta* 2007, **1774**, 1128-1138.
51. F. Ferrone, W. Ronald, Analysis of protein aggregation kinetics. *In Methods in Enzymology*, Academic Press: 1999, **309**, 256-274.
52. M. Alatorre-Meda, P. Taboada, J. Sabin, B. Krajewska, L. M. Varela, J. R. Rodriguez, *Colloids Surfaces A* 2009, **339**, 145-152.
53. P. Shahi, R. Sharma, S. Sanger, I. Kumar, R. S. Jolly, *Biochemistry* 2007, **46**, 7365-7373.
54. J. T. Jarrett, P. T. Lansbury, *Biochemistry* 1992, **31**, 12345-12352.
55. A. Lomakin, D. B. Teplow, D. A. Kirschner, G. B. Benedek, *Proc. Natl. Acad. Sci. USA* 1997, **94**, 7942-7947.
56. R. Bader, R. Bamford, J. Zurdo, B. F. Luisi, C. M. Dobson, *J. Mol. Biol.* 2006, **356**, 189-208.
57. Q. Xu, T. A. Keiderling, *Biochemistry* 2005, **44**, 7976-7987.
58. A. J. Rader, B. M. Hespenheide, L. A. Kuhn, M. F. Thorpe, *Proc. Natl. Acad. Sci. USA* 2002, **99**, 3540-3545.
59. L. Nielsen, R. Khurana, A. Coats, S. Frokjaer, J. Brange, S. Vyas, V. N. Uversky, A. L. Fink, *Biochemistry* 2001, **40**, 6036-6046.
60. S. Goda, K. Takano, Y. Yamagata, R. Nagata, H. Akutsu, S. Maki, K. Namba, K. Yutani, *Protein Sci.* 2000, **9**, 369-375.
61. Y. Yonezawa, S. Tanaka, T. Kubota, K. Wakabayashi, K. Yutani, S. Fujiwara, *J. Mol. Biol.* 2002, **323**, 237-251.
62. N. A. P. Ulrih, G. Anderluh, P. Macek, T. V. Chalikian, *Biochemistry* 2004, **43**, 9536-9545.
63. M. Dockal, D. C. Carter, F. Ruker, *J. Biol. Chem.* 2000, **275**, 3042-3050.
64. Y. Kumar, S. Tayyab, S. Muzammil, *Archiv. Biochem. Biophys.* 2004, **426**, 3-10.

65. L. A. Sikkink, M. Ramirez-Alvarado, *Biophys. Chem.* 2008, **135**, 25-31.
66. I. I. Stepuro, E. A. Lapshina, N. A. Chaikovskaia, *Mol Biol (Mosk)* 1991, **25**, 337-347.
67. S. Grudzielanek, R. Jansen, R. Winter, *J. Mol. Biol.* 2005, **351**, 879-894.
68. L. M. C. Sagis, C. Veerman, E. van der Linden, *Langmuir* 2004, **20**, 924-927.
69. Y. Fezoui, D. B. Teplow, *J. Biol. Chem.* 2002, **277**, 36948-36954.
70. K. Sasahara, H. Yagi, H. Naiki, Y. Goto, Y. *J. Mol. Biol.* 2007, **372**, 981-991.
71. V. N. Uversky, A. L. Fink, *Biochim. Biophys. Acta* 2004, **1698**, 131-153.
72. M. Bhattacharya, N. Jain, S. Mukhopadhyay, *J. Phys. Chem. B* 2011, ***115***, 4195-4205.
73. N. Hirota-Nakaoka, K. Hasegawa, H. Naiki, Y. Goto, *J. Biochem.* 2003, **134**, 159-164.
74. S. Jordens, J. Adamcik, I. Amar-Yuli, R. Mezzenga, *Biomacromolecules* 2011, ***12***, 187-193.

THE JOURNAL OF PHYSICAL CHEMISTRY Letters

pubs.acs.org/JPCL

Obtention of Metallic Nanowires by Protein Biotemplating and Their Catalytic Application

Josué Juárez, Adriana Cambón, Sonia Goy-López, Antonio Topete, Pablo Taboada,* and Víctor Mosquera

Grupo de Física de Coloides y Polímeros, Departamento de Física de la Materia Condensada, Facultad de Física, Universidad de Santiago de Compostela, E-15782 Santiago de Compostela, Spain

ABSTRACT Gold nanowires were obtained by a seeded growth process using protein lysozyme fibrils as biotemplates. The degree of metal coverage until full biotemplate coverage onto the fibril was controlled by the gold salt concentration and the number of sequential additions of metal growth solutions. The hybrid fibrils might have a potential use as catalysts since they display enhanced catalytic activity in the reduction of *p*-nitrophenol to *p*-aminophenol by $NaBH_4$.

SECTION Nanoparticles and Nanostructures

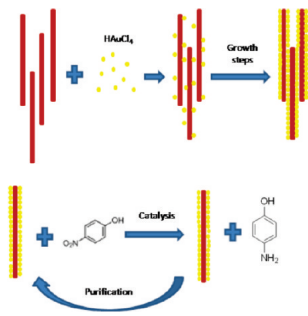

Metal nanoparticles have received considerable attention in past decade because of their particular optical, electronic, magnetic, and catalytic properties and their important applications in many fields such as nanosensors,[1−4] catalysis,[5−8] biomedicine,[9−11] biological labeling,[12−14] and surface-enhanced Raman scattering (SERS).[15−18] To optimize and extend the application of metal NPs, methods must be developed to control the assembly and organization of these nanomaterials. Assemblies of NPs provide optical and electronic properties that are distinct compared to individual particles or disorganized macroscale agglomeration. In this regard, Nature offers us the possibility to take advantage of the well-defined structures and special properties of biomolecules and their supramolecular structures to organize nanoparticles into predefined, topologically intricate nanostructures or to synthesize miscellaneous materials in order to control the properties of nanoparticle assemblies for potential applications in electronic, optical, and chemical devices.[19−23] In particular, functionalizing one-dimensional (1D) supporting biomaterials with metal NPs that combine the properties of two functional nanomaterials, such as high conductivity surface area or precise chemical functionality of the biotemplate and the unique plasmonic or catalytic properties of metal NPs, to achieve a wider range of applications will therefore play an important role in the development of nanoscience and nanotechnology. As a result, considerable efforts have been directed toward the use of 1D biotemplates such as DNA,[24−27] viruses,[28−31] peptides,[32−34] proteins,[35−38] or fungus[39] to construct corresponding multifunctional hybrid 1D nanostructures such as nanowires,[40−43] nanotubes,[44−46] or nanodumbbells.[47]

The spontaneous fibrillation mechanism which different proteins undergo under suitable conditions results in the formation of amyloid-like fibrils,[37,48,49] which should be valid as alternative templating agents for the construction of 1D hybrid materials. In particular, lysozyme (Lys) is a protein which is known to fibrillate under different solution conditions to form protein fibrils with diameters ranging from 10 to 50 nm and lengths up to several micrometers (see Figure 1a).[50−52] The dimensions of the fibrils can be tuned by varying the solution conditions and the incubation time. They are also thermally stable at high temperatures and different pHs, and they contain multiple potential ion-binding sites within their amino acid sequences, which enables their use in metallization reactions under relatively harsh conditions. Thus, we exploit all of these features to generate 1D nanoparticle assemblies and nanowires by in situ nanoparticle formation and seeding growth on the fibril surface and to analyze their potential applicability as biocatalysts.

Although biotemplating of 1D metallic nanoparticle assemblies and nanowires by peptides and protein fibrils has been previously reported[35,37,38,40,43] and their electric and magnetic properties have been evaluated,[35,53] less attention has been paid to the obtention of 1D protein-fibril-templated metallic nanostructures with a controlled degree of metallization and their potential application as a catalyst. Here, we present a seeded-mediated method for the controlled coverage by Au NPs on the surface of the fibrils formed by the protein Lys in order to find the optimal conditions for the use of the present biohybrid systems as a catalyst. We test their catalytic capability using the model reduction reaction of *p*-nitrophenol by $NaBH_4$.

Lys fibrils were prepared as previously described (see Experimental Section). Au-nanoparticle-coated protein fibrils were obtained by the addition of preformed citrate-stabilized Au seeds to an aqueous solution containing self-assembled fibrils at pH 2.0. Provided that the isoelectric point of Lys is around 11,[54] it is expected that negatively charged gold seed

Received Date: July 26, 2010
Accepted Date: August 23, 2010

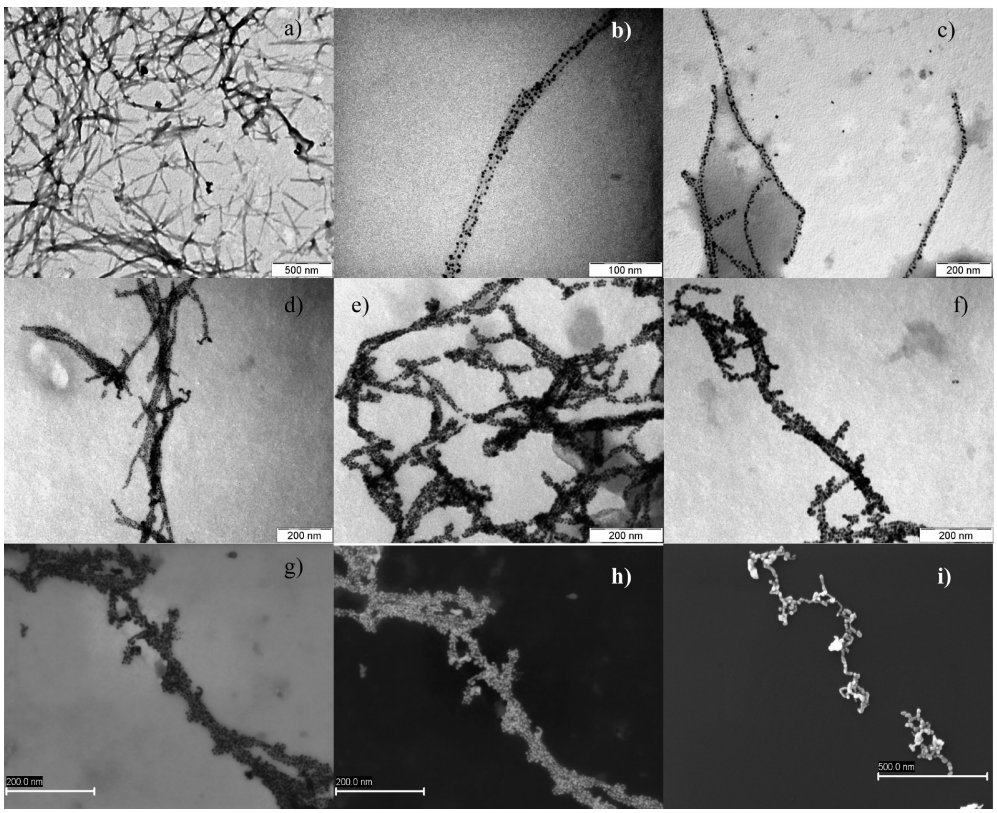

Figure 1. TEM images of (a) bare Lys fibrils and Au−fibril biohybrids obtained after (b) zero, (c) one, (d) two, (e) three, and (f) four sequential additions of the Au growth solution; (g) bright field and (h) dark field TEM images of fully covered fibrils; (i) SEM image of a Au−metallic biohybrid nanowire. Scale bars are (a,i) 500, (b) 100, and (c−h) 200 nm.

Table 1. Au Content of the Obtained Nanohybrids

sample ([Au]/[protein] MR)	Au concentration (10^{-5} M)
biohybrid 1(50)	3.4
biohybrid 2 (100)	3.9
biohybrid 3 (125)	4.6
biohybrid 4 (150)	5.3
biohybrid 5 (200)	6.0

ions would interact electrostatically with electrically charged amine groups located at the fibril surfaces after incubation. Subsequently, different sequential additions of a solution containing $HAuCl_4$ and ascorbic acid were performed in order to achieve a full coverage of the hybrid composites. Different initial [Au seeds]/[protein] molar ratios (MR) were tested in order to find an initial suitable MR to ensure full coverage after a few additions and to avoid both precipitation of the nanohybrid and the generation of free gold NPs. An initial [Au seed]/[protein] MR = 50 was found to be the optimal one and was further used during the sequential additions of Au ions to achieve the formation of the metallic nanowires (see Table 1).

The morphologies of the resulting products were investigated by transmission electron microscopy (TEM) and scanning transmission microscopy (SEM). Figure 1a shows a typical TEM image of the as-prepared Lys fibrils, with lengths ranging from 0.4 to 8 μm and widths of 12−20 nm. The metallic coverage of the nanofibrils could be easily controlled by changing the number of sequential additions of gold growth solution into the fibril solution over already preformed Au nanocrystals. Figure 1b−e shows the progressive coverage of the nanofibrils after increasing the number of sequential additions, with the formation of more metallic nanoparticles onto the fibril surface. TEM revealed that metallic nanoparticles on the fibril surfaces possess a size ranging from 3.7 to 8.0 ± 2.0 nm, depending on the number of sequential additions of the gold growth solution. The continuous coverage is a result of the growth of pre-existing NPs and generation of new ones on the fibril surface and subsequent fusion of adjacent as-synthesized NPs. The fully covered fibrils display a relatively rougher surface than pristine and partially covered fibrils, as can be observed from the TEM image obtained in the backscattering mode and the SEM picture obtained without the need for metallic contrast (see Figure 1h,i). Also, the size of the metallic NPs clearly increases, and the size population can also broadened (see Figure S1, Supporting Information). In addition,

DOI: 10.1021/jz101029f | J. Phys. Chem. Lett. 2010, 1, 2680–2687

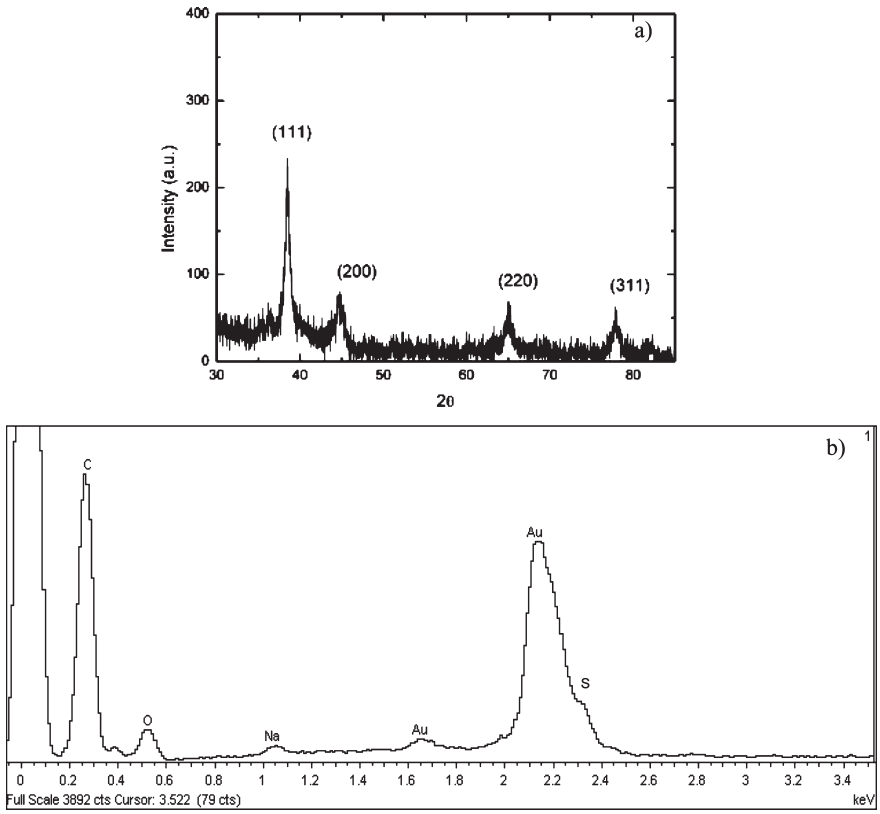

Figure 2. (a) XRD pattern of spherical Au NPs on the surface of protein fibrils; (b) EDX pattern of a gold hybrid fibril.

under conditions of excessive addition of Au ions in solution, an increasing presence of fibril networks is observed as a consequence of fibril bundling, which leads to precipitation of the nanowires after several days (see Figure S2, Supporting Information).

The formation of hybrid fibrils was further characterized by energy dispersive X-ray (EDX) spectroscopy and X-ray diffraction (XRD). XRD patterns of the resulting hybrid fibrils display the classical peaks corresponding to metallic spherical gold NPs. The crystallite sizes calculated according to the modified Scherrer relation[55] for the hybrid fibrils range from 5 to 8 nm depending on the number of additions of Au growth solution. The EDX spectrum (Figure 2b) of protein-fibril-supported Au NPs shows the peaks corresponding to C, O, S, and Au, confirming the existence of Au NPs on the surface of the Lys fibrils. The S peak is characteristic of protein samples.[56]

To study the performance of the Au NP hybrid fibrils as catalysts, we have chosen the borohydride reduction of *p*-nitrophenol as a model reaction. It is well documented that this reaction can be catalyzed by noble metal nanoparticles, and the color changes involved in the reduction also provide a simple way based on spectroscopic measurements for monitoring the reaction kinetics.[57,58] Under a neutral or acidic condition, *p*-nitrophenol solution exhibits a strong absorption peak at 317 nm. Upon the addition of $NaBH_4$, the alkalinity of the solution increases, and *p*-nitrophenolate ions would become the dominating species, together with a spectral shift to 400 nm for the absorption peak.[59,60] This peak remains unaltered with time, suggesting that the reduction did not take place in the absence of a catalyst, as reported elsewhere.[61,62] However, the addition of a small amount of the Au-based catalyst (i.e., metal hybrid fibrils with a Au concentration ranging from 0.002 to 0.02 mM) to the above reaction mixture causes fading and ultimate bleaching of the yellow color of the reaction mixture quickly. Time-dependent absorption spectra of this reaction mixture show the disappearance of the peak at 400 nm that is accompanied by a gradual development of a new peak at 300 nm corresponding to the formation of *p*-aminophenol (Figure 3a). The UV spectra also exhibit an isosbestic point between two absorption bands, indicating that only two principal species, *p*-nitrophenol and *p*-aminophenol, influence the reaction kinetics. Similar spectral changes were also observed with other hybrid fibrils with different Au NP concentrations. These results indicate that the hybrid fibrils can successfully catalyze the reduction reaction. Several research groups have also reported similar kinds of spectral changes of *p*-nitrophenol during its catalytic reduction in the presence of both supported and unsupported spherical metallic nanoparticles.[63−65] In this reduction process, as the concentration of $NaBH_4$ in the reaction mixture far

DOI: 10.1021/jz101029f | *J. Phys. Chem. Lett.* 2010, *1*, 2680–2687

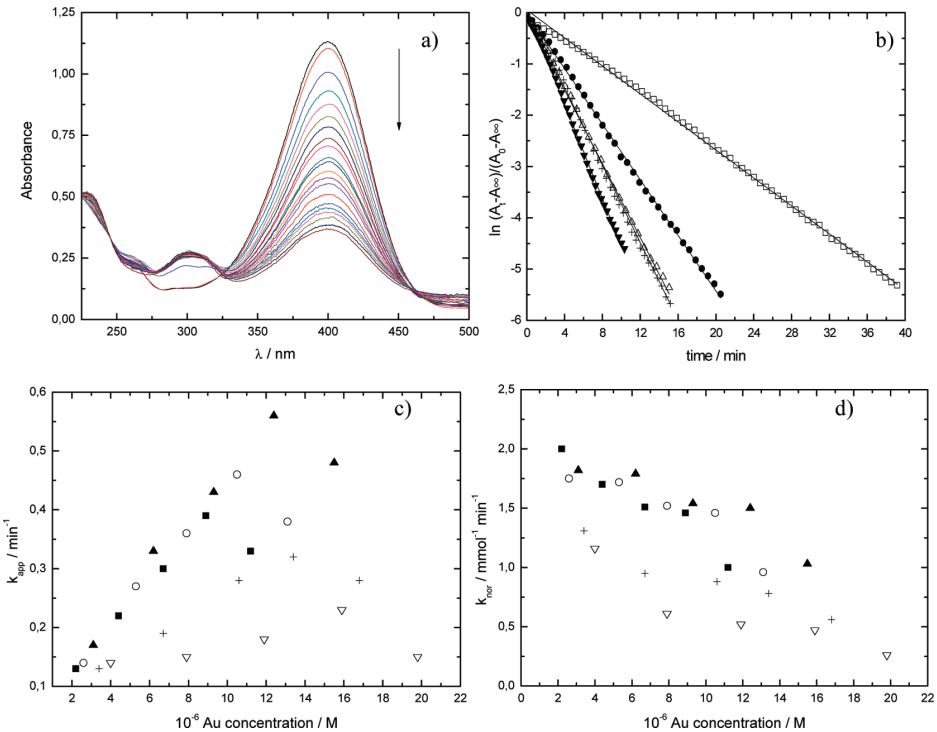

Figure 3. (a) Time evolution of UV−vis spectra and (b) variation of absorbance with time upon conversion of *p*-nitrophenol to *p*-aminophenol in the presence of biohybrid 2 with Au concentrations of (□) 0.26, (●) 0.53, (△) 0.79, (▼) 1.05, and (+) 1.31×10^{-5} M. The arrow in (a) denotes the decreasing presence of *p*-nitrophenol in the mixture as the reduction reaction proceeds. Variation of (c) k_{app} and (d) k_{nor} with Au concentration present in the reduction reaction: (■) biohybrid 1, (○) biohybrid 2, (▲) biohybrid 3,; (+) biohybrid 4, and (▽) biohybrid 5.

exceeds the concentration of *p*-nitrophenol, the reaction rate is assumed to follow first-order kinetics. Keeping this in mind, we decided to measure the concentrations of *p*-nitrophenolate ions and thus to monitor the progress or kinetics of the reaction by recording the absorbance at 400 nm because the latter peak was much stronger than that at 315 nm. We calculated the values of the apparent rate constants (k_{app}) of the catalytic reaction in the presence of different concentrations of the hybrid fibrils possessing different degrees of Au coverage from the change of absorbance with time (Figures 3b and S3, Supporting Information). These plots are straight lines, indicating that the reduction reaction effectively follows first-order kinetics. The k_{app} values of the hybrid fibrils rise linearly with an increase of their concentration (and, thus, also with increases in Au concentration) in the reaction medium until reaching a maximum to decrease further (see Figure 3c). In addition, values of k_{app} for *p*-nitrophenol reduction using hybrid fibrils were ∼1.5−4 times larger than those reported for glucose-reduced Au nanoparticle networks,[64] poly(amidoamine) (PAMAM)-dendrimer-supported spherical nanoparticles,[59] solid 1D Au nanobelts[66] and nanorods,[67] polymer-micelle-supported Au NPs,[68,69] multicomponent microgels,[70] and 1D assemblies of Au NPs,[71] and they were of similar order as those obtained for porous 1D nanobelts[66] or Au yolk-shell NPs.[72] Nevertheless, we have to note that we used very small amounts of gold catalysts in our experiments.

Thus, to get a clearer picture of the efficacy of the composite material as a catalyst and also to compare the catalytic activity between hybrid fibrils with different degrees of coverage, the catalytic activities are also presented in terms of a normalized rate constant (k_{nor}) obtained by normalization of k_{app} to the total amount (mmol) of catalyst (gold) used in the reaction. Figure 3d shows that the values of k_{nor} for *p*-nitrophenol reduction in the presence of the different types of hybrid fibrils prepared at different [Au]/[protein] MR values are also different. In particular, k_{nor} remains relatively constant from hybrid 1 to 3, that is, as the coverage of the fibrils increases, while for hybrids 4 and 5, k_{nor} progressively reduces. This behavior might be a consequence of (i) changes in nanoparticle sizes on the fibril surfaces and (ii) a decrease in the available metal surface area for the catalytic reaction to take place as the fibril coverage is almost complete. In this regard, it is well-known that the catalytic activity increases as the size of Au NPs decreases because of the increase of effective surface area. In our case, although the crystallite size increases as the concentration of the growth solution increases, we have noted a larger increase in nanoparticle mean size accompanied with an important polydispersity for nanohybrids 4 and 5, as previously

DOI: 10.1021/jz101029f | J. Phys. Chem. Lett. 2010, 1, 2680–2687

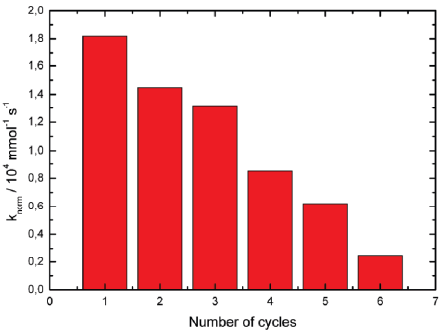

Figure 4. Normalized rate constant (k_{nor}) (with respect to the initial amount of catalyst used) in different cycles of catalytic reduction of *p*-nitrophenol.

mentioned. In addition, for biohybrid 5 fibrils are almost fully covered, which also reduces the accessible metal surface area for reduction to take place. This would explain the decreasing values for such systems. In contrast, hybrids 1, 2, and 3 involve the progressive coverage of the fibrils without a significant increase in crystallite size, which involves an increase in the available metal surface area and, thus, of k_{app}. Interestingly, the k_{nor} values for hybrid fibrils are also 5000 times larger than those obtained for citrate-stabilized gold nanoparticles.[31] In addition, k_{nor} values for the present biohybrids are 2 orders of magnitude larger than those obtained, for example, in the presence of polygonal Au nanostructures,[73] Au−PEDOT/PSS$^-$ composites,[74] or poly(propylene imine) (PPI)-dendrimer-supported spherical nanoparticles.[59] The 1D structure of the protein support can affect more efficiently the adsorption/diffusion of *p*-nitrophenol toward the surface of the gold nanoparticle catalyst, thereby increasing the catalytic activity.[63] Also, the predominance of {111} crystal planes in the nanoparticle structure might also favor the catalytic efficiency.[75]

On the other hand, it is known that reusability is the main advantage of using a heterogeneous catalyst rather than a homogeneous catalyst for industrial applications. To check the reusability of these nanohybrids as catalysts, we have recovered the solid catalyst (e.g., biohybrid 3) from the reaction mixture after completion of the first cycle of nitrophenol reduction by centrifugation. The recovered nanohybrids were stable as confirmed by TEM (Figure S4, Supporting Information). These recovered hybrid nanofibrils were then used as the catalyst in a consecutive run of $NaBH_4$ reduction of nitrophenol, and the k_{app} and k_{nor} of each cycle were calculated as previously. Figure 4 clearly indicates that the activity of the hybrid nanofibrils slightly decreases as the number of reduction cycles increases. However, it is necessary to mention that during the recycling process, a weight loss of ~10% after each reduction cycle occurred. This involved an effective loss of metallic material, which might explain the decrease in catalytic activity compared to that of the pristine hybrid nanofibrils. Also, some increase in fibril bundling due to successive centrifugation steps might also result in a negative influence in the catalytic efficiency of the biohybrid.

In summary, we report a method to obtain metallic Au nanowires by using Lys protein fibrils as bioscaffolds to generate a complete gold coating layer on the biotemplate surface by the attachment of gold seeds and further growth of the coating layer by sequential addition of a gold salt growth solution (seeded-mediated mechanism). To obtain full coverage of the protein fibrils, a suitable initial [Au]/[protein] MR must be selected, and a suitable number of sequential additions of Au ions must be performed. If these requirements are not fulfilled, partial coverage and/or protein bundling and further fibril precipitation are observed. The hybrid metallic fibrils have been proved to be useful as catalytic substrates, provided their superior catalytical activity when incorporated in the reduction reaction of *p*-nitrophenol to *p*-aminophenol by $NaBH_4$. The reaction rates obtained were 1.5−4 times larger than those reported for glucose-reduced Au nanoparticle networks, (PAMAM)-dendrimer-supported spherical nanoparticles, solid 1D Au nanobelts and nanorods, polymer-micelle-supported Au NPs, multicomponent microgels, or 1D assemblies of Au NPs. Also, the hybrid fibrils maintained their catalytical activity when recovered after several cycles of *p*-nitrophenol reduction.

EXPERIMENTAL SECTION

Materials. Lys and $HAuCl_4$ were obtained from Sigma Chemical Co. The protein was used after further purification by liquid chromatography using a Superdex 75 column equilibrated with 0.01 M phosphate. All other chemicals were of the highest purity available. Experiments were carried out using doubly distilled, deionized, and degassed water.

Preparation of Lys Fibril Solutions. Protein fibril solutions were prepared according to previously well-established protocols.[50−52] Briefly, Lys fibrils were obtained by forming a 2 mg/mL stock solution in glycine buffer of pH 2.0 (ionic strengths: 136.7 mM NaCl, 2.68 mM NaCl). Protein stock solution was dialyzed extensively against proper buffer. Protein concentrations were determined spectrophotometrically using a molar absorption coefficient of 37609 at 280 nm.[76] Before incubation, the solutions were filtered through a 0.2 μm filter into sterile test tubes. Samples were incubated at 55 °C in a refluxed reactor for 3 days.

Characterization of the Fibrils. Protein suspensions were applied to carbon-coated copper grids, blotted, washed, negatively stained with 2% (w/v) of phosphotungstic acid, air-dried, and then examined with a Phillips CM-12 transmission electron microscope operating at an accelerating voltage of 120 kV. Samples were diluted between 20- and 200-fold where needed prior to deposition on the grids.

Au Seed Solution. A volume of 0.06 mL of a $HAuCl_4$ solution (0.025 M) was set in a glass vial. Immediately, 3 mL of sodium citrate (1 mM) and 26 mL of Milli Q water were added, and the mixture was stirred for 15 min. After, 1 mL of a $NaBH_4$ solution (1 M) was added under agitation, and the reduction reaction was conducted. Excess reagents were eliminated by extensive dialysis.

Metallic Nanowire Synthesis. In a typical synthesis, 0.2 mL of the Lys stock solution of typically 2 g/L was diluted 300-fold to avoid undesired aggregates during the synthesis of the biohybrids; 5 mL of the former solution was heated to 55 °C

DOI: 10.1021/jz101029f | J. Phys. Chem. Lett. 2010, 1, 2680–2687

under magnetic stirring. Then, 2.7 mL of the gold seed solution was added in order to get a [Au seed]/[protein] MR of 50. The mixture was kept at 55 °C for 2 h. Next, a number of sequential additions of suitable volumes of a solution containing $HAuCl_4$ (0.4 mM) and ascorbic acid (60 μL, 2 mM) were performed. After each addition, the mixture was left to incubate at 55 °C for 4 h. Excess reactants were eliminated by dialysis using a cellulose membrane of cutoff 100 000 Da (Spectra/Por, Netherlands).

Characterization of Metallic Hybrids. TEM images were obtained with the Phillips CM-12 transmission electron microscope operating at an accelerating voltage of 120 kV, previously described. SEM images were recorded with a LEO-435VP scanning electron microscope (Leica Microsystems GmbH, Wetlar, Germany) operating at an accelerating voltage of 30 kV. XRD experiments were carried out using a Siemens D5005 rotating anode X-ray generator. Twin Göbel mirrors were used to produce a well-collimated beam of Cu Kα radiation (λ = 1.5418 A). XRD patterns were recorded with an imaging plate detector AXS F.Nr. J2-394. Au concentrations of each biohybrid system were determined via inductively coupled plasma atomic emission spectroscopy (ICP-AES, Varian).

Catalysis of p-Nitrophenol. Typically, a reaction mixture of water (1−1.8 mL), aqueous *p*-nitrophenol solution (0.5 mL; 0.025 mM), and purified biohybrid 1 (0.2−1 mL), were first taken in a quartz cuvette. To this stirring reaction mixture, aqueous $NaBH_4$ (0.5 mL, 1 M) was then added, and the mixture was quickly placed in the cell holder of the spectrophotometer (Cary 100 Bio UV−vis, Varian Inc. Palo Alto, U.S.A.). The progress of the conversion of *p*-nitrophenol to *p*-aminophenol was then monitored via UV−vis spectroscopy by recording the time-dependent absorption spectra of the reaction mixture. The ratio of absorbance A_t of *p*-nitrophenol at time t to its value A_0 measured at t = 0 directly gives the corresponding concentration ratio (C_t/C_0) of *p*-nitrophenol. Thus, the kinetic equation of the reduction could be shown as follows

$$dC_t/dt = k_{app}t \quad \text{or} \quad \ln(C_0/C_t) = \ln(A_0/A_t) = k_{app}t$$

where C_t is the concentration of *p*-nitrophenol at time t and k_{app} is the apparent rate constant, which can be obtained from the decrease of peak intensity at 400 nm with time. Similarly, we have also carried out the reduction of *p*-nitrophenol in the presence of other biohybrids under reaction conditions similar to that used for biohybrid 1.

Recycling of the Catalyst. After the first batch of *p*-nitrophenol reduction with the metallic fibrils, the solid mass was isolated from the reaction mixture by centrifugation at 3000*g* for 15 min. The collected product was purified using two cycles of centrifugation, supernatant removal, and resuspension in water. The recovered nanohybrids were then used for further catalytic reduction of *p*-nitrophenol with $NaBH_4$, maintaining similar reaction conditions. This process was repeated five times.

SUPPORTING INFORMATION AVAILABLE

Crystallyte size distributions, complementary hybrid fibrils images, and catalytic activity plots. This material is available free of charge via the Internet at http://pubs.acs.org.

AUTHOR INFORMATION

Corresponding Author:

*To whom correspondence should be addressed. E-mail: pablo.taboada@usc.es.

ACKNOWLEDGMENT Authors thank financial support from Ministerio de Ciencia e Innovación (MICINN) through Research Project MAT 2007-6107, Xunta de Galicia through Project INCITE09206020PR, and Fundación Ramón Areces through Project 2010/CL509. S.G.-L. thanks MICINN for her FPI scholarship.

REFERENCES

(1) Sepúlveda, B.; Angelomé, P. C.; Lechuga, L. M.; Liz-Marzán, L. M. LSPR-Based Nanobiosensors. *Nano Today* **2009,** *4*, 244–251.

(2) Cobley, C. M.; Skrabalak, S. E.; Xia, Y. Shape-Controlled Synthesis of Silver Nanoparticles for Plasmonic and Sensing Applications. *Plasmonics* **2009,** *4*, 171–179.

(3) Daniel, W. L.; Han, M.; Lee, J. S.; Mirkin, C. A. Colorimetric Nitrite and Nitrate Detection with Gold Nanoparticle Probes and Kinetic End Points. *J. Am. Chem. Soc.* **2009,** *131*, 6362–6363.

(4) Zheng, D.; Seferos, D. S.; Giljohann, D. A.; Patel, P. C.; Mirkin, C. A. Aptamer Nano-flares for Molecular Detection in Living Cells. *Nano Lett.* **2009,** *9*, 3258–3261.

(5) Wang, C.; Daimon, H.; Lee, Y.; Kim, J.; Sun, S. Synthesis of Monodisperse Pt Nanocubes and Their Enhanced Catalysis for Oxygen Reduction. *J. Am. Chem. Soc.* **2007,** *129*, 6974–6975.

(6) Sun, S. H.; Yang, D. Q.; Villers, D.; Zhang, G. X.; Sacher, E.; Dodelet, J. P. Template- and Surfactant-free Room Temperature Synthesis of Self-Assembled 3D Pt Nanoflowers from Single-Crystal Nanowires. *Adv. Mater.* **2008,** *20*, 571–574.

(7) Mahmoud, M. A.; Tabor, C. E.; El-Sayed, M. A.; Ding, Y.; Wang, Z. L. A New Catalytically Active Colloidal Platinum Nanocatalyst: The Multiarmed Nanostar Single Crystal. *J. Am. Chem. Soc.* **2008,** *130*, 4590–4591.

(8) Zeng, J.; Zhang, Q.; Chen, J.; Xia, Y. A Comparison Study of the Catalytic Properties of Au-Based Nanocages, Nanoboxes, and Nanoparticles. *Nano Lett.* **2010,** *10*, 30–35.

(9) Chen, J.; Wang, D.; Xi, J.; Au, L.; Siekkinen, A.; Warsen, A.; Li, Z. Y.; Zhang, H.; Xia, Y.; Li, X. Immuno Gold Nanocages with Tailored Optical Properties for Targeted Photothermal Destruction of Cancer Cells. *Nano Lett.* **2007,** *7*, 1318–1322.

(10) Cobley, C. M.; Au, L.; Chen, J.; Xia, Y. Targeting Gold Nanocages to Cancer Cells for Photothermal Destruction and Drug Delivery. *Expert Opin. Drug Delivery* **2010,** *7*, 577–587.

(11) Au, L.; Zhang, Q.; Cobley, C. M.; Gidding, M.; Schwartz, A. G.; Chen, J.; Xia, Y. Quantifying the Cellular Uptake of Antibody-Conjugated Au Nanocages by Two-Photon Microscopy and Inductively Coupled Plasma Mass Spectrometry. *ACS Nano* **2010,** *4*, 35–42.

(12) Hurst, S. J.; Han, M. S.; Lytton-Jean, A. K. R.; Mirkin, C. A. Screening the Sequence Selectivity of DNA-Binding Molecules Using a Gold Nanoparticle-Based Colorimetric Approach. *Anal. Chem.* **2007,** *79*, 7201–7205.

(13) Qian, X. M.; Nie, S. M. Single-Molecule and Single-Nanoparticle SERS: From Fundamental Mechanisms to Biomedical Applications. *Chem. Soc. Rev.* **2008,** *37*, 912–920.

(14) Zheng, G.; Daniel, W. L.; Mirkin, C. A. A New Approach to Amplified Telomerase Detection with Polyvalent Oligonucleotide Nanoparticle Conjugates. *J. Am. Chem. Soc.* **2008,** *130*, 9644–9645.

(15) Banholzer, M. J.; Millstone, J. E.; Qin, L.; Mirkin, C. A. Rationally Designed Nanostructures for Surface-Enhanced Raman Spectroscopy. *Chem. Soc. Rev.* **2008,** *37*, 885–897.
(16) Li, W.; Camargo, P. H. C.; Lu, X.; Xia, Y. Dimers of Silver Nanospheres: Facile Synthesis and Their Use as Hot Spots for Surface-Enhanced Raman Scattering. *Nano Lett.* **2009,** *9*, 485–490.
(17) Rodríguez-Lorenzo, L.; Álvarez-Puebla, R. A.; Pastoriza-Santos, I.; Mazzucco, S.; Stéphan, O.; Kociak, M.; Liz-Marzán, L. M.; García de Abajo, F. J. Zeptomol Detection Through Controlled Ultrasensitive Surface-Enhanced Raman Scattering. *J. Am. Chem. Soc.* **2009,** *131*, 4616–4618.
(18) Alvarez-Puebla, R. A.; Liz-Marzán, L. M. SERS-Based Diagnosis and Biodetection. *Small* **2010,** *6*, 604–610.
(19) van Bommel, K. J. C.; Friggeri, A.; Shinkai, S. Organic Templates for the Generation of Inorganic Materials. *Angew. Chem., Int. Ed.* **2003,** *42*, 980–999.
(20) Baron, R.; Willner, B.; Willner, I. Biomolecule−Nanoparticle Hybrids as Functional Units for Nanobiotechnology. *Chem. Commun.* **2007,** 323–332.
(21) Ofir, Y.; Samanta, B.; Rotello, V. M. Polymer and Biopolymer Mediated Self-Assembly of Gold Nanoparticles. *Chem. Soc. Rev.* **2008,** *37*, 1814–1825.
(22) Sotiropoulou, S.; Sierra-Sastre, Y.; Mark, S. S.; Batt, C. A. Biotemplated Nanostructured Materials. *Chem. Mater.* **2008,** *20*, 821–834.
(23) Behrens, S. S. Synthesis of Inorganic Nanomaterials Mediated by Protein Assemblies. *J. Mater. Chem.* **2008,** *18*, 3788–3798.
(24) Warner, M. G.; Hutchison, J. E. Linear Assemblies of Nanoparticles Electrostatically Organized on DNA Scaffolds. *Nat. Mater.* **2003,** *2*, 272–277.
(25) Gun, Q.; Chen, C.; Haynie, D. T. Cobalt Metallization of DNA: Toward Magnetic Nanowires. *Nanotechnology* **2005,** *16*, 1358–1363.
(26) Kundu, S.; Liang, H. Photochemical Synthesis of Electrically Conductive CdS Nanowires on DNA Scaffolds. *Adv. Mater.* **2008,** *20*, 826–831.
(27) Wirges, C. T.; Timper, J.; Fischler, M.; Sologubenko, A. S.; Mayer, J.; Simon, U.; Carell, T. Controlled Nucleation of DNA Metallization. *Angew. Chem., Int. Ed.* **2009,** *48*, 219–223.
(28) Knez, M.; Bittner, A. M.; Boes, F.; Wege, C.; Jeske, H.; Maiβ, E.; Kern, K. Biotemplate Synthesis of 3-nm Nickel and Cobalt Nanowires. *Nano Lett.* **2003,** *3*, 1079–1082.
(29) Dujardin, E.; Peet, C.; Stubbs, G.; Culver, J.; Mann, S. Organization of Metallic Nanoparticles Using Tobacco Mosaic Virus Templates. *Nano Lett.* **2003,** *3*, 413–417.
(30) Tsukamoto, R.; Muraoka, M.; Seki, M.; Tabata, H.; Yamashita, I. Synthesis of CoPt and $FePt_3$ Nanowires Using the Central Channel of Tobacco Mosaic Virus as a Biotemplate. *Chem. Mater.* **2007,** *19*, 2389–2391.
(31) Balci, S.; Leinberger, D. M.; Knez, M.; Bittner, A. M.; Boes, F.; Kadri, A.; Wege, C.; Jeske, H.; Kern, K. Printing and Aligning Mesoscale Patterns of *Tobacco mosaic* Virus on Surfaces. *Adv. Mater.* **2008,** *20*, 2195–2200.
(32) Fu, X.; Wang, Y.; Huang, L.; Sha, Y.; Gui, L.; Lai, L.; Tang, Y. Assemblies of Metal Nanoparticles and Self-Assembled Peptide Fibrils — Formation of Double Helical and Single-Chain Arrays of Metal Nanoparticles. *Adv. Mater.* **2003,** *15*, 902–906.
(33) Gazit, E. Self-Assembled Peptide Nanostructures: the Design of Molecular Building Blocks and Their Technological Utilization. *Chem. Soc. Rev.* **2007,** *36*, 1263–1269.
(34) Sharma, N.; Top, A.; Kiick, K. L.; Pochan, D. J. One-Dimensional Gold Nanoparticle Arrays by Electrostatically Directed Organization Using Polypeptide Self-Assembly. *Angew. Chem., Int. Ed.* **2009,** *48*, 7078–7082.
(35) Scheibel, T.; Parthasarathy, R.; Sawicki, G.; Lin, X. M.; Jaeger, H.; Lindquist, S. L. Conducting Nanowires Built by Controlled Self-Assembly of Amyloid Fibers and Selective Metal Deposition. *Proc. Natl. Acad. Sci. U.S.A.* **2003,** *100*, 4527–4532.
(36) Behrens, S.; Wu, J.; Habitch, W.; Unger, E. Silver Nanoparticle and Nanowire Formation by Microtubule Templates. *Chem. Mater.* **2004,** *16*, 3085–3090.
(37) Cherny, I.; Gazit, E. Amyloids: Not Only Pathological Agents but Also Ordered Nanomaterials. *Angew. Chem., Int. Ed.* **2008,** *47*, 4062–4069.
(38) Slocik, J. M.; Kim, S. N.; Whitehead, T. A.; Clark, D. S.; Naik, R. R. Biotemplated Metal Nanowires Using Hyperthermophilic Protein Filaments. *Small* **2009,** *5*, 2038–2042.
(39) Bigall, N. C.; Reitzing, M.; Naumann, W.; Simon, P.; van Pée, K.-H.; Eychmüller, A. Fungal Templates for Noble-Metal Nanoparticles and Their Application in Catalysis. *Angew. Chem., Int. Ed.* **2008,** *47*, 7876–7879.
(40) Retches, M.; Gazit, E. Casting Metal Nanowires Within Discrete Self-Assembled Peptide Nanotubes. *Science* **2003,** *300*, 625–627.
(41) Kinsella, J. M.; Ivanisevic, A. Enzymatic Clipping of DNA Wires Coated with Magnetic Nanoparticles. *J. Am. Chem. Soc.* **2005,** *127*, 3276–3277.
(42) Bai, H.; Xu, K.; Xu, Y.; Matsui, H. Fabrication of Au Nanowires of Uniform Length and Diameter Using a Monodisperse and Rigid Biomolecular Template: Collagen-like Triple Helix. *Angew. Chem., Int. Ed.* **2007,** *46*, 3319–3322.
(43) Ostrov, N.; Gazit, E. Genetic Engineering of Biomolecular Scaffolds for the Fabrication of Organic and Metallic Nanowires. *Angew. Chem., Int. Ed.* **2010,** *49*, 3018–3021.
(44) Guha, S.; Banerjee, A. Self-Assembled Robust Dipeptide Nanotubes and Fabrication of Dipeptide-Capped Gold Nanoparticles on the Surface of these Nanotubes. *Adv. Funct. Mater.* **2009,** *19*, 1949–1961.
(45) Ryu, J.; Lim, S. Y.; Park, C. B. Photoluminescent Peptide Nanotubes. *Adv. Mater.* **2009,** *11*, 1577–1581.
(46) Górzny, M. L.; Walton, A. S.; Evans, S. D. Synthesis of High-Surface-Area Platinum Nanotubes Using a Viral Template. *Adv. Funct. Mater.* **2010,** *20*, 1295–1300.
(47) Balci, S.; Noda, K.; Bittner, A.; Kadri, A.; Wege, C.; Jeske, H.; Kern, K. Self-Assembly of Metal-Virus Nanodumbbells. *Angew. Chem., Int. Ed.* **2007,** *46*, 3149–3151.
(48) Dobson, C. M. Protein Folding and Misfolding. *Nature* **2003,** *426*, 884–890.
(49) Jahn, T. R.; Radford, S. E. Folding Versus Aggregation: Polypeptide Conformations on Competing Pathways. *Arch. Biochem. Biophys.* **2008,** *469*, 100–117.
(50) Frare, E.; De Laureto, P. P.; Zurdo, J.; Dobson, C. M.; Fontana, A. A Highly Amyloidogenic Region of Hen Lysozyme. *J. Mol. Biol.* **2004,** *340*, 1153–1165.
(51) Pawar, A. P.; Dubai, K. F.; Zurdo, J.; Chiti, F.; Vendruscolo, M.; Dobson, C. M. Prediction of "Aggregation-Prone" and "Aggregation-Susceptible" Regions in Proteins Associated with Neurodegenerative Diseases. *J. Mol. Biol.* **2005,** *350*, 379–392.
(52) Lieu, V. H.; Wu, J. W.; Wang, S. S. S.; Wu, C. H. Inhibition of Amyloid Fibrillization of Hen Egg-White Lysozymes by Rifampicin and *p*-Benzoquinone. *Biotechnol. Prog.* **2007,** *23*, 698–706.
(53) Yu, L.; Banerjee, I. A.; Shima, A.; Rajan, K.; Matsui, H. Size-Controlled Ni Nanocrystal Growth on Peptide Nanotubes and Their Magnetic Properties. *Adv. Mater.* **2004,** *16*, 709–712.

(54) Almeida, N. L.; Oliveira, C. L. P.; Torriani, I. L.; Loh, W. Calorimetric and Structural Investigation of the Interaction of Lysozyme and Bovine Serum Albumin with Poly(Ethylene Oxide) and its Copolymers. *Colloids Surf., B* **2004,** *38*, 67–76.
(55) Dutta, P.; Manivannan, A.; Seehra, M. S.; Shah, N.; Huffman, G. P. Magnetic Properties of Nearly Defect-Free Maghemite Nanocrystals. *Phys. Rev. B* **2004,** *70*, 174428/1–174428/7.
(56) Shiomi, T.; Tsunoda, T.; Kawai, A.; Mizukami, F.; Sakaguchi, K. Biomimetic Synthesis of Lysozyme−Silica Hybrid Hollow Particles Using Sonochemical Treatment: Influence of pH and Lysozyme Concentration on Morphology. *Chem. Mater.* **2007,** *19*, 4486–4493.
(57) Schrinner, M.; Ballauff, M.; Talmon, Y.; Kauffmann, Y.; Thun, J.; Moller, M.; Breu, J. Dynamical Quorum Sensing and Synchronization in Large Populations of Chemical Oscillators. *Science* **2009,** *323*, 617–620.
(58) Qin, G.; W. Pei, W.; Ma, X.; Xu, X.; Ren, Y.; Sun, W.; Zuo, L. Enhanced Catalytic Activity of Pt Nanomaterials: From Monodisperse Nanoparticles to Self-Organized Nanoparticle-Linked Nanowires. *J. Phys. Chem. C* **2010,** *114*, 6909–6913.
(59) Hayakawa, K.; Yoshimura, T.; Esumi, K. Preparation of Gold-Dendrimer Nanocomposites by Laser Irradiation and Their Catalytic Reduction of 4-Nitrophenol, Immobilization and Recovery of Au Nanoparticles from Anion Exchange Resin: Resin-Bound Nanoparticle Matrix as a Catalyst for the Reduction of 4-Nitrophenol. *Langmuir* **2003,** *19*, 5517–5521.
(60) Praharaj, S.; Nath, S.; Gosh, S. K.; Kundu, S.; Pal, T. Immobilization and Recovery of Au Nanoparticles from Anion Exchange Resin: Resin-Bound Nanoparticle Matrix as a Catalyst for the Reduction of 4-Nitrophenol. *Langmuir* **2004,** *20*, 9889–9892.
(61) Rashid, M. H.; Bhattacharjee, R. R.; Kotal, A.; Mandal, T. K. Synthesis of Spongy Gold Nanocrystals with Pronounced Catalytic Activities. *Langmuir* **2006,** *22*, 7141–7143.
(62) Rashid, M. H.; Mandal, T. K. Organic Ligand-Mediated Synthesis of Shape-Tunable Gold Nanoparticles: An Application of Their Thin Film as Refractive Index Sensors. *J. Phys. Chem. C* **2007,** *111*, 9684–9693.
(63) Esumi, K.; Isono, R.; Yoshimura, T. Preparation of PAMAM− and PPI−Metal (Silver, Platinum, and Palladium) Nanocomposites and Their Catalytic Activities for Reduction of 4-Nitrophenol. *Langmuir* **2004,** *20*, 237–243.
(64) Liu, J.; Qin, G.; Raavendran, P.; Ikushima, Y. Facile "Green" Synthesis, Characterization, and Catalytic Function of β-D-Glucose-Stabilized Au Nanocrystals. *Chem.—Eur. J.* **2006,** *12*, 2131–2138.
(65) Chen, X.; Zhao, D.; An, Y.; Shi, L.; Hou, W.; Chen, L. Catalytic Properties of Gold Nanoparticles Immobilized on the Surfaces of Nanocarriers. *J. Nanopart. Res.* **2010,** *12*, 1877–1887.
(66) Li, L.; Wang, Z.; Huang, T.; Xie, J.; Qin, L. Porous Gold Nanobelts Templated by Metal−Surfactant Complex Nanobelts. *Langmuir* **2010,** *26*, 12330–12335.
(67) Bai, X.; Gao, Y.; Liu, H.-g.; Zheng, L. Synthesis of Amphiphilic Ionic Liquids Terminated Gold Nanorods and Their Superior Catalytic Activity for the Reduction of Nitro Compounds. *J. Phys. Chem. C* **2009,** *113*, 17730–17736.
(68) Wang, Y.; Wei, G.; Zhang, W.; Jiang, X.; Zheng, P.; Shi, L.; Dong, A. Responsive Catalysis of Thermoresponsive Micelle-Supported Gold Nanoparticles. *J. Mol. Catal. A: Chem.* **2007,** *266*, 233–238.
(69) Chen, X.; An, Y.; Zhao, D.; He, Z.; Zhang, Y.; Cheng, J.; Shi, L. Core−Shell−Corona Au−Micelle Composites with a Tunable Smart Hybrid Shell. *Langmuir* **2008,** *24*, 8198–8204.
(70) Hain, J.; Schrinner, M.; Lu, Y.; Pich, A. Design of Multicomponent Microgels by Selective Deposition of Nanomaterials. *Small* **2008,** *4*, 2016–2024.
(71) Huang, T.; Meng, F.; Qi, L. Facile Synthesis and One-Dimensional Assembly of Cyclodextrin-Capped Gold Nanoparticles and Their Applications in Catalysis and Surface-Enhanced Raman Scattering. *J. Phys. Chem. C* **2009,** *113*, 13636–13642.
(72) Lee, J.; Park, L. C.; Song, H. A Nanoreactor Framework of a Au@SiO_2 Yolk/Shell Structure for Catalytic Reduction of *p*-Nitrophenol. *Adv. Mater.* **2008,** *20*, 1523–1528.
(73) Rashid, M. H.; Mandal, T. K. Templateless Synthesis of Polygonal Gold Nanoparticles: An Unsupported and Reusable Catalyst with Superior Activity. *Adv. Funct. Mater.* **2008,** *18*, 2261–2271.
(74) Kumar, S. S.; Kumar, C. S.; Mathiyarasu, J.; Phani, K. L. Stabilized Gold Nanoparticles by Reduction Using 3,4-Ethylenedioxythiophene-polystyrenesulfonate in Aqueous Solutions: Nanocomposite Formation, Stability, and Application in Catalysis. *Langmuir* **2007,** *23*, 3401–3408.
(75) Burda, C.; Chen, X.; Narayanan, R.; El-Sayed, M. A. Chemistry and Properties of Nanocrystals of Different Shapes. *Chem. Rev.* **2005,** *105*, 1025–1102.
(76) Knubovets, T.; Osterhout, J. J.; Connolly, P. J.; Klibanov, A. M. Structure, Thermostability, And Conformational Flexibility of Hen Egg-White Lysozyme Dissolved in Glycerol. *Proc. Natl. Acad. Sci. U.S.A.* **1999,** *96*, 1262–1267.

DOI: 10.1021/jz101029f | *J. Phys. Chem. Lett.* **2010,** *1*, 2680–2687

CHEMISTRY
A EUROPEAN JOURNAL

DOI: 10.1002/chem.201003679

One-Dimensional Magnetic Nanowires Obtained by Protein Fibril Biotemplating

Josué Juárez, Adriana Cambón, Antonio Topete, Pablo Taboada,* and Víctor Mosquera[a]

Abstract: Magnetic nanowires were obtained through the in situ synthesis of magnetic material by Fe-controlled nanoprecipitation in the presence of two different protein (human serum albumin (HSA) and lysozyme (Lys)) fibrils as biotemplating agents. The structural characteristics of the biotemplates were transferred to the hybrid magnetic wires. They exhibited excellent magnetic properties as a consequence of the 1D assembly and fusion of magnetite nanoparticles as ascertained by SQUID magnetometry. Prompted by these findings, we also checked their potential applicability as MRI contrast agents. The magnetic wires exhibited large r_2* relaxivities and sufficient contrast resolution even in the presence of an extremely small amount of Fe in the magnetic hybrids, which would potentially enable their use as T_2 contrast imaging agents.

Keywords: biotemplating · imaging agents · magnetic nanowires · nanostructures · protein fibrils

Introduction

A key issue in nanotechnology is the development of conceptually simple construction techniques for the mass fabrication of identical nanoscale structures. Interest in one-dimensional (1D) nanoscale materials and devices, often called nanowires, nanotubes or nanorods, has risen sharply in recent years. In particular, 1D magnetic nanostructures exhibit unique magnetic properties due to geometric confinement, magnetostatic interactions and nanoscale domain formation,[1] which endow them with potential applicability in data storage and logic devices,[2a] magneto-transport behaviour,[2b] micromechanical sensors[2c] and biomedicine.[2d] As a result of their high aspect ratios, 1D magnetic entities possess larger dipole moments than individual nanoparticles. This allows their manipulation with lower field strengths[3] and provides them with improved imaging contrast capabilities, which opens up the possibility of their use in new biomedical applications, specifically in the advent of low-field MRI.[4] Here we report the formation of 1D magnetic nanowires and assemblies of magnetic nanoparticles over linear nanosized biopolymer templates formed by spontaneous fibrillation, under suitable conditions, of two proteins—human serum albumin (HSA) and lysozyme (Lys)—by in situ co-precipitation of iron under suitable conditions. These magnetic 1D nanostructures possess both high saturation magnetisations and spin–spin relaxivities at low magnetic fields, which makes them suitable candidates for use as imaging contrast agents in MRI.

There are many literature reports on the fabrication of 1D magnetic nanostructures, which can be assembled by (bio)templating, spontaneous self-assembly by magnetic dipolar interactions of nanoparticles, chemical synthesis, lithographic methods, laser etching or microcontact printing.[5] Owing to its relative simplicity, template-directed synthesis is one of the most attractive methods for preparing magnetic 1D nanomaterials.[5a,b] This approach offers exciting alternatives to the costly nanolithography-based "top-down" technologies or multi-step chemical procedures. Various linear nanometer-scale materials, including molecular dispersed and assembled polymers,[6] carbon nanotubes[5a,7] or biological scaffolds, have been employed to prepare 1D magnetic structures and assemblies.[8] In particular, the capability of biopolymers to generate 1D magnetic nanostructures is really exciting because nature provides a renewable and highly diverse source of nanometer-scale ordered complexes that can be used to replicate inorganic materials as well-defined structures.[9] Dextran, for example, has been used in the creation of elongated assemblies of spherical nanoparticles suitable for use as MRI contrast agents and tumour targeting species.[2d,10] DNA was also used as a stabiliser for the formation of ordered nanowires of magnetic nanoparticles.[2b,11] These nanowire assemblies resulted in stable magnetic fluids with high relaxivities at low fields useful for MRI imaging. The protein cage of cowpea chlorotic mottle virus (CCMV) was explored with the same goal, to incorporate high payloads of Gd^{3+} with elevated molecular relaxivities,[12] and the formation either of magnetic nanotubes or of magnetic nanowires with the aid of magnetic bacteria (*Mag-*

[a] J. Juárez, A. Cambón, A. Topete, P. Taboada, V. Mosquera
Grupo de Física de Coloides y Polímeros
Departamento de Física de la Materia Condensada
Facultad de Física, Universidad de Santiago de Compostela
15782 Santiago de Compostela (Spain)
Fax: (+34) 881814112
E-mail: pablo.taboada@usc.es

Supporting information for this article is available on the WWW under http://dx.doi.org/10.1002/chem.201003679.

netospirillum magneticum strain AMB-1),[13] and tobacco mosaic virus[14] were also investigated.

The spontaneous fibrillation undergone by different proteins under suitable conditions results in the formation of amyloid-like fibrils,[15] potentially applicable as alternative templating agents for the construction of 1D magnetic materials. In particular, the proteins HSA and Lys are two proteins known to fibrillate under different solution conditions to form fibrils with diameters ranging from 10 to 50 nm and lengths up to several microns[16] (see Figure S1 in the Supporting Information). The dimensions of the fibrils can be tuned by varying the solution conditions and the incubation times. They are also thermally stable at high temperatures and different pH values and they contain multiple potential ion-binding sites within their amino acid sequences, which enables their use in metallisation reactions under relatively harsh conditions. We have thus exploited these features to generate 1D magnetic nanoparticle assemblies and nanowires by in situ nanoparticle formation on the fibril surface by use of the electrostatic interaction between Fe^{2+} and Fe^{3+} ions and the negatively charged amino acid residues located on the protein surfaces (mainly glutamic and aspartic acids)[17] and analysis of their magnetic properties and potential applicability as MRI contrast agents. Although biotemplating of metallic nanowires by peptides and protein fibrils has been reported previously,[8a,18] less attention has been paid to the production of 1D protein fibril-templated magnetic structures, and their magnetic properties have not been analysed in detail. Bolaamphiphile peptide fibrils, for example, have been used to template the growth and size of nickel nanocrystals on their surfaces and to tune their magnetic properties,[19] self-assembled peptides have also been conjugated to gadolinium ions,[20] and iron bionanomineralisation has been found to occur in human serum transferrin fibrils.[21]

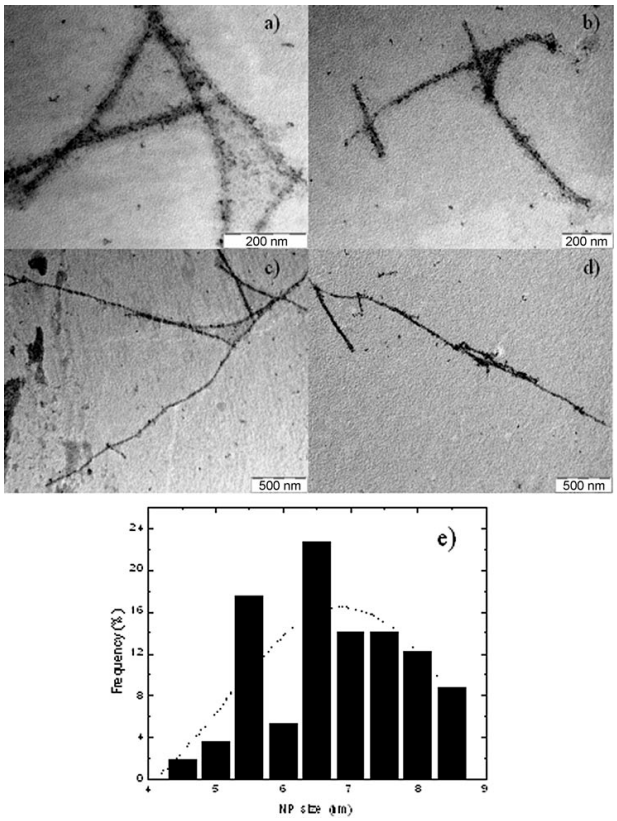

Figure 1. TEM images showing the progressive coverage of lysozyme fibrils to afford magnetic nanowires after a single addition of Fe ions at [Fe]/[protein] molar ratios of: a) 25, b) 50, c) 100 and d) 100 together with one additional sequential addition of Fe ions at the same molar ratio. e) Size distributions of as-synthesised magnetic nanoparticles on the biotemplate surfaces. The dotted line represents the fit of the distribution.

Results and Discussion

Nanowire synthesis and characterisation: For in situ magnetic nanoparticle formation and subsequent fibril coverage, nanoparticle-coated protein fibrils were obtained by sequential addition of Fe^{2+} and Fe^{3+} ions (1:2 molar ratio) and ammonium hydroxide (NH_4OH) solutions to aqueous solutions containing self-assembled fibrils, with subsequent incubation at 80 °C (see the Experimental Section for protein fibrillation and nanoparticle growth details). The controlled precipitation of iron ions leads to the formation of magnetic nanoparticles on the fibrils (see Figure 1). The effects of iron concentration, iron/protein molar ratio, number of sequential additions and/or the presence of different reagents/stabilisers were tested to provide progressive full coverage of the biotemplate and to generate a magnetic wire. A protocol composed of sequential additions of Fe ions in several steps (seeded-growth mechanism) was therefore performed (see the Experimental Section). A suitable [Fe]/[protein] molar ratio (MR) was necessary to ensure full coverage after a small number of addition steps and to avoid both precipitation of the nanohybrid and generation of free magnetic NPs. We should note that if the [Fe]/[protein] molar ratio (MR = 10, 25, 50) is low, complete fibril coverage is not achieved even after several sequential additions; in contrast, if the [Fe]/[protein] MR is too large, bundling and precipitation of the nanohybrids occurs (see Figure S2 in the Supporting Information). For these reasons an initial [Fe]/[protein] MR = 100 was found to be optimal and was further used for three sequential additions of Fe ions to achieve the formation of the magnetic wires. Figure 1 a–d shows the progressive coverage of the nanofibrils at different [Fe]/[protein] molar ratios, with the formation of magnetic nanoparticles on the fibril surface. TEM revealed the primary magnetic nanoparticles to be fairly uniformly distributed on the biotemplate and to have sizes of about 6.8 ± 2.0 nm with a relatively narrow size distribution (Figure 1 e), in fair agreement with those magnetic particles obtained in the absence of the protein template (see Figure S3 in the Supporting Information).

Also, it is necessary to note that fibril integrity and stability was perfectly maintained under these reaction conditions (see Figure S4 in the Supporting Information).

With more addition steps carried out the fibrils became progressively covered with more magnetic material without any apparent increase in nanoparticle size. The continuous fibril coverage is a result of the fusion of adjacent as-synthesised magnetic nanoparticles (see Figure S5 in the Supporting Information). When a progressive and sufficient excess of Fe was added, the nanowire widths increased and their surfaces also appeared rougher, which might indicate that more than one layer of magnetic material had been deposited onto the template (Figure 2a–b). In this regard, the

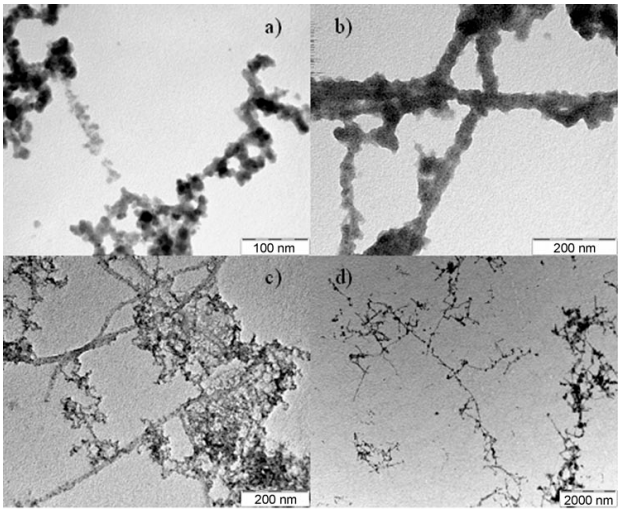

Figure 2. TEM images showing the progressive increases in the widths of the magnetic wires and subsequent bundling after a) three, b) four or c) five sequential additions of Fe ions at MR = 100. d) After 5 sequential additions at MR = 100 in the presence of sodium citrate as stabiliser.

widths of the magnetic wires could be modified from 6 to 50 nm by increasing the number of sequential additions of Fe ions onto the biotemplate. These values depend on the type of fibril used as the template, the [Fe]/[protein] molar ratio and the number of sequential additions performed (see Figure 1 and Figure S2 in the Supporting Information). Nevertheless, constant width along the whole nanofibrils could not be achieved, due to the non-uniform deposition of the ions onto the template. We are currently modifying the synthetic protocol with the goals both of improving uniformity in fibril coverage and of achieving perfect control over the magnetic nanowire dimensions and their resulting magnetic properties. In addition, under conditions of excessive Fe ions in solution an increasing presence of fibril networks as a consequence of fibril bundling was observed, leading to precipitation of the nanowires after several days (see Figure 2c). This can be a result either of magnetic interaction between nanowires or of inefficient stabilisation of the 1D nanostructures. To prevent these phenomena, we decided to stabilise the magnetic nanowires further by the addition of sodium citrate, which has been shown to be an effective stabiliser for water-soluble magnetic nanoparticles.[22] In this process, no fibril precipitation was observed for at least one month and a lower level of bundling was confirmed, probably as a consequence of the generation of a surface organic layer that moderately screens the magnetic interactions between magnetic covered fibrils (Figure 2d).

On the other hand, the morphologies and sizes of the fully covered fibrils made of HSA and Lys present some differences irrespective of the method used to create the magnetic nanowires. This is a consequence of the inherent structural differences between the fibrils assembled from the two proteins. In this respect, HSA-derived nanowires have shorter lengths (between 0.1 and 2 μm) and widths (4–10 nm), and have a curly morphology as a direct consequence of the template structure (see Figure S6 in the Supporting Information).[16a,b] In contrast, Lys-derived wires appear to be straighter and longer (lengths and widths of 0.4–8 μm and 12–20 nm, respectively).[16c,d] This observation additionally confirms that the overall structures of the fibril templates remain intact after surface modification.

XRD analysis, selected area electron diffraction (SAED) patterns, high-resolution TEM (HR-TEM) images and FTIR spectroscopic examination of the fully covered fibrils confirmed the formation and nature of the magnetic coverage on the template surface. The XRD pattern showed reflections indexed to (111), (220), (311), (222), (400), (422), (511), (440) and (533) planes, corresponding to the cubic spinel crystal structure of iron oxides (see Figure 3a, JPCDS file No. 19-0629, magnetite, or JCPDS file 39-1346, maghemite). In addition, XRD demonstrated a polycrystalline structure with cell constant $a_0 = 0.8381$ nm, which is in good agreement with the standard card of iron oxides. The peak broadening of the XRD pattern also indicates that the resulting iron oxide crystallites were rather small. The crystallite sizes calculated from the modified Scherrer relation[23] for the magnetic fibrils of both Lys and HSA were about (6.2 ± 2) nm, consistent with the size distributions measured from TEM images. SAED, HR-TEM and FTIR confirm the predominance of the magnetite phase on the biotemplate. The SAED pattern consisted of spots on the rings corresponding to the diffraction planes (111), (220), (311), (400), (511) and (440) characteristic of the magnetite phase, which also revealed the polycrystalline nature of the nanocomposites (see Figure 3b). The difference between the polycrystalline electron diffraction patterns of magnetite and maghemite phases is solved by the presence of the (111) diffraction plane, distinctive of the magnetite fcc structure.[24] From the HR-TEM images (Figure 3c) we can observe that the obtained magnetite nanoparticles are single crystalline, as indicated by the well-resolved lattice fringes. The distance between two adjacent planes is about 0.255 nm, which corresponds to the (311) lattice plane in the spinel structure of Fe_3O_4.[25] The strong peak at 580 cm^{-1} in the FTIR plot (Figure 3d) additionally confirms that the phase is magnetite

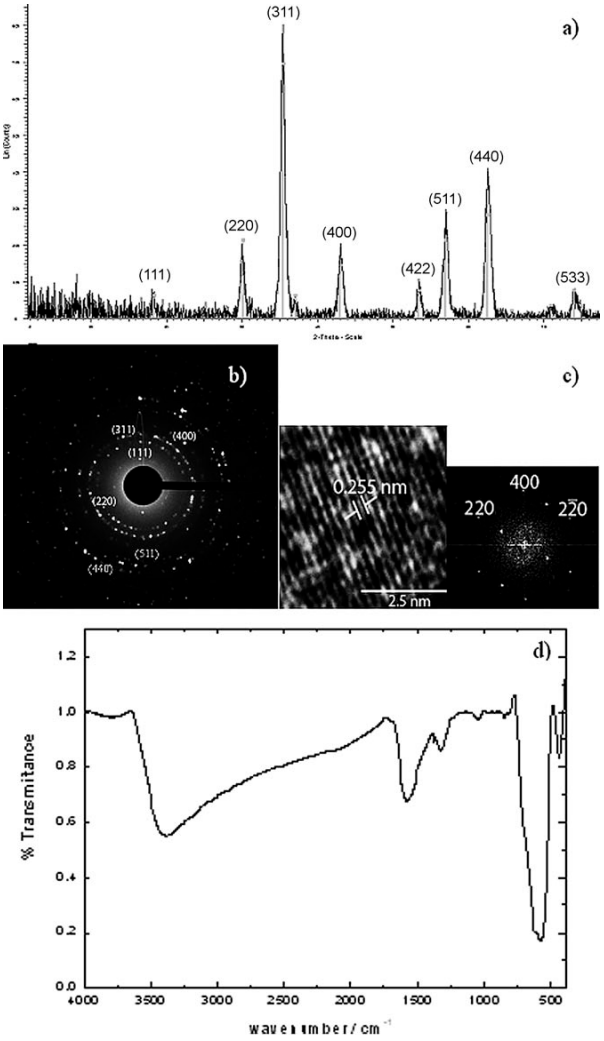

Figure 3. a) XRD pattern and b) SAED pattern of the fully covered magnetic nanowires. c) HR-TEM image of a magnetite nanoparticle showing the interplanar distance; the FFT indicates that the nanoparticle is oriented in the [001] direction. d) FTIR spectrum of fully covered magnetic nanowires.

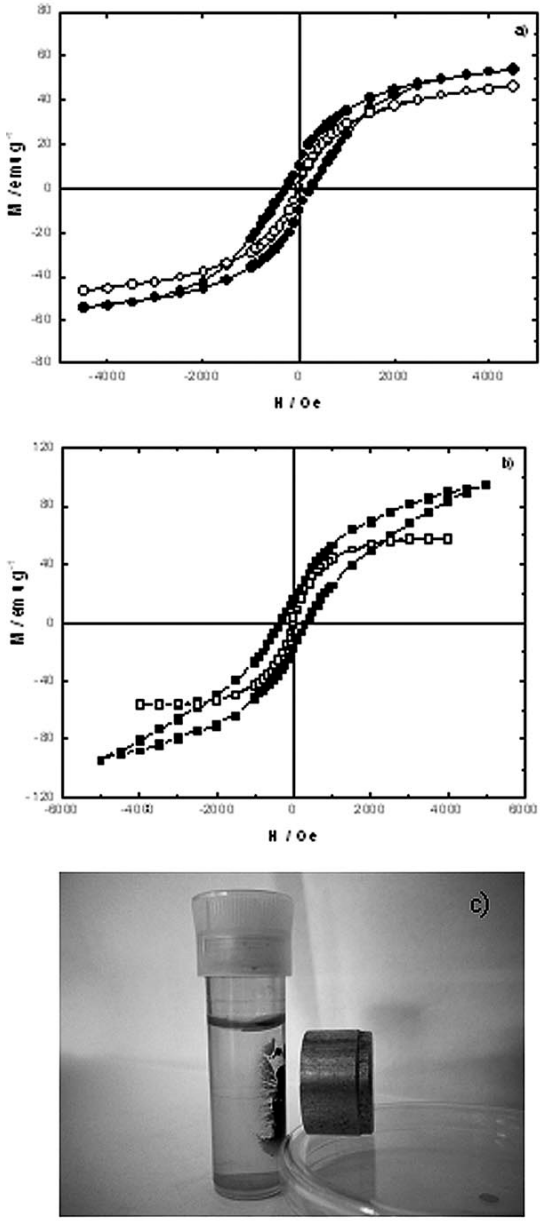

Figure 4. Magnetisation versus applied magnetic field for: a) dispersed magnetite nanoparticles, and b) fully covered magnetic nanowires at 5 K (closed symbols) and 300 K (open symbols). c) Image showing the attraction of the nanowires to a magnet.

rather than maghemite. The peaks at about 591 and 456 cm^{-1} in the spectrum indicate the presence of both magnetite and maghemite.[26]

Magnetic and imaging contrast properties: To evaluate the potential use of these 1D hybrid magnetic nanostructures for bioimaging, we first investigated the magnetic properties of fully magnetite-covered hybrid lysozyme nanofibrils with the aid of a superconducting quantum interference device (SQUID), and compared them with those of dispersed magnetic nanoparticles synthesised under the same solution conditions in the absence of protein fibrils. Figure 4 shows the field-dependent magnetisation of the fully covered fibrils and dispersed magnetic nanoparticles measured at 300 and 5 K, respectively. Their M/H curves at 300 K show nonlinear, reversible characteristics with no hysteresis (zero coercivity), features of superparamagnetic behaviour, with saturation magnetisation (M_s) values of about 60 and 47 emu g^{-1} for fully covered and isolated nanoparticles, respectively. The observed magnetic behaviour is consistent with the common understanding that one-dimensionally stacked magnetic nanoparticles forming a uniform layer behave like single elongated particles, and so their cooperative response is more sensitive to a magnetic field.[27] Nevertheless, all the

above values are lower than the theoretical value of the bulk magnetite (92 emu g^{-1}).[28] A decrease in M is often observed and is attributed to the surface contribution: spin canting, surface disorder, stoichiometry deviation, ion distribution and adsorbed species.[29] The elongated structures of the nanowires apparently enhance the orientation of the magnetic moments of the individual nanoparticle constituents, increasing the net magnetisation.[13,30] On the other hand, the magnetisation curves at 5 K show that all samples have hysteresis with coercitive fields (H_c) of 352 and 270 Oe, remnant magnetisation of 16.5 and 10.2 emu g^{-1} and M_s values of about 90 and 56 emu g^{-1} for fully covered and isolated nanoparticles, respectively. The magnetic properties of the hybrid fibrils were also tested by placing a magnet near the cuvette. The hybrid nanowires were completely attracted to the side of the cuvette nearest to the magnet as displayed in Figure 4c, which additionally confirms the magnetic properties of the hybrid samples.

Measurements of magnetisation versus temperature were performed by standard experimental zero-field-cooling (ZFC) and field-cooling (FC) protocols with the external magnetic field set at 500 Oe when necessary. Field-cooled (FC) magnetisation measurements provide information about coupling between the magnetic materials because a FC experiment suppresses thermal fluctuations and increases net magnetisation. The ZFC and FC magnetisation curves split below 150 and 195 K, and the ZFC magnetisation curves exhibit peaks around $T=35$ and 105 K for fully covered fibrils and dispersed Fe_3O_4 nanoparticles, respectively (see Figure 5), identified as the blocking temperatures (T_B). These data clearly show that there is a temperature range in which magnetic hybrid fibrils show collective ferromagnetic behaviour that is unique due to their aggregation status, as was also the case for nanoparticle chains.[5c,21a] Nevertheless, superparamagnetism remains after T_B as a consequence of the anisotropic barrier blockage of the magnetisation orientation of the magnetic layer forming the hybrid fibril cooled with the ZFC process.[31] The larger T_B and the less steep slope for magnetite nanoparticles in the above figure could be consistent with: i) a larger dipolar coupling,[27,32] or ii) larger size and anisotropy in the dispersions as a result of some degree of aggregation between the particles, which involves a larger number of nearest neighbouring particles than in the case of magnetic wires and a non-regular distribution of the particles in the aggregates, in contrast to what would be expected in the 1D nanowires. This implies that dipolar interactions will not equally affect all particles in the nanoparticle aggregates, giving rise to the observed broadening in T_B.

From the relationship $T_B=K_aV/25k_B$ (in which K_a is the anisotropic constant, and k_B the Boltzmann constant), for uniaxial non-interacting magnetite nanoparticles with a diameter of 10 nm, T_B is found to be 20 K, in contrast to the values of about 35 K found for the nanowires and 105 K for dispersed nanoparticles, respectively. From this equation we can also derive an estimated value for the crystallite size in the hybrid fibrils and for the dispersed nanoparticles by use

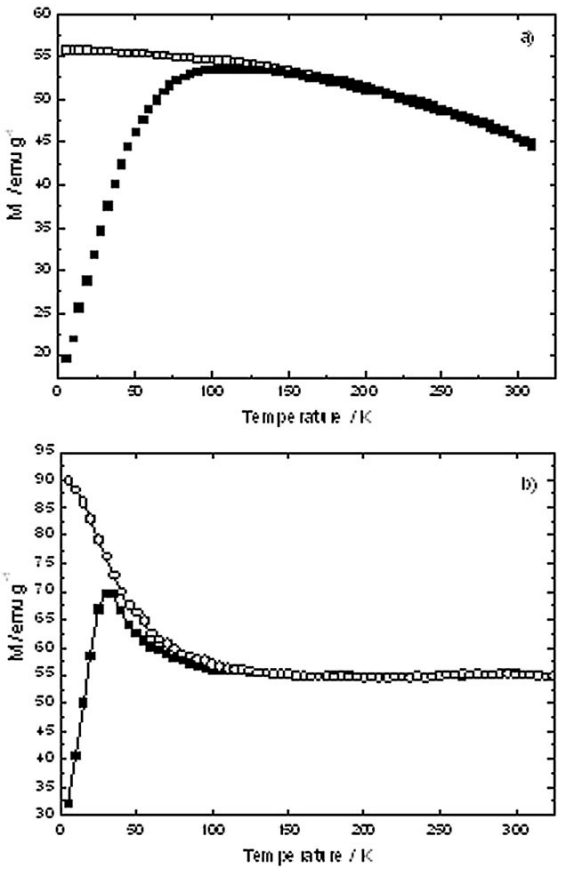

Figure 5. ZFC-FC plots for: a) dispersed magnetite nanoparticles, and b) fully covered magnetic nanowires at 5 K (closed symbols) and 300 K (open symbols). FC curves were obtained in the presence of a magnetic field of 500 Oe.

of a K_a value of 1.35×10^4 J m^{-3} corresponding to bulk magnetisation. In this way, the estimated sizes are about 12 and 16 nm, larger than those calculated from XRD data. Possible reasons for these differences might be the wide size distribution populations, the magnetic dipole interactions between nanowires and nanoparticles, the magnetic texture formed in nanowires due to strong shape anisotropy, the aggregation state in the dispersed nanoparticles or the disordered surface spins. These factors can have strong influences on magnetic properties and, therefore, on calculated sizes. Additionally, the effective magnetic anisotropy constants of Fe_3O_4 nanoparticles are normally less than its bulk value and vary with particle size.[29] All these factors lead to differences in the estimated particles sizes according to XRD and magnetic data.

To check the possible efficiency of the biohybrids as novel T_2 contrast agents, the relaxation times T_1 and T_2* were measured by NMR dispersion (NMRD) at 9.4 T (400 MHz proton Larmor frequency, 37 °C). The T_1 (spin–lattice) relaxation process is the result of the interaction between the excited nuclei and their surrounding environment, and the T_2*

(spin–spin) relaxation process of the interaction between the excited nuclei and those with lower energy. The efficiency of an MRI contrast agent is commonly assessed in terms of its relaxivities (r_1 and r_2), which are rates of proton relaxation determined by Equation (1):

$$1/T_{i,obs} = 1/T_{i,d} + r_i[M]\ (I = 1, 2) \quad (1)$$

in which $1/T_{i,obs}$ is the observed solvent relaxation rate in the presence of a contrast agent, $1/T_{i,d}$ is the relaxation rate of the pure diamagnetic solvent, and $[M]$ is the concentration of the contrast agent.[33] For a T_2 contrast agent, the higher the r_2*/r_1 ratio the better the contrast efficacy. The spin–spin and spin–lattice relaxation times weighted spin-echo MRI of the fully-covered hybrid nanofibrils are shown in Figure 6a and Figure S7 in the Supporting Information, respectively. As shown in the former, the fully covered fibrils exhibited much stronger enhancement in T_2*-weighted relaxation times than the dispersed magnetic nanoparticles at the same

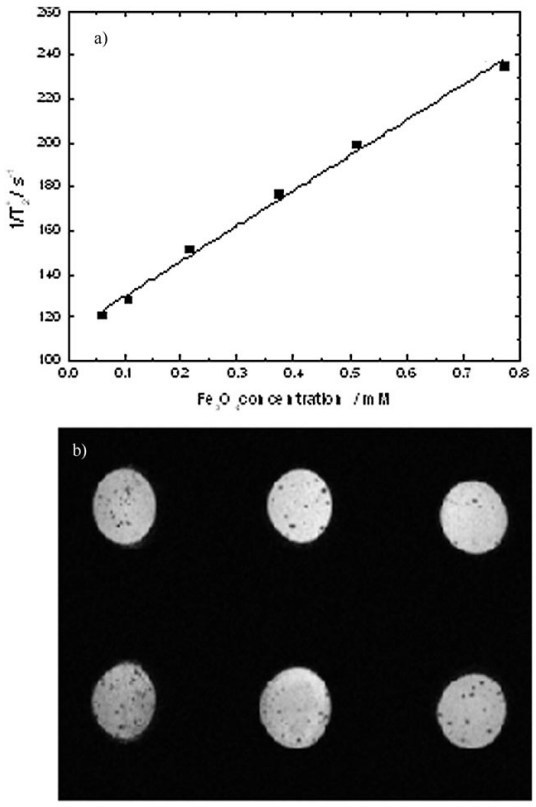

Figure 6. a) T_2 relaxation rates as a function of iron concentration (mM Fe) for fully covered magnetic nanowires obtained by fibril biotemplating; r_2* = 161 mM^{-1}s^{-1}. b) T_2*-weighted MR images of phantoms in the presence of different amounts of magnetic nanowires (expressed in Fe concentration). 1) 0.1×10^{-7}, 2) 0.2×10^{-7}, 3) 0.3×10^{-7}, 4) 0.5×10^{-7}, 5) 1×10^{-7} and 6) 2×10^{-7} M.

Fe concentration, with an r_2* value of 161 mM^{-1}s^{-1} (r_1 = 0.42 mM^{-1}s^{-1}) and an r_2*/r_1 ratio of about 390. The effect of the protein was found to be negligible. The former behaviour might be a result of the enhanced MR sensitivity due to clustering of individual magnetic nanocrystals on the fibrils.[34] Nevertheless, it is necessary to bear in mind that the large r_2*/r_1 ratio is a result of the different behaviour displayed by T_1 and T_2 with the applied magnetic field strength: both T_1 and T_2 generally increase at relatively low applied magnetic field, but T_1 reaches a maximum around 0.5–1.0 T and then drastically decreases at larger magnetic fields. In contrast, T_2 remains almost constant or even slightly increases at larger applied magnetic fields, so the r_2*/r_1 ratio definitely increases with applied magnetic field.[35] Thus, when comparing r_2*/r_1 ratios it is necessary to bear in mind the applied magnetic field at which the experiment was performed. Interestingly, the r_2* relaxivities of the hybrid fibrils are slightly larger than those obtained for DNA-templated magnetic nanowires,[11a] (bio)polymer-templated nanowires,[20,36] magnetic nanoworms[2d,10b] or conventional superparamagnetic iron oxide nanoparticles.[37] Such a strong T_2 shortening effect, typically from stronger magnetic susceptibility, leads to spin dephasing and substantial MRI drop, which generated a "darkening" contrast, as seen in the T_2*-weighted MR images of the hybrids in phantoms measured at 9.4 T in a preclinical MRI. The mean T_2* values of the phantoms get lower as the amount of fully covered nanofibrils increases in solution (seen as black spots in the images) even though the amount of Fe present is extremely small, which avoids full darkness of the image (Figure 6b). The increased MRI contrast observed for nanowires is the result of the increase in the susceptibility effects caused by the presence of Fe that can enhance spin–spin relaxation of water molecules caused by the slightly larger magnetisation value[38] and the 1D assembly.[39]

Conclusion

We report a method for obtaining magnetic Fe_3O_4 nanowires based on the use of HSA and Lys protein fibrils as bioscaffolds for generation of a complete magnetic Fe_3O_4 coating layer on the biotemplate surface by controlled Fe nanoprecipitation in situ in the presence of NH_4OH. To achieve full coverage of the protein fibrils a suitable initial [Fe]/[protein] molar ratio must be selected and a suitable number of sequential additions of Fe ions must be performed. If these requirements are not fulfilled, partial coverage and/or protein bundling and further fibril precipitation are observed. Thanks to their large saturation magnetisation, the 1-dimensional magnetic nanowires can serve as efficient MRI contrast agents, with transverse relaxivities larger than those obtained previously for other 1D nanostructures derived by different methods. Their capability as contrast agents was verified by obtaining several MRI images at different Fe concentrations in phantoms. In spite of the very low concentrations used, the hybrid nanowires

exhibit an important contrast imaging effect, which confirms their potential use as MRI contrast agents. Future work will involve the refinement of the synthetic process to achieve perfect control of magnetic coverage, and thus hybrid fibril widths, magnetic nanowire lengths, population distribution and in vivo assays.

Experimental Section

Materials: Human serum albumin, lysozyme, $FeCl_2$ and $FeCl_3$ were obtained from Sigma Chemical. Proteins were used after further purification by liquid chromatography over a Superdex 75 column equilibrated with phosphate (0.01 M). All other chemicals were of the highest purity available. Experiments were carried out with doubly distilled, deionised and degassed water.

Preparation of HSA and lysozyme fibril solutions: Protein fibril solutions were prepared by well-established protocols.[16] Briefly, HSA fibril stock solution was made by dissolving the protein to a final concentration typically of 2 mg mL^{-1} in phosphate buffer (pH 7.4, ionic strength 10 mM) and brought to pH 2.0 by addition of HCl. Lysozyme fibrils were obtained by forming a stock solution (2 mg mL^{-1}) in glycine buffer (pH 2.0, ionic strength 10 mM). Both protein stock solutions were dialysed extensively against pure buffer. Protein concentrations were determined spectrophotometrically, with use of molar absorption coefficients of 35219 and 37609 M^{-1} cm^{-1} at 280 nm for HSA and Lys, respectively.[40] Before incubation, the solutions were filtered through a 0.2 μm filter into sterile test tubes. Samples were incubated at 65 °C in a reactor under reflux for 10 and 3 days for HSA and Lys, respectively.

Characterisation of the fibrils: Protein suspensions were applied to carbon-coated copper grids, blotted, washed, negatively stained with phosphotungstic acid (2 %, w/v), air dried and then examined with a Phillips CM-12 transmission electron microscope operating at an accelerating voltage of 120 kV. Samples were diluted 20–200-fold when needed prior to deposition on the grids.

Magnetic nanowire synthesis: A stock solution (typically 2 g L^{-1}) of either lysozyme or HSA fibrils was diluted 600-fold to avoid the presence of undesired aggregates during the synthesis of the magnetite nanowire. Different [Fe]/[protein] molar ratios (10:1, 25:1 50:1, 100:1, 200:1 and 400:1) and sequential additions (one to five) of the iron salts were tested to enable the formation of magnetite nanoparticles on the biotemplate surface and to ensure full coverage of the fibril surface. In a typical synthesis, an aliquot (100 μL) of lysozyme fibril solution (2 g L^{-1}, 1.34×10^{-4} M) was placed in a flask reactor and diluted with doubly distilled, deionised water (60 mL). Fibril solution was left to incubate at 65 °C for 1 h with magnetic stirring. Separately, two aqueous solutions containing $FeCl_2$ (25.4 mg, 0.1 M) and $FeCl_3$, respectively, (64.9 mg, 0.1 M) were prepared and mixed in a 1:2 molar ratio. After the incubation period at 65 °C, the temperature of the fibril solution was raised to 80 °C, and a specific volume of the iron salt mixed solution suitable to get the desired [Fe]/[protein] molar ratio was then added under nitrogen. The solution was left to incubate for 3 h before the addition of NH_4OH (1.5 M, 2 mL); the resulting solution was allowed to react for an additional 1 h and allowed to cool to room temperature. Stabilisation of the nanowires was additionally achieved by addition of sodium citrate solution (10 mM, 1 mL) to the resulting nanowires at 80 °C and allowing to incubate for 90 min. The resulting biohybrid solution was dialysed through a dialysis membrane (SpectraPor, Netherlands, 100 kDa) to remove remaining iron salts, NH_4OH and sodium citrate. If required, fresh additions of the same volume of Fe salt solutions were carried out under the same conditions as previously specified to ensure the full magnetic coverage of fibrils and to create a nanowire.

Characterisation of magnetic 1D assemblies and nanowires: TEM images were obtained with a transmission electron microscope (Phillips CM-12) operating at an accelerating voltage of 120 kV as previously described. HR-TEM images and SAED patterns were obtained with a transmission electron microscope (Carl-Zeiss Libra 200 FE-EFTEM) operating at 200 kV. X-ray diffraction experiments were carried out with a rotating anode X-ray generator (Siemens D5005). Twin Göbel mirrors were used to produce a well-collimated beam of $Cu_{K\alpha}$ radiation ($\lambda = 1.5418$ A). X-ray diffraction patterns were recorded with an imaging plate detector (AXS F.Nr. J2–394). FTIR spectra of HSA in aqueous solutions were determined with a FTIR spectrometer (model IFS-66v from Bruker) with a horizontal ZnS ATR accessory. The spectra were obtained at a resolution of 2 cm^{-1} and generally 200 scans were accumulated to provide a reasonable signal-to-noise ratio. Magnetic susceptibility measurements were carried out with a SQUID magnetometer (Quantum Design MPMS5, San Diego, CA). Iron concentrations of each sample for SQUID, relaxivity and MRI were determined by inductively coupled plasma atomic emission spectroscopy (ICP-AES, Varian).

Magnetic resonance measurements and MRI imaging: Transverse and longitudinal relaxation times were also measured at 9.4 T (400 MHz) and 37 °C with a Bruker Biospin USR94/20 instrument (Ettlingen, Germany). An inversion-recovery pulse sequence was used to measure the longitudinal relaxation times with 16 inversion recovery times logarithmically spaced. Both Carr–Purcell–Meiboom–Gill (CPMG) and spin-echo pulse sequences were used to measure transverse relaxation times. MRI phantoms were constructed in agarose solutions (Sigma–Aldrich, 4 %, w/v), heated and stirred at 80 °C until complete solution of the solid agarose. Then, with the system still remaining fluid, six HPLC vials (Cromlab, Spain, 250 μL) were filled with the agarose solution (100 μL) and allowed to cool to room temperature. Protein solution (5, 10, 15, 25, 50 or 100 μL) was then deposited over the surfaces of the agarose gels, and distilled water (49, 45, 40, 35, 25 and 0 μL, respectively) was added to the solutions to make the final volumes even at 150 μL per vial. After a waiting period of at least 30 min, most of the deposited fluid had been absorbed by the agarose gels, after which semi-gelificated agarose solution (50 μL, 10 %, w/v, heated to 80 °C for solution and cooled to about 40–50 °C before addition) was added to each phantom to seal them. Imaging of the phantoms was performed with the previously described Bruker Biospin system with 440 mT m^{-1} gradients. A 3D-Gradient Echo image was acquired (T_2*-weighting) with the following parameters: field of view: $28.8\times19.2\times2$ mm, matrix size: $288\times192\times40$ points giving a spatial resolution of $100\times100\times200$ μm, echo time TE = 8 ms, repetition time TR = 100 ms and flip angle = 30.

Acknowledgements

The authors thank the Ministerio de Ciencia e Innovación (MICINN) for research project MAT 2010–17336, the Xunta de Galicia for research project INCITE09206020PR and for European Regional Development Funds (research project 2010/50), and the Fundación Ramón Areces for additional financial support. We acknowledge the contributions of B. Argibay, P. Ramos-Cabrer and J. Castillo from the Clinical Neurosciences Research Laboratory of the Clinical Hospital of Santiago de Compostela for the MR images acquired with the 9.4 T MR system.

[1] Y. N. Xia, P. D. Yang, Y. G. Sun, Y. Y. Wu, B. Mayers, B. Gates, Y. D. Yin, F. Kim, Y. Q. Yan, *Adv. Mater.* **2003**, *15*, 353–389.
[2] a) C. Ross, *Annu. Rev. Mater. Res.* **2001**, *31*, 203–235; b) J. M. Kinsella, A. Ivanisevic, *J. Phys. Chem. C* **2008**, *112*, 3191–3193; c) C. Goubault, P. Jop, M. Fermigier, J. Baudry, E. Bertrand, J. Bibetter, *Phys. Rev. Lett.* **2003**, *91*, 260802; d) J.-H. Park, G. von Maltzahn, L. Zhang,, M. P. Schwartz, E. Ruoslathi, S. N. Bathia, M. J. Sailor, *Adv. Mater.* **2008**, *20*, 1630–1635.
[3] S. Minko, A. Kiriy, G. Gorodyska, M. Stamm, *J. Am. Chem. Soc.* **2002**, *124*, 10192.
[4] a) N. Duxin, F. T. Liu, H. Vali, A. Eisenberg, *J. Am. Chem. Soc.* **2005**, *127*, 10063–10069; b) Y. Piao, J. Kim, H. B. Na, D. Kim, J. S. Baek, M. K. Ko, J. H. Lee, M. Shokouhimehr, T. Hyeon, *Nat. Mater.* **2008**, *7*, 242–247.

[5] a) V. Salgueiriño-Maceira, M. A. Correa-Duarte, M. Bañobre-López, M. Grzelczak, M. Farle, L. M. Liz-Marzán, J. Rivas, *Adv. Funct. Mater.* **2008**, *18*, 616–621; b) M. L. Górzny, A. S. Walton, S. D. Evans, *Adv. Funct. Mater.* **2010**, *20*, 1295–1300; c) K. Nakata, Y. Hu, O. Uzun, O. Bakr, F. Stellacci, *Adv. Mater.* **2008**, *20*, 4294–4299; d) S. H. Sun, *Adv. Mater.* **2006**, *18*, 393–403; e) L. Fu, X. G. Liu, Y. Zhang, V. P. Dravid, C. A. Mirkin, *Nano Lett.* **2003**, *3*, 757–760; f) S. Palacin, P. C. Hidber, J. P. Bourgoin, C. Miramond, C. Fermon, G. M. Whitesides, *Chem. Mater.* **1996**, *8*, 1316–1325.
[6] a) H. Wang, A. J. Patil, S. Petrov, S. Mann, M. A. Winnik, I. Manners, *Adv. Mater.* **2009**, *21*, 1805–1808; b) J. Fresnais, J.-F. Berret, B. Frka-Petesic, O. Sandre, R. Perzynski, *Adv. Mater.* **2008**, *20*, 3877–3881; c) K. Keren, M. Krueger, R. Girald, G. Ben-Yoseph, U. Sivan, E. Braun, *Science* **2002**, *297*, 72–75.
[7] a) L. W. Yin, Y. Bando, Y. C. Zhu, D. Goldberg, M. S. Li, *Adv. Mater.* **2004**, *16*, 929–933; b) J. Sharma, R. Chiabra, A. Cheng, J. Brownell, Y. Liu, H. Yan, *Science* **2009**, *323*, 112–116; c) T. Kodama, A. Jain, K. E. Goodson, *Nano Lett.* **2009**, *9*, 2005–2009.
[8] a) N. C. Bigall, M. Reitzig, W. Naumann, P. Simon, K.-H. Van Pée, A. Eychmüller, *Angew. Chem.* **2008**, *120*, 7994–7997; *Angew. Chem. Int. Ed.* **2008**, *47*, 7876–7879; b) S. Banerjee, M. G. C. Kahn, S. S. Wong, *Chem. Eur. J.* **2003**, *9*, 1898–1908; c) W. Q. Han, A. Zettl, *Nano Lett.* **2003**, *3*, 681–683; d) M. B. Dickerson, K. H. Sandhage, R. R. Naik, *Chem. Rev.* **2008**, *108*, 4935–4978.
[9] S. S. Behrens, *J. Mater. Chem.* **2008**, *18*, 3788–3798.
[10] a) D. Walsh, L. Arcelli, T. Ikoma, J. Tanaka, S. Mann, *Nat. Mater.* **2003**, *2*, 386–390; b) J.-H. Park, G. von Maltzahn, L. Zhang, A. M. Derfus, D. Simberg, T. J. Harris, E. Ruoslathi, S. N. Bathia, M. J. Sailor, *Small* **2009**, *5*, 694–700.
[11] a) S. J. Byrne, S. A. Corr, Y. K. Gun'ko, J. M. Kelly, D. F. Brougham, S. Ghosh, *Chem. Commun.* **2004**, 2560–2561; b) J. M. Kinsella, A. Ivanisevic, *Langmuir* **2007**, *23*, 3886–3890; c) Q. Gu, D. T. Haynie, *Mater. Lett.* **2008**, *62*, 3047–3050.
[12] a) M. Allen, J. W. M. Bulte, L. Liepold, G. Basu, H. A. Zywicke, J. A. Frank, M. Young, T. Douglas, *Magn. Reson. Med.* **2005**, *54*, 807–812; b) A. A. Martinez-Morales, N. G. Portney, Y. Zhang, G. Destito, G. Budak, E. Ozbay, M. Manchester, C. S. Ozkan, M. Ozkan, *Adv. Mater.* **2008**, *20*, 4816–4820.
[13] I. A. Banerjee, L. Yu, M. Shima, T. Yoshino, H. Takeyama, T. Matsunaga, H. Matsui, *Adv. Mater.* **2005**, *17*, 1128–1131.
[14] a) R. Tsukamoto, M. Muraoka, M. Seki, H. Tabata, I. Yamashita, *Chem. Mater.* **2007**, *19*, 2389–2391; b) M. Knez, A. M. Bittner, F. Boes, C. wege, H. Jeske, E. Maiß, K. Kern, *Nano Lett.* **2003**, *3*, 1079–1082.
[15] a) C. M. Dobson, *Nature* **2003**, *426*, 884–890; b) I. Cherny, E. Gazit, *Angew. Chem.* **2008**, *120*, 4128–4136; *Angew. Chem. Int. Ed.* **2008**, *47*, 4062–4069; c) T. R. Jahn, S. E. Radford, *Arch. Biochem. Biophys.* **2008**, *469*, 100–117.
[16] a) P. Taboada, S. Barbosa, E. Castro, V. Mosquera, *J. Phys. Chem. B* **2006**, *110*, 20733–20736; b) J. Juárez, P. Taboada, V. Mosquera, *Biophys. J.* **2009**, *96*, 2353–2370; c) E. Frare, P. P. De Laureto, J. Zurdo, C. M. Dobson, A. Fontana, *J. Mol. Biol.* **2004**, *340*, 1153–1165; d) A. P. Pawar, K. F. Dubai, J. Zurdo, F. Chiti, M. Vendruscolo, C. M. Dobson, *J. Mol. Biol.* **2005**, *350*, 379–392; e) V. H. Lieu, J. W. Wu, S. S. S. Wang, C. H. Wu, *Biotechnol. Prog.* **2007**, *23*, 698–706.
[17] T. Peters, Jr., *All About Albumin: Biochemistry Genetics, and Medical Applications*, Academic Press, New York, **1996**.
[18] a) W. J. Crookes-Goodson, J. M. Slocik, R. N. Naik, *Chem. Soc. Rev.* **2008**, *37*, 2403–2412; b) N. Ostrov, E. Gazit, *Angew. Chem.* **2010**, *122*, 3082–3085; *Angew. Chem. Int. Ed.* **2010**, *49*, 3018–3021; c) M. Malisauskas, R. Meskys, L. A. Morozova-Roche, *Biotechnol. Prog.* **2008**, *24*, 1166–1170.
[19] L. Yu, I. A. Banerjee, M. Shima, K. Rajan, H. Matsui, *Adv. Mater.* **2004**, *16*, 709–712.
[20] S. R. Bull, M. O. Guller, R. A. Bras, T. J. Meade, S. I. Stupp, *Nano Lett.* **2005**, *5*, 1–4.
[21] S. Ghosh, A. Mukherjee, P. J. Sadler, S. Verma, *Angew. Chem.* **2008**, *120*, 2249–2253; *Angew. Chem. Int. Ed.* **2008**, *47*, 2217–2221.
[22] Y. Sahoo, A. Goodarzi, M. T. Swihart, T. Y. Ohulchanskyy, N. Kaur, E. P. Furlani, P. N. Prasad, *J. Phys. Chem. B* **2005**, *109*, 3879–3885.
[23] P. Dutta, A. Manivannan, M. S. Seehra, N. Shah, G. P. Huffman, *Phys. Rev. B* **2004**, *70*, 174428.
[24] I. Martínez-Mera, M. E. Espinosa-Pesqueira, R. Pérez-Hernández, J. Arenas-Alatorre, *Mater. Letters.* **2007**, *61*, 4447–4451.
[25] J. Wan, W. Cai, J. Feng, X. Meng, E. Liu, *J. Mater. Chem.* **2007**, *17*, 1188–1192.
[26] a) H. Wang, Q.-W. Chen, L.-X. Sun, H.-p. Qi, X. Yang, S. Zhou, J. Xiong, *Langmuir* **2009**, *25*, 7135–7139; b) T. J. Daou, G. Pourroy, S. Bégin-Colin, J. M. Grenèche, C. Ulhaq-Bouillet, P.- Legaré, P. Bernhardt, C. Leuvrey, G. Rogez, *Chem. Mater.* **2006**, *18*, 4399–43404.
[27] a) A. F. Gross, M. R. Diehl, K. C. Beverly, E. K. Richman, S. H. Tolbert, *J. Phys. Chem. B* **2003**, *107*, 5475–5482; b) D. Baldomir, D. Serantes, M. Pereiro, J. Botana, J. E. Arias, S. H. Masunaga, J. Rivas, *J. Nanosci. Nanotechnol.* **2010**, *10*, 2717–2721.
[28] D. H. Han, H. L. Wang, J. Luo, *J. Magn. Magn. Mater.* **1994**, *136*, 176–182.
[29] G. F. Goya, T. S. Berquó, F. C. Fonseca, M. P. Morales, *J. Appl. Phys.* **2003**, *94*, 3520–3528.
[30] J. Qin, S. Laurent, Y. S. Jo, A. Roch, M. Mikhaylova, Z. M. Bhujwalla, R. N. Muller, M. Muhammed, *Adv. Mater.* **2007**, *19*, 1874–1878.
[31] Y. Wang, Y. W. Ng, Y. Chen, B. Shuter, J. Yi, J. Ding, S.-c. Wang, S.-S. Feng, *Adv. Funct. Mater.* **2008**, *18*, 308–318.
[32] L. Zhang, Y. Zhang, *J. Magn. Magn. Mater.* **2009**, *321*, L15–L20.
[33] N. Bloembergen, E. M. Purcell, R. V. Pound, *Phys. Rev.* **1948**, *73*, 679–712.
[34] J. F. Berret, N. Schonbeck, F. Gazeau, D. El Kharrat, O. Sandre, A. Vacher, M. Airiau, *J. Am. Chem. Soc.* **2006**, *128*, 1755–1761.
[35] P. Caravan, C. T. Farrar, L. Frullano, R. Uppal, *Contrast Media Mol. Imaging* **2009**, *4*, 89–100.
[36] a) S. A. Corr, S. J. Byrne, R. Tekoriute, C. J. Meledandri, D. F. Brougham, M. Lynch, C. Kerskens, L. O'Dwyer, Y. K. Gun'ko, *J. Am. Chem. Soc.* **2008**, *130*, 4214–4215; b) M. Y. Shin, S. I. Kim, S. J. Lee, K. E. Lee, S.-S. Han, D.-P. Jang, Y.-B. Kim, Z.-H. Cho, I. So, G. M. Spinks, *Langmuir* **2008**, *24*, 12107–12111.
[37] H. B. Na, I. C. Song, T. Hyeon, *Adv. Mater.* **2009**, *21*, 2133–2148.
[38] J. H. Lee, Y. M. Huh, Y. Jun, J. Seo, J. Jang, H. T. Song, S. Kim, E. J. Cho, H. G. Yoon, J. S. Suh, J. Cheon, *Nat. Med.* **2006**, *13*, 95–99.
[39] J. M. Perez, L. Josephson, T. O'Loughlin, D. Hogemann, R. Weissleder, *Nat. Biotechnol.* **2002**, *20*, 816–820.
[40] a) C. N. Pace, F. Vajdos, L. Fee, G. Grimsley, T. Gray, *Protein Sci.* **1995**, *4*, 2411–2423; b) T. Knubovets, J. J. Osterhout, P. J. Connolly, A. M. Klibanov, *Proc. Natl. Acad. Sci. USA* **1999**, *96*, 1262–1267.

Received: December 20, 2010
Revised: March 7, 2011
Published online: May 6, 2011

6.7.- Relevant aspects on the HSA fibril formation

I. HSA has the ability to self-assemble into amyloid-like aggregates under different solution conditions, i.e., under both physiological and acidic pH at elevated temperature and different ionic strengths. Under these solution conditions, the HSA native state is destabilized generating partially folded states that can aggregate to form fibrils.

II. At physiological pH, fibrillation is progressively faster and more efficient in the presence of up to 50 mM NaCl due to electrostatic shielding. ThT fluorescence, CD, FT-IR and Trp fluorescence spectra confirm the structural changes in both tertiary and secondary structure along the HSA fibrillation process. In this way, large extents of β-sheet structure at large salt concentrations are also corroborated from the analysis of far UV-CD spectra.

III. Under acidic conditions, a progressive enhancement of HSA fibrillation is observed as electrolyte concentration in solution increases.

IV. The fibrillation process of HSA does not show a lag-phase growth, except at acidic pH in the absence of NaCl. The HSA fibrillation is a downhill process which does not require a highly organized and unstable nucleus, with a progressive increase of the β-sheet (up to 26%) and an unordered conformation at the expense of the α-helical conformation.

V. The fibrils obtained show a curly morphology and differ in length. Besides, suprafibrillar assemblies (spherulites and fibrillar gels) formed by the protein human serum albumin under different solution conditions.

VI. Upon incubation at 65 ^{0}C at both acidic (pH 2.5) and physiological (pH 7.4) pH in the presence of different amounts of added electrolyte, suprafibrillar assemblies, spherulites and fibrillar gels, are formed under different solution conditions. Fibrillar gels are formed through intermolecular nonspecific association of amyloid fibrils. Meanwhile, at a pH close to the isoelectric point of HSA (pH 5.5), particulate gels were observed as a consequence of a faster protein aggregation, which does not allow the necessary structural reorganization to enable the formation of more ordered structures.

VII. Within spherulites, fibrils display a radial arrangement around a disorganized protein core with sizes of several micrometers, as revealed by POM and confocal microscopy.

VIII. Protein structure destabilization and subsequent aggregation (into amorphous or well-defined structured aggregates) were conditioned by the experimental pH,

temperatures, and solvent polarity.

IX. Ethanol regulated the hydrogen bonding extension, the attractive hydrophobic interactions, and the protein accessible surface area which, in turn, give rise to intermediate structural states prone to form aggregate.

X. The HSA aggregation rate at physiological condition is faster than under acidic one owing to the pre-existing structural differences of the protein molecules in solution and to changes in the nature and strength of intermolecular interaction upon incubation.

XI. Ethanol promoted an α-helix to β-sheet conformational transition at intermediate alcohol concentrations, whereas at low and high ethanol contents α-helix prevailed as the predominant structure at room temperature and physiological pH.

XII. Electrostatic and hydrophobic interactions are important to control stacking of β-sheets favouring the formation of amyloid-like fibrils at physiological pH and high temperature.

6.8.- Relevant aspects on the gold and magnetic nanowires

I. We report a method to obtain metallic Au nanowires by using Lys protein fibrils as bioscaffolds. The metallic coverage of nanofibrils could be easily controlled by changing the numbers of sequential additions of gold growth solution into the fibril solution overall already preformed Au nanocrystals. In this way, a continuous coverage of the fibril surface is obtained as a result of the growth of pre-existing nanoparticles and generation of new ones on the fibrils surface and subsequent fusion of adjacent as-synthesized nanoparticles.

II. UV-Vis spectra results showed that the hybrid fibrils can successfully catalyze the reduction reaction from *p*-nitrophenol to p-aminophenol by $NaBH_4$. Moreover, the fibril metallic fibrils provide larger reaction rates values 1.5-4 than other hybrid materials reported, previously, as for example glucose-reduced Au nanoparticle networks, PAMAM-dendrimer-supported spherical nanoparticles amongst others.

III. On the other hand, we report a method for obtaining magnetic Fe_3O_4 nanowires based on the use of HSA and Lys protein fibrils as bioscaffolds for generation of a complete magnetic coating layer on the biotemplate surface by controlled Fe nanoprecipitation *in situ* in the presence of NH_4OH.

IV. Thanks to their large saturation magnetization, the 1D magnetic nanowires can serve

as efficient MRI contrast agents, with transverse relaxivities larger than those obtained previously for other 1D nanostructures derived from different methods. Their capability as contrast agents was verified by obtaining MRI images at different Fe concentrations in phantoms.

Conclusions

The work has two parts: The first one was focused on the characterization of three block copolymers ($EO_{12}SO_{10}$, $EO_{10}SO_{10}EO_{10}$, and $EO_{137}SO_{18}EO_{137}$), meanwhile the second part was dedicated to the study of the fibrillation of the protein human serum albumin that was cover with gold and magnetic nanoparticles.

The general conclusions are:

1. - Characterization of the block copolymers $EO_{12}SO_{10}$, $EO_{10}SO_{10}EO_{10}$, y $EO_{137}SO_{18}EO_{137}$, in solution at the air/water and chloroform/water interfaces.

   I. For $E_{12}S_{10}$ dilute solutions, the coexistence of spherical micelles with vesicular structures has been observed. In addition, the spontaneous formation of vesicles by poly(oxystyrene)-poly(oxyethylene) block copolymers is reported for the first time, as confirmed by light scattering, polarized light microscopy, and transmission and cryo-scanning electron microscopy data.

   II. In dilute solution, the self-assembly of copolymer $E_{10}S_{10}E_{10}$ leads to the formation of elongated micelles as supported by light scattering and transmission electron techniques.

   III. In the case of copolymer $E_{137}S_{18}E_{137}$, typical spherical micelles are observed. Tube inversion and rheological measurements were used to define the sol- soft- and gel-hard boundaries of this copolymer.

   IV. $E_{12}S_{10}$ and $E_{10}S_{10}E_{10}$ copolymers did not form gels in the concentration range analysed. However, only certain concentrations of copolymer $E_{10}S_{10}E_{10}$ were analysed by rheometry. From experimental data, an upturn in the low-frequency range of the stress moduli was observed, denoting the existence of an emerging slow process, which was assigned to the formation of an elastic network.

   V. Block copolymers $E_{12}S_{10}$, $E_{10}S_{10}E_{10}$ and $E_{137}S_{18}E_{137}$ showed spontaneous adsorption at the air-water interface, which slowed down when the hydrophobicity of the molecule was increased. In contrast, at the chloroform/water interface no measurable effect is observed for copolymer $E_{12}S_{10}$ due to the slow diffusion of its chains to the interface in

combination with a low bulk concentration; this slow diffusion is associated with the fact that chloroform is a good solvent for both E and S blocks.

VI. Copolymer $E_{137}S_{18}E_{137}$ displays an adsorption isotherm with the four classical regions representing the pancake, mushroom, brush and condensed states; the presence of a pseudo-plateau is attributed to the pancake-to-brush transition as E chains submerge into the aqueous sub-phase. On the other hand, for $E_{12}S_{10}$ and $E_{10}S_{10}E_{10}$ copolymers only two regions are observed in their adsorption isotherms as a consequence of their low molecular weights, short S and E block lengths, and much larger S/E ratio. This involves the disappearance of the pseudo-plateau region due to the decrease in the fractional interfacial area occupied by EO segments.

VII. According to AFM images, circular micelles are observed on Langmuir-Blodgett films of the copolymers obtained at two surface transfer pressures. A decrease in micelle size and an increase in monolayer thickness are observed with increases in transfer pressure. Aggregation numbers derived from AFM images increase with the increase of the S weight fraction at a certain deposition pressure, which can be a consequence of stronger attractive interactions between the S blocks to avoid contact with the solvent.

2. - On the HSA fibrillation:

I. HSA has the ability to self-assemble into amyloid-like aggregates under different solution conditions, i.e., under both physiological and acidic pH at elevated temperature and different ionic strengths and solvent compositions. Under these solution conditions, the HSA native state is destabilized generating partially folded states that can aggregate to form fibrils.

II. At physiological pH, fibrillation is progressively faster and more efficient in the presence of up to 50 mM NaCl due to electrostatic shielding. ThT fluorescence, CD, FT-IR and Trp fluorescence spectra confirm the structural changes in both tertiary and secondary structure along the HSA fibrillation process. In this way, large extents of β-sheet structure at large salt concentrations are also corroborated from the analysis of far UV-CD spectra.

III. Under acidic conditions, a progressive enhancement of HSA fibrillation is observed as electrolyte concentration in solution increases.

IV. The fibrillation process of HSA does not show a lag-phase growth, except at acidic pH in the absence of NaCl. The HSA fibrillation is a downhill process which does not

require a highly organized and unstable nucleus, with a progressive increase of the β-sheet (up to 26%) and an unordered conformation at the expense of the α-helical conformation.

V. The fibrils obtained show a curly morphology and differ in length. Besides, suprafibrillar assemblies (spherulites and fibrillar gels) formed by the protein human serum albumin under different solution conditions.

VI. Upon incubation at 65 ^{0}C at both acidic (pH 2.5) and physiological (pH 7.4) pH in the presence of different amounts of added electrolyte, suprafibrillar assemblies, spherulites and fibrillar gels, are formed under different solution conditions. Fibrillar gels are formed through intermolecular nonspecific association of amyloid fibrils. Meanwhile, at a pH close to the isoelectric point of HSA (pH 5.5), particulate gels were observed as a consequence of a faster protein aggregation, which does not allow the necessary structural reorganization to enable the formation of more ordered structures.

VII. Within spherulites, fibrils display a radial arrangement around a disorganized protein core with sizes of several micrometers, as revealed by POM and confocal microscopy.

VIII. Protein structure destabilization and subsequent aggregation (into amorphous or well-defined structured aggregates) were conditioned by the experimental pH, temperatures, and solvent polarity.

IX. Ethanol regulated the hydrogen bonding extension, the attractive hydrophobic interactions, and the protein accessible surface area which, in turn, give rise to intermediate structural states prone to form aggregate.

X. The HSA aggregation rate at physiological condition is faster than under acidic one owing to the pre-existing structural differences of the protein molecules in solution and to changes in the nature and strength of intermolecular interaction upon incubation.

XI. Ethanol promoted an α-helix to β-sheet conformational transition at intermediate alcohol concentrations, whereas at low and high ethanol contents α-helix prevailed as the predominant structure at room temperature and physiological pH.

XII. Electrostatic and hydrophobic interactions are important to control stacking of β-sheets favouring the formation of amyloid-like fibrils at physiological pH and high temperature.

3. - On the metal and magnetic nanowires :

I. We report a method to obtain metallic Au nanowires by using Lys protein fibrils as

bioscaffolds. The metallic coverage of nanofibrils could be easily controlled by changing the numbers of sequential additions of gold growth solution into the fibril solution overall already preformed Au nanocrystals. In this way, a continuous coverage of the fibril surface is obtained as a result of the growth of pre-existing nanoparticles and generation of new ones on the fibrils surface and subsequent fusion of adjacent as-synthesized nanoparticles.

II. UV-Vis spectra results showed that the hybrid fibrils can successfully catalyze the reduction reaction from *p*-nitrophenol to p-aminophenol by $NaBH_4$. Moreover, the fibril metallic fibrils provide larger reaction rates values 1.5-4 than other hybrid materials reported, previously, as for example glucose-reduced Au nanoparticle networks, PAMAM-dendrimer-supported spherical nanoparticles amongst others.

III. On the other hand, we report a method for obtaining magnetic Fe_3O_4 nanowires based on the use of HSA and Lys protein fibrils as bioscaffolds for generation of a complete magnetic coating layer on the biotemplate surface by controlled Fe nanoprecipitation *in situ* in the presence of NH_4OH.

IV. Thanks to their large saturation magnetization, the 1D magnetic nanowires can serve as efficient MRI contrast agents, with transverse relaxivities larger than those obtained previously for other 1D nanostructures derived from different methods. Their capability as contrast agents was verified by obtaining MRI images at different Fe concentrations in phantoms.

References

1. **Hiemenz, Paul C.** *Polymer Chemistry: The basic consepts.* New York: Marcel Dekker, Inc., 1984. 0-8247-7082-X.

2. **Ebewele, R. O.** *Polymer science and technology.* New York: CRC Press, 2000.

3. **Sun, S. F.** *Physical Chemistry of Macromolecules: Basic principles and issues.* New York: John Wiley & Sons, Inc., 2004. 0-471-28138-7.

4. **Berg, J. M.; Tymoczko, J. L.; Stryer, L.; Clarke, N. D.** *Biquímica.* Barcelona: Editorial Reverté, S. A., 2003.

5. **Vicent, María C.; Álvarez, Silvia; Zaragozá, José L.** *Ciencia y tecología de Polímeros.* Valencia : Universdiad Politécnica de Valencia, 2006.

6. *Beyond molecules: Self-assembly of mesoscopic and macroscopic components.* **Whitesides, G. M.; Boncheva, M.** 2002, PNAS, Vol. 99, pp. 4769-4774.

7. **Rao, C. N. R.; Müller, A.; Cheetham, A. K.** *Nanomaterials chemistry: recent developments and new directions.* Weinheim : WILEY-VCH, 2007.

8. *Self-assembling materials for therapeutic delivery.* **Branco, M. C.; Schneider, J. P.** 2009, Acta Biomaterialia, Vol. 5, pp. 817-831.

9. *Directing the self-assembly of block copolymers.* **Darling, S. B.** 2007, Prog. Pol. Sci., Vol. 32, pp. 1152-1204.

10. *Solution self-assembly of tailor-made macromolecular building blocks prepared by controlled radical polymerization techniques.* **Lutz, Jean F.** 2006, Polym Int, Vol. 55, pp. 979-993.

11. *Self-Assembly at All Scales.* **Whitesides, George M.; Grzybowski, Bartosz.** 2002, Science, Vol. 295, pp. 2418-2421.

12. **Rotello, V. M.; Thayumanavan, S.** *Molecular recognitionand polymers: Control of polymer structure and self-assembly.* Hoboken, New Jersey: John Wiley & Sons, Inc., 2008.

13. *Bottom-up Nanoelectronics.* **Hadley, Peter.** Amsterdam: 34 European Microwave Conference, 2004, pp. 141-145.

14. *Technologies for nanofluidic systems: top-down vs. bottom-up—a review.* **Mijatovic, D.; Eijkel, J. C. T.; van den Berg, A.** 2005, Lab Chip 5, Vol. 5, pp. 492-500.

15. **Hamley, I. W.** *Block copolymers in solutions: fundamentals and application.* John Wiley & Sons, Ltd, 2005.

16. **Hiemenz, P. C.; Rajagopalan, R.** *Principles of Colloid and Surface Chemistry.* New York: Marcel Dekker, 1997.

17. **Hamley, I. W.** *Introduction to soft matter: synthetic and biological self-assembling materials.* Chichester: John Wiley & Sons, Ltd, 2007.

18. **Petty, M. C.** *Langmuir-blodgett films: an introduction.* Cambridge: Cambridge University Press, 1996.

19. **Adamson, A. W.; Gast, A. P.** *Physical chemistry of surfaces.* 6th ed. New York: John Wiley & Sons, Inc., 1997.

20. *Dynamic surface tension and dilational viscoelasticity of adsorption layers of a hydrophobically modified chitosan.* **Babak, Valery G.; Desbrièresb, Jacques; Tikhonova, Vladimir E.** 2005, Colloids and Surfaces A: Physicochem. Eng. Aspects, Vol. 255, pp. 119-130.

21. *Adsorption kinetics of hydrophobic polysoaps at the methylene chloride–water interface.* **Babak, Valery; Boury, Frank.** 2004, Colloids and Surfaces A: Physicochem. Eng. Aspects, Vol. 243, pp. 33-42.

22. *Dilational viscoelasticity and relaxation properties of interfacial electrostatic complexes between oppositely charged hydrophobic and hydrophilic polyelectrolytes.* **Babak, V. G.; Barosb, F.; Desbrièresd, J.** 2008, Colloids and Surfaces B: Biointerfaces, Vol. 65, pp. 43-49.

23. **Schärtl, Wolfgang.** *Light Scattering from Polymer Solutions and Nanoparticles Dispersions.* Berlin: Springer, 2007.

24. **Berne, B. J.; Pecora, R.** *DYNAMIC LIGHT SCATTERING: with application to chemistry, biology, and physics.* New York: John Wiley & Sons, INC., 2000.

25. **Xu, R.** *Particle characterization: light scattering methods.* New York: Kluwer Academic Publishers, 2002.

26. **Teraoka, I.** *Polymer Solutions: An Introduction to Physical Properties. Iwao Teraoka.* Brookling: John Wiley & Sons, Inc, 2002.

27. *Some applications of light scattering in materials science.* **Holoubek, J.** 2007, Journal of Quantitative Spectroscopy & Radiative Transfer, Vol. 106, pp. 104-121.

28. **Uchegbu, I. F.; Schätzlein, A. G.** *Polymer in drug delivery.* Boca Raton: Taylor & Francis, 2006.

29. **Young, R. J.; Lovell, P. A.** *Introduction to polymers.* London: Chapman & Hall, 1991.

30. **Huglins, M. B.** *Ligth scattering from polymer solution.* New York: Plenum Press, 1972.

31. **Kokhanovsky, A. A.** *Light Scattering Reviews 4: single light scattering and radiative transfer.* Chichester: Praxis Publishing, 2009.

32. *Static and dynamic light scattering of biological macromolecules: what can we learn?* **Murphy, R. M.** 1997, Current Opinion in Biotechnology, Vol. 8, pp. 25-30.

33. **Wang, Z. L.** *HANDBOOK OF MICROSCOPY FOR NANOTECHNOLOGY.* Boston: KLUWER ACADEMIC PUBLISHERS, 2005.

34. *Electron Diffraction Using Transmission Electron Microscopy.* **Bendersky, L. A.; Gayle, F. W.** 2001, J. Res. Natl. Inst. Stand. Technol., Vol. 106, pp. 997-1012.

35. **van Dyck, S. A.; van Landuyt, D. J.; van Tendeloo, G.** *Electron Microscopy: Principles and Fundamentals.* VCH, 1997.

36. **Yao, N.; Wang, Z. L.** *HANDBOOK OF MICROSCOPY FOR NANOTECHNOLOGY.* BOSTON: KLUWER ACADEMIC PUBLISHERS, 2005.

37. **Goldstein, J. I.; Newbury, D. E.; Echlin, P.; Joy, D. C.; Lyman, C. E.; Lifshin, E.; Sawyer, L.; Michael, J. R.** *Scanning Electron Microscopy and X-Ray Microanalysis.* New York: Kluwer Academic/Plenum Publishers, 2003.

38. **Bowen, W. R.; Hilal, N.** *Atomic force microscopy in process engineering: an introduction to AFM for improved processes and products.* Elsevier, 2009. pp. 1-24. Vol. 1.

39. **Valeur, B.** *Molecular fluorescence principles and application.* Weinheim: Wiley-VCH, 2002.

40. **van Holde, K. E.; Johnson, W. C.; Ho, P. S.** *Principles of Physical Biochemistry.* Upper Saddle River: Pearson Prentice-Hall, 2006.

41. *The binding of thioflavin-T to amyloid fibrils: localisation and implications.* **Krebs, M. R. H.; Bromley, E. H. C.; Donald, A. M.** 2005, Journal of Structural Biology, Vol. 149, pp. 30-37.

42. **Wallace, B. A.; Janes, R. W.** *Modern techniques for circular dichroism and synchrotron radiation ciicular dichroism spectroscopy.* Amsterdam: IOS Press, 2009.

43. *A Holistic Approach for Protein Secondary Structure Estimation from Infrared Spectra in H2O Solutions.* **Vedantham, G.; Sparks, H. G.; Sane, S. U.; Tzannis, S.; Przybycien, T. M.** 2000, Analytical Biochemistry, Vol. 285, pp. 33-49.

44. **Schrander, B.** *Infrered and raman spectroscopy: methods and applications.* Weinheim: VCH, 1995.

45. *Protein secondary structures in water from second-derivative amide I infrared spectra.* **Dong, A.; Huang, P.; Caughey, W. S.** 1990, Biochemistry, Vol. 29, pp. 3303-3308.

46. *Secondary structures of proteins adsorbed onto aluminum hydroxide: Infrared spectroscopic analysis of proteins from low solution concentrations.* **Dong, A.; Jones, L. S.; Kerwin, B. A.; Krishnan, S.; Carpenter, J. F.** 2006, Analytical Biochemistry, Vol. 351, pp. 282-289.

47. *Conformational studies of alanine-rich peptide using CD and FTIR spectroscopy.* **Bagínska, K.; Makowska, J.; Wiczk, W.; Kasprzykowski, F.; Chmurzynski, L.** 2008, J. Pept. Sci., Vol. 14, pp. 283-289.

48. **Hunt, B. J.; James, M. I.** *polymer Characterisation.* New York: Marcel Dekker, 1993.

49. **Goodwin, J. W.; Hughes, R. W.** *Rheology for chemists: an introduction.* Cambridge: RSC Plublishing, 2008.

50. **Guinebretière, R.** *X-ray Diffraction by Polycrystalline Materials.* London: ISTE Ltd, 2007.

51. **He, B. B.** *Two-dimensional X-Ray diffraction.* New Jersey: John Wiley & Sons, 2009.

52. **Sun, S. F.** *Physical Chemistry of Macromolecules: Basic principles and issues.* John Wiley & Sons, Inc., 2004. 0-471-28138-7.

53. **He, B. B.** *Two-dimensional X-Ray diffraction.* New Jersey : John Wiley & Sons, 2009.

54. **Buchner, J.; Kiefhaber, T.** *Protein folding handbook.* Weinheim : WILEY-VCH, 2005.

55. **Skoog, D. A.; Holler, F. J.; Crouch, S. R.** *Principles of instrumental analysis.* Canada: Thomson Brooks/Cole, 2007.

56. **Murphy, D. P.** *Fundamentals of light microscopy and electronic imaging.* Sumerset: WILEY-LISS, 2001.

57. *A Novel Bottom-Viewed Inductively Coupled Plasma-Atomic Emission Spectrometry.* **Chan, G. C. Y.; Chan, W. T.** 2004, Spectrochimica Acta Part B, Vol. 59, pp. 41-58.

58. **Clarke, J.; Braginski, A. I.** *The SQUID handbook.* Weinheim : WILEY-VCH, 2004. Vol. II Applications of SQUIDs and SQUID systems.

59. *Magnetic Nanoparticles for Drug Delivery.* **Arruebo, M.; Fernández-Pacheco, R.; Ibarra, M. R.; Santamaría, J.** 2007, Nanotoday, Vol. 2, pp. 22-32.

60. **Mørup, S.; Hansen, M. F.** Superparamagnetic Particles. H. Kronmüller and S. Parkin. *Handbook of Magnetism and Advanced Magnetic Materials.* John Wiley & Sons, 2007, Vol. 4.

61. **Andrä, W.; Häfeli, U.; Hergt, R.; Misri, R.** Application of Magnetic Particles in Medicine and Biology. [book auth.] H. Kronmüller and S. Parkin. *Handbook of Magnetism and Advanced Magnetic Materials.* John Wiley & Sons, 2007, Vol. 4.

62. **Nikiforov, V. N.; Filinova, E. Y.** Biomedical Applications of Magnetic Nanoparticles. [book auth.] S. P. Gubin. *Magnetic Nanoparticles.* Weinheim: WILEY-VCH, 2009, Vol. 10.

63. **Goyen, M.** *Real whole-body MRI: requirements, indications, perspectives.* New York: The McGraw-Hill Companies, Inc, 2008.

64. **Stroman, P. W.** *Essentials of functional MRI.* Boca Raton, London, New York : CRC Press, 2011.

65. **Lecommandoux, SébastienLazzari, Massimo; Liu, Guojun.** An Introduction to Block Copolymer Applications: State-of-the-Art and Future Developments. Massimo Lazzari, Guojun Liu and Sébastien Lecommandoux. *Block Copolymers in Nanoscience.* Germany: WILEY-VCH, 2006.

66. **Hamley, Ian W.** *The Physics of Block Copolymers.* Oxford: Oxford University Press, 1998.

67. *Polymers Get Organized.* **Bucknall , David G.; Anderson, Harry L.** 2003, Science, Vol. 302, pp. 1904-1905.

68. *Aggregation of water-soluble block copolymers in aqueous solutions: Recent trends.* **Nakashima, Kenichi; Bahadur, Pratap.** 2006, Advances in Colloid and Interface Science , Vols. 123-126, pp. 75–96.

69. *Polydispersity and block copolymer self-assembly.* **Lynda, Nathaniel A.; Meulerb, Adam J.; Hillmyer, Marc A.** 2008, Progress in Polymer Science, Vol. 33, pp. 875-893.

70. **Ozin, Geoffrey A.; Arsenault, André C.** Self-Assemblig Block Copolymers. Geoffrey A. Ozin and André C. Arsenault. *Nanochemistry: A chemical approach to nanomaterials.* Toronto: RSC Publishing, 2005.

71. *Structural Properties of Self-assembled Polymeric Aggregates in Aqueous Solutions.* **Mortensen, Kell.** 2001, Polym. Adv. Technol. , Vol. 12, pp. 2-22.

72. *Self-Assembly of Block Copolymer Micelles in an Ionic Liquid.* **He, Y.; Li, Z.; Simone, P.; Lodge, T. P.** 2006, J. Am. Chem. Soc., Vol. 128, pp. 2745-2750.

73. **Hubbard, A. T.** *Encyclopedia of Surface and Colloid Science.* New York: Marcel Dekker, Inc., 2002.

74. *Interaction of polymerizing systems with rubber and its homologs. Part II. Interaction of rubber in the polymerization of methyl methacrylate and of styrene.* **Merrett, F. M.** 1954, Trans. Faraday Soc., Vol. 50, pp. 759-767.

75. *A Supramolecularly Assisted Transformation of Block-Copolymer Micelles into Nanotubes.* **Kim, Sung H.; Nederberg, Frederick; Jakobs, Robert; Tan, Jeremy P. K.; Fukushima, Kazuki; Nelson, Alshakim ; Meijer, E. W.; Yang, Yi Y.;.** 2009, Angew. Chem. Int. Ed., Vol. 48, pp. 4508-4512.

76. *Self-Assembled Block Copolymer Aggregates: From Micelles to Vesicles and their Biological Applications.* **Blanazs, A.; Armes, S. P.; Ryan, A. J.** 2009, Macromol. Rapid Commun., Vol. 30, pp. 267-277.

77. *Structural study on the micelle formation of poly(ethylene oxide)-poly(propylene oxide)-poly(ethylene oxide) triblock copolymer in aqueous solution.* **Mortensen, K.; Pedersen, J. S.** 1993, Macromolecules, Vol. 26, pp. 805-812.

78. *Structure of (Deuterated PEO)–(PPO)–(Deuterated PEO) Block Copolymer Micelles As Determined by Small Angle Neutron Scattering.* **Goldmints, I.; Yu, G. E.; Booth, C.; Smith, K. A.; Hatton, T. A.** 1999, Langmuir, Vol. 15, pp. 1651-1656.

79. *Small-Angle Neutron Scattering Investigation of the Temperature-Dependent Aggregation Behavior of the Block Copolymer Pluronic L64 in Aqueous Solution.* **Yang, L.; Alexandridis, P.; Steyler, D. C.; Kositzia, M. J.; Holwarth, J. F.** 2000, Langmuir, Vol. 16, pp. 8555-8561.

80. *A Supramolecularly Assisted Transformation of Block-Copolymer Micelles into Nanotubes.* **Kim, Sung H.; Nederberg, Frederick; Jakobs, Robert; Tan, Jeremy P. K.; Fukushima, Kazuki;**

Nelson, Alshakim ; Meijer, E. W.; Yang, Yi Y. 2009, Angew. Chem. Int. Ed., Vol. 48, pp. 4508-4512.

81. *Influence of Ionic Surfactants on the Aggregation of Poly(Ethylene Oxide)-Poly(Propylene Oxide)-Poly(Ethylene Oxide) Block Copolymers Studied by Differential Scanning and Isothermal Titration Calorimetry .* **da Silva, R. C.; Olofsson, G.; Schillén, K.; Loh, W.** 2002, J. Phys. Chem. B, Vol. 106, pp. 1239-1246.

82. *Association and Surface Properties of Poly(ethylene oxide)−Poly(styrene oxide) Diblock Copolymers in Aqueous Solution.* **Mai, S. M.; Booth, C.; Kelaraskis, A.; Haverdraki, V.; Ryan, A. J.** 2000, Langmuir, Vol. 16, pp. 1681-1688.

83. *Association Properties of a Diblock Copolymer of Ethylene Oxide and Styrene Oxide in Aqueous Solution Studied by Light Scattering and Rheometry.* **Kelaraski, A.; Havedraki, V.; Rekatas, C. J.; Mai, S. M.; Attwood, D.; Booth, C.; Ryan, A. J.; Hamley, I. W.; Martini, I.** 2001, Macromol. Chem Phys., Vol. 202, pp. 1345-1354.

84. *Micellization and Gelation of Triblock Copolymers of Ethylene Oxide and Styrene Oxide in Aqueous Solution.* **Yang, Z.; Crothers, M.; Ricardo, N. M. P. S.; Chaibundit, C.; Taboada, P.; Mosquera, V.; Kelarakis, A.; Havredaki, V.; Mart, L.; Collect, H. J.; Attwood, D.; Heatley, F.; Booth, C.** 2003, Langmuir, Vol. 19, pp. 943-950.

85. **Katime, I.** *Química Física Macromolecular.* Universidad del País Vasco : Servicio Editorial del País Vasco Euskal Herriko , 1994.

86. *Bilayers and Interdigitation in Block Copolymer Vesicles.* **Battaglia, G.; Ryan, A. J.** 2005, J. Am. Chem. Soc., Vol. 127, pp. 8757-8764.

87. *Shear-Induced Formation of Multilamellar Vesicles ("Onions") in Block Copolymers.* **Zipfel, J.; Lindner, M.; Tsinou, M.; Alexandridis, P.; Richtering, W.** 1999, Langmuir, Vol. 15, pp. 2599-2602.

88. *The evolution of vesicles from bulk lamellar gels.* **Battaglia, G.; Ryan, A. J.** 2005, Nature Materials, Vol. 4, pp. 869-876.

89. *Spontaneous Vesicle Formation in a Block Copolymer System.* **Bryskhe, K.; Jansson, J.; Topgaard, D.; Schillén, K.; Olsson, U. J.** 2004, J. Phys. Chem. B, Vol. 108, pp. 9710-9719.

90. *Association behavior of mixed triblock copoly(oxyalkylene)s (type EBE and ESE) in aqueous solution.* **Ricardo, N. M. P. S.; Chaibundit, C.; Yang, Z.; Attwood, D.; Booth, C.** 2006, Langmuir, Vol. 22, pp. 1301-1306.

91. *Mixtures of triblock copolymers E62P39E62 and E137S18E137 potential for drug delivery from in situ gelling micellar formulations.* **Pinho, M. E. N.; Costa, F. M. L. L.; Filho, F. B. S.; Ricardo, N. M. P. S.; Yeates, S. G.; Attwood, D.; Booth, C.** 2007, Int. J. Pharm., Vol. 328, pp. 95-98.

92. **Creighton, T. E.** *Proteins: structure and molecular.* New York: Freeman, 1993.

93. **Nelson, D. L.; Cox, M. M.** *Principles of biochemistry.* New York: Freeman, 2008.

94. *Are there Pathways for Protein Folding?* **Levinthal, C.** 1968, J. Chim. Phys. Phys. Chim. Biol., Vol. 65, pp. 44-45.

95. *Protein Folding and Unfolding at Atomic Resolution.* **Fersht, A. R.; Daggett, V.** 2002, Cell , Vol. 108, pp. 573-582.

96. *Understanding protein folding via free-energy surfaces from theory and experiment.* **Dinner, A. R.; Sali, A.; Smith, L. J.; Dobson, C. M.; Karplus, M.** 2000, Trends Biochem. Sci. 25 (2000) 331–339., Vol. 25, pp. 331-339.

97. *Navigating the Folding Routes.* **Wolynes, P. G.; Onuchic, J. N; Thirumalai, D.** 1995, Science, Vol. 267, pp. 1619-1620.

98. *Folding versus aggregation: Polypeptide conformations on competing pathways.* **Jahn, T. R.; Radford, S. E.** 2008, Archives of Biochemistry and Biophysics, Vol. 469, pp. 100-117.

99. *Towards complete descriptions of the free–energy landscapes of proteins.* **Vendruscolo, M.; Dobson, C. M.** 2005, Philos. Transact. A Math. Phys. Eng. Sci., Vol. 363, pp. 433-450.

100. *Protein Aggregation and Amyloid Fibril Formation by an SH3 Domain Probed by Limited Proteolysis.* **Polverino de Laureto, P.; Taddei, N.; Frare, E.; Capanni, C.; Costantini, S.; Zurdo,J.; Chiti, F.; Dobson, C. M.; Fontana, A.** 2003, J. Mol. Biol., Vol. 334, pp. 129-141.

101. *Folding funnels, binding funnels, and protein function.* **Tsai, C. J.; Kumar, S.; Nussinov, R.** 1999, Protein Sci., Vol. 8, pp. 1181-1190.

102. *Kinetics and thermodynamics of amyloid fibril assembly.* **Wetzel, R.** 2006, Acc. Chem. Res., Vol. 39, pp. 671-679.

103. *The protofilament structure of insulin amyloid fibrils.* **Jimenez, J. L.; Nettleton, E. J.; Bouchard, M.; Robinson, C. V.; Dobson, C. M.; Saibil, H. L.** 14, 2002, PNAS, Vol. 99.

104. *Hierarchical assembly of β2-microglobulin amyloid in vitro revealed by atomic force microscopy.* **Kad, N. M.; Myers, S. L.; Smith, D. P.; Smith, D. A.; Radford, S. E.; Thomson, N. H.** 2003, J. Mol. Biol., Vol. 330, pp. 785–797.

105. *Einige Bemerkungen über den vegetabilischen Faserstoff und sein Verhältniss zum Stärkemehl.* **Schleiden, M. J.** 1838, Ann. Physik., Vol. 119, pp. 391-397.

106. *On the structural definition of amyloid fibrils and other polypeptide aggregates.* **Fändrich, M.** 2007, Cell. Mol. Life Sci., Vol. 64, pp. 2066-2078.

107. *Amyloids: Not only pathological agents but also ordered nanomaterials.* **Cherny, I.; Gazit, E.** 2008, Angew. Chem. Int., Vol. 47, pp. 4062-4069.

108. *Prediction of the aggregation propensity of proteins from the primary sequence: Aggregation properties of proteomes.* **Castillo, V.; Graña-Montes, R.; Sabate, R.; Ventura, S.** 2011, Biotechnol. J., Vol. 6, pp. 674-685.

109. *Unraveling the Mysteries of Protein Folding and Misfolding.* **Ecroyd, H.; Carver, J. A.** 2008, IUBMB Life, Vol. 60, pp. 769-774.

110. *Mechanisms of amyloid fibril formation–focus on domain-swapping.* **Zerovnik, E.; Stoka, V.; Mirtic, A.; Guncar, G.; Grdadolnik, J.; Staniforth, R. A.; Turk, D.; Turk, V.** 2011, FEBS Journal, Vol. 278, pp. 2263-2282.

111. *Solid-State NMR Study of Amyloid Nanocrystals and Fibrils Formed by the Peptide GNNQQNY from Yeast Prion Protein Sup35p.* **van der Wel, P. C. A.; Lewandowski, J. R.; Griffin, R. G.** 2007, J. Am. Chem. Soc., Vol. 129, p. 5117.

112. *Structural integrity of β-sheet assembly.* **Marshall, K. E.; Serpell, L. C.** 2009, Biochem. Soc. Trans., Vol. 37, pp. 671-676.

113. *Amyloids Fibrils in Bionanobiotechnology.* **Waterhouse, S. H.; Gerrad, J. A.** 2004, Aust. J. Chem., Vol. 57, pp. 519-523.

114. *Design of model systems for amyloid formation: lessons for prediction and inhibition.* **Pastor, M. T.; Esteras-Chopo, A.; de la Paz, M. L.** 2005, Current Opinion in Structural Biology, Vol. 15, pp. 57-63.

115. *A designed system for assessing how sequence affects α to β conformational transitions in proteins.* **Ciani, B.; Hutchinson, E. G.; Sessions, R. B.; Woolfson, D. N.** 2002, J Biol Chem, Vol. 277, pp. 10150-10155.

116. *Mutational analysis of designed peptides that undergo structural transition from α-helix to β-sheet and amyloid fibril formation.* **Takahashi, Y.; Ueno, A.; Mihara, H.** 2000, Structure Fold Des., Vol. 8, pp. 915-925.

117. *Amyloid architecture: complementary assembly of heterogeneous combinations of three or four peptides into amyloid fibrils.* **Takahashi, Y.; Ueno, A.; Mihara, H.** 2002, Chem. Bio. Chem., Vol. 3, pp. 637-642.

118. *Exploring amyloid formation by a de novo design.* **Kammerer, R. A.; Kostrewa, D.; Zurdo, J.; Detken, A.; Garcia-Echeverria, C.; Green, J. D.; Muller, S. A.; Meier, B. H.; Winkler, F. K.; Dobson, C. M.** 2004, Proc. Natl. Acad. Sci., Vol. 101, pp. 4435-4440.

119. *Hacking the code of amyloid formation.* **Pastor, M. T.; Esteras-Chopo, A.; Serrano, L.** 2007, Prion, Vol. 1, pp. 1-14.

120. *Why are "natively unfolded" proteins unstructured under phisiologic condition?* **Uversky, V. N.; Gillespie, J. R.; Fink, A. L.** 2000, PROTEINS: Structure, Function, and Genetics, Vol. 41, pp. 415-427.

121. *Conformational constraints for amyloid fibrillation: the importance of being unfolded.* **Uversky, V. N.; Fink, A. L.** 2004, Biochim. Biophys. Acta, Vol. 1698, pp. 131-153.

122. *Partial denaturation of transthyretin is sufficient for amyloid fibril formation in vitro.* **Colon, W.; Kelly, J. W.** 1992, Biochemistry, Vol. 31, pp. 8654-8660.

123. *Designing conditions for in vitro formation of amyloid protofilaments and fibrils.* **Chiti, F.; Webster, P.; Taddei, N.; Clark, A.; Stefani, M.; Ramponi, G.; Dobson, G. M.** 1999, Proc. Natl. Acad. Sci., Vol. 96, pp. 3590-3594.

124. *Partially Unfolded States of β2-Microglobulin and Amyloid Formation in Vitro.* **McParland, V. J.; Kad, N. M.; Kalverda, A. P; Brown, A.; Kirwin-Jones, P.; Hunter, M. G.; Sunde, M.; Radford, E. S.** 2000, Biochemistry, Vol. 32, pp. 8735-8746.

125. *Assembly of Amyloid Protofibrils via Critical Oligomers-A Novel Pathway of Amyloid Formation.* **Modler, A. J.; Gast, K.; Lutsch, G.; Damaschun, G.** 2003, J. Mol. Biol., Vol. 325, pp. 135-148.

126. *Competing Pathways Determine Fibril Morphology in the Self-assembly of β2-Microglobulin into Amyloid.* **Gosal, W. S.; Morten, I. J.; Hewitt, E. W.; Smith, D. A.; Thomson, N. H.; Radford, S. E.** 2005, J. Mol. Biol., Vol. 351, pp. 850-864.

127. *Direct Observation of Oligomeric Species formed in the Early Stages of Amyloid Fibril Formation using Electrospray Ionisation Mass Spectrometry.* **Smith, A. M.; Jahn, T. R.; Ashcroft, A. E.; Radford, S. E.** 2006, J. Mol. Biol., Vol. 364, pp. 9-19.

128. *Amyloid β-protein (Aβ) assembly: Aβ40 and Aβ42 oligomerize through distinct pathways.* **Bitan, G.; Kirkitadze, M. D.; Lomakin, A.; Voller, S. S.; Benedek, G. B.; Teplow, D. B.** 2003, Proc. Natl. Acad. Sci., Vol. 100, pp. 330-335.

129. *Small Molecule Inhibitors of Aggregation Indicate That Amyloid β Oligomerization and Fibrillization Pathways Are Independent and Distinct.* **Necula, M.; Kayed, R.; Milton, S.; Glabe, C. G.** 2007, J. Biol. Chem., Vol. 282, pp. 10311-10324.

130. *Thermodynamic features of the thermal unfolding of human serum albumin.* **Picó, G. A.** 1997, International Journal of Biological Macromolecules, Vol. 20, pp. 63-73.

131. *Atomic structure and chemistry of human serum albumin.* **He, X. M.; Carter, D. C.** 1992, Vol. 358, pp. 209-215.

132. *Two-dimensional/attenuated total reflection infrared correlation spectroscopy studies on secondary structural changes in human serum albumin in aqueous solutions: pH-dependent structural changes in the secondary structures and in the hydrogen bondings of.* **Murayama, K.; Wu, Y.; Czarnik-Matusewicz, B.; Ozaki, Y.** 2001, J. Phys. Chem. B, Vol. 105, pp. 4763-4769.

133. *Spectroscopic studies on the effect of temperature on pH-induced folded states of human serum albumin.* **Shaw, A. K.; Pal, S. K.** 2008, Journal of Photochemistry and Photobiology B: Biology, Vol. 90, pp. 69-77.

134. *Unfolding of acrylodan-labeled human serum albumin probed by steady-state and time-resolved fluorescence methods.* **Flora, K.; Brennan, J. D.; Baker, G. A.; Doody, M. A.; Bright, F. V.** 1998, Biophysical Journal, Vol. 75, pp. 1084–1096.

135. *Thermal stability of bovine serum albumin DSC study.* **Michnik, A.** 2003, Journal of Thermal Analysis and Calorimetry, Vol. 71, pp. 509-519.

136. *Dilatational Rheology of BSA Conformers at the Air/Water Interface.* **Cascão Pereira, L. G.; Theódoly, O.; Blanch, H. W.; Radke, C. J.** 2003, Langmuir, Vol. 19, pp. 2349-2356.

137. *The three recombinant domains of human serum albumin: structural characterization and ligand binding properties.* **Dockal, M.; Carter, D. C.; Rüker, F.** 41, 1999, The journal of biological chemistry, Vol. 274, pp. 29303–29310.

138. *The behavior of polyamino acids reveals an inverse side chain effect in amyloid structure formation.* **Fändrich, M.; Dobson, C. M.** 2002, The EMBO J., Vol. 21, pp. 5682–5690.

139. *Existence of different structural intermediates on the fibrillation pathway of human serum albumin.* **Juárez, J.; Taboada, P.; Mosquera, V.** 2009, Biophysical Journal, Vol. 96, pp. 2353-2370.

140. *Influence of electrostatic interactions on the fibrillation process of human serum albumin.* **Juárez, J.; Taboada, P.; Mosquera, V.** 2009, J. Phys. Chem. B, Vol. 113, pp. 10521-10529.

141. *Additional supra-self-assembly of human serum albumin under amyloid-like-forming solution conditions.* **Juárez, J.; Taboada, P.; Goy-López, S.; Cambón, Adriana; Madec, M. B.; Yeates, S. G.; Mosquera, V.** 2009, J. Phys. Chem. B, Vol. 113, pp. 12391-12399.

142. *Electrochemical devices made from conducting nanowire networks self-assembled from amyloid fibrils and alkoxysulfonate PEDOT.* **Hamedi, M.; Herland, A.; Karlsson, R. H.; Inganäs, O.** 2008, Nano Lett., Vol. 8, pp. 1736-1740.

143. *Nanomaterials: amyloids reflect their brighter side.* **Mankar, S.; Anoop, A.; Sen, S.; Maji, S. K.** 2011, Nano Reviews, Vol. 2, pp. 1-12.

144. *Nanomechanics of functional and pathological amiloid materials.* **Knowles, T. P. J.; Buehler, M. J.** 2011, Nature nanotechnology, Vol. 6, pp. 469-479.

145. *Seeding-induced self-assembling protein nanowires dramatically increase the sensitivity of immunoassays.* **Men, D.; Guo, Y. C.; Zhang, Z. P.; Wei, H. P.; Zohug, Y. F.; Cui, Z. Q.; Liang, X. S.; Li, K.; Leng, Y.; You, X. Y.; Zhang, X. E.** 2008, Nano Lett., Vol. 9, pp. 2246-2250.

146. *Protofilaments, filaments, ribbons, and fibrils from peptidomimetic self-assembly: implications for amyloid fibril formation and materials science.* **Lashuel, H. A.; LaBrenz, S. R.; Woo, L.; Serpell, L. C.; Kelly, J. W.** 2000, J. Am. Chem. Soc., Vol. 12, pp. 5262-5277.

147. *Ultrathin silver nanowires produced by amyloid biotemplating.* **Malisauskas, M.; Meskys, R.; Morozova-Roche, L. A.** 2008, Biotechnol. Prog., Vol. 2004, pp. 1166-1170.

148. *LSPR-based nanobiosensors.* **Sepúlveda, B.; Angelomé, P. C.; Lechuga, L. M.; Liz-Marzán, L. M.** 2009, Nano today, Vol. 4, pp. 244-251.

149. *Shape-controlled synthesis of silver nanoparticles for plasmonic and sensing applications.* **Cobley, C. M.; Skrabalak, S. E.; Xia, Y.** 2009, Plasmonic, Vol. 4, pp. 171-191.

150. *A comparison study of the catalytic properties of Au-based nanocage, nanoboxes, and nanoparticles.* **Zeng, J.; Zhang, Q.; Chen, J.; Xia, Y.** 2010, Nano lett., Vol. 10, pp. 30-35.

151. *SERS-based diagnosis and biodetection.* **Alvarez-Puebla, R. A.; Liz-Marzán, L. M.** 2010, Small, Vol. 6, pp. 604-610.

152. *A refined solution structure of hen lysozyme determined using residual dipolar coupling data.* **Schwalbe, H.; Grimshaw, S. B.; Spencer, A.; Buck, M.; Boyd, J.; Dobson, C. M.; Redfield, C.; Smith, L. J.** 2001, Protein Science, Vol. 10, pp. 677-688.

153. *Amyloid fibril formation of hen lysozyme depends on the instability of the C-helix (88-99).* **Harada, A.; Azakami, H.; Kato, A.** 2008, Biosci. Biotechnol. Biochem., Vol. 72, pp. 1523-1530.

154. *Comparative study of inactivation and conformational change of lysozyme induced by pulsed electric fields and heat.* **Zhao, W.; Yang, R.** 2008, Eur. Food. Res. Technol., Vol. 228, pp. 47-54.

155. *Thermally induced fibrillar aggregation of hen egg white lysozyme.* **Arnaudov, L. N.; de Vries, R.** 2005, Biophysical Journal, Vol. 88, pp. 515-526.

156. *Catalytic properties of gold nanoparticles immobilized on the surfaces of Nanocarriers.* **Chen, X.; Zhao, D.; An, Y.; Shi, L.; Hou,W.; Chen, L.** 2010, J. Nanopart. Res., Vol. 12, pp. 1877-1887.

157. *Preparation of gold-dendrimer nanocomposites by laser irradiation and their catalytic reduction of 4-nitrophenol, immobilization and Recovery of Au Nanoparticles from anion exchange resin.* **Hayakawa, K.; Yoshimura, T.; Esumi, K.** 2003, Langmuir, Vol. 19, pp. 5517-5521.

158. *A nanoreactor framework of a Au@SiO2 yolk/shell structure for catalytic reduction of p-nitrophenol.* **Lee, J.; Park, L. C.; Song, H.** 2008, Adv. Mater. 2008, 20, 1523–1528., Vol. 20, pp. 1523-1528.

159. *Responsive catalysis of thermoresponsive micelle-supported gold nanoparticles.* **Wang, Y.; Wei, G.; Zhang, W.; Jiang, X.; Zheng, P.; Shi, L.; Dong, A.** 2007, J. Mol. Catal. A: Chem., Vol. 266, pp. 233-238.

160. *Magnetic nanoparticle assemblies on denatured DNA show unusual magnetic relaxivity and potential applications for MRI.* **Byrne, S. J.; Corr, S. A.; Gun'ko, Y. K.; Kelly, J. M.; Brougham, D. F.; Ghosh , S.** 2004, Chem. Commun., pp. 2560-2561.

161. *Linear assemblies of magnetic nanoparticles as MRI contrast agents.* **Corr, S. A.; Byrne, S. J.; Tekoriute, R.; Meledandri, C. J.; Bougham, D. F.; Lynch, M.; Kerskens, C.; O'Dwyer, L.; Gun'ko, Y. K.** 2008, J. Am. Chem. Soc., Vol. 130, pp. 4214-4215.

162. *Wrap–bake–peel process for nanostructural transformation from bold beta-FeOOH nanorods to biocompatible iron oxide nanocapsules.* **Piao, Y.; Kim, J.; Na, H. B.; Kim, D.; Baek, J. S.; Ko, M. K.; Lee, J. H.; Shokouhimehr, M.; Hyeon, T.** 2008, Nat. Matter., Vol. 7, pp. 242-247.